

NORTHWESTERN UNIVERSITY

Self-Assembly of Small Molecules for Organic Photovoltaic Applications

A DISSERTATION

SUBMITTED TO THE GRADUATE SCHOOL
IN PARTIAL FULFILLMENT OF THE REQUIREMENTS

for the degree

DOCTOR OF PHILOSOPHY

Field of Materials Science and Engineering

By

Taner Aytun

EVANSTON, ILLINOIS

December 2016

© Copyright by Taner Aytun 2016
All Rights Reserved

ABSTRACT

Self-Assembly of Small Molecules for Organic Photovoltaic Applications

Taner Aytun

Organic photovoltaic (OPV) solar cells aim to provide efficient, flexible and lightweight photovoltaics (PV) with simple processing and low-cost. Advances in device optimization, structural and molecular design, as well as mechanistic understanding have helped increase device efficiency and performance. Within the framework of active layer optimization, systematically improving bulk heterojunction (BHJ) morphology could improve the power conversion efficiency of OPVs. However, most strategies aimed at improving morphology focus on annealing methods or the use of solvent additives. Rational approaches in supramolecular self-assembly can potentially offer additional control over the morphology of BHJ active layers and lead to improved power conversion efficiencies. In Chapter 2, the author explores the effect of molecular shape on the assembly of electron donating small molecules, and its ensuing effect on OPV performance. Two tripodal 'star-shaped' donor molecules with diketopyrrolopyrrole (DPP) side chains were used to generate solution-processed BHJ OPVs. It was found that the tripod molecules neither aggregate in solution nor form crystalline domains in thin films when a branched alkyl solubilizing group is used. On the other hand, linear alkyl chains promote the formation of one-dimensional (1D) nanowires and crystalline domains as well. This work demonstrated that the one-dimensional assembly of donor molecules enhances the performance of the corresponding solution-processed OPVs by 50%. This is attributed to the reduction of trap states in the 1D nanowires, resulting in a significant increase in the fill factor of the devices. In Chapter 3, experiments are described in which the electron donor is a hairpin-shaped molecule containing a trans-1,2-diamidocyclohexane core and two DPP conjugated segments, and a fullerene derivative as the electron acceptor. Self-assembly of the donor molecule is driven by the synergistic interaction between hydrogen bonds and $\pi - \pi$ stacking, and

under proper conditions this results in the formation of long supramolecular nanowires that enhance charge transport and device efficiencies. The efficiencies of these devices were found to be 54% greater than those built with analogous donor small molecules containing only the conjugated structure. In addition, it was shown that a stepwise cooling process with minimal solution stirring is necessary to create robust wires that are not disrupted upon addition of acceptor molecules. This resulted in a 400-fold increase in device efficiency compared to those formed by simple mixing of donor and acceptor molecules. To further improve OPV device efficiency using hydrogen bonding in small molecule electron donors, the use of hydrogen bonding in linear molecules with DPP was investigated and this work is described in chapter 4. Two asymmetric derivatives were compared: one containing an amide bond, capable of forming hydrogen bonds, and a second one contained an ester bond in the same position. Although both molecules have very similar optoelectronic properties, films of the ester revealed greater crystallinity and $\pi - \pi$ stacking, as characterized by grazing incidence x-ray diffraction. In great contrast, active layers formed with the amide derivative formed short fiber-like supramolecular aggregates with much smaller domain sizes and less order as characterized by atomic force microscopy and X-ray diffraction. Interestingly, devices fabricated with the amide-fullerene donor-acceptor combination have greater short circuit currents, leading to devices that are 50% more efficient than those built with the ester derivative. We concluded that the effective competition of hydrogen bonding over extensive $\pi - \pi$ stacking results in morphologies that lead to higher photovoltaic efficiencies. Taken together, the findings in this work demonstrate improved OPV device efficiency by use of supramolecular self-assembly and the control of shape of donor molecules.

ACKNOWLEDGEMENTS

Collaborations are a vital part of research and most of these collaborations are often more than just sharing data and techniques as in the case of this thesis. I feel really lucky to be able to collaborate with amazing people who not only share some scientific data but also shared their valuable time to listen and to help; shared their passion, and sometimes their life experiences and stories. I would not be able to write this thesis without the dedicated collaboration of many wonderful people. First and foremost, I would like to express my gratitude to Professor Samuel Stupp for his advisory and support throughout my PhD. He has worked really hard to create the best research environment for his students. Easy access to most resources gave an immense confidence for many of us to carry out all the experiments with a great flexibility and creativity.

I would like to thank the committee members: Prof. Kennett Shull, Prof. Lincoln Lauhon, Prof. Koray Aydin, and Prof. Michael Bedzyk for their valuable time and advice that encourage me to think critically in my research. I would not have come to Northwestern and had the opportunity to do PhD without the help and guidance from my previous advisor during the undergraduate education and my Master's, Prof. Cleve Ow-Yang, who continues to support me throughout my academic career. I am also grateful to my co-advisor during my Master's, Prof. Ayse Turak, who was the first one to get me interested in organic photovoltaics.

The Stupp Group members have always made a very friendly and diverse research environment both culturally and scientifically. The projects that I have accomplished would not be possible without the direct collaboration of many group members. Starting with my partner in crime: Leonel Barreda, who is an incredible chemist! We have gone through many difficulties together but still made few projects work. I cannot say enough to show my appreciation to him and the amount of time he put into making those complex molecules. His dedication to the chemistry side of the projects always made me extra responsible and careful with the duties I need to do. Another great chemist I worked with was Dr. Carson Bruns who started the tripod project. His positive attitude

to our failures made it possible to bring the project to fruition in the end. One of his greatest gifts to the project was recruiting our beloved undergraduate PJ Santos who did significant amount of chemistry even though he was a MatSci major. PJ put more effort than a regular undergrad and played a key role in our project. He also made me proud with all the great achievements and awards he got during his time in our lab. The first chemist I worked with was Dr. Amparo Ruiz Carretero who also had significant contribution into my thesis. She was not only very hard working and pushy in the projects but also a fun person to work with; several times she made people in the lab roll in the aisles with her tomato jokes.

Different expertise of several Stupp Group members became really handy when I was trying to answer some hard questions. Dongxu Huang's contribution with the simulations he did was really important for tripod projects. So does Andrew Koltonow, who not only helped with impedance measurements for tripod project but also was my buddy in several Argonne trips. I cannot forget the time we went together during a Thanksgiving holiday! This proved his great friendship and sacrifices that he can make for his friends! Dr. Jessica Lehrman was very helpful with her TEM skills as well. We spent great amount of time on her project and had adventurous trips to clean room to characterize her "noodle" samples while struggling to hold several components of the experimental set-up tight. Another person that helped with TEM was Dr. Cristina Newcomb who was a master at cryo-TEM that she had to characterize almost everyone's sample at some time point. Recently, I had a privilege to work with Adam Dannenhoffer, who is a hard working Material Scientist with valuable chemistry skills. I really hope our efforts in the new research avenue will result in a great paper.

I was able to learn more and get amazed with the science that other people do either in our group or in other groups when they recruited me to their research. It was always interesting to see wonders of self-assembly in nano-scale when I look at samples of Dr. Roman Kazantsev and Dr. Adam Weingarten, both did a great job in their PhD. Similarly, Dr. Christopher Synatschke's and Stacey Chin's samples in polymer matrixes were challenging but fun to analyze. Dr. Charles Rubert's

life saving molecules never disappoint me with the artistic and beautiful assemblies they made. I am thankful to many Stoddart group members who included me in their research, in particular to Dr. Deniz Yilmaz who always had a strong commitment to projects, and also to Dr. Ashish Basuray, Dr. Srinivasan Sampath, Dr. Karel Hartlieb and Dr. Albert Fahrenbach for their collaboration and for teaching interesting science to me.

I am greatly indebted to few senior graduate students and mentors in the Stupp Group who initiated some of the projects I worked on and taught me how to use several equipments and techniques. Dr. Ian Tevis was really helpful when I first came to lab and the things he taught me was useful throughout my PhD. The project they started with Dr. Wei-Wen Tsai was really interesting and gave us a good direction to pursue. Dr. Dave Herman was not only a great and a wise officemate with interesting stories every other day but also a great mentor for organizing Argonne trips and teaching X-ray techniques in my first few years. We had a great time with Alok Tayi when he came to visit me in Istanbul for few days; I hope he enjoyed me being a tour guide as much I enjoyed his tour and guidance when I first joined the lab. Dr. Liam Palmer was always very accommodating and open to help whenever I had a problem in the lab or in general. His editing and critical thinking especially right before submitting important papers and proposals were really crucial to achieve success.

Being able to use state of art equipment and techniques was one of the important aspects of my PhD at Northwestern. I am indebted to several people who tried their best to keep equipments running and do necessary upgrades. I especially thank to Dr. Gajendra Shekhawat for his technical support to AFM, Dr. Xinqi Chen for his technical support to XPS/UPS, Dr. Nasir Basit for his technical support to clean room and probe station and Dr. Joseph Strzalka from Argonne National Lab for his support to GIWAXS at APS 8-ID-E beamline. The following shared facilities at Northwestern University are used: IMSERC, Keck Biophysics and the NIFTI facility of NUANCE Center and NU-FAB. NUANCE Center is supported by NSF-NSEC, NSF-MRSEC, the Keck Foundation, the State of Illinois and Northwestern University; IMSERC NMR usage under award NSF CHE-1048773 is

appreciated. Micro/Nano Fabrication Facility (NUFAB) is supported by the State of Illinois and Northwestern University. Use of Advanced Photon Source sector 8-ID-E, an Office of Science User Facility operated for the U.S. Department of Energy (DOE) Office of Science by Argonne National Laboratory, was supported by the U.S. DOE under Contract No. DE-AC02-06CH11357. Moreover, the administrative staff of the Stupp group made all sorts of paperwork, purchasing and paper submissions extremely easy. I especially thank to Laura Fields for always finding a solution to my problems, the other administrative staff we had over the years including Maura Walsh, Matthew Irwin, Jill Johnson, Sharon Jacknow, Rebekah Hastad and Bryan Runkel.

Special shout out to Cook Hall office mates that made a really warm and enjoyable office environment. Ashwin Narayanan was great at motivating me to graduate by being a pain in the neck nonstop! I hope I was able to teach him enough in the lab that pays back his patient squash lessons he gave me for free. It was always pleasurable to spend time with him, even in that little AFM room! I especially thank him for editing part of my thesis. Nick Sather also helped me with the thesis edits, and besides that his chill attitude towards life and things happening in the lab was always calming. I had a lot of fun by just being around him as much as the times I beat him in squash. Another person that helped editing several of my writings was Garrett Lau who was also super patient with my annoying snap-chats! Garrett's support and leadership to our little coffee club was very instrumental in keeping me awake and motivated. DJ Fairfield was really helpful with several lab related things, either fixing equipments or ordering supplies or trying new experiments. His presence in the lab was always very comforting and made several things much easier including the GIWAXS trips to Argonne. Dr. Hiroaki Sai was a very valuable addition to our office, he was always open to help and discussion and also never felt short with office snacks and cute cat pictures on his screen.

My classmates who already became doctors were very supportive companions throughout the grad school. Both Dr. Tuncay Ozel and Dr. Faifan Tantakitti were always open to help when I face a challenge either in lab or in life. They were always available for a brunch, or coffee or fun cultural dinner nights along with our biryani chef Dr. Deep Jariwala and board game master Jessie

Ku. Speaking of board games, Dr. Eduard Sleep was a welcoming host for nerd board games and it was my pleasure to challenge the whole Stupp group postdoc team including Dr. Christopher Synatschke and Dr. Kohei Sato.

One of the benefits of being in a big city as Chicago, I was able to gain amazing friends who were like a family to me and always made me feel like at home. My best friend Osmaan Akhtar was like a true brother to me and a constant support in every means in the last three years. He and his amazing family hosted me several times for dinners and other gatherings and never stop praying for my success. Osmaan not only took trips around US and to 4 other countries with me, but also he introduced me to several other great friends in the Chicago area. Talha Ali is one of those great friends whom I enjoy “partying” with, either while biking, or while getting fat with kebabs and ice-creams, or just partying while we were practicing bhangra for weddings. He was also very patient when we were making fun of his losses after every Catan game we played with Zain Lodhia-Romaytha Abdullah couple (or so called Zoma). Zoma were great hosts for parties, board games or GoT nights all the time, never short of snacks or smiling faces that warmed my heart and give me motivation in difficult times. Sarah Ahmed and Iman Sediqe were my fellow grad-Northwestern friends that I knew through my non-Northwestern circle, together with Osmaan we formed OTIS. We had so many fun memories as OTIS including water marbling classes we took together or random coffee-ice cream-icafe gatherings. Both Sarah and Iman were very positive grad students I had around who were able to overcome challenges easily and also encourage me to overcome the challenges I had. Shaz Kaseruddin and Ahmed Minhaj couple has been great cheerleaders to get my PhD and join the “elite” group of advance degree holders. They were always inclusive and energetic in any gatherings, and very warm hosts for so many random events. Another cheerleader for many people, Amena Qureshi who cannot say “No” to anyone, never get board of hosting people or listening my nerd conversations, Amena is a true social butterfly with a great network. Kazmi siblings (Omer-Yasir-Sanaa) and their wonderful family have invited me for so many dinners and cool events and they have constantly looked after me, I cannot tell how happy that made me for

so many times and made me feel really lucky to be surrounded with them. Another person that I met through them and very recently married with my best friend Talha, Maryam Arfeen is a great friend with a great character and she is never out of interesting questions leading to deeper and more serious conversations that I enjoy a lot. Cem who is a dear friend from Turkey and moved to Chicago recently has never disappointed me with spontaneity and being courageous to get bonus points from random events such as inviting 40 people over a dinner on the spur of the moment and making me a co-host was just a mere example of the “normal” things we did together. Another Turkish friend that I knew from undergrad and has been in Chicago is Begum who was like an elder sister to me since I have started grad school; she and her mom Ayca Teyze, never left me without authentic Turkish food and baklava. Kezban-Gurkan couple also did not leave me hungry and invited me over for several Turkish dinners at their place with a growing number at the table with the addition of little Efe. I should not forget my dear friend Suleyman Dost at UChicago and his wife Ryma who were very welcoming and entertaining hosts. It was a pleasure to have enjoyable practice Turkish conversations with my Greek friend Alex Papulis who has been a great learner and also and has been open to intellectual discussions we hold together with Jack and others. Special thanks to Team “Manda Kaymagi”, Huseyin-Alim-Ahmet, my friends from undergrad that they never stop supporting me or visiting me either in Chicago or in my hometown. Our mutual visits gave me a little break each time and they were pleasant remembrance of undergraduate years.

Last but not the least I am thankful to my parents for their unwavering love and support. I am thankful to my sister Aysun Kural and her whole family who lives in France: her husband Ilker Kural, my nephew Orkun, my niece Senanur. I was able to visit them several times and they were always a great host with great food and cool tours, it was fun to ski on the beautiful French Alps and hang out with their friends. I am also thankful to my brother Ali Aytun and his wife Humay Aytun and their son, my little nephew Ali Burak, who were very welcoming hosts every time I visited home and they tried their best to take me around and help me with all my shopping. I cannot forget my

sister from another mister, Selda Balaban and her entire family for their sincere care and delicious food they cook for me whenever they invited me over.

*This dissertation is dedicated to
my family and teachers.*

CONTENTS

ACKNOWLEDGEMENTS	5
LIST OF ABBREVIATIONS	18
1 INTRODUCTION	23
1.1 Objective and Significance of Solar Research	23
1.2 The Basics of Organic Solar Cells	28
1.2.1 Device Geometry	28
1.2.2 Device Operation and Performance Evaluation	30
1.2.3 Theoretical Limits	34
1.3 Strategies to Increase the Efficiency of OPVs	36
1.3.1 Material Design for Polymers and Small Molecules	36
1.3.2 Interface Engineering	41
1.3.3 Control of Morphology	44
1.4 Thesis overview	59
2 SELF-ASSEMBLING TRIPODAL SMALL-MOLECULE DONORS FOR BULK HETEROJUNCTION SOLAR CELLS	61
2.1 Objectives and significance	61
2.2 Background	61
2.3 Results and discussion	63
2.3.1 Synthesis and Characterization	63
2.3.2 Supramolecular Self-Assembly of Tripodal Molecules	65
2.3.3 Morphology of the Active Layer	69
2.3.4 Photovoltaic Properties of Tripodal Molecules	73
2.3.5 Hole mobility and Impedance Spectroscopy of Tripod Solar Cells	76
2.4 Conclusion	78
2.5 Outlook	79
2.6 Materials and methods	84
3 STEPWISE SELF-ASSEMBLY TO IMPROVE SOLAR CELL MORPHOLOGY	89
3.1 Objectives and Significance	89
3.2 Background	89
3.3 Results and Discussion	91
3.3.1 Synthesis of hairpin-shaped diketopyrrolopyrrole molecule	91
3.3.2 DPPHP performance in organic photovoltaics. Influence of self-assembly on device efficiency	91

3.4	Conclusion	105
3.5	Materials and methods	108
4	IMPROVING SOLAR CELL EFFICIENCY THROUGH COMPETITIVE HYDROGEN BONDING: A METHOD FOR TUNING ACTIVE LAYER MORPHOLOGY	114
4.1	Objectives and Significance	114
4.2	Background	114
4.3	Results and Discussion	116
4.3.1	Photovoltaic Properties and Morphology of Symmetric Donors	121
4.3.2	Photovoltaic Properties of Asymmetric Donor Molecules	126
4.3.3	Active Layer Morphology	130
4.3.4	Structural Order in the Active Layer	131
4.4	Conclusion	137
4.5	Outlook	138
4.6	Materials and methods	142
5	SUMMARY AND FUTURE OUTLOOK	156
	REFERENCES	159
	VITA	176

LIST OF TABLES

2.1	Optical Properties of Solutions and Films of Tripod Molecules	66
2.2	Optimized solar cell results of tripod molecules with PC ₇₁ BM.	75
3.1	Photovoltaic Characteristics of DPPHP:PC ₇₁ BM Blends	101
3.2	Photovoltaic Characteristics of DPPHP:PC ₇₁ BM Blends with Different Spin Rates	103
4.1	Electronic Properties of Donors.	120
4.2	Photovoltaic Device Performance of Symmetric Donor Molecules	121
4.3	Photovoltaic Device Performance of Symmetric Donor Molecules with Additives	124
4.4	Photovoltaic Device Performance of Asymmetric Donor Molecules with Additives	127
4.5	Photovoltaic Device Performance of Asymmetric Donor Molecules with Different Additives	128
4.6	Calculated GIXD Parameters for Asymmetric DonorPC ₇₁ BM Blends	135
4.7	Thicknesses of Active Layer Blends	154

LIST OF FIGURES

1.1	Global Energy Consumption	24
1.2	Energy Generation by Source Over Years	25
1.3	NREL Best Cell Efficiency Chart	26
1.4	Energy Payback Time for Cells	27
1.5	Different OPV Architectures	29
1.6	Illustration of OPV Device Operation with Common Materials	31
1.7	JV Curve for P ₃ HT:PCBM with a Equivalent Circuit Model	32
1.8	AM 1.5G Spectrum and P ₃ HT:PCBM Spectral Response	33
1.9	Maximum Efficiency and Fill Factor Predicted for OPVs	34
1.10	Efficiency Contour Plot for OPVs	35
1.11	Molecular Orbital Reconstruction in Push-Pull Molecules	36
1.12	Common Electron Donating and Withdrawing Groups	37
1.13	Common Electron Donor Polymers	39
1.14	Common Electron Donor Small Molecules	40
1.15	Common Electron Acceptor Fullerene Derivatives	40
1.16	Metal-Semiconductor Junction	42
1.17	Energy Diagram of Recent Electron Transport and Hole Transport Layers	44
1.18	Cros-section of P ₃ HT:PCBM and the Ideal Morphology	46
1.19	TEM Imaging and Electron Tomography of OPV Active Layer	48

1.20	AFM Imaging of OPV Active Layer in Tapping Mode and Conductive Mode	49
1.21	GIWAXS Measurement for P ₃ HT Film	51
1.22	SACS and SANS Measurements on P ₃ HT:PCBM Active Layer	52
1.23	AFM Images Revealing Affect of Thermal Annealing on P ₃ HT:PCBM Active Layers	54
1.24	Schematic Depicting the Affect of Thermal Annealing on P ₃ HT:PCBM Active Layers	55
1.25	TEM Images Revealing Affect of DIO on Morphology of PTB7:PC ₇₁ BM Active Layer	56
1.26	Face-Face Stacking of P ₃ HT Resulting in Nanowire Morphology	58
2.1	Chemical Structure and Opto-electronic Properties of Tripodal Molecules	64
2.2	UP Spectra and Extracted HOMO Levels	65
2.3	AFM Images of Native Films of Tripodal Molecules	67
2.4	AFM Images of Native T _{EH} Films	68
2.5	2D-GIXD Results for Native Films of Tripodal Molecules	68
2.6	Molecular Dynamics Simulations Results for Tripodal Molecules	70
2.7	AFM Images of Active Layer Morphology of T _{EH} Molecule	71
2.8	AFM Images of Active Layer Morphology of T _{C12} Molecule	72
2.9	Absorption spectra of Tripodal Molecule Solar Cells in Solid Film.	73
2.10	GIXD of of Tripodal Molecule Solar Cells in Solid Film	74
2.11	Optimized Solar Cell Results of Tripodal Molecules	75
2.12	Hole Mobility Measurements of Tripodal Solar Cells with SCLC	77
2.13	Impedance Measurements of Tripodal Solar Cells	78
3.1	DPPHP Chemical Structure and Synthetic Route	92
3.2	Absorption Spectra of DPPHP	93
3.3	Solar Cell Results for DPPHP	94
3.4	Solar Cell and AFM Results for DPPHP without Self-Assembly	94
3.5	Step-wise Self-Assembly illustration of DPPHP	96
3.6	AFM images of DPPHP Films	97
3.7	Cryo-TEM of DPPHP and DPPHP:PC ₇₁ BM in Solution	98
3.8	Absorption Spectra of DPPHP Thin Films	99
3.9	AFM of DPPHP Active Layers from Chlorobenzene	99
3.10	AFM of DPPHP Active Layers from Toluene	100
3.11	AFM Image of DPPHP After Stirring for 12 hours	104
3.12	AFM Image of LDM Control Molecule	105
3.13	Absorption Spectra of LDM Control Molecule	106
3.14	AFM Image of LDM Active Layer	106
3.15	Dark Current Density Plot for DDPHP and LDM Device Blends	107

4.1	Synthesis of Symmetric and Asymmetric Donors	117
4.2	Absorption Spectra of Donor Molecules	119
4.3	Absorption Spectra of Donors with Extinction Coefficients	119
4.4	Cyclic Voltammograms of Donor Molecules	120
4.5	Infrared Spectra of Donor Molecules	122
4.6	Infrared Spectra of Donor Molecules and N-benzyl-2-cyanoacetate	123
4.7	Schematic Illustration of Solar Cell Architecture	124
4.8	AFM Images of Symmetric Molecule - PC ₇₁ BM Active Layers	125
4.9	Optimized Solar Cell Results for Symmetric Donor Molecules	125
4.10	Optimized Solar Cell Results for Asymmetric Donor Molecules	127
4.11	Solar Cell of Asymmetric Molecules with Different Additives	128
4.12	SCLC Results for Asymmetric Molecule:PC ₇₁ BM Active Layers	129
4.13	AFM Results for Asymmetric Molecule:PC ₇₁ BM Active Layers	131
4.14	TEM Results for Asymmetric Molecule:PC ₇₁ BM Active Layers	132
4.15	GIXD Results for Asymmetric Molecule:PC ₇₁ BM Active Layers	134
4.16	GIXD Results for Asymmetric Molecule for Neat Films	134
4.17	AFM Results for Neat Films of Asymmetric Molecules	136
4.18	Schematic Illustration of Active Layer Morphology for Asymmetric Molecules	137

LIST OF ABBREVIATIONS

1D One Dimensional

2D Two Dimensional

6T Sexithiophene

6THP Sexithiophene Hairpin-Shaped Molecule

A Acceptor

A-Amide Asymmetric Amide Molecule

A-Ester Asymmetric Ester Molecule

AFM Atomic Force Microscopy

Ag Silver

Al Aluminum

Au Gold

BDT Benzodithiophene

BHJ Bulk Heterojunction

CB Chlorobenzene

CHCl₃ Chlorofom

COF Covalent Organic Frameworks

CryoTEM Cryogenic Transmission Electron Microscopy

CT Charge Transfer

CV Cyclic Voltammetry

D Donor

D-A Donor-Acceptor

DCM Dicholoromethane

DI Deionized

DIO 1-8,Diiodooctane
DLC Discotic Liquid Crystal
DMF Dimethylformamide
DPP Diketopyrrolopyrrole
DPPHP Diketopyrrolopyrrole Hairpin-Shaped Molecule
DSC Differential Scanning Calorimetry
DSSC Dye-Synthesized Solar Cells
 E_b Energy barrier
 E_g Bandgap
EQE External Quantum Efficiency
eV Electron Volts
FF Fill Factor
 g Paracrystallinity
GIXD Grazing Incidence X-Ray Diffraction
GIWAXS Grazing Incidence Wide Angle X-ray Scattering
GO Graphene Oxide
H₂O Water
HCl Hydrochloric Acid
HOMO Highest Occupied Molecular Orbital
IR Infrared
ITO Indium Tin Oxide
 J Current
 J_{sc} Short-Circuit Current
 η efficiency
kW Kilowatt
 L_a Crystal Size

LC Liquid Crystal
LiF Lithium Fluoride
LUMO Lowest Unoccupied Molecular Orbital
 μ Mobility
 μ_e Electron Mobility
 μ_h Hole Mobility
mA Milliamps
MC m-cresol
MD Molecular Dynamics
MeOH Methanol
mg Milligrams
min Minutes
mL Milliliters
mm Millimeters
MoOx Molybdenum Oxide
MS Mass Spectroscopy
Mw Weight Average Molecular Weight
N₂ Nitrogen
NB Nitrobenzene
NIST National Institute of Standards and Technology
nm Nanometers
NMR Nucleic Magnetic Resonance
NREL National Renewable Energy Laboratory
 Ω Ohms
O₂ Oxygen
OFET Organic Field Effect Transistor

OPV Organic Photovoltaic

PCBM Phenyl-C₆₁-Butyric Acid Methyl Ester

PC₇₁BM Phenyl-C₇₁-Butyric Acid Methyl Ester

PCE Power Conversion Efficiency

PEDOT:PSS Poly(3,4-ethylenedioxythiophene):Poly(styrenesulfonate)

PV Photovoltaic

rpm Revolutions per Minute

R_S Series Resistance

R_{SH} Shunt Resistance

RT Room Temperature

S Herman's Orientation Parameter

S-Amide Symmetric Amide Molecule

S-Ester Symmetric Ester Molecule

SAXS Small-angle X-ray Scattering

SCLC Space-Charge Limited Current

SEM Scanning Electron Microscopy

SiO₂ Silicon Dioxide

SOF Supramolecular Organic Frameworks

T Thiophene

T_{C12} Tripodal Molecule with Dodecyl

T_{EH} Tripodal Molecule with Ethylhexyl

TEM Transmission Electron Microscopy

TFA Trifluoroacetic Acid

THF Tetrahydrofuran

TPA Triphenyl Amine

UPS Ultraviolet Photoelectron Spectroscopy

UV Ultraviolet

V Voltage

V_{OC} Open-Circuit Voltage

v/v Volume Ratio

W Watt

w/w Weight Ratio

ZnO Zinc Oxide

1 INTRODUCTION

1.1 OBJECTIVE AND SIGNIFICANCE OF SOLAR RESEARCH

Traditional energy sources are being depleted every day while mankind's energy demand is increasing. For many nations, fuel supplies are serving as an engine for economic growth and influence the lives of a vast number of people. As many countries in the world continue to develop, growth in energy demand will be inevitable. Currently, to meet the energy demands, using hydrocarbon sources are enough in terms of energy density, shelf-life, and transportability. However, relying on such sources in the long term can negatively affect the global climate and biosphere due to the emitted byproducts such as carbon dioxide.¹ Conserving the energy through improving the efficiency of current systems represents the most-cost effective and impactful approaches in the short-term to decrease the carbon dioxide emission but conservation alone will not be enough to meet the expected future need. In this respect, using and investing on renewable energy sources in our daily lives is becoming indispensable.

Today we consume 18 terawatts (TW) of energy worldwide and this is anticipated to increase over 25 TW by 2035 and 30 TW by the year 2050.² This is almost doubling the need for energy and it raises two main concerns: (1) which sources can be utilized for this and (2) what will be the consequences of utilizing these sources. These will be among the main issues of humanity that will affect lives of future generations. Before making estimates about the future energy supplies, it is important to understand the current mix. As it can be seen in the figure, most of the current energy demands is being met by fossil fuels (including natural gas, liquids and coal), while only 11% of it comes from renewable sources (Fig. 1.1). Hydroelectric occupies the large portion of renewable energy mix and only 2% of renewable energy comes from the contribution of solar energy worldwide. Abundance of fossil fuels and the existing infrastructure to utilize these resources make it a low cost and attractive energy source.

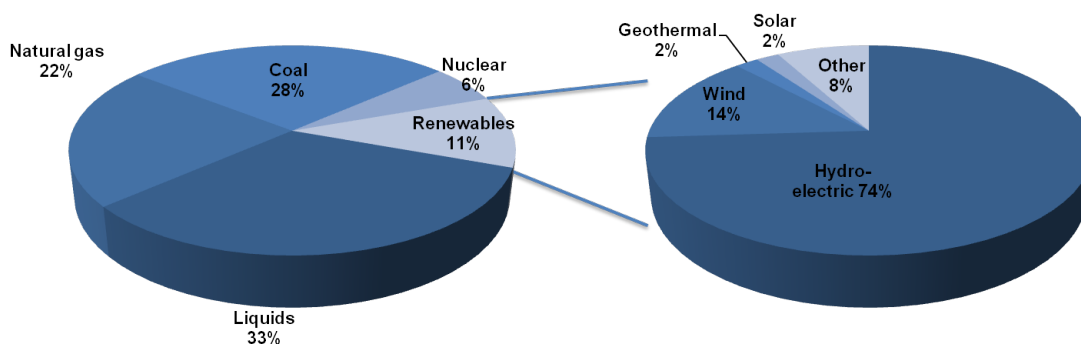


Figure 1.1: Global energy consumption breakdown by energy source in 2013 derived from the EIA reference case1.^{2,3}

However, there are hidden costs associated the use of fossil fuels and their by products. Use of these resources cause irreversible destruction of habitat of planet, acid rains, toxic and heavy metals, air and water pollution.⁴ The hidden costs come with these are medical bills, higher insurance and food costs and the cost of cleaning the environment. In addition to these hidden costs, change in the climate and difficulty of handling some of these resources put lives in danger through floods, droughts, storms and nuclear waste spills. All of these problems and concerns further necessitate the investment and adaptation of renewable sources.

Among other renewable energy sources such as wind and geothermal, solar energy is the most abundant and most promising alternative energy source. With a basic assumption of covering 2% of Earth's surface with 12% efficient solar cells, the power output can be as high as 67TW which is much larger than the projected energy need.⁵ Furthermore, the projected growth for the solar until 2050 is really significant as shown in the Fig. 1.2. The assumptions that go into this study are that government policies promote alternative energy (with large investment in solar), natural gas remains the main source of energy and nuclear electricity is led and controlled by government. Based on this study, the annual growth of solar energy implementation is 15%. Although there are different ways of utilizing solar energy such as concentrated solar power⁶, solar water and air heating⁷, natural lighting, and solar fuels⁸, this thesis will focus on photovoltaics – directly converting sunlight to electricity.

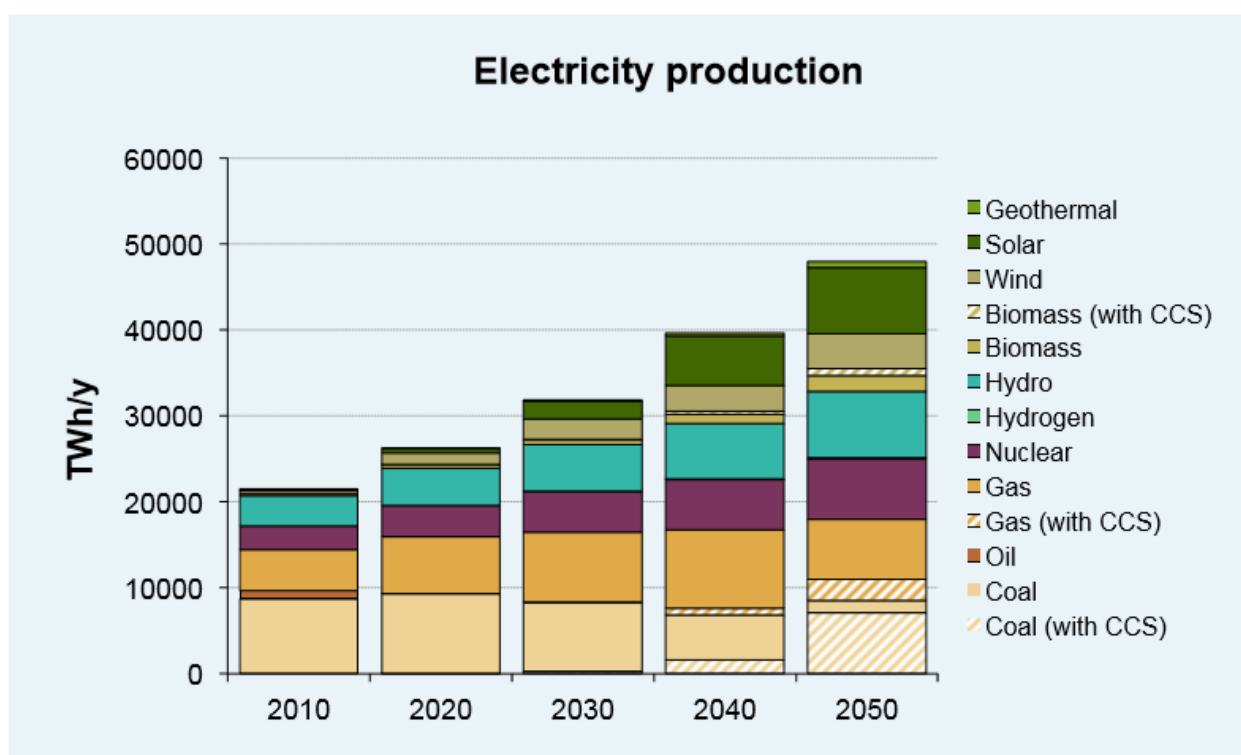


Figure 1.2: Installed electricity generation capacity by primary energy type Source: World Energy Council (2013)²

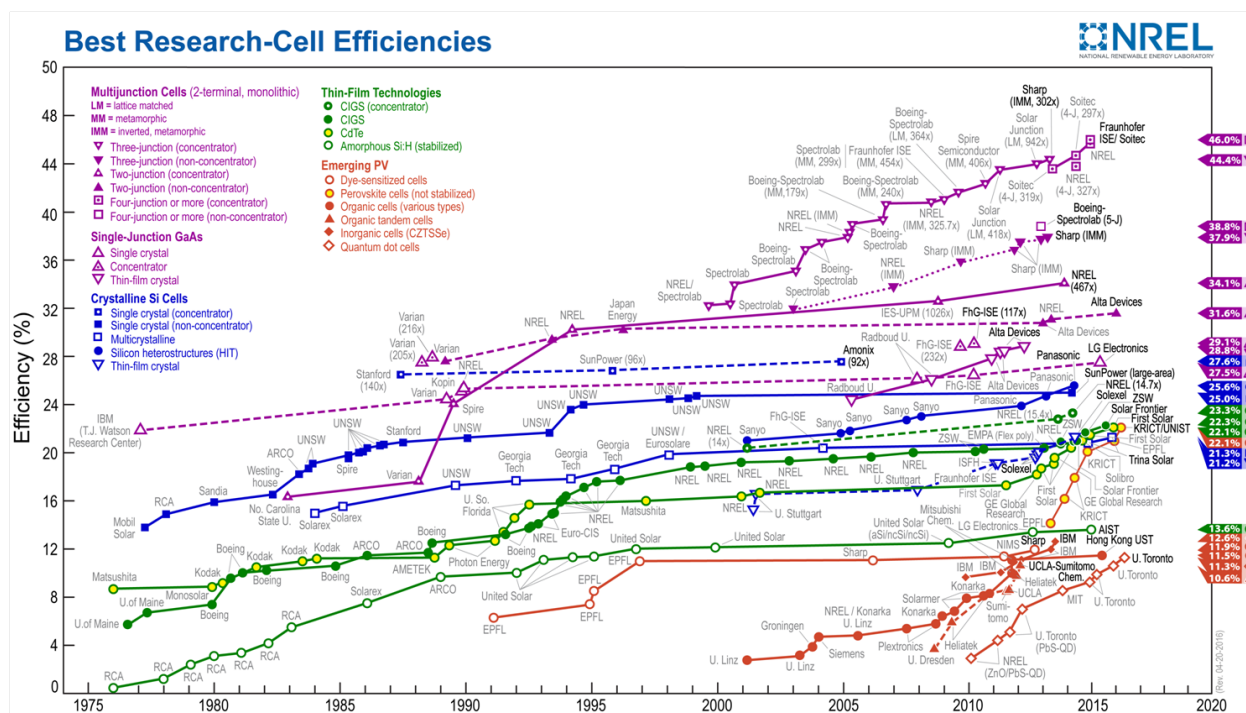


Figure 1.3: National Renewable Energy Laboratory (NREL) best research cell efficiencies.⁹

Photovoltaics (PVs) can be made from several materials with different efficiencies which are tabulated in Fig. 1.3⁹. Although there are several systems that achieve high efficiency, adoption of these technologies are primarily determined by their costs. Existing processing technologies and mediocre performances make monocrystalline silicon solar cells easier to commercialize and more affordable compared to other systems, and it accounted for 90% of the PV sales so far.¹⁰ To compare different energy systems, levelized cost of energy (LCOE) is the term that is used most commonly. LCOE is defined by the lifetime cost of an energy system divided by its lifetime energy production.¹¹ Even the LCOE of existing silicon-based PV systems is not competitive enough with fossil fuels unless it is located on the extremely sunny geographical regions.¹²

Some of the emerging technologies such as inorganic thin film PVs, dye synthesized solar cells (DSCC) and organic photovoltaics (OPVs) have potential to offer cheaper alternatives to silicon-based PV systems. In particular OPVs, which are the main subject of this thesis, can decrease the production cost fourfold compared to commercial silicon-based PVs based on some preliminary

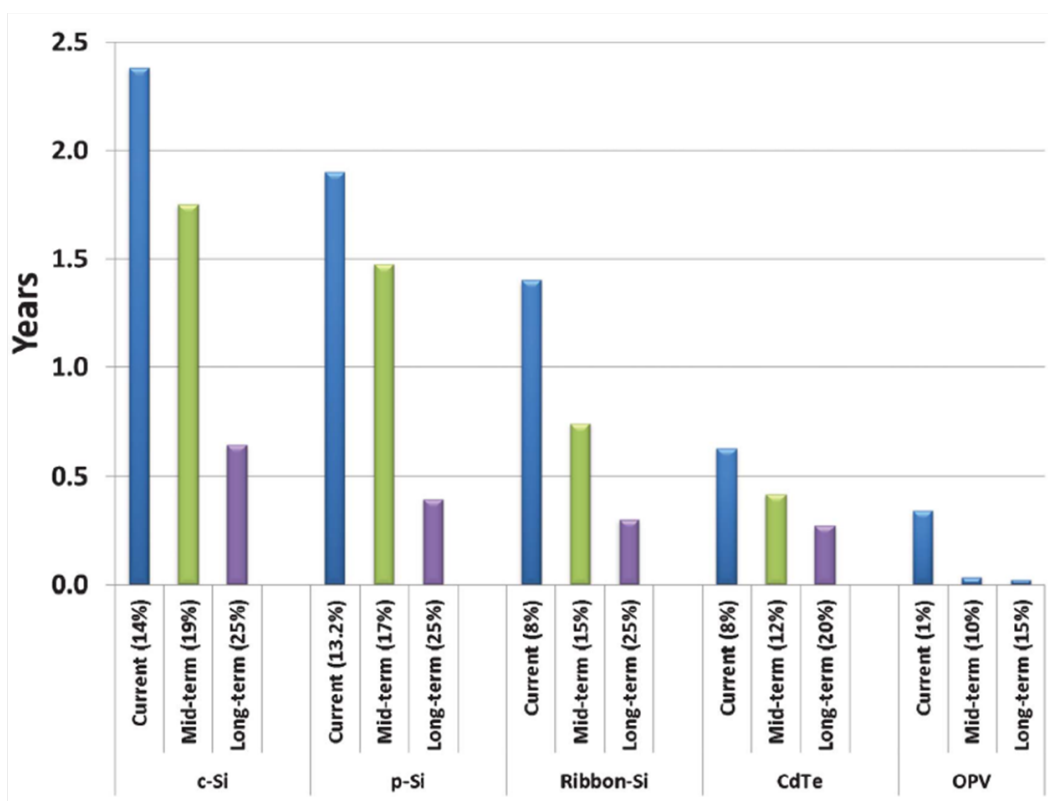


Figure 1.4: Energy payback time for silicon, CdTe, and OPV modules for current, mid-term, and long-term future scenarios. Adapted from Darling et al.⁵

research.¹³ One of the most important reasons for decreased costs of OPVs is the use of cheap, simple and fast processing technologies such as roll-to-roll coating and direct printing on flexible substrates.¹⁴ A detailed cost analysis of different PV systems takes into account the material and energy required for production, transportation, installation, maintenance along with lifetime performance to calculate the energy payback time given in Fig. 1.4.¹⁵⁻¹⁸ Evaluation for energy payback time was for short-term (1-5 years), mid-term (5-10 years) and long-term (>10 years) estimates for each PV technology. As can be seen in the Fig. 1.4, the payback time for current OPVs (with only few percent efficiency) are much lower compared to existing technologies and it decreases even further in the long run.

On the laboratory scale, OPVs have already reached a benchmark efficiency of 10% with a good reproducibility.¹⁹ However, usually lab scale efficiencies are difficult to translate to commercially

available devices. For that reason, several advancements need to be made to achieve the goal of 15% efficiency with a lifetime of 20 years for large-scale commercialization of OPVs.¹³ Hopefully, the advances in the field will be motivated by several other benefits of OPVs on top of the low production cost. These benefits can be summarized as:²⁰ 1. Low weight and flexibility of the PV modules. 2. Semitransparency of devices. 3. Easy integration into other products and production lines. 4. New market opportunities, e.g. wearable PV. 5. Significantly lower manufacturing costs compared to conventional inorganic technologies. 6. Manufacturing of OPV in a continuous process using state of the art printing tools. 7. Short energy payback times and low environmental impact during manufacturing and operations.

1.2 THE BASICS OF ORGANIC SOLAR CELLS

1.2.1 *Device Geometry*

The major component of a solar cell is its active layer that is responsible for light absorption and charge generation. For that reason, solar cells are usually classified by their active material type, e.g. silicon is the active layer in silicon solar cells. For organic solar cells, generally it is only the active layer that is organic and the other parts of the cell can be inorganic. Usually, a single layer of an organic is not enough to generate enough current itself because OPVs operate much differently than most other solar cells. Formation of free charges in the inorganic systems occurs almost spontaneously as the light is absorbed. However, formation of free charges does not occur immediately for OPVs because the low dielectric medium in these devices increases the coulombic attraction between the electron and hole pair that forms upon light absorption.²¹ In order to separate this bound electron-hole pair usually two different organic materials are used in the active layer, one being an electron donor (p type) and the other being an electron acceptor (n type). These layers can be coated on top of each other to form a bilayer (Fig. 1.5a), however better performances are obtained usually when the donor and the acceptor materials are intimately mixed to form a bulk heterojunction

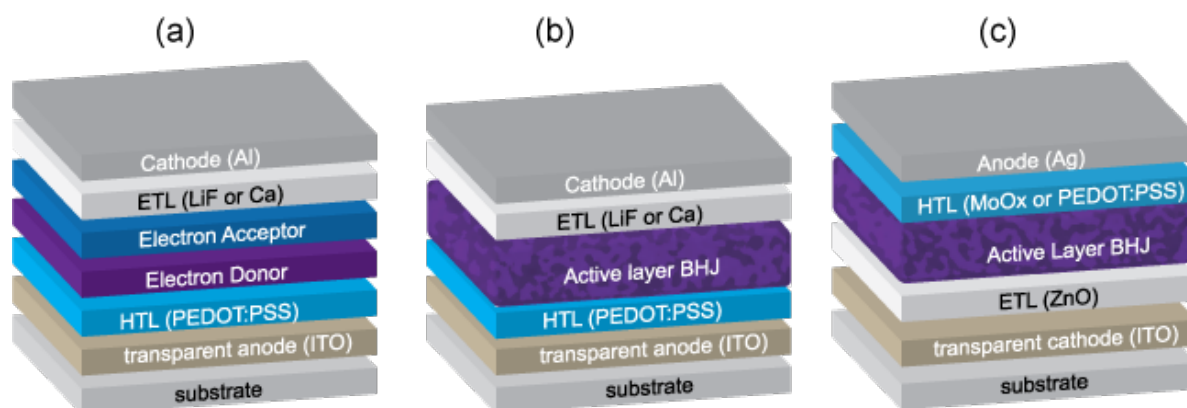


Figure 1.5: Schematics of common layers structures of OPVs in (a) bilayer normal geometry (b) BHJ normal geometry (c) BHJ inverted geometry (HTL=hole transport layer, ETL=electron transport layer).

(BHJ) (Fig. 1.5b). After generation of the free charge carriers, these charges need to be collected and for that reason there are usually multiple layers in a typical solar cell. For OPVs, to collect the electrons at the cathode that is usually a low work function metal such as Al, an electron transport layer is used. In typical devices, this electron transport layer can be lithium fluoride (LiF) or calcium (Ca). Holes are usually collected at the transparent anode which is indium tin oxide (ITO) in most of the cases. Between ITO and the active layer, a hole transport layer (which is usually electron blocking as well) is used and this layer can be a conductive polymer like poly(3,4-ethylenedioxythiophene) polystyrene sulfonate (PEDOT:PSS) or a higher work function oxide such as molybdenum oxide (MoOx). For some active materials, better performances and higher lifetime is achieved with an inverted device geometry (Fig. 1.5c) in which the electrons are collected by ITO. In such devices, zinc oxide (ZnO) is usually used as the electron transport layer and either PEDOT:PSS or MoOx is used for the hole transport layer. For inverted devices silver (Ag) is a common choice to collect the holes.²²

1.2.2 Device Operation and Performance Evaluation

As mentioned in the previous section, OPVs are excitonic solar cells and separation of the electron-hole pair and their collection in the electrodes require several processes. These processes usually depend on the energy levels of each layer and for that reason the energy band diagram of most commonly used p-type poly(3-hexylthiophene) (P3HT) and n-type [6,6]-phenyl C61-butric acid methyl ester (PCBM) are given in Fig. 1.6. The four basic physical processes in an OPV can be summarized as the following:²³

- 1 Absorption of light leading to exciton formation: When either the donor (D) or the acceptor (A) material is photoexcited, electron moves to lowest unoccupied molecular orbital (LUMO) leaving a hole in the highest occupied molecular orbital (HOMO). The efficiency of this process depends on the energy band gap (E_g) of the active layer materials as well as their extinction coefficient at different wavelengths.

- 2 Diffusion of exciton to interface: Even if these electron-hole pairs are in different molecular orbitals, they are still strongly bound to each other and they must diffuse to the interface before relaxing back to the ground state. Usually for OPVs, the distance for that exciton to travel before relaxing back is limited to 5-20 nm²⁴⁻²⁶ and that usually determines the optimal domain size for donor and acceptor phases.

- 3 Separation of electron-hole pair: Once the exciton is able to travel to the D-A interface successfully, the energy difference in their LUMOs and HOMOs can result in separation of the electron-hole pair. Electrons will be transferred to the acceptor that has lower LUMO compared to the donor while holes will be transferred to the higher HOMO of the donor material. Increasing the area of D-A interface will give more chances to generate free charges in the device.

- 4 Collection of charges in the electrodes: The free charges in the D-A phases will be pulled by the electrodes due to the existing electric field that is caused by work function difference of anode and the cathode. During the collection, there is a chance of charge annihilation due to the attractive forces between free electrons and holes. Higher mobility of these charges in the D-A phases will be

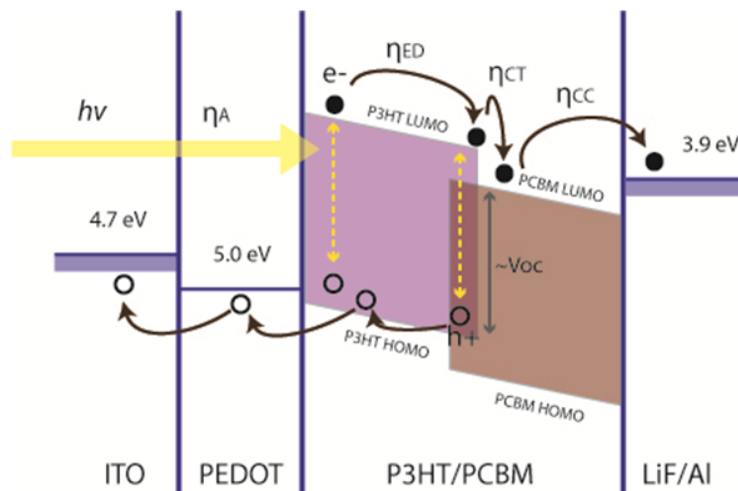


Figure 1.6: Illustration of OPV device operation with common materials.

one key factor that helps the charges to be collected easily before getting annihilated. In addition, once they reach the other interfacial layers that selectively help either electron transport or hole transport, charges will be collected more efficiently. Moreover, better energy level alignment of each layer will facilitate this process.

Usually a common way to probe the performance of a solar cell is done by varying the voltage under illuminated conditions (using a solar simulator) and measuring the current output. Current-voltage characteristics of a typical P3HT-PCBM solar cell fabricated in our lab under illumination is given in Fig. 1.7. Current flow occurs in the opposite direction of the applied bias and is normalized by the surface area of the cell. At zero bias, maximum photogenerated current flows under short-circuit conditions. Photocurrent at this point is named the short-circuit current density (J_{SC}). Photocurrent will become zero at open circuit condition (V_{OC}), which corresponds to almost the difference between the HOMO level of donor and LUMO level of acceptor and balances the built-in field. At this voltage, there is not a driving force for charge carriers and hence the current will be zero. Thus, in the fourth quadrant of I-V curve, there will be a maximum power point (MPP) where the power generation will be maximum. Power conversion efficiency (PCE) of solar cell will be basically the ratio of generated power in the cell and power of incident light. Fill factor (FF) will

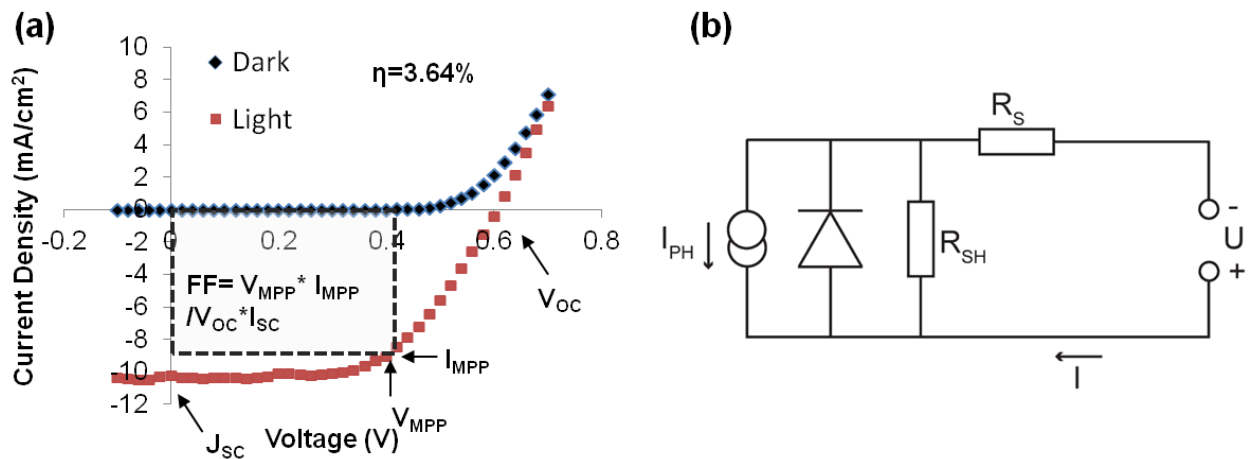


Figure 1.7: (a) Current density (J)- voltage (V) curve of a P3HT:PCBM standard device built in our lab. (b) equivalent circuit for a solar cell, described by the equation 2.

be part of the I_{SC} and V_{OC} product that can be used: $FF = \frac{(I_{MPP} \times V_{MPP})}{(I_{SC} \times V_{OC})}$. The PCE equation will then be²⁷:

$$\eta = \frac{P_{OUT}}{P_{IN}} = \frac{I_{MPP} \cdot V_{MPP}}{P_{IN}} = \frac{FF \cdot I_{SC} \cdot V_{OC}}{P_{IN}} \quad (1)$$

J-V characteristic that is observed in the Figure-a can be described with the following equation:

$$I = I_0 \cdot \left\{ \exp\left(\frac{e}{nkT}(U - IR_S)\right) - 1 \right\} + \frac{U - IR_S}{R_{SH}} - I_{PH} \quad (2)$$

where I_0 is the dark current, e the elementary charge, n the diode ideality factor, U the applied voltage, R_S the series, R_{SH} the shunt resistance, and I_{PH} is the photocurrent. Equivalent circuit model for this equation is given in the Fig. 1.7b. In this model the various types of resistance are the main parameters that control the FF. To obtain a higher FF in a solar cell, shunt resistance should be large so that it prevents leakage current, and series resistance should be low to allow more efficient charge transport through each interface to the contacts.²⁸ Another set of parameters that are important for determining the performance of a solar cell are the quantum efficiencies (QE) which measure the ratio of incident photons to converted electrons for a given wavelength. There are two differ-

ent QEs, external quantum efficiency (EQE) and internal quantum efficiency (IQE). EQE reflects the percentage of incident photons that are converted to electrons while IQE reflects percentage of absorbed photons that are converted to electrons. The difference between two parameters comes from the amount of light that is reflected or transmitted in a system (which is usually more difficult to measure) and this difference can be described by the following equation²⁹:

$$IQE = \frac{EQE}{1 - \%reflected - \%transmitted} \quad (3)$$

Both EQE and IQE are usually represented with percentages at different wavelengths comparing it to the standard air mass of 1.5 (AM 1.5) sun illumination that was set as a standard for PV research by American Society for Testing Materials (ASTM).³⁰ In Fig. 1.8, AM 1.5G spectrum can be compared with the common P₃HT:PCBM solar film spectral response. OPVs usually absorb in the yellow part of this spectrum (up to 800 nm) while silicon-PV spectrum can extend up to 1100 nm.

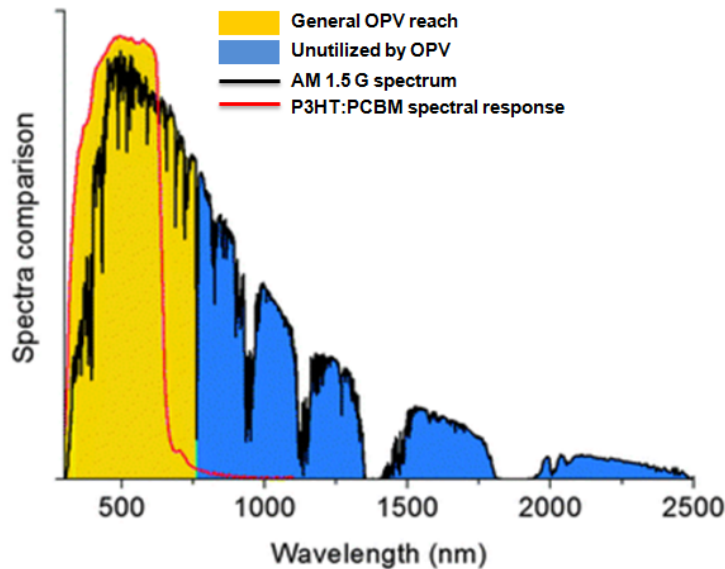


Figure 1.8: AM 1.5G spectrum and P₃HT:PCBM spectral response, yellow band represents the reach of OPVs and blue band shows the non-utilized light. Take from Beliaty et al.³¹

1.2.3 Theoretical Limits

Even with suitable energy level alignments of D/A for photoinduced charge transfer in OPVs, there are still energy losses due to the presence of charge transfer (CT) state at the interface. It is possible to quantitatively assess the thermodynamic efficiency limit of OPVs by understanding the effects of these interfacial CT states. The most important parameters that go into the calculation are E_g of the light absorbing molecules, as well as energy and relative absorptivity of the CT state.³² Gruber et al. demonstrated that by modelling the efficiency limit as a function of E_g (Fig. 1.9a) and the CT absorptivity (Fig. 1.9b), they were able to achieve an efficiency limit of 33% for organic planar heterojunction solar cells.³²

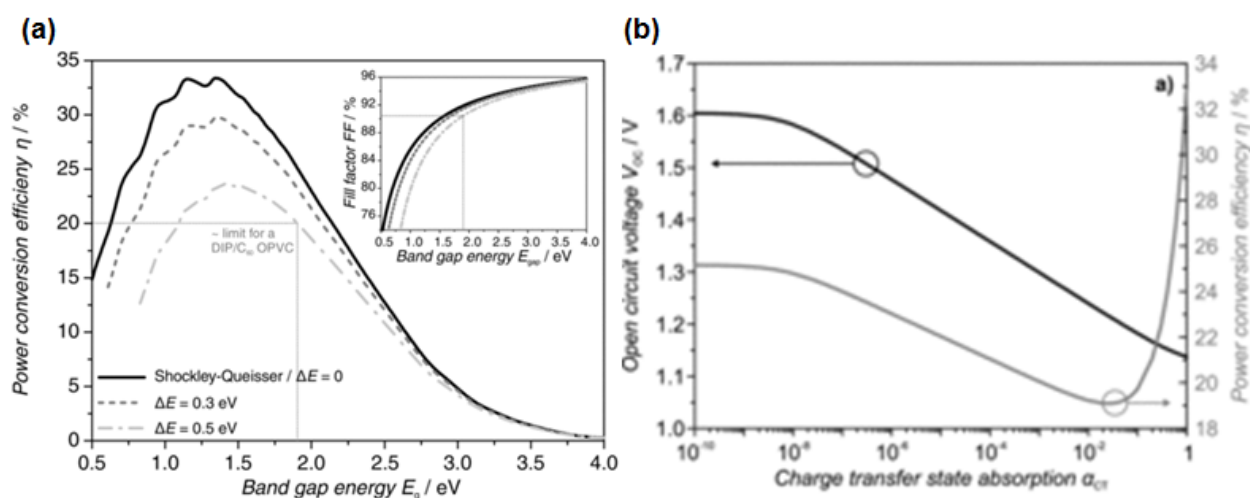


Figure 1.9: a) Maximum efficiency η and fill factor FF (inset) predicted for an organic heterojunction solar cell as a function of band gap energy E_g for $\alpha_{CT} = 10^{-3}$ and several different offset energies ΔE , assuming the AM1.5g solar radiation spectrum and the solar cell as black body radiator at a temperature $T_C = 300$ K b) Maximum open circuit voltage V_{OC} and power conversion efficiency η predicted for an organic heterojunction solar cell as a function of CT absorption α_{CT} , assuming an offset energy of $\Delta E = 0.5$ eV, a band gap of $E_g = 1.9$ eV and the AM1.5 g solar radiation spectrum. The maximum efficiency of 33% at $\alpha_{CT} = 1$ corresponds to the case of a homojunction in the classical SQ theory with $E_g = 1.4$ eV. Image taken from Gruber et al.³²

In another approach that considers the common materials used in OPVs, Brabec et al. presented (Fig. 1.10) a model based on HOMO and LUMO levels of the donor polymers.³³ To obtain highest

power conversion efficiencies, (i) the difference between the LUMO levels of the donor and acceptor molecules should be at least 0.3 eV, (ii) the donor band gap (E_g) should be 1.2-1.7 eV, and (iii) the HOMO level of the donor should be between -5.2 and -5.7 eV. Using Phenyl-C61-butyric acid methyl ester (PCBM) as the electron acceptor, the following equation was established to predict the V_{OC} of solar cells:

$$V_{OC} = (1/e)(|E^{\text{Donor HOMO}}| - |E^{\text{PCBM LUMO}}|) - 0.3 \text{ V}$$

where e is elementary charge, -4.3 eV is the LUMO energy level for PCBM and 0.3 V is the empirical factor discussed above. So, an ideal donor should have LUMO around -3.9 eV and HOMO of -5.4 eV leading a band gap 1.5 eV and V_{OC} of 0.8 V. This LUMO is lower than P3HT LUMO (-3.3 eV) and V_{OC} is larger than P3HT (0.6 V).

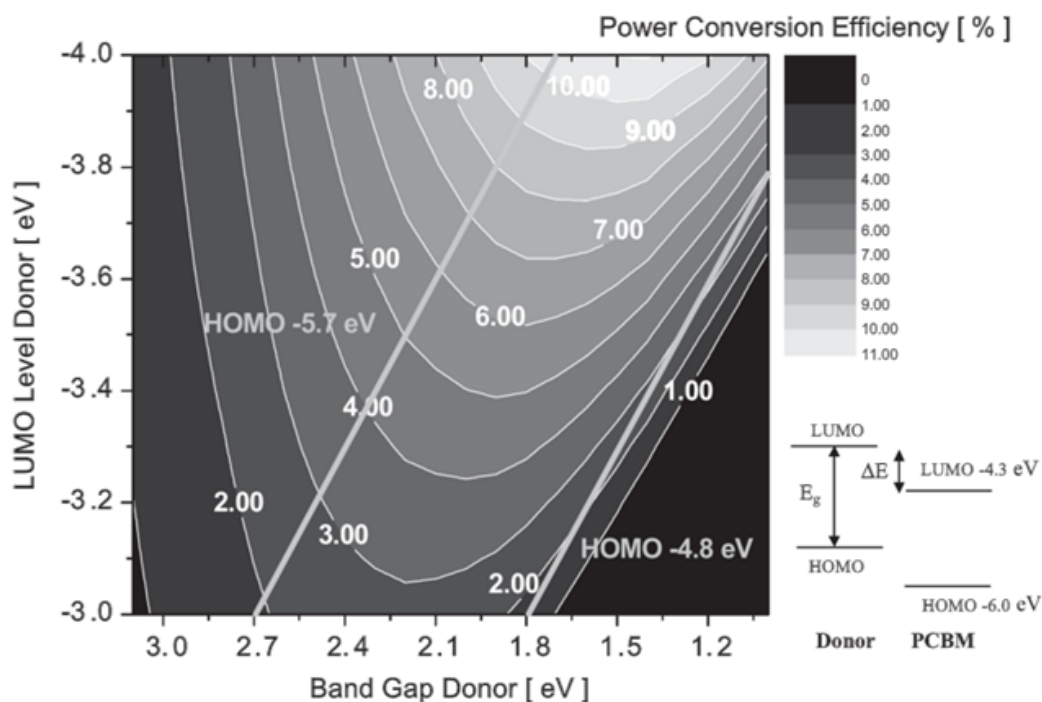


Figure 1.10: Contour plot showing the calculated energy-conversion efficiency (contour lines and colors) versus the bandgap and the LUMO level of the donor polymer according to the model described above. Straight lines starting at 2.7 eV and 1.8 eV indicate HOMO levels of -5.7 eV and -4.8 eV, respectively. A schematic energy diagram of a donor PCBM system with the bandgap energy (E_g) and the energy difference (ΔE) is also shown. Reproduced from Brabec et al.³³

1.3 STRATEGIES TO INCREASE THE EFFICIENCY OF OPVS

1.3.1 Material Design for Polymers and Small Molecules

The properties of conjugated molecules heavily depend on the nature of the bond and the functional components in the chemical structure. Covalent bonding of two conjugated units usually results in restructuring of the frontier molecular orbitals. In this restructuring, the addition of electron donating functional groups increases the energy of HOMO and addition of electron withdrawing functional groups lowers the energy of LUMO, resulting in a reduction of the overall band gap (Fig. 1.11). This strategy, known as “push-pull” (electron density is “pushed” by electron donating groups, and “pulled” by electron accepting groups), is a common strategy to engineer different conjugated architectures.³⁴ This push-pull design motif provides a powerful way of tuning the energy levels of newly designed donor molecules.³⁵

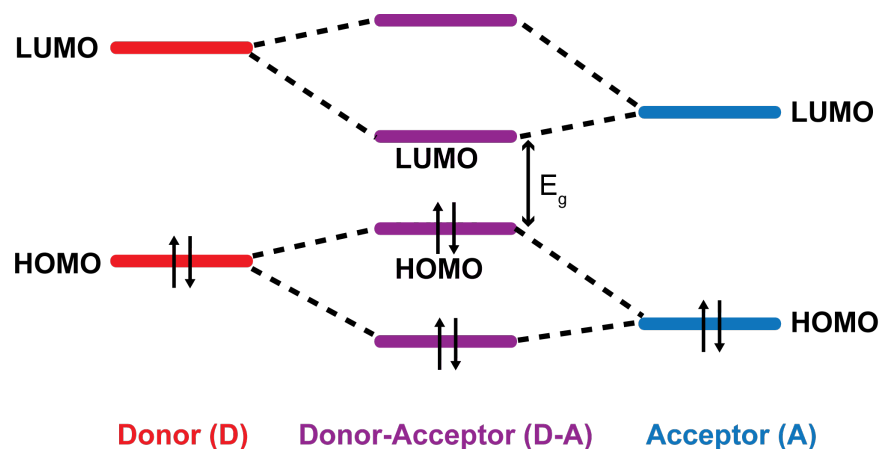


Figure 1.11: Diagram of molecular orbital restructuring when D and A type molecules are covalently bonded.

Alternating electron donating (push) and electron withdrawing (pull) groups within polymers used in solar cells not only decreases the band gap of the polymer donors, but also helps charge separation through formation of delocalized bad states.³⁶ Common electron donating groups used in push-pull architectures are thiophene (T), oligothiophenes, benzodithiophene (BDT), dithiophene-

benzodithiophene (2T-BDT), naphthodithiophene (NDT), carbazole (C), dithienosilole (DTS), dibenzosilole (DBS), and dithienopyrrole (DTP). Common electron withdrawing groups are benzothiadiazole (BT), pyridalthiadiazole (PT), diketopyrrolopyrrole (DPP), thienopyrroledione (TPD) and difluorobenzothiadiazole (DFBT). (Fig. 1.12)

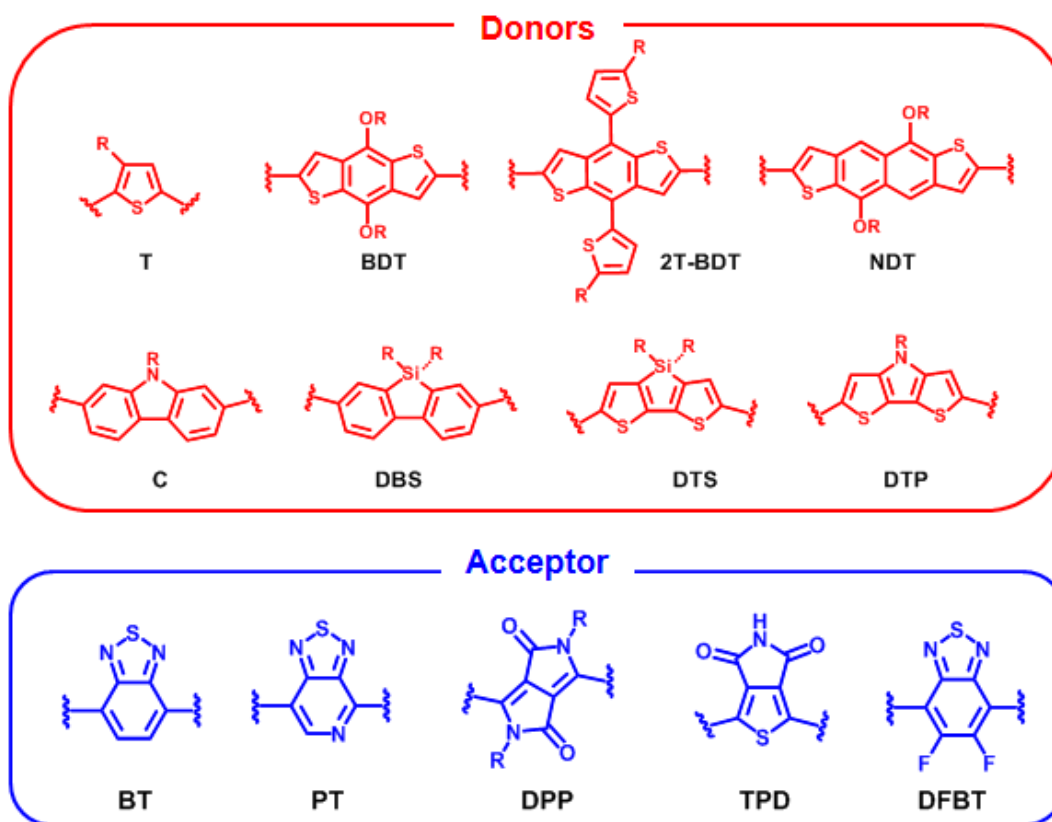


Figure 1.12: Electron donating and electron withdrawing units used in a typical donor material for OPVs.

One example of using the “push-pull” approach to develop donor polymers for OPVs is of poly[N-9'-heptadecanyl-2,7-carbazole-alt-5,5-(4',7'-di-2-thienyl-2',1',3'-benzothiadiazole)] (PCDT-BT) (Fig. 1.13). In this polymer, carbazole-dithiophene group acts as an electron donating group while benzothiadiazole acts as an electron withdrawing group. The polymer boasted a low band gap (1.88 eV), and optimal HOMO (5.5 eV) and LUMO (3.6 eV) levels, enabling a PCE of 5.5% for the OPV.³⁷ In addition, Hou et al. showed that replacing the C atom in carbazole unit with Si

increased the crystallinity of the donor phase and resulted in similar PCE.³⁸ Yu et al. reported solar cell devices with thieno[3,4-b]thiophene and benzodithiophene polymer (PTB7) blended with PC₇₁BM led to PCE of 7.4%.¹⁷ Another example of a “push-pull” donor is a polymer with an alternating dithienogermole – thienopyrrolodione repeat unit (PDTG – TPD) with certified PCE of 7.4%.³⁹ Here, the electron donating group is the dithienogermole moiety and the electron withdrawing group is thienopyrrolodione. In this study, solution based ZnO used as an optical spacer in an inverted device architecture which is compatible with roll-to-roll process. A third example with BDT groups is the polymer that has fluorinated BTD groups.⁴⁰ This polymer has a deep lying HOMO (-5.54 eV) and an E_g of 1.7 eV. A lower HOMO level leads to higher V_{OC} of 0.91 V, achieved with added fluorines on the BT groups. The fluorine substitution on BT increased both the V_{OC} of the device, as well as the overall device performance (7.2 % PCE). One of the more recent findings on BDT-based polymers is that the further conjugation of BDT with 2T groups results in a two dimensional assembled morphology, enabling devices with 10% efficiency.⁴¹

Similar push-pull strategies are also used for small molecule-based solar cells (Fig. 1.14). In most cases, the common way of arranging the electron donating (D) and electron withdrawing (A) motifs are in an A-D-A fashion. For example, when electron donating NDT and two DPP units are bridged with thiophene to give NDT(TDPP)₂, a small band gap molecule with HOMO of -5.4 eV and LUMO of -3.7 eV is obtained.⁴² Mixing this donor molecule with PCBM resulted in a device that has 4.1% PCE, at the time among the highest for small molecule based OPVs. Another efficiency record-breaking small molecule donor based on dithienosilole (DTS) and pyridalthiadiazole (PT) groups synthesized in a D-A-D-A-D fashion, which resulted in 6.7% PCE.⁴³ The HOMO of the DTS(PTTh)₂ molecule was -5.2eV while LUMO is -3.6 eV, both of which aligned well with PC₇₁BM. The success of the BDT functional group in an A-D-A push-pull small molecule was also demonstrated when used in small molecule donors, as in the case of alkylthio-thienyl conjugated side chains with the addition of rhodanine to give BDTT-S-TR. The reported efficiency for this molecule was 9.2%⁴⁴, a result of years of optimization on similar BDT-based molecules (references

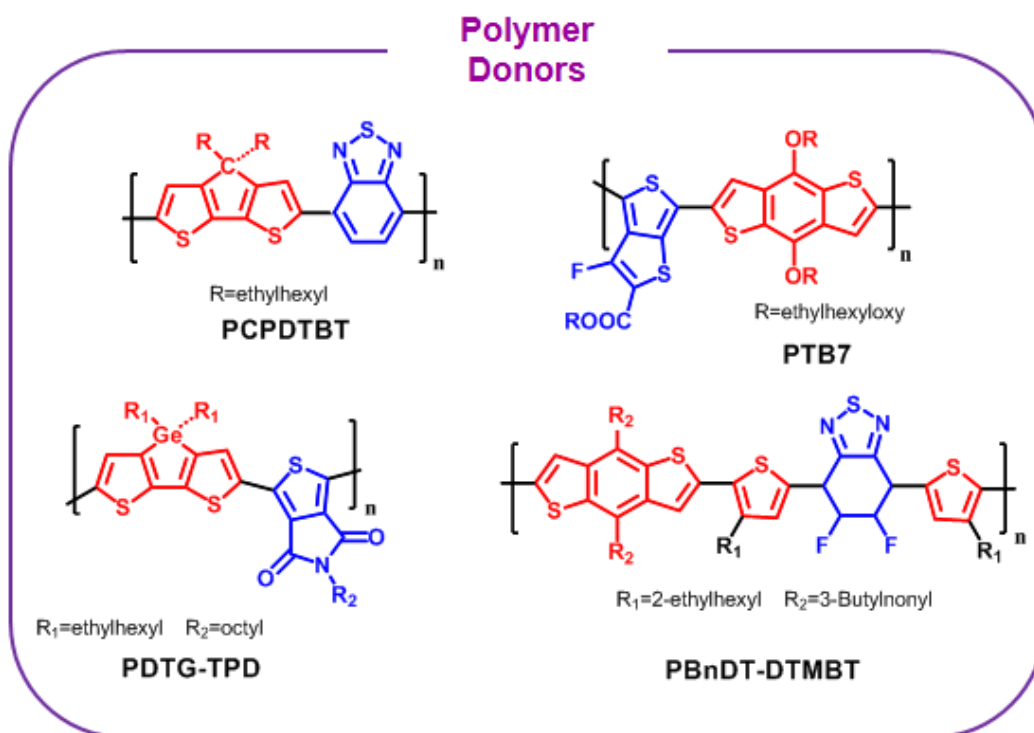


Figure 1.13: Common electron donor polymers with high efficiency

from that paper or 2014 GM). Aside from the central BDT, the electron withdrawing group rhodanine has two arms at the end of the molecule that were key for tuning the energy levels and device performance. A similar rhodanine electron withdrawing group gave high-performance solar cells when coupled to a thiophene oligomer (γ T) core.⁴⁵ The addition of electron withdrawing cyano-groups enhanced the electron “pulling” capability of the rhodanine unit, improving the PCE to 9.3%. This is currently among the highest reported efficiencies for small molecule-based OPVs.

Most of the studies cited thus far used fullerene-based PCBM as the electron acceptor (Fig. 1.15). It was demonstrated that replacing C₆₀-PCBM with C₇₀-PCBM (PC₇₁BM) increases the absorption of the fullerene in the visible range of the electromagnetic spectrum. This in turn increased the external quantum efficiency (EQE) of the resulting solar cell, when compared to the same blend prepared from C₆₀-PCBM.⁴⁶ For this reason, PC₇₁BM has been adopted more often than PC₆₁BM, usually resulting in higher solar cell efficiencies. In addition, in some cases indene-C₆₀-bisadduct

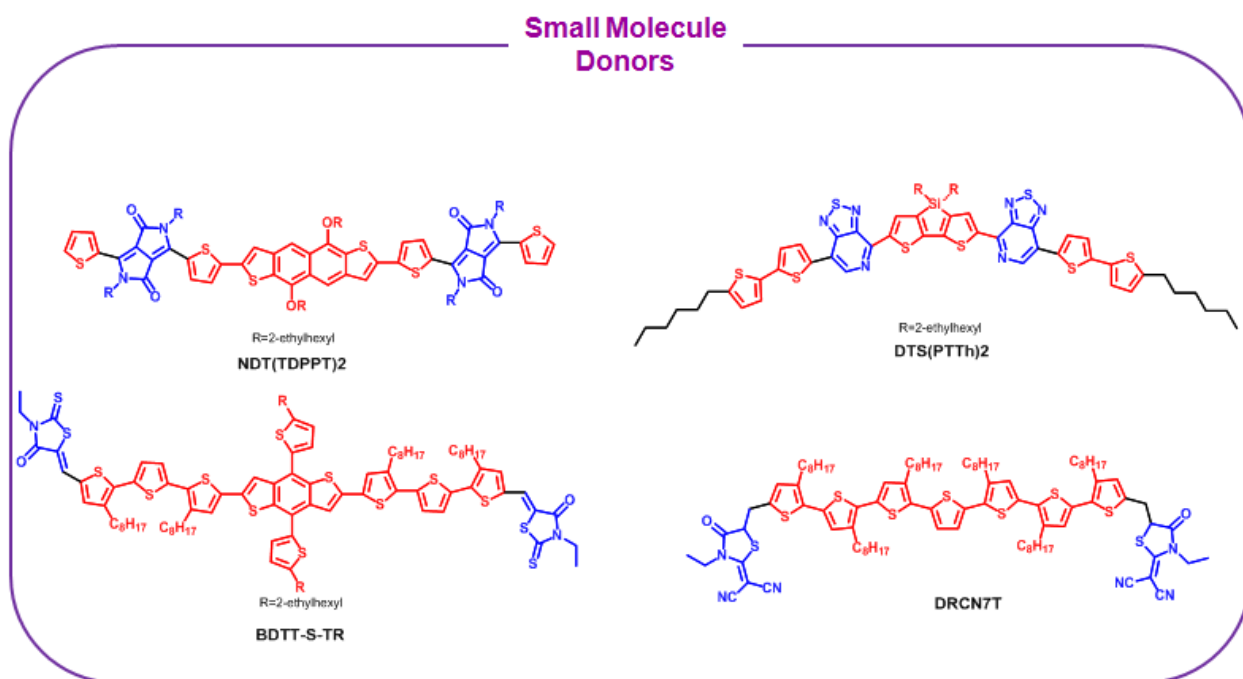


Figure 1.14: Common electron donor small molecules with high efficiency

(ICBA) is used as an acceptor because its higher LUMO energy level can result in higher V_{OC} and higher device efficiency (7%).^{47,48} However, the number of polymers that can display enhanced efficiency with ICBA is limited.^{49,50}

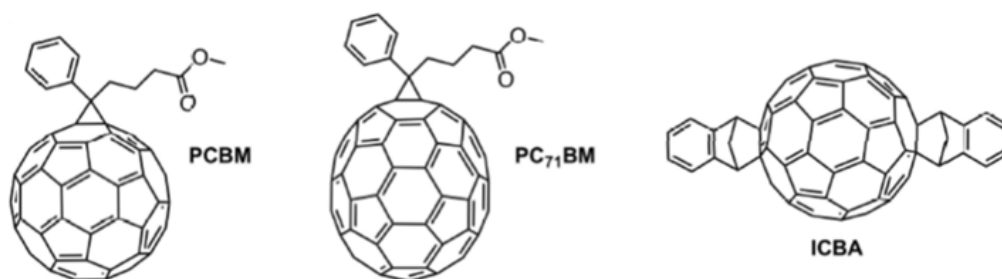


Figure 1.15: Common electron acceptor fullerene derivative molecules

1.3.2 Interface Engineering

Having multiple layers in OPV device architectures requires extensive research and optimization of the interfaces. Conventionally, the active layer is sandwiched between a high-work function transparent ITO anode and low work function metal cathode. After exciton dissociation at the donor-acceptor interface, the electron and hole charges drift under the influence of the built-in electric field that is caused by work function difference of the electrodes. As these free charges move to the interfaces, there is always a probability that they can recombine, resulting in net efficiency losses.⁵¹⁻⁵³

In general, there are two types of interfaces between a semiconductor and a metal, namely Schottky and Ohmic (Fig. 1.16) interfaces. When there is a large difference in Fermi levels between a metal and semiconductor, there will be charge transfer from (or towards) the metal, creating a depletion zone that has considerably fewer mobile charge carriers. This type of interface is known as a Schottky interface or Schottky (rectifying) junction. In a Schottky junction, additional energy will have to be provided to force an electron to diffuse from the semiconductor, through the depletion layer, and to the metal contact. On the other hand, when the difference in Fermi levels between the metal and semiconductor is small, there will not be significant charge transfer between the metal and semiconductor and hence there will not be a depletion zone. This interface is called Ohmic interface or Ohmic (non-rectifying) junction and it will not require a lot of energy (usually less than kT) to push an electron from the semiconductor to the metal.⁵⁴ For OPVs, where the diffusion of electrons from the semiconducting layer to the metal contact defines performance and efficiency, the formation of Ohmic interfaces with low resistance between the metal and semiconducting layer is imperative.⁵⁵ Forming an Ohmic interface between a metal and semiconductor is not a trivial job, and usually requires matching the energy levels of the materials at the interface.

Both theoretical^{56,57} and experimental^{58,59} studies showed that a large Schottky barrier can form at the organic semiconductor-metal interface irrespective of the metal work function (known as Fermi-level pinning). This gives rise to poor contact properties and unfavorable OPV performance. Besides energy level matching, it is important that the charge transport layers be selective i.e. inject

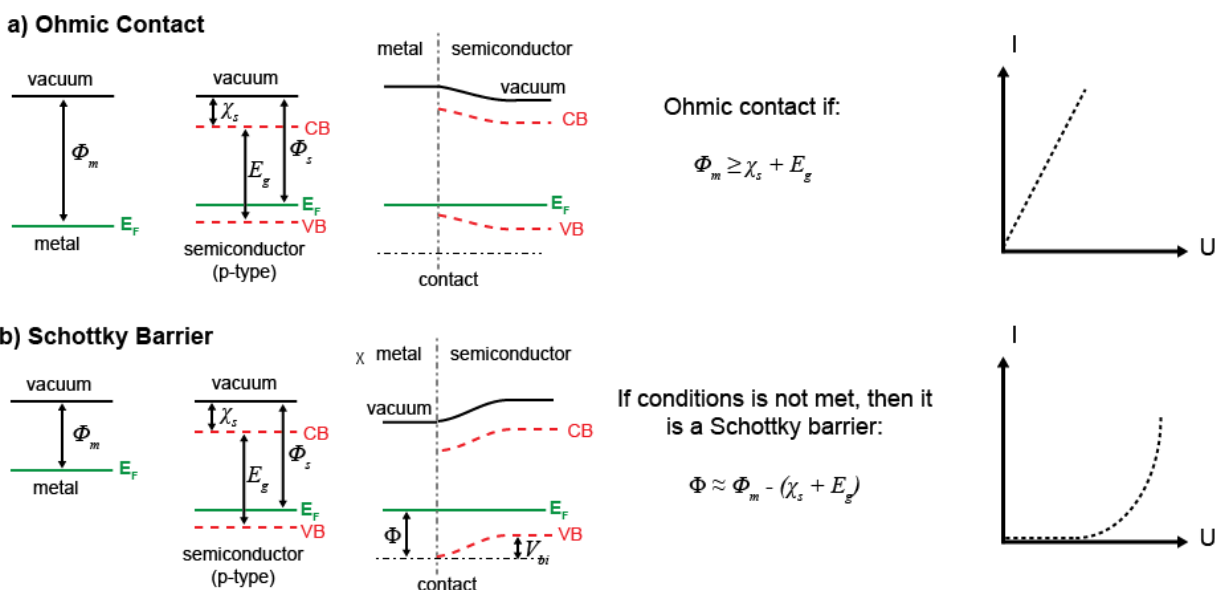


Figure 1.16: Energy levels for an Ohmic and a Schottky junction between a metal and a semiconductor. The current – voltage characteristics are shown schematically. Adapted from Ref.[54]

one type of charge carrier while blocking the other. On that account, charge transport layers can be labelled electron transport (hole-blocking) layers and hole transport (electron-blocking).

Electron Transport Layers

Between the active layer and Al (cathode) materials, LiF and Ca are the most commonly used interfacial layers to improve electron transport. Several groups have reported that insertion of a thin LiF layer improves device performance and increases the efficiency, but the mechanism behind this observation is not well understood.⁶⁰ It is believed that LiF reduces the barrier height between the polymer blend film and the electrode either through the lower effective work function of LiF or through the dipole alignment of LiF nanoparticles.⁶¹ Moreover, it has been also reported that for an C₆₀-Al interface, introducing LiF provides effective passivation for the contacts by preventing Al oxidation.⁶² This is noteworthy for C₆₀-Al contacts because it was previously reported that these contacts degrade from an ohmic to a blocking contact after exposure to air, likely due to the

emergence of a potential barrier between the top electrode Al and C₆₀ film.⁶³ In addition, C₆₀ is very sensitive to oxygen and moisture. Upon oxygen adsorption, the conductivity of C₆₀ decreases by several orders of magnitude.⁶⁴ A more accepted theory is that LiF forms a dipole in the Al-organic interface and decreases the work function of Al (4.1 eV). This brings the work function of Al closer to that of PCBM and enhances injection of electrons while blocking the holes.⁶⁵ Ca also has a lower work function (2.87 eV), and decreases the series resistance and leakage current , improving device performance.⁶⁶ Recent studies have also reported using polymers in the electron transport layer. In particular, poly[(9,9-bis(3-(N,N-dimethylamino)propyl)-2,7-fluorene)-alt-2,7-(9,9-dioctylfluorene)] (PFN) improved the PCDTBT:PC₇₁BM efficiency to 6.8%⁶⁷ and PTB7:PC₇₁BM up to 9.2%.⁶⁸

Hole Transport Layers

There has been more research on hole transport layers because most of the time, the limiting factor in solar cell efficiency is hole mobility, which is typically lower than electron mobility. As a result, enhancing hole injection to the anode enhances the device performance greatly.⁶⁹ Until now, the most commonly used hole-transport layer is the conducting polymer poly(3,4-ethylenedioxythiophene) poly(styrenesulfonate) (PEDOT:PSS), which has a higher work function (5.0 eV) than ITO (4.7 eV). PEDOT:PSS forms an intermediate energy step between the work function of ITO and the donor HOMO, enhancing hole injection and blocking electrons. Moreover, it forms an Ohmic contact, reduces shunt resistance and can act as a buffer to the roughness of the underlying electrode.⁷⁰ However, due to its reactive (acidic) behavior, PEDOT:PSS limits stability of OPVs in the long term. Therefore, several studies have explored alternative material for hole transport layers. Introducing a discontinuous interlayer of metals such as Au, nanopatterned Ag and oxides, MoOx or ZnO nanoparticles, has been shown to greatly enhance the hole collection efficiency in organic solar cells.⁷¹⁻⁷⁴ There have also been reports on optimizing the interface of donor and acceptor materials. Swager et al. used pentafluorophenoxy-containing polymer as an additive to form an interfacial

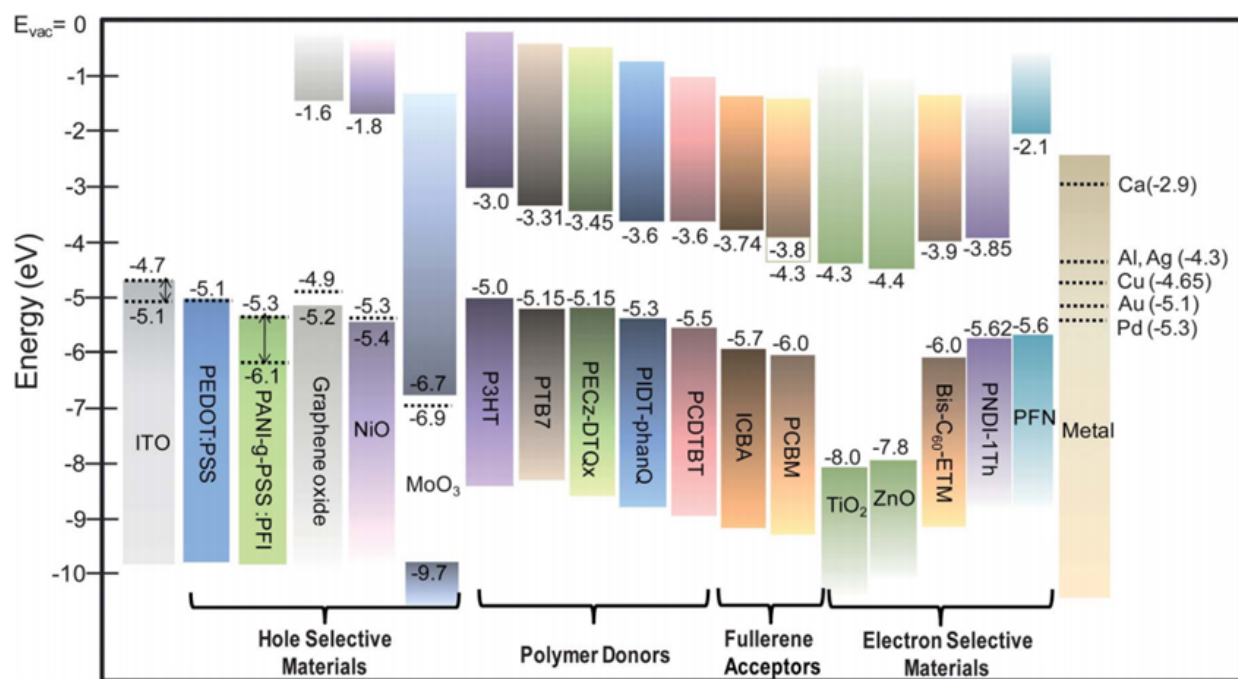


Figure 1.17: Schematic view of the energy gaps and energy levels of some of the components of recent OPVs including transparent electrodes, hole selective (transport) materials, polymer donors, fullerene acceptors, electron selective (transport) materials and metal electrodes. The dotted lines correspond to the work functions of the materials. Adapted from Ref.[55]

dipole, reducing the bimolecular recombination and increasing the PCE by 30% for a P3HT:PCBM standard device.⁷⁵ Energy levels of hole and electron transport materials from the literature is depicted in Fig. 1.17. There is still a room to improve the interface of donor and acceptor materials as well as the other interfaces in OPVs to achieve higher efficiency and longer lifetime.

1.3.3 Control of Morphology

Major achievements with BHJ OPVs were obtained with the optimization of nanomorphology. The limitation on the exciton diffusion length (usually < 20 nm) put several constraints on the active layer. Although, increasing the active layer thickness increases the absorption of light, after a certain increase in the thickness, photocurrent of the device does not increase. This is mainly because of the recombination of the charges in the bulk of the active layer. After a certain thickness, some

of the formed exciton in the bulk of the active layer cannot reach the electrode due to the limited diffusion length and the probability of recombination increases. For this reason, the thickness of active layer in OPVs is usually around 100 nm. Another constraint that exciton diffusion length brings is the size of the donor and acceptor domains in the active layer. Having completely mixed donor and acceptor material results in low performing devices and this is due to the lack of continuous pathways for charge transport. On the other hand, having much larger domains compared to exciton diffusion length results in more charge recombination events and limits the photocurrent. Optimal sized and percolated network of acceptor and donor domains have been proved both with electron tomography and cross-sectional transmission electron microscope (TEM) imaging as shown in Fig. 1.18a-b. Although this resultant morphology increases the interfacial area between donor and acceptor phases required for exciton dissociation, controlling the size of the domains and the orientation of molecules remains a challenge with these processing techniques. The ideal morphology of a BHJ solar cell, illustrated in Fig. 1.18c, requires an interpenetrated network of donor and acceptor materials on the order of tens of nanometers in order to accommodate the short exciton diffusion length in organic materials. This morphology will improve both the interfacial area between donor and acceptor materials and build the interdigitated network necessary for ideal charge migration to the electrodes. Overall, this should show a dramatic increase in the power conversion efficiency of devices. Computer simulation comparison of a typical percolating and idealized morphology revealed short-circuit current gain of more than twice for the latter.⁷⁶ There are also different length scales of interest in the active layer besides the domains size. For example, molecular ordering and orientation can directly influence charge transport, exciton separation and recombination. In addition, persistence length of this ordering, inhomogeneities in crystallinity and donor-acceptor mixing at the interface are all important features of active morphology that influence the device performance.⁷⁷ Thus, research towards achieving the ideal morphology in OPVs can be pivotal to achieve even higher efficiencies leading to broader commercialization.

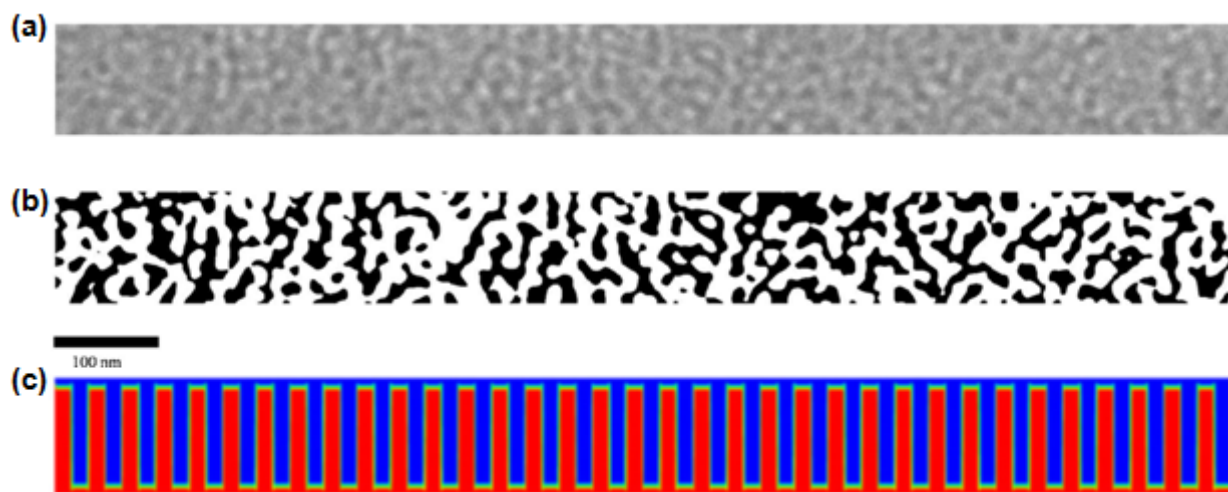


Figure 1.18: (a) Defocused (ΔZ) $\sim 25 \mu\text{m}$) cross-sectional TEM images of the rrP₃HT:PCBM BHJ active layer for 60 nm thinned slice, taken from Ref.[78] (b) Binary enhanced TEM image shown in (a) to be used as a guide to the eye. (c) Idealized BHJ active layer morphology showing interdigitated donor and acceptor with a width less than 20 nm, taken from Ref.[76].

1.3.3.1 Nanoscale Characterization of OPV Morphology

The advances in the nanoscale characterization techniques for OPVs in the recent years increased the understanding of the nanoscale morphology in these systems. This understanding also brought up better guidelines for material design and processing to enhance device performance. Although there are vast number of techniques that are used to characterize OPV morphology, we will only focus on few techniques that are specialized on smaller scale characterization.

1.3.3.1.1 Microscopy

Transmission Electron Microscopy

Transmission electron microscopy (TEM). Imaging, diffraction and spectroscopy modes of TEM are usually used to characterize phase composition of OPVs in nanometer spatial resolution. Especially energy filtering is a useful technique to make a contrast between two soft materials that

are usually difficult to assign in bright field.⁷⁹ Fig. 1.19a shows bright field (BF) TEM image of a P3HT:PCBM blend annealed at 190 °C.⁸⁰ Phase assignment can only be done when energy filtering around the sulfur absorption edge is done that shows the sulfur enrichment of the fibril like structures. Knowing that PCBM does not have sulfur atom, it is easy to assign these fibril-like structures as crystallized P3HT. Specialized sample preparation protocols such as microtoming, focused ion beam (FIB) sectioning allows cross-sectional TEM characterization through the active layer thickness and combining with tilting, collecting series of images can allow visualization of the 3D structure. The tomographic reconstruction presented in Fig. 1.19b is blend of PF10TBT:PCBM, and it shows the interconnected polymer-rich strands forming a truly three dimensional network within the film.⁸¹

Atomic Force Microscopy

As in the case of many soft material systems, one of the concerns of using TEM for OPV active layer is the beam damage. For that reason, AFM is a more common characterization technique to understand phase composition of the active layer. Especially, tapping mode (intermittent contact) suits really well for probing soft materials in nanoscale. In this mode, besides the conventional AFM-topography image, phase image is collected as well. The phase images reflects the phase shift of the oscillation and this shift depends on the tip-sample interaction. Usually, both the material stiffness⁸² and adhesion play an important role for the contrast formation in the phase image. Thus, a phase image reflects a combination of the sample's elastic and viscous properties. AFM of P3HT film after annealing at 150 °C is shown in Fig. 1.20a. Here, while topography image remained largely unchanged, fibril-like contrast was observed in the phase images after annealing.⁸³ Besides the traditional AFM modes, conductive AFM (C-AFM) is also a useful technique to characterize both morphology and local electrical properties of active layer. This is achieved with two terminal electrical measurement through metal coated AFM probe and the bulk conductor underneath the OPV material. C-AFM can be used as a photocurrent microscopy as well if sample is illuminated during

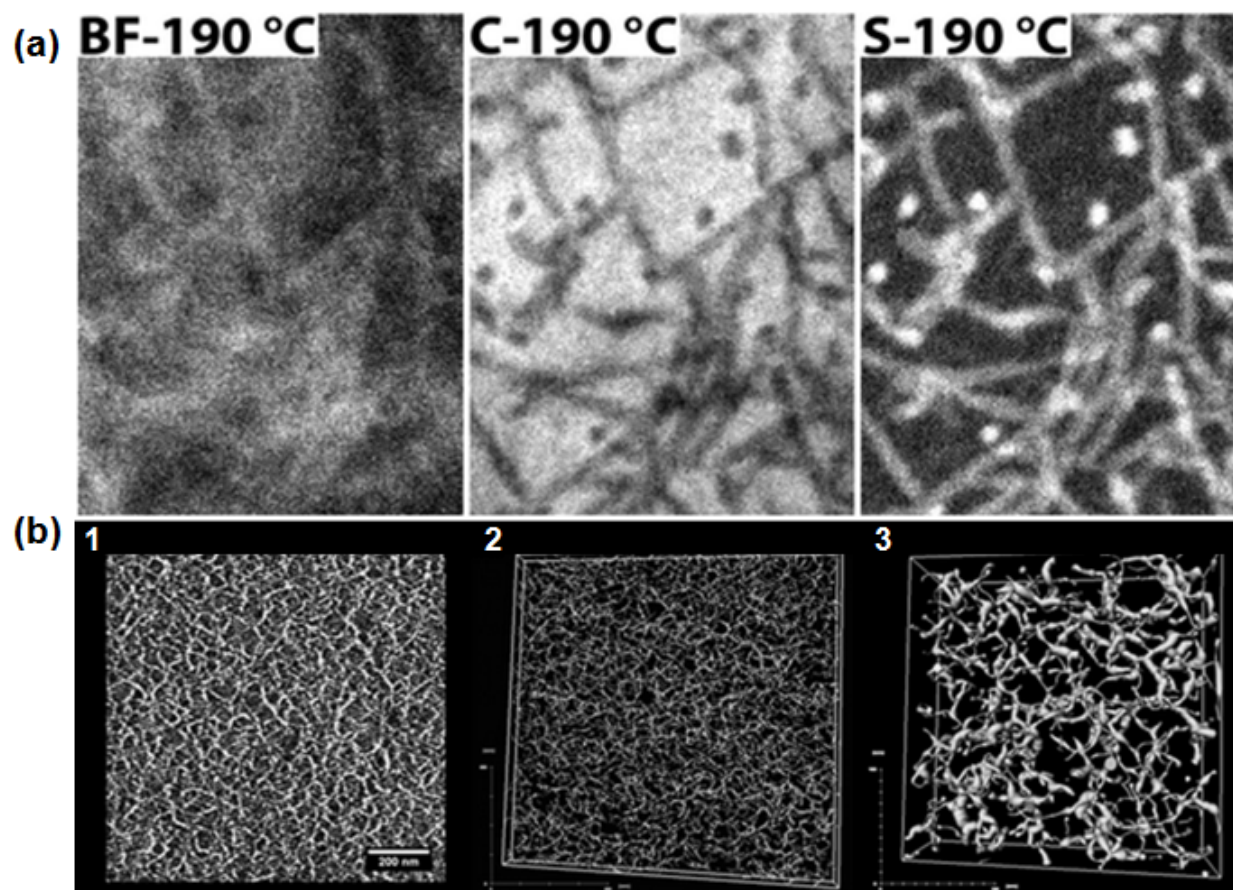


Figure 1.19: (a) Upper image, Bright field (BF), sulfur map (S), and carbon map (C) for a 1-1 P₃HT – PC₆₁BM film annealed for 30 min. Films annealed at high temperatures, such as 190 C, exhibit the presence of P₃HT fibers in a PCBM-rich matrix (Ref.[80])(b)Outcome of electron tomography applied to the PF₁₀TBT – PCBM films (with high molecular weight PF₁₀TBT-polymer): (1) one slice taken out of the (x,y)-plane of the final 3D dataset with bright-looking polymer strands and darker PCBM-rich regions; (2) a snapshot of the corresponding volume reconstruction showing the existence of a 3D nanoscale polymer network (volume dimensions are 1112 nm -1090 nm - 75 nm, the polymer strands are made thinner here than they are in reality to facilitate visualization); (3) zoom-in of the same volume (with volume dimensions of 227 nm - 227 nm- 75 nm and the thickness of the polymer strands to scale).(Reproduced from Ref.[81])

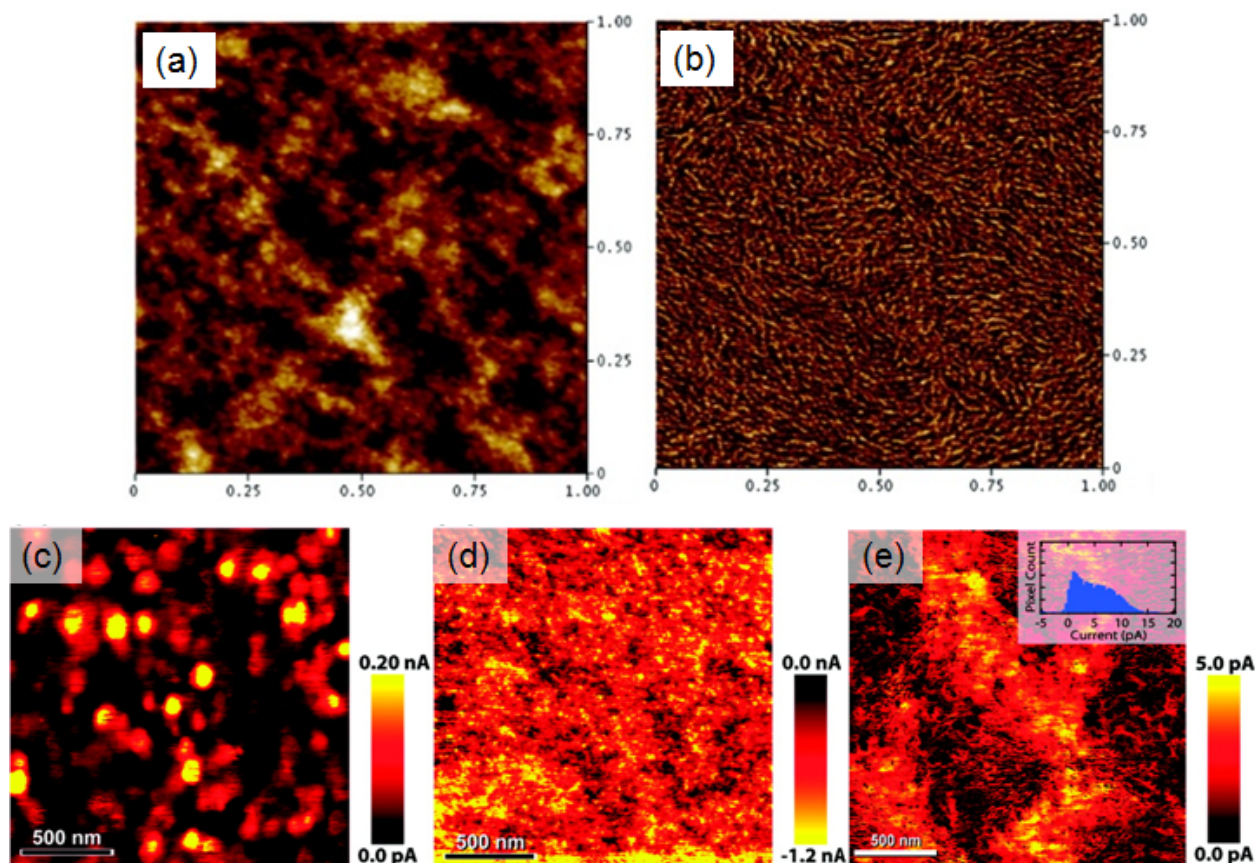


Figure 1.20: a) Tapping mode AFM topographic and phase images (1 mm 1 mm) of annealed films of pure P₃HT (Ref.[83]) b)C-AFM Images taken on a P₃HT/PC₆₁BM solar cell after 2 min of annealing: electron-dominated dark current (collected at 5 V tip bias), hole-dominated dark current (collected at +5 V tip bias), and short-circuit photocurrent when excited with 532 nm laser light. Inset to right panel shows the photocurrent histogram. (Ref.[84])

the operation of AFM probe-surface junction. Ginger and co-workers used this technique to analyze P₃HT:PCBM and produce dark hole current, dark electron current and photocurrent maps of the active layer(Fig. 1.20b).

1.3.3.1.2 X-ray and Neutron Techniques Most powerful and smaller scale characterization methods for OPV active layer are based on X-ray and neutron scattering/reflection/transmission techniques. Among these, the most commonly used technique is synchrotron based grazing incidence wide angle scattering (GIWAXS). GIWAXS cannot only give angstrom level information about the

molecular packing but also when combined with a 2D-detector, it can show the alignment of these molecular packing with respect to substrate. In Fig. 1.21a, schematic cartoon of the GIWAXS pattern based on molecular orientation is given. When this technique is used to characterize P₃HT, the resulting image shows lamellar structure with two dimensional conjugated sheets formed by interchain stacking, leading to (100) reflections due to the lamellar layer structure and (010) reflections due to π - π interchain stacking (Fig. 1.21b). Orientations of P₃HT crystallites with respect to the substrate can be identified from the different intensity distributions of (100) and (010) reflections. It was found that, in samples with high regioregularity (>91%) and low molecular weight, the preferential orientation of ordered domains is with the (100)-axis normal to the film and the (010)-axis in the plane of the film, also called “edge-on” orientation. In contrast, in samples with low regioregularity (81%) and high molecular weight, the crystallites are preferentially oriented with the (100)-axis in the plane and the (010)-axis normal to the film, called the “face-on” orientation.⁸⁵

Grazing incidence small angle scattering (GISAXS) is another X-ray technique that is used to elucidate nanoscale active layer morphology and used by Wu et al to investigate crystallization of P₃HT:PCBM films.⁸⁷ As shown in Fig. 1.22a, the PCBM exhibited short-range packing during the annealing process, resulting in a prompt and drastic increase of scattering intensity in the low-q region. The selected GISAXS profiles for 60, 600, and 1800 s at 150 °C roughly overlapped, revealing quickly saturated PCBM aggregation (inset of Fig. 1.22a). A broad interference shoulder at $qx=0.025\text{\AA}$ shaped during the annealing, corresponding to the formation of a liquid-like or distorted face-centered-cubic-like packing of PCBM aggregates with a mean spacing of around 25 nm. For comparison, the GISAXS profile similarly measured for a pristine P₃HT film annealed at 150 °C for 1800 s contributed only marginally in this monitored q-region revealing that scattering in the low-q region was mainly dominated by large PC₆₁BM aggregates. Neutron scattering has also been used to investigate the lateral structure of P₃HT:PCBM systems. To characterize the phase separated morphology, Kiel et al. modeled PCBM agglomerates as polydisperse spheres having hard sphere interactions surrounded by a matrix of P₃HT and solubilized PCBM, as shown in Fig. 1.22b.⁸⁸ The

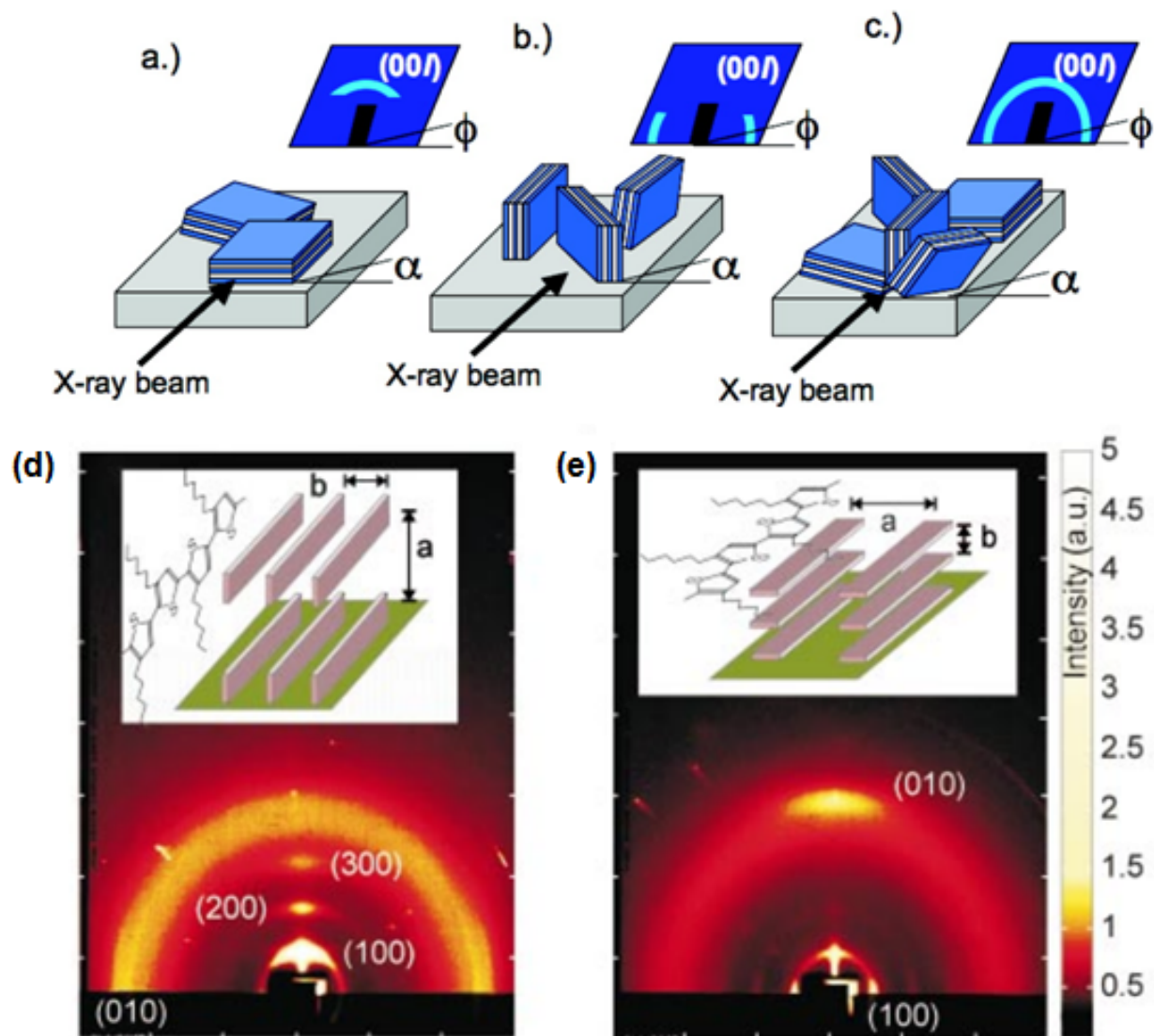


Figure 1.21: a) Schematic diagram showing the relationship between lamellar orientation and the resulting 2D-GIWAXS pattern: (a) lamellar structures oriented mostly parallel to the substrate surface; (b) lamellar structures oriented perpendicular to the substrate surface; (c) lamellar structures oriented randomly with respect to the substrate surface. (Ref.[86]) b) two different orientations of ordered P₃HT domains with respect to SiO₂/Si substrates (Reproduced from Ref.[85])

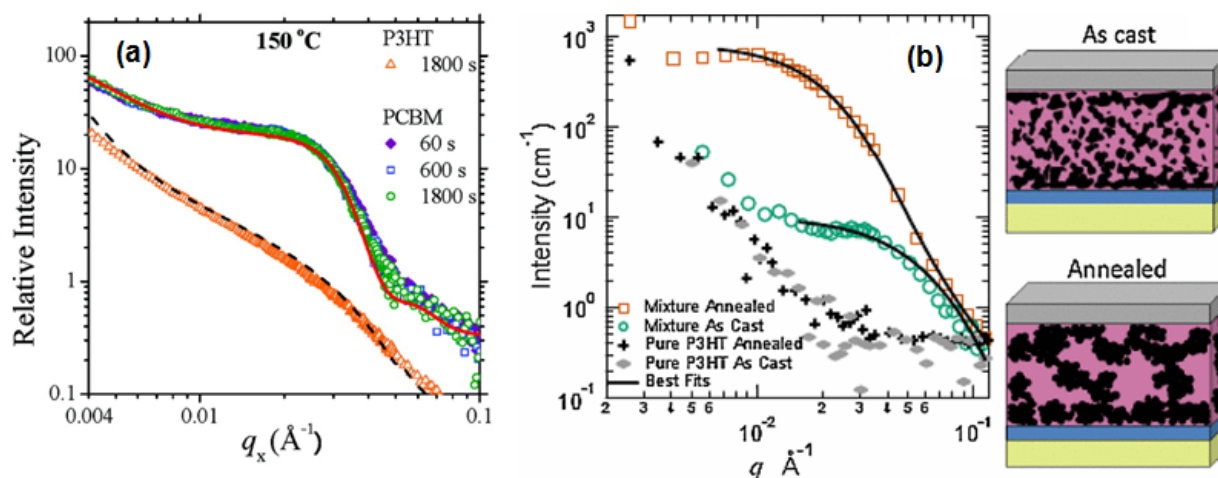


Figure 1.22: a) Approximately overlapped GISAXS data collected after 60, 600, and 1800 s of thermal annealing of P₃HT films. For comparison, the GISAXS data for a pristine P₃HT film annealed at 150 °C for 1800 s are also shown; the data are fitted (dashed curve) with polydisperse (in rod length) rods. Inset: corresponding mean size (b) evolution of PCBM aggregates (reproduced from Ref.[87]). (right) plot of SANS intensity ($I(q)$) vs. wavevector (q) for both annealed and unannealed samples of 1 : 1 by weight ratio of PCBM and P₃HT as well as annealed and unannealed samples of pure P₃HT. Right: cartoon of morphology change after thermal annealing showing the coarsening of the PCBM phase separated structures (reproduced from Ref.[88]).

fitting results indicated that annealing increases the PCBM aggregate size and volume fraction, suggesting a coarsening of the phase separated morphology and that PCBM is soluble up to 16 volume-percent concentration in the P₃HT matrix.

1.3.3.2 Device Processing

The fabrication of solution processed OPVs involve dissolving donor and acceptor materials in an organic solvent, spin coating this mixture on a substrate followed with a post-processing. As a solvent, usually non-polar solvents such as chloroform (CHCl_3), chlorobenzene (CB), 1,2-dichlorobenzene (ODCB) that dissolve PCBM are used. Sometimes, either to improve the solubility of one phase in solution or film, or to crystallize one phase in film, additives are used in the active layer solution. Spin coating usually defines the thickness through selection of solvent, spin-coating speed

and acceleration. These parameters play a critical role in the evolution of morphology as well. Moreover, post processing such as thermal annealing and solvent annealing are used to tune the active layer morphology further. The common goal in these device processing methods are obtaining a fine-sized, monodisperse and percolated domains through the active later thickness.

1.3.3.2.1 Thermal Annealing Thermal annealing is a well-know materials science processing that is used to change the microstructure and thus properties of materials via thermal energy. With a similar motivation, thermal annealing is a common method used to improve OPV device morphology and performance. In the earlier studies on P₃HT:PCBM solar cells, it was reported that device efficiency is improved by six-fold from 0.4 to 2.5% PCE upon annealing spin-coated film at 75 °C.⁸⁹ This improvement in PCE comes from several morphological changes in the active later that are: 1) increased crystallinity, especially in P₃HT chains enhancing charge mobility in the film 2) change in the P₃HT:PCBM domain mixing, from well mixed phase to enlarged phases which provides percolated network for the charges to be collected at the electrodes, so improving the fill factor and possibly J_{SC} of the device 3) decreasing the small impurities and voids and improving both V_{OC}, FF and J_{SC}. Some of these changes can be observed in the AFM image given in Fig. 1.23.

The time of thermal annealing is as important as the temperature that is used. Usually, polymers are less crystalline and they can be annealed at higher temperatures for longer times. However, small molecules usually needs less annealing because the mobility of these molecules are higher than polymers in a film and they can crystallize fairly easily.⁹¹ Nevertheless, excess thermal annealing can also have negative consequences in polymer solar cells. Photoluminescence (PL) and near-field optical imaging results on annealed P₃HT:PCBM revealed that increasing annealing time from 5 to 30 minutes resulted in growth of the PCBM domains and aggregates and caused spherical bumps and topographical features on the film (Fig. 1.24).⁹²

1.3.3.2.2 Solvent Annealing For P₃HT:PCBM solar cells from made from high boiling solvent such as ODCB, it was observed that controlled drying of the solvent can improve the device effi-

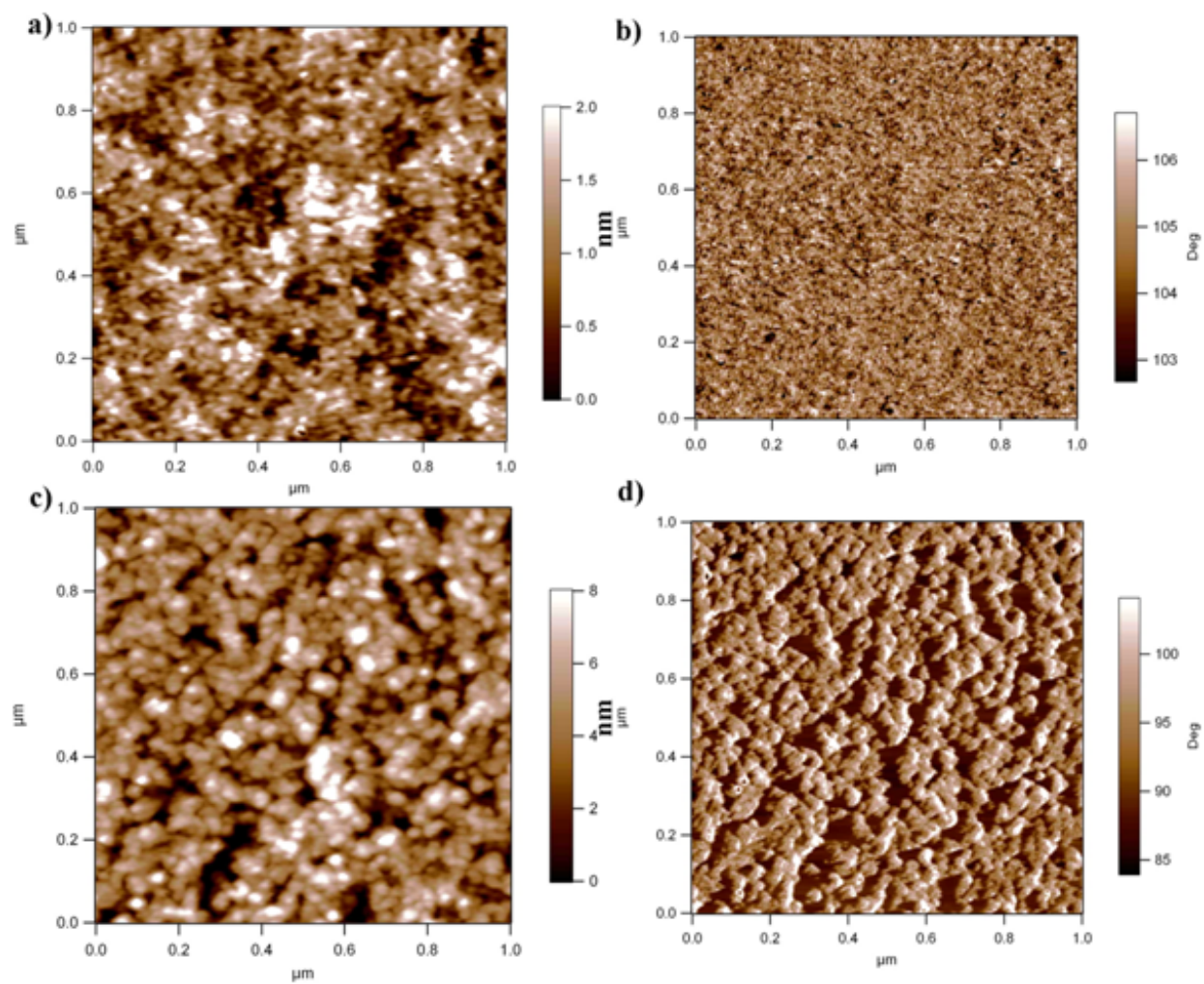


Figure 1.23: Topography (left) and phase (right) AFM images for (a, b) not annealed P₃HT:PCBM (2000 rpm) and (c, d) annealed P₃HT:PCBM (2000 pm). (reproduced from Ref.[90])

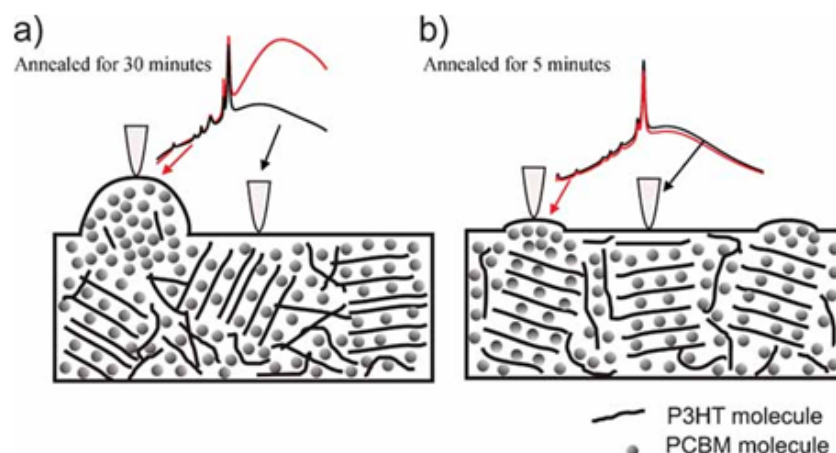


Figure 1.24: P₃HT:PCBM blend films after a) 30-min. and b) 5-min. thermal annealing at 140°C. The red spectra were collected when the tip was positioned above the regions where PCBM aggregates were present. The black spectra were collected when the tip was away from the PCBM aggregates (Ref.[92]).

ciency. Slow spin coating (usually around 600 rpm) high concentrated P₃HT:PCBM solution in ODCB for a minute usually leaves ODCB solvent residues in the film. If this film is placed in a small petri dish, crystallization of P₃HT happens slowly over 30 minutes and this can be observed by the color change of the film from orange-yellow to dark purple. This method allows high degree of crystallinity in the P₃HT of active layer while keeping the domain size fairly small. P₃HT:PCBM devices fabricated with this processing resulted PCE up to 4.4%.⁹³ Similarly, sometimes OPV active layers were exposed to different solvent vapors (through annealing) to initiate morphology reconstruction in the film. Depending on the solvent selection, higher crystallinity or increased domain size in the solar cell films can be achieved.⁹⁴ Moreover, sometimes brief soaking of the active layer directly into a polar solvent can also modify the interface of the solar cell. For example, MeOH treatment on PTB7:PC₇₁BM increased the PCE from 7.1 to 7.9%.⁹⁵

1.3.3.2.3 Solvent Additive One of the key findings that helped pushing OPV efficiency above 5% limit was the use of solvent additives in the device fabrication. 1,8-diiodooctane (DIO) is one of the mostly used solvent additives in the literature.⁹⁶ There has been several reports that showed increase

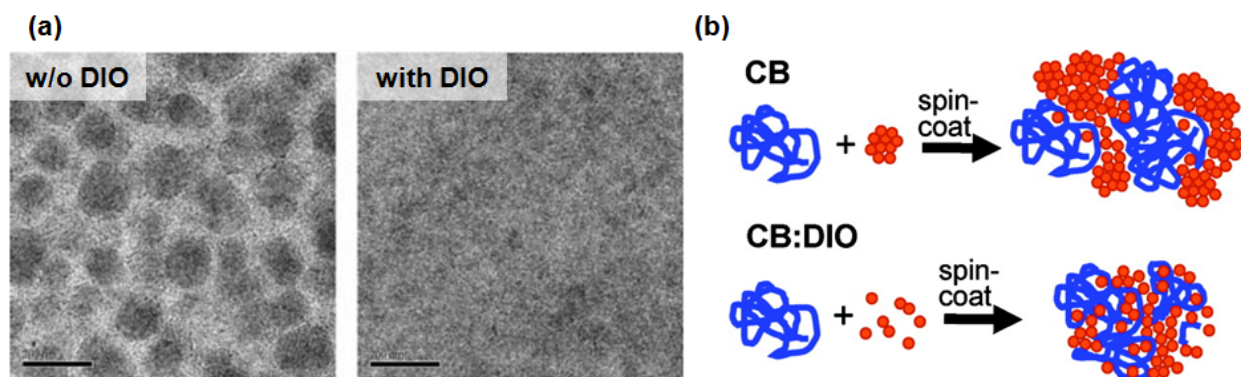


Figure 1.25: Examples of suppressing large-scaled phase segregation by solvent additives. (a) TEM images of PTB7/PC₇₁BM BHJs (the scale bar is 200nm). (Reproduced from Ref.[17]) b) Schematics of PTB7/PC₇₁BM blends in solution and thin-film states. (Reproduced from Ref.[97])

in the device efficiency by use of DIO. For example, it increased the efficiency of PCPDTBT:PC₇₁BM from 3.4 to 5.1 and the efficiency of PTB7:PC₇₁BM from 3.9 to 7.4%.¹⁷ It was later revealed that DIO helps by selectively dissolving PCBM aggregates in the solution and decreases the domain size in the film allowing better intercalation of PCBM into PTB7 phases (Fig. 1.25).⁹⁷

Having a strong influence to the film comes from higher boiling point of DIO because even the solvent such as CB leaves the film, DIO stays in the film much longer and if not completely removed, can react with the Al contacts. So, in general most of the solvent additives have higher boiling point compared to the parent solvent. Besides, some of them dissolve one component better, or sometimes is does not dissolve one component and help it to crystallize. The key point here is that the role of solvent additives can be varied depending on their interaction with donor and acceptor materials. For example, 1-chloronaphthalene (1-CN) is usually is a non-solvent for the donor material and can improve its crystallinity. It was shown that CN is used in easily obtainable poly(2,3-bis-(3-octyloxyphenyl)quinoxaline-5,8-dyl-alt-thiophene-2,5-diy) (TQ1)-based systems with PC₇₁BM as an acceptor to optimize the active layer nanomorphology. Different characterization techniques revealed that that the addition of 5% (v/v) CN leads to smoother films, less heterogeneous surface features, and well-distributed TQ1:PC₇₁BM phases, resulting in more balanced charge transport

in the devices and a highly efficient power conversion efficiency (PCE) of 7.08%.⁹⁸ Similarly, 1,8-octanedithiol (ODT) is used as a poor solvent for both P₃HT and PCBM to aggregate when the major solvent (CB) starts to evaporate out during the spin coating process. The comparable J_{SC} values obtained with thinner film (less absorption) compared with solvent annealed devices suggest that the exciton dissociation and carrier collection are rather efficient in the devices made with ODT due to smaller interlayer spacing confirmed with GIXD.⁹⁹

1.3.3.3 *Molecular Design*

Besides changing the conjugated part of the donor and acceptor materials, sometimes tuning the solubilizing groups or side chains of those materials can improve the solar cell performance dramatically due to the strong influence on the active layer morphology. There is usually a trade-off between solubility and crystallinity when designing the solubilizing groups such that in most cases longer and branched alkyl tails give higher solubility while shorter and straight ones give better crystallinity. In order to achieve the best performance from a given conjugated polymer or small molecule, a well balance between solubility and crystallinity needs to be established. For example, it was demonstrated that both π - π stacking distance and film morphology of PTB7:PC₇₁BM blends are highly sensitive to side-chain structure.¹⁰⁰ In addition, it can also influence the stacking direction as in the case of PTzBT:PCBM solar cells in which with the right choice of side chains face on stacking is obtained that resulted in PCEs up to 7.5%.¹⁰¹

1.3.3.4 *Self-Assembly*

One of the less explored frontiers in the OPV research is the role of self-assembly on the OPV performance. The outstanding problem here is that most of the good working OPV morphologies are found by luck and understood the nature of it much later rather than programming it. In this sense, supramolecular strategies that use non-covalent forces to construct well defined organic nanostructures can be useful.^{102,103} Most of the successful studies done in the self-assembly area comes

from the aromatics and their ability to form π -stacks.^{104,105} These studies are merely programmed or foreseen, mostly observed in a well-known conjugated polymer or molecules that are to known give high solar cell efficiency. This type of interactions can give self-assembled nanowires as in the case of poly(3-alkylthiophene (P3AT) through face-to-face stacking of polymer backbone with the stacking direction being parallel to the long axis of the wire as shown in Fig. 1.26.¹⁰⁶ Similar nanowires can be obtained in P3HT through processing or solvent choice resulting in 15-fold higher hole mobility in the active layer.¹⁰⁷

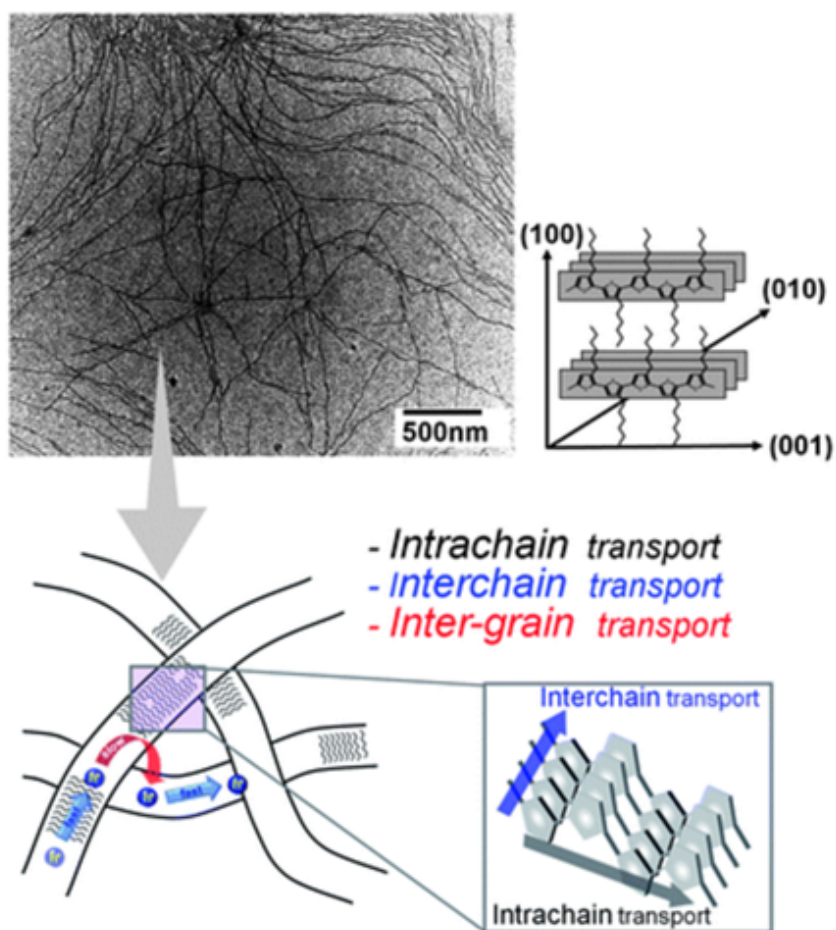


Figure 1.26: Schematic of the face-face stacking of polymer chains in P3HT nanowires. (Reproduced from Ref.[106])

1.4 THESIS OVERVIEW

Extensive studies on active layer morphology of OPVs have demonstrated that chemical design of the donor materials play a critical role in nanomorphology and device efficiency. A large body of research in chemical design focuses either on engineering the conjugated part of the dyes or optimizing the solubilizing alkyl-groups. However, different approaches to guide the self-assembly in these donor dyes have not been explored as much. The first chapter in this thesis examines the use of molecular shape to guide self-assembly of donor dyes to obtain enhanced OPV device efficiency. The latter chapters highlight the use of hydrogen bonding interactions to influence nanomorphology and molecular packing. It was found that hydrogen bonding interactions can be used in both cooperative or competing fashion to realize more efficient OPV cells.

In detail, chapter 2 summarizes an investigation of molecular stacking in two homologous tripodal shaped donor molecules with different solubilizing units. Characterization and simulation results revealed distinctive stacking behavior for tripodal molecules that have branched (2-ethylhexyl) and straight (dodecyl) alkyl tail. Different stacking behavior led to contrasting nanomorphology both in native films and blended active layer films of tripodal molecules. Specifically, tripod molecule with dodecyl group promoted assembly of 1D nanowires that was translated onto active layer under certain solvent conditions while tripod molecule with ethylhexyl did not result in definite nanostructures. Impact of stacking and morphology of tripodal molecules on hole mobility, trap states and power conversion efficiency in the OPV device was reported.

Chapter 3 describes an effort to utilize hydrogen bonding groups in a hairpin shaped conjugated molecule. Distinct shape and position of hydrogen bonds in the molecule led to supramolecular nanowires. It was found out that the processing conditions were equally important as molecular design to make sure supramolecular nanowires present in the active layer morphology. Besides the processing conditions, analogous molecule was also used to highlight the effect of synergistic action of hydrogen bonds and π -stacking on the charge transport and OPV device efficiency.

In chapter 4, hydrogen bonds were used in a linearly shaped donor molecules in both symmetric and asymmetric way. Clear difference in morphology and molecular stacking was observed especially for asymmetric molecule pair one containing an amide bond capable of forming hydrogen bonds with one containing an ester bond in the same position. It was found out that presence of amide moiety in asymmetric molecules provided competitive interaction between hydrogen bonding and π -stacking, that resulted in smaller domain size in the active layer compared to ester homologue. The smaller domain size in amide derivative allowed significant increase in the short-circuit current and efficiency of the solar cells.

The final chapter (chapter 5) includes the summary and future outlook based on the work presented throughout.

2 SELF-ASSEMBLING TRIPODAL SMALL-MOLECULE DONORS FOR BULK HETEROJUNCTION SOLAR CELLS

2.1 OBJECTIVES AND SIGNIFICANCE

The power conversion efficiency of organic solar cells (OSCs) could benefit from systematic studies to improve bulk heterojunction (BHJ) morphology by modifying donor compounds. Supramolecular self-assembly is an attractive strategy to combine the beneficial properties of polymeric donors, such as a well-controlled morphology, with the homogeneous composition of small molecule donors for OSCs. We report here on two tripodal ‘star-shaped’ small-molecule donor compounds based on diketopyrrolopyrrole (DPP) side chains for solution-processed BHJ OSCs. The tripod molecules were found not to aggregate in solution or form crystalline domains in thin films when a branched alkyl chain (2-ethylhexyl) substituent was used, whereas linear (dodecyl) alkyl chains promote the formation of one-dimensional (1D) nanowires and more crystalline domains in the solid state. We demonstrate that the 1D self-assembly of these tripods enhances the performance of the corresponding solution-processed OSCs by 50%, which is attributed to the significant increase in the fill factor of devices resulting from a reduction of trap states.

2.2 BACKGROUND

Solution-processed bulk heterojunction (BHJ) organic photovoltaic (OPV) materials remain under intensive investigation after almost two decades of fundamental research driven by their potential to bring low-cost, lightweight, flexible solar-to-electric energy conversion devices to market.^{108–111} OPV power conversion efficiencies (PCEs) have been rising steadily, now exceeding 10%.⁶⁸ The active layer of a BHJ OSC typically utilizes a fullerene-based acceptor (n-type) material in a phase-separated blend with polymeric or small-molecule organic donor (p-type) material.^{112,113} The morphological elements of the active layer’s p-n heterojunction include the topology of its percolation

network, domain sizes, distribution of trap sites, and spatial orientation of molecules. These features collectively play a critical role in the physical phenomena that ultimately lead to charge extraction.¹¹⁴ Research efforts to increase OPV PCEs often involve controlling BHJ morphology through covalent modification of the donor compounds¹¹⁵ or optimization of processing conditions,¹¹⁶ (e.g., thermal annealing,⁸⁹ solvent vapor annealing,^{93,117} solvent additives¹¹⁸). These two factors influence the process of spinodal decomposition during formation of the active layer. An alternative strategy for controlling active layer morphology is the use of programmed self-assembly in an attempt to control molecular organization within the active layer at specific length scales.^{119,120} There have been several strategies used to promote self-assembly of donor molecules in solution, including discotic liquid crystals,^{121,122} nematic liquid crystals,¹²³ liquid crystalline polymers,¹²⁴ nanostructured block copolymers,¹²⁵ bimolecular crystals,¹²⁶ hydrogen bonded networks,¹²⁷ and one-dimensional (1D) nanostructures.¹²⁸ Our group has focused recently on the use of small molecule donors that assemble into 1D nanofibers for OSCs in order to form high interfacial area percolated networks when blended with fullerenes.¹²⁹⁻¹³¹

Small molecules with linear architecture have been used to create devices with efficiencies of 6%-9%.^{42,43,132-135} Several 'star-shaped' donors with more complex architectures (C-3 symmetric or tripodal) have also been reported, with efficiencies that have now surpassed 4%.¹³⁶⁻¹⁴⁰ We envisioned that the increased $\pi - \pi$ stacking interactions of these disc-like molecules would promote fiber assembly when appended with alkyl side chains for solubility. We chose diketopyrrolopyrrole (DPP) units flanked by thiophene groups to serve as the chromophoric 'arms' of our tripods because of DPP's favorable optoelectronic properties and well-established use in efficient OPVs.^{42,131,141}

We designed tripodal donor molecules T_{EH} (with 2-ethylhexyl) and T_{C12} (with dodecyl) in which an electron-donating triphenylamine (TPA) unit serves as the central trifurcated core.¹⁴² A recent study by Giuseppone and coworkers has shown that TPA exhibits a remarkable propensity to form fibers and conduct charge carriers via the generation and sharing of free radicals upon photoexcitation.¹⁴³ While several tripodal molecules incorporating similar TPA-DPP designs have been

reported for OPVs,^{144,145} there was no indication that they self-assemble into well-defined nanostructures. A similar set of tripodal molecules with the 2-ethyl hexyl groups and differing number of thiophenes was recently reported and yielded devices with PCEs as high as 2.95%.¹⁴⁶ The true potential of tripodal chromophore solar cells will not be realized until the role of self-assembly in determining the morphology and performance is understood. In this work we investigate the influence of side chains on molecular packing of TPA-DPP tripods and therefore solar cell performance. As a complement to T_{EH} , we study a related new tripod molecule, T_{C12} , with straight side chains that will not interfere with molecular packing. The dodecyl (C12) side chain is used because shorter straight chains were not able to solubilize the molecule enough to form homogenous thin films and working devices.

2.3 RESULTS AND DISCUSSION

2.3.1 *Synthesis and Characterization*

The tripodal donors were synthesized by Stille cross coupling of tris(4-(5-(tributylstannyl)thiophen-2-yl)phenyl)amine and monobrominated thiophene-flanked DPP compounds (BrTDPP) with 2-ethylhexyl (EH) or dodecyl (C12) side-chains to afford T_{EH} and T_{C12} , respectively. Detailed synthetic procedures can be found in the experimental section. Variations with hexyl (C6) and octyl (C8) side chains were made as well, but were found to be unsuitable for device work due to poor solubility.

In order to study the impact of self-assembly on solar device performance, two homologous molecules, T_{EH} and T_{C12} (see Fig. 2.1a), were synthesized. These were found to have similar electronic and optical properties. The highest occupied molecular orbital (HOMO) levels were calculated by ultraviolet photoelectron spectroscopy (UPS) (see Fig. 2.2), and the band gaps were calculated from the onset of thin film UV-vis absorption spectra. T_{EH} has a HOMO of -5.65 eV relative to vacuum level, and T_{C12} has a similar one of -5.60 eV. The HOMO levels of both compounds

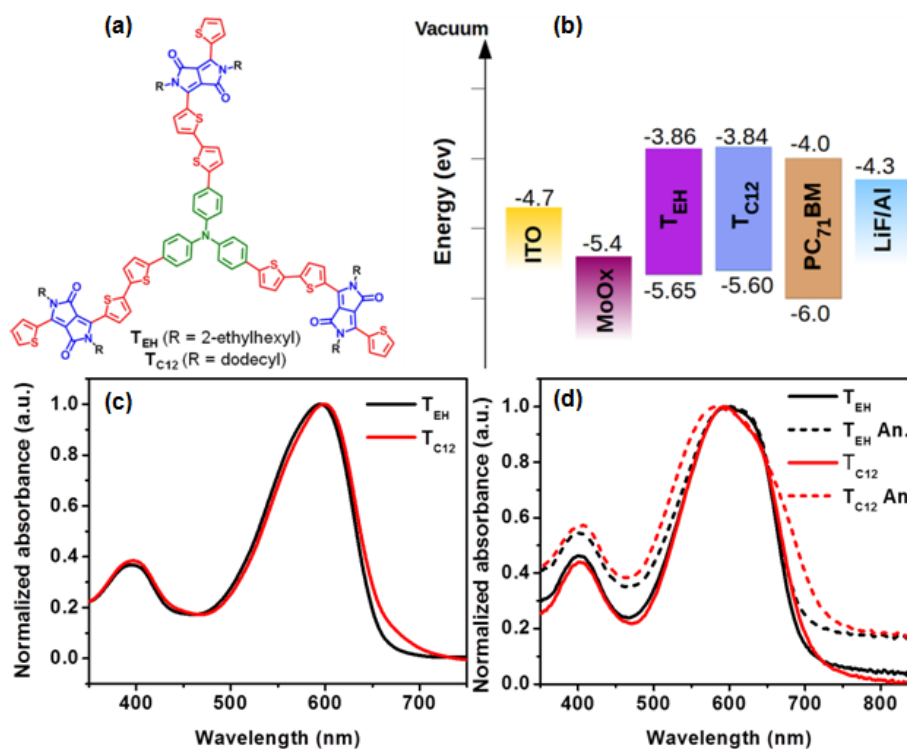
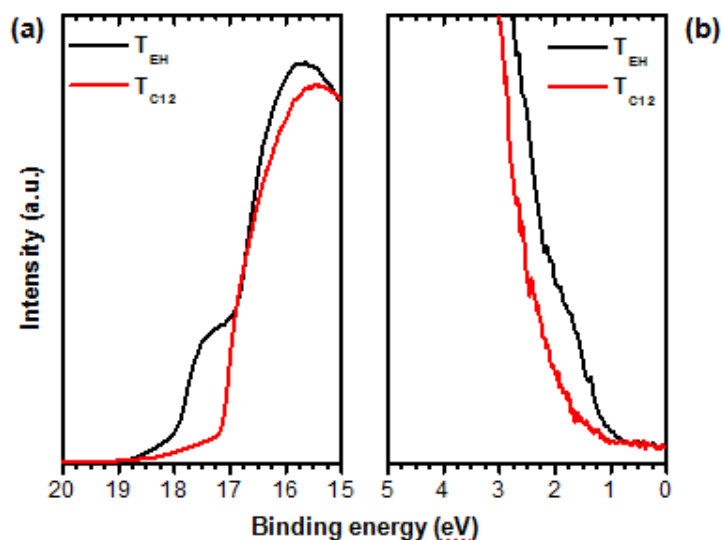


Figure 2.1: (a) Chemical structure of T_{EH} and T_{C12} molecules. (b) Energy levels of T_{EH} and T_{C12} molecules with the energy levels of other device layers. (c) Absorption spectra of T_{EH} and T_{C12} in chloroform solution and (d) in solid film cast from chloroform before and after annealing.

show slight offsets from MoOx, which is favorable for hole transport out of the active layer. The band gaps of T_{EH} and T_{C12} are 1.79 eV and 1.76 eV, respectively. The compounds show offsets from the lowest unoccupied molecular orbital (LUMO) of PC₇₁BM of 0.16 eV and 0.14 eV. As can be seen in Fig. 2.1b, the energy levels of the two compounds are comparable, and their small offsets to PC₇₁BM are favorable for effective exciton splitting. The UV-vis absorption spectra of T_{EH} and T_{C12} in CHCl₃ (Fig. 2.1c) confirm that the optical properties between the two molecules are analogous (both with extinction coefficients higher than $10^5 \text{ M}^{-1} \text{ cm}^{-1}$). T_{EH} shows an absorption maximum at 595 nm and T_{C12} at 598 nm, and they both absorb up to wavelengths of approximately 700 nm. We also observed some differences in the absorption spectra of the two tripods as thin films spin coated from CHCl₃ (Fig. 2.1d).



Calculated values from UP Spectra

Sample	Hel (eV)	E_{sc} (eV)	E_o (eV)	HOMO (eV)
T_{EH}	21.2	17.25	1.7	-5.65
T_{C12}	21.2	17.24	1.64	-5.6

Figure 2.2: UP spectra of (a) the high binding energy cut-off region and (b) the HOMO onset region of T_{EH} and T_{C12} with calculated values given in the bottom

The absorption maximum of the T_{EH} film is red-shifted, while that of T_{C12} is blue-shifted relative to the solution spectra. Both of these shifts are magnified upon annealing. The red-shift in the case of T_{EH} indicates the formation of J-aggregates involving the stacking of T_{EH} molecules in an end-to-end manner. Similarly, the blue-shift can be attributed to the formation of H-aggregates, providing evidence for the cofacial stacking of T_{C12} molecules in the film. Additionally, a shoulder in the T_{C12} film at 670 nm most likely arises from J-aggregate formation involved in nanowire bundling. The optical properties of the compounds are summarized in Table 2.1.

2.3.2 Supramolecular Self-Assembly of Tripodal Molecules

The assembly of the tripodal molecules was further characterized by atomic force microscopy (AFM) and grazing incidence X-ray diffraction (GIXD). AFM topography and phase images in Fig. 2.3a and

Fig. 2.3d show that T_{EH} forms featureless films when cast from chloroform, even after annealing for 5 minutes at 120 °C. Conversely, Fig. 2.3b and Fig. 2.3e show that T_{C12} forms short nanowires when cast under same conditions. When a T_{C12} solution is cast from chlorobenzene, the self-assembly of the nanowire morphology is further enhanced, as shown in Fig. 2.3c and Fig. 2.3f. The height of the nanowires in Fig. 2.3c is around 2.5 – 3 nm which scales with the molecular diameter of T_{C12} molecules. On the other hand, there was no such morphology change for T_{EH} when it was cast from chlorobenzene (Fig. 2.4).

2D GIXD data collected from films of the tripodal molecules are shown in Fig. 2.5. A T_{EH} film drop cast from chloroform and slowly dried produces diffuse and weak diffraction rings (Fig. 2.5a). The ring around 0.5 \AA^{-1} corresponds to a 1.3 nm distance, which can be attributed to the center-to-center distance when one arm of each molecule overlaps. The ring around 1.47 \AA^{-1} corresponds to 0.43 nm, which can arise from the cofacial packing of each arm of adjacent molecules in a stack. This spacing is greater than what is expected for π - π stacking distances (0.37 nm) in conjugated small molecules. In addition, neither of the diffuse rings have a directional preference with respect to the substrate. We conclude that the T_{EH} molecules do not self-organize with a significant order parameter. On the other hand, T_{C12} films prepared under similar conditions exhibit diffraction rings with much higher intensities (Figure 3b). Two distinct rings at 0.22 \AA^{-1} (2.9 nm) and 0.31 \AA^{-1} (2.0 nm) appear in the low q region (Fig. 2.5c). The 2.9 nm distance can be attributed to the center-to-center spacing between two adjacent nanowires, in agreement with AFM observations. The ring around 1.4 \AA^{-1} (0.45 nm) is similar to T_{EH} but in this case there is a small hump in the line profile

	Solution λ_{\max} (nm)	Film λ_{\max} (nm)	ϵ at $\lambda_{\max} \times 10^5$ ($M^{-1}cm^{-1}$)	$E_{gOptical}$ (eV)
T_{EH}	595	596	1.7	1.79
T_{C12}	598	592	1.3	1.76

Table 2.1: Optical properties of solutions and films of tripod molecules.

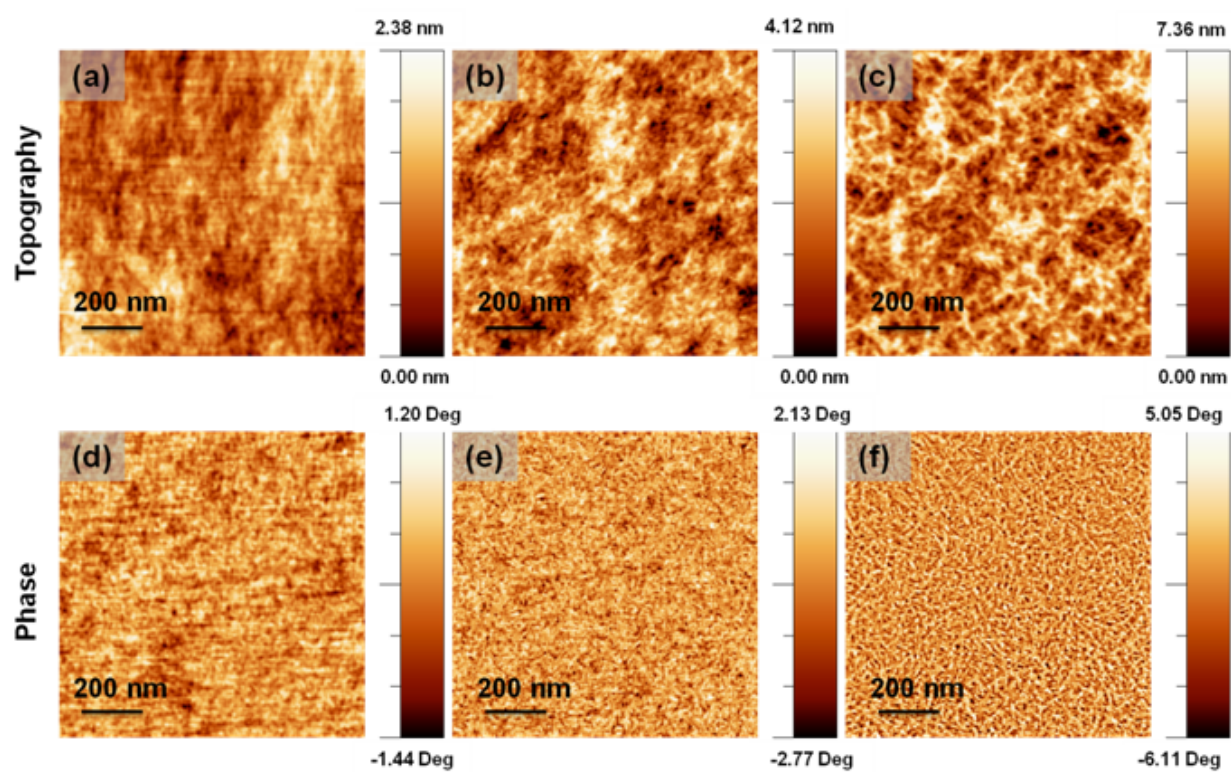


Figure 2.3: AFM topography images of T_{EH} cast from chloroform (a), $T_{C_{12}}$ cast from chloroform (b), and $T_{C_{12}}$ cast from chlorobenzene (c), with the corresponding phase images (d), (e), and (f), respectively.

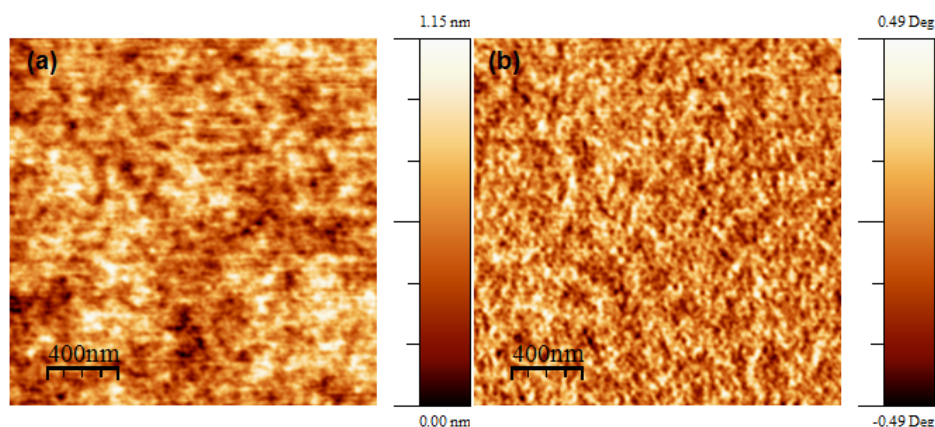


Figure 2.4: AFM topography (a) and phase (b) images of T_{EH} cast from chlorobenzene

around 1.6 \AA^{-1} (0.38 nm) which is very close to conventional π - π stacking distances. In summary, GIXD results show that T_{C12} molecules tend to organize with cofacial stacking to a greater extent than T_{EH} molecules, which is consistent with the “nanowire” morphologies observed by AFM.

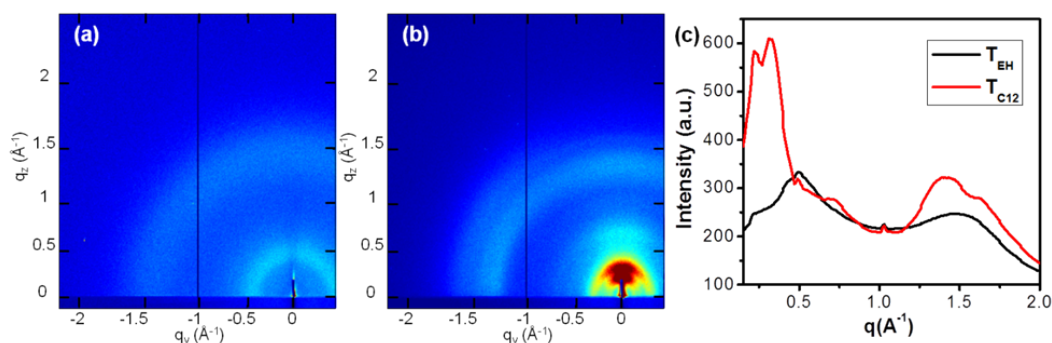


Figure 2.5: GIXD of T_{EH} (a) and T_{C12} (b) drop cast from chloroform. (c) Line profiles of GIXD data for T_{EH} and T_{C12} .

To support this hypothesis, a classical molecular dynamics (MD) simulation was performed with Groningen Machine for Chemical Structures (GROMACS) package^{147,148}. The objective of the simulation was to compare the relative ordering capacity in solution of the two donor molecules investigated here. We carried this out using explicit solvent molecules since interaction potentials for MD are parameterized against solvent environments. In vacuum we would expect to predict an overly packed structure.^{149,150} The simulations were therefore done in water and chloroform.

The final supramolecular structures predicted by the simulations of the two molecules are shown in Fig. 2.6a and Fig. 2.6b. $T_{C_{12}}$ shows ordering and alignment of molecules in the assembly, while T_{EH} exhibits a significant degree of disorder. Moreover, $T_{C_{12}}$ molecules appear from the simulation to be much less challenged by sterics along the stacking direction (Fig. 2.6d) relative to T_{EH} molecules (Fig. 2.6e). We have quantified further the ordering stability in both supramolecular systems using the intermolecular radial distribution functions (RDF) shown in Fig. 2.6c. The RDF of $T_{C_{12}}$ assemblies contains sharper and more intense peaks than that of the T_{EH} system indicating a higher local density of π - π stacking. The peaks of the $T_{C_{12}}$ compound yield an intermolecular spacing of 0.45 nm compared to 0.52 nm for T_{EH} . One might expect that the larger spacing between molecules predicted by the simulation relative to GIXD data can be attributed to the explicit use of a solvent environment. Also, a degree of periodicity can be observed in the peaks of $T_{C_{12}}$, which provides further evidence of the stronger interactions $T_{C_{12}}$ relative to T_{EH} . The Leonard-Jones energy calculations are shown in the inset in Fig. 2.6c, quantifying the relative strengths of non-covalent interactions in the two systems, -186 kJ/nm^2 for $T_{C_{12}}$ and -82 kJ/nm^2 for T_{EH} .

2.3.3 Morphology of the Active Layer

AFM was utilized to evaluate the morphology of active layer films containing donor molecules and $PC_{71}BM$ as the electron acceptor. Chloroform was used as the solvent for devices because the limited solubility of $T_{C_{12}}$ in chlorobenzene resulted in devices with lower efficiencies. As shown in Fig. 2.7a and Fig. 2.7d, $T_{EH}:PC_{71}BM$ cast from chloroform without any additives forms predominantly flat, featureless films. Two solvent additives were used in this study, 1,8-diiodoctane (DIO) and m-cresol (MC). DIO is a high boiling point solvent additive that is known to solubilize $PC_{71}BM$, and therefore allows the film to reach a more crystalline morphology by slowing the precipitation of the fullerene phase.¹⁵¹ MC was used to increase the solubility of the donor molecule. Upon the addition of DIO, the root mean square (RMS) roughness of the film increases from 0.3 to 1.2 nm (Fig. 2.7b), but the phase image (Fig. 2.7e) indicates that the film remains homogeneous without any obvious

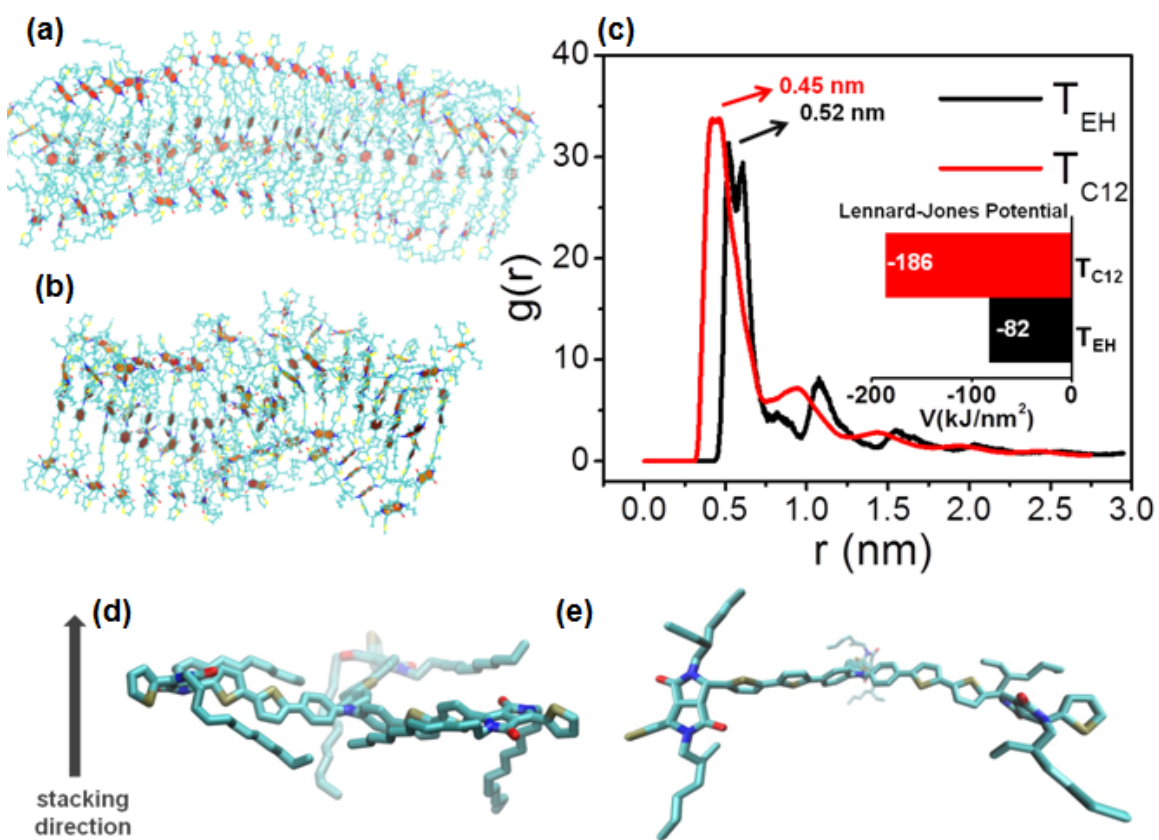


Figure 2.6: MD simulation of stacked (a) T_{C12} and (b) T_{EH} and (c) radial distribution function of the molecules with an inset of Lennard-Jones potential values. Single molecules from the MD stacking simulation for (d) T_{C12} and (e) T_{EH}

sign of textures resulting from supramolecular self-assembly. The incorporation of MC as a solvent additive flattens the film (Fig. 2.7c), returning the roughness to 0.3 nm, but does not induce any obvious nanoscale organization (Fig. 2.7f).

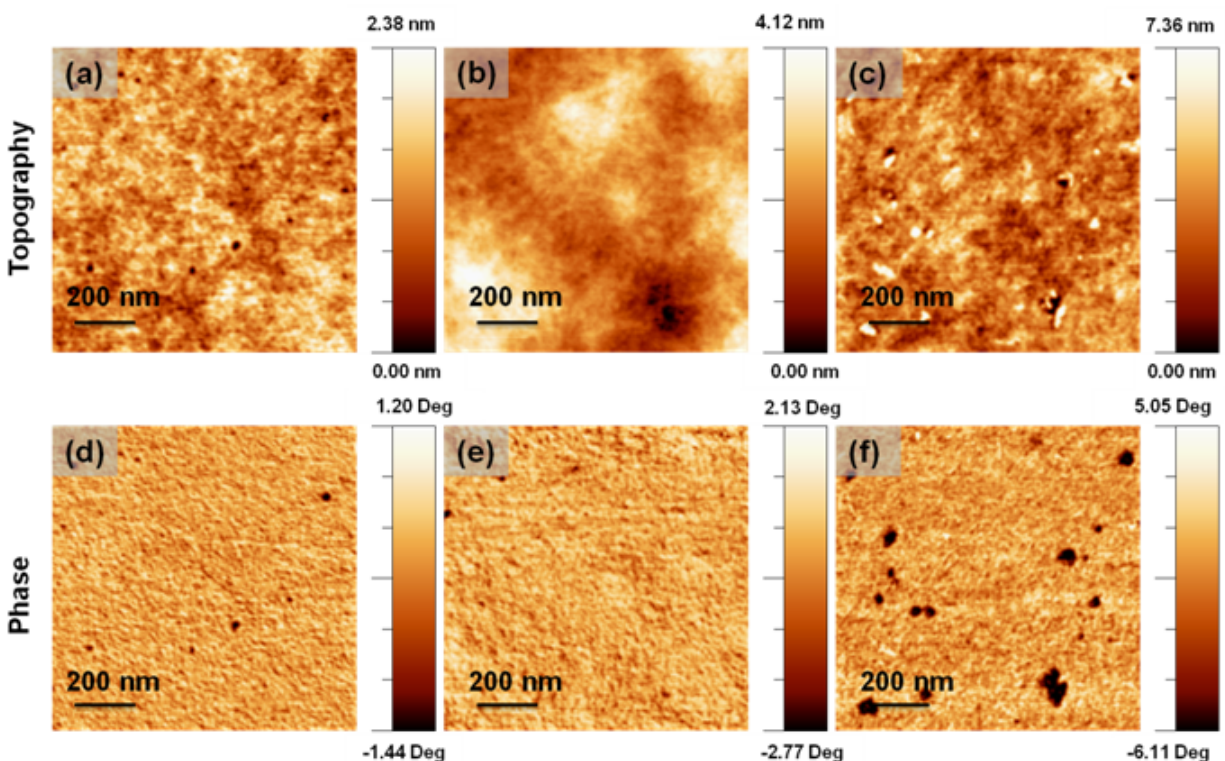


Figure 2.7: AFM topography and phase images of films created with the T_{EH} donor. (a) and (d) are respectively the height and phase image of the material without any solvent additives, (b) and (e) with 0.8 volume percent DIO, and (c) and (f) contain both the same amount of DIO and 1.0 volume percent m-cresol.

$T_{C_{12}}$: $PC_{71}BM$ films (Fig. 2.8a) are equally featureless in the absence of any solvent additives. Although $T_{C_{12}}$ forms small nanowires in chloroform, it forms featureless films after blending with $PC_{71}BM$ (Fig. 2.8d). One of the reasons for this could be that $PC_{71}BM$ disrupts the stacking of tripodal molecules. Another reason could be that chloroform leaves the film quickly during the spin coating process and does not provide enough time for $T_{C_{12}}$ molecules to stack effectively. However, the incorporation of DIO increases both the roughness of the film from 0.3 to 2.6 nm (Fig. 2.8b) and creates large, seemingly amorphous features in the phase image (Fig. 2.8e). The aggregates that

appear in the phase image are potentially bundled nanowires that are too dense to be clearly resolved by AFM. In the third set of images, it is apparent that the combination of MC and DIO promotes assembly of $T_{C_{12}}$ into a well-dispersed network of nanowires. Instead of lowering the roughness of the film as in the case of T_{EH} , the nanowires that form in the presence of MC and DIO additives raise the RMS roughness to 3.5 nm (Fig. 2.8c).

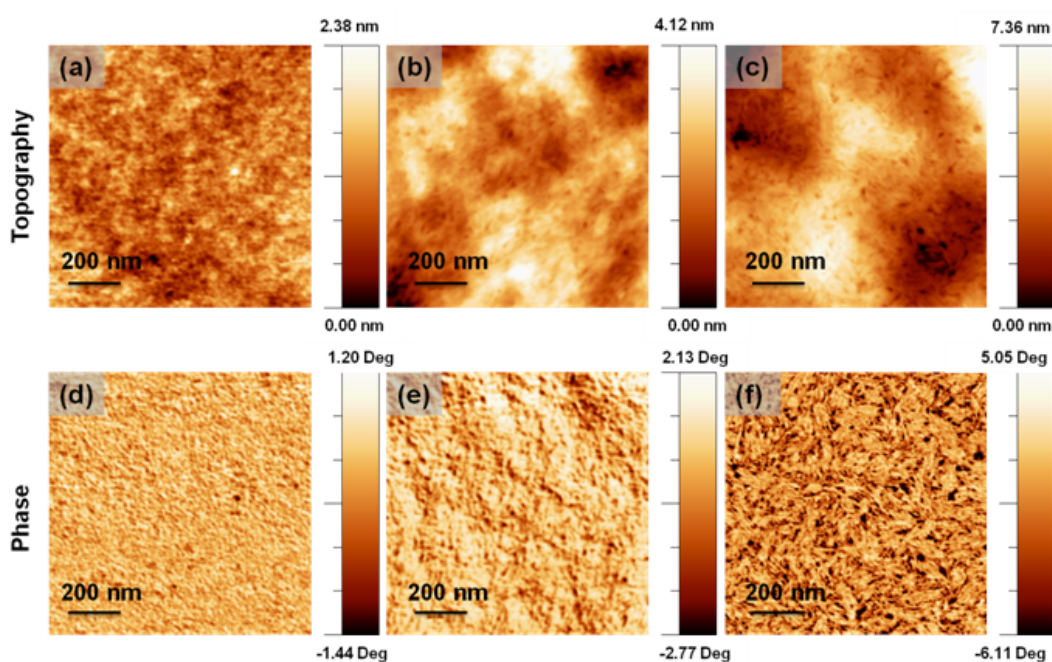


Figure 2.8: AFM topography and phase images of films created with the $T_{C_{12}}$ donor. (a) and (d) are respectively the height and phase image of the material without any solvent additives, (b) and (e) with 0.8 volume percent DIO, and (c) and (f) contain both the same amount of DIO and 1.0 volume percent m-cresol.

The nanowires visible in Fig. 2.8f are likely well-dispersed but otherwise identical to the bundles present in Fig. 2.8e, since the UV-vis spectra of the two active layer films show the same features with minimal spectral shift (see Fig. 2.9). GIXD characterization was also performed on the active layer blends but few features could be resolved, indicating that the stacking of tripodal donors is disrupted by $PC_{71}BM$ during spin casting (Fig. 2.10).

2.3.4 Photovoltaic Properties of Tripodal Molecules

Solar cells containing $T_{C_{12}}$ and T_{EH} were fabricated using optimized weight ratios of donor:PC71BM of 1:2 and 1:3, respectively. Each blend used chloroform as the primary solvent. Annealing conditions for T_{EH} and $T_{C_{12}}$ devices were optimized separately. For T_{EH} , annealing at 100 °C for 5 minutes resulted in the best performing devices. By contrast, the $T_{C_{12}}$ devices performed best when not annealed. The results of optimized devices are summarized in Table 2.2, Fig. 2.11a and Fig. 2.11b.

Without any solvent additives, devices based on T_{EH} show higher performance than those of $T_{C_{12}}$, with PCEs of 2.41% and 1.29%, respectively. $T_{C_{12}}$ exhibits slightly lower open circuit voltage (V_{OC}) and significantly lower short circuit current (J_{SC}) than T_{EH} . The drop in V_{OC} matches the difference in HOMO levels between the two donors, and the change in J_{SC} can be attributed to a lower solubility of the $T_{C_{12}}$ donor and its longer, electrically insulating alkyl tails. The addition of 0.8 volume percent DIO, however, greatly increases the performance of both donors. As demonstrated by the AFM images (Fig. 2.7 and Fig. 2.8), DIO induces the formation of molecular nanowires in

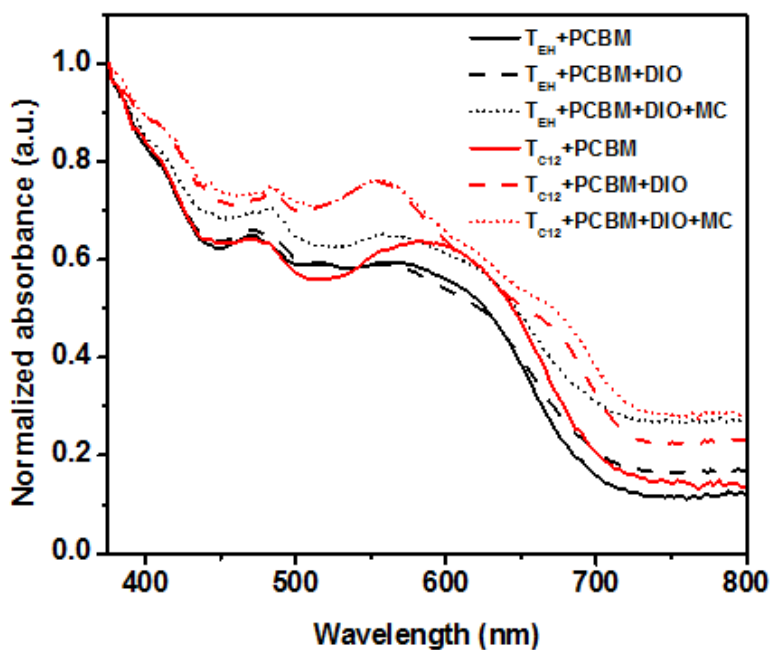


Figure 2.9: Absorption spectra of T_{EH} and $T_{C_{12}}$ solar cells in solid film.

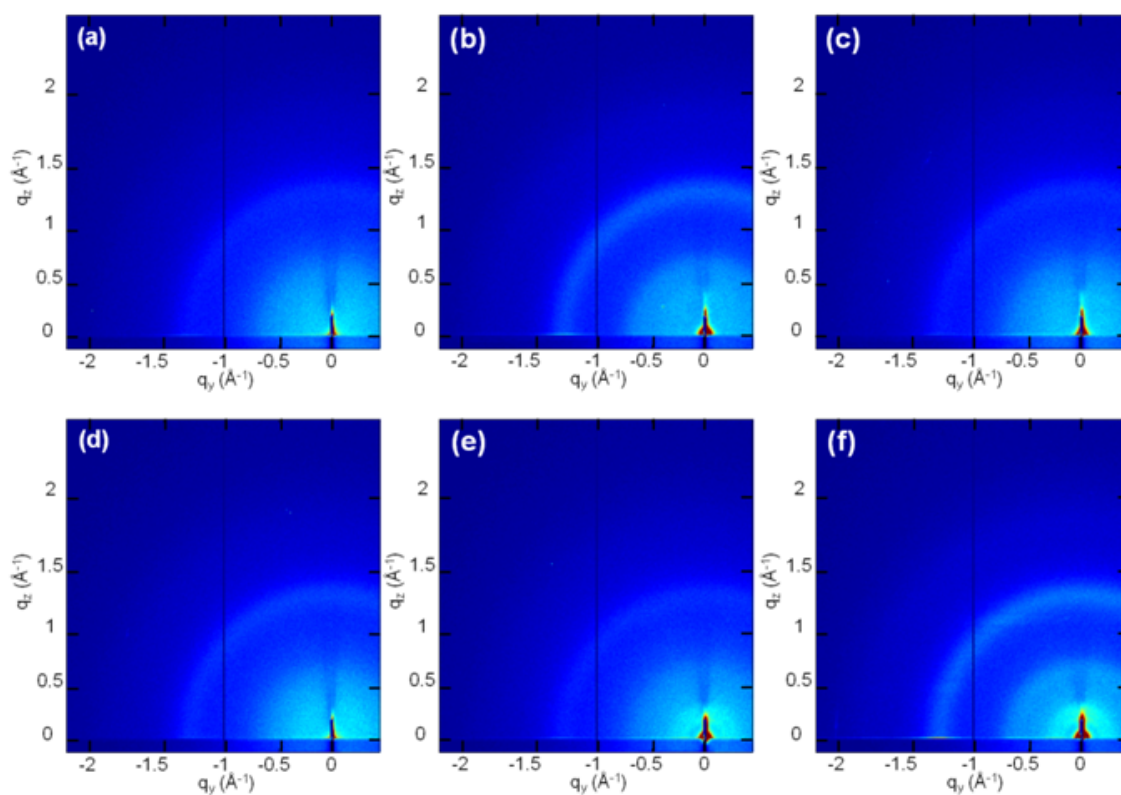


Figure 2.10: GIXD of T_{EH} : PC_{71} BM blend casted from chloroform (a), chloroform + DIO (0.8% v/v) (b) and chloroform + DIO (0.8% v/v) + MC (1% v/v) (c); T_{C12} : PC_{71} BM casted from chloroform (d), chloroform + DIO (0.8% v/v) (e) and chloroform + DIO (0.8% v/v) + MC (1% v/v) (f).

Sample	J_{SC} (mA/cm^2)	V_{OC} (V)	FF (%)	PCE (%)	R_{sh} ($\Omega \cdot \text{cm}^2$)	R_s ($\Omega \cdot \text{cm}^2$)
T_{EH} :PC ₇₁ BM	7.78	0.89	0.35	2.41 (2.34) ^a	212.41	29.88
T_{EH} :PC ₇₁ BM – with DIO	8.61	0.87	37	2.75 (2.63)	166.95	22.35
T_{EH} :PC ₇₁ BM – with DIO+MC	8.95	0.89	0.36	2.91 (2.82)	200.23	27.38
T_{C12} :PC ₇₁ BM	4.92	0.83	0.32	1.29 (1.23)	230.42	57.45
T_{C12} :PC ₇₁ BM – with DIO	10.10	0.73	0.57	4.19 (4.04)	322.14	8.17
T_{C12} :PC ₇₁ BM – with DIO+MC	10.17	0.75	0.58	4.39 (4.26)	389.54	9.41

^aAverage performance of four devices

Table 2.2: Optimized solar cell results of tripod molecules with PC₇₁BM.

the active layer for T_{C12} , which can explain the significant increase in fill factor (FF) from 0.32 to 0.54, and J_{sc} from 7.78 to 10.19 $\text{mA} \cdot \text{cm}^{-2}$. Moreover, the series resistance of T_{C12} decreases significantly from 57 to 8 $\Omega \cdot \text{cm}^2$, while T_{EH} had a much smaller decrease from 30 to 22 $\Omega \cdot \text{cm}^2$. Interestingly, the V_{oc} of T_{C12} devices was further depressed by the addition of DIO. This decrease can be attributed to the assembly of the nanowires with long alkyl tails further impeding the donor-

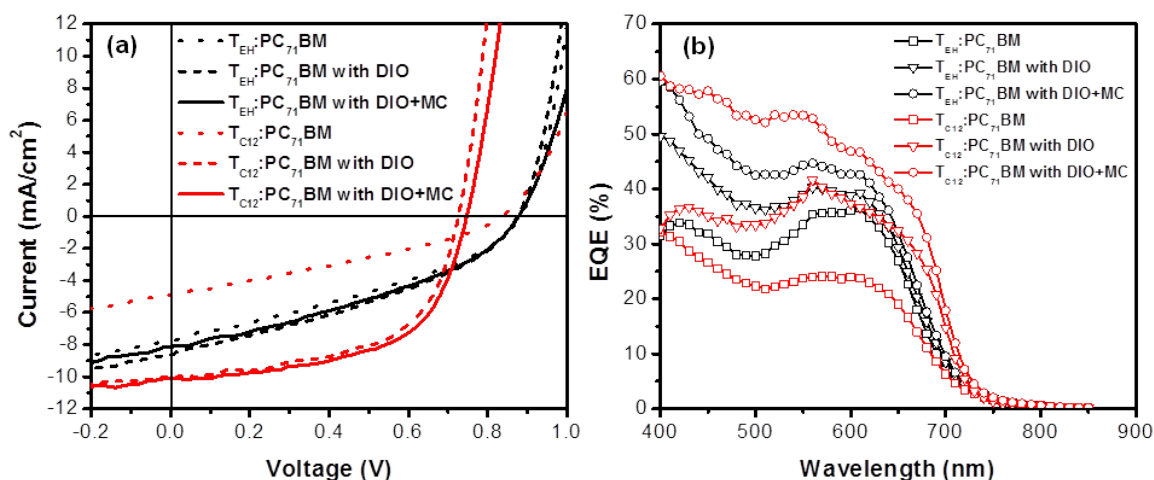


Figure 2.11: (a) J-V characteristics of optimized organic solar cells of tripod molecules with PC₇₁BM under illumination (AM 1.5). (b) External quantum efficiency (EQE) of the same devices.

fullerene interactions and to a narrowing of the band gap and increase in the donor HOMO level on account of π - π stacking. Since the two molecules show very similar optical properties, we believe the difference in performance is due to the self-assembly of $T_{C_{12}}$ into a supramolecular nanostructure. T_{EH} does not form nanowires in the film, and exhibits inferior performance compared to $T_{C_{12}}$ after DIO is added. The performance of the solar cells was further improved by the addition of 1.0 volume percent MC as a solvent additive, which most likely functions as a dispersant. The addition of MC increased the shunt resistance of the T_{EH} active layer from 167 to 200 $\Omega \cdot \text{cm}^2$, while $T_{C_{12}}$ active layers rose from 322 to 389 $\Omega \cdot \text{cm}^2$. The fully optimized devices have a PCE of 4.39% for $T_{C_{12}}$ and 2.91% for T_{EH} . Our optimized results for T_{EH} are in agreement with what has been reported previously.¹⁴⁶ We conclude that the use of linear alkyl tails rather than branched ones promotes supramolecular self-assembly in these tripodal molecules, imparting a 50% improvement in device performance while minimally affecting the optoelectronic properties of the molecules.

2.3.5 Hole mobility and Impedance Spectroscopy of Tripod Solar Cells

To explain the relative increase in FF for the $T_{C_{12}}$ devices with additives, we performed hole mobility measurements and impedance spectroscopy on active layers cast from solutions containing both solvent additives (DIO+MC). It has been shown that increases in FF are correlated with increases in hole mobility and reduction of trap states.¹⁵² The hole mobilities of the active layers were measured for hole-only devices fabricated with gold top electrodes and using the space-charge limited current (SCLC) method.¹⁵³ The SCLC regime occurs at higher voltages, and so the hole mobilities were extracted from a fit of those data points, as shown in Fig. 2.12a and Fig. 2.12b. The hole mobility values for the T_{EH} device ($5.2 \times 10^{-5} \text{ cm}^2 \cdot \text{V}^{-1} \cdot \text{s}^{-1}$) and the $T_{C_{12}}$ device ($4.0 \times 10^{-5} \text{ cm}^2 \cdot \text{V}^{-1} \cdot \text{s}^{-1}$) are very similar. Thus, changes in hole mobility do not explain the improved FF in the $T_{C_{12}}$ device. Furthermore, the device mobilities measured cannot be used to draw conclusions about differences in mobilities corresponding to the two molecules used, since this property in the device is influenced

by other factors including molecular packing and alignment, nanoscale morphology, the presence of PC₇₁BM, interfaces, and trap states.

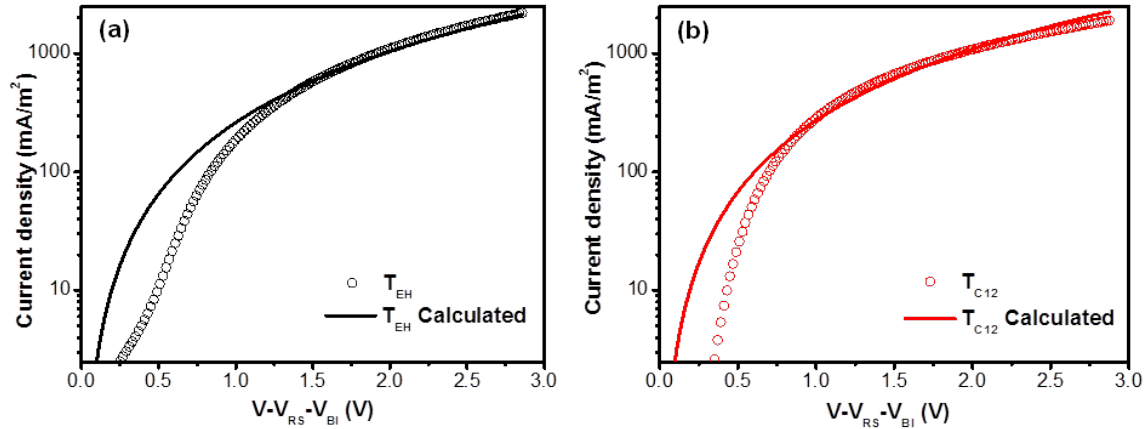


Figure 2.12: Experimental dark-current densities measured at room temperature in a hole-only device configuration (open circles) superimposed with curves calculated from SCLC theory (solid lines) for (a) T_{EH}:PC₇₁BM with DIO+MC and (b) T_{C12}:PC₇₁BM with DIO+MC.

In order to study the recombination kinetics of our system, impedance spectroscopy was carried out on devices under open circuit conditions. Upon varying the illumination, the photovoltage of the T_{C12} film scales linearly, with $dV_{OC} / d(\ln(\Phi)) = 1.3 \text{ kBT}/q$, reasonably close to the expected value of unity for a system experiencing bimolecular recombination.¹⁵⁴ However, the photovoltage of the T_{EH} film is far more sensitive to light intensity, its slope changing from 2.4 at higher light intensities to 6.8 at lower light intensities, indicating the presence of an additional recombination mechanism (Fig. 2.13a). Furthermore, while the carrier lifetime in the T_{C12} film shows the predicted dependence on V_{oc} , the carrier lifetime in the T_{EH} film is nonlinear, trending towards a smaller slope at low illumination intensities (Fig. 2.13b), which suggests that trap-mediated recombination is far more prevalent in the T_{EH} film than in the T_{C12} film.¹⁵⁵

The device with a larger degree of trap recombination would be expected to have a higher series resistance. When the bias is swept (Fig. 2.13c) the series resistance of the T_{EH} film is nearly unchanged until it dramatically decreases as the V_{oc} is approached, implying that the traps lie deep in

the energy landscape of the system. In contrast, the series resistance of the $T_{C_{12}}$ film decreases gradually as the bias is swept, suggesting that that device's trap states are shallow and easily surmounted. Based on these impedance spectroscopy experiments, we conclude that trap states in the T_{EH} active layer are more numerous and deeper seated than those in the $T_{C_{12}}$ active layer. Therefore, the supramolecular self-assembly of $T_{C_{12}}$ molecules creates ordered domains, while steric effects prevent T_{EH} molecules from stacking thus forming amorphous domains with more structural defects that may lead to electronic trap states.

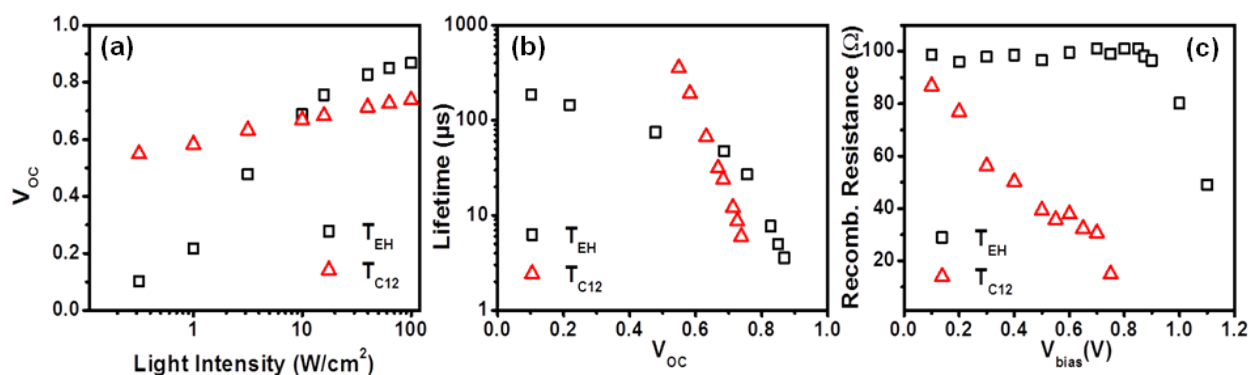


Figure 2.13: (a) V_{OC} versus light intensity, (b) lifetime versus V_{OC} (c) and recombination resistance versus applied bias (V_{bias}) of the optimized T_{EH} and $T_{C_{12}}$ devices.

2.4 CONCLUSION

Two homologous tripodal small molecule electron donors with triphenylamine cores and diketopyrrolopyrrole chromophoric arms were synthesized and used to study the impact of supramolecular self-assembly on OPV performance. We found that branched alkyl solubilizing chains inhibit the self-assembly of these tripodal molecules, while linear side chains promote the self-assembly of bundled one-dimensional nanowires. The two molecules have comparable optoelectronic properties in solution and neat films, but respond differently to the addition of solvent additives. This in turn generates significantly different film morphologies and device performances. The compound with linear side chains ($T_{C_{12}}$) assembles into nanowires, and also shows a 50% increase in PCE relative

to its branched counterpart (T_{EH}) owing to a significant gain in FF. We attribute the improvement in performance to the nanowires reducing trap states in the active layer, which is supported by impedance spectroscopy. This work demonstrates that creating supramolecular structures via self assembly is a useful strategy for improving the photovoltaic performance of small molecules by helping to control morphology across length scales.

2.5 OUTLOOK

Conjugated molecules with distinct shapes can be utilized in OPVs in different ways. One of the promising fields is discotic liquid crystals (DLC) especially when they form columnar phases that are desirable for obtaining high electron mobility up to $1.1 \text{ cm}^2 \text{ V}^{-1} \text{ s}^{-1}$.¹⁵⁶ This is comparable to amorphous silicon and can be achieved with lamellar organization of carbonaceous mesophase. In general, disk-shaped anisotropic molecules promote self-assembly into 1D columns eventually leading to 2D columnar mesophase. The mesogens with their rigid and flat cores self-assemble into columns that is resulted from steric packing and pi-pi interactions between cores. On the other hand, 3D crystal is hindered because of the high entropy and disorder of the flexible aliphatic chains on the periphery. For OPV applications, this is a preferred scenario because the organic part of the OPV is approximately a 100 nm-thick film. Second reason why this favorable for OPV applications is that the charge carrier mobility is enhanced along the columns of DLCs and this can be perpendicular to the substrate which is the most important charge transfer direction for OPVs. If the columnar stacking in the perpendicular direction is well-organized, the thickness of the OPV can be even increased further to 200-300 nm. However, in this case, the exchange of the charge carriers between neighboring columns is strongly hindered due to insulating alkyl chains for most of the design. It has been shown anisotropy of the electronic transport in columnar phases of mononuclear triphenylene derivatives is typically 1000-fold larger than the conductivity in the parallel direction.¹⁵⁷ For that reason, a molecular design like our tripod T_{C12} can be useful because in this design alkyl chains are mostly in the arms of the molecule and thiophene groups present at the very edge of the

molecule. Having even an extended conjugated part from core to the edges of the molecule can allow a better charge transfer between the columns of the columnar phases.

One of the considerations that needs to be taken care in this design is eliminating the trap states. As it was also discussed in this chapter when comparing solar cells made from T_{C12} and T_{EH} , trap states can limit the charge collection efficiency of the device and resulting in a lower FF. There can be different trap states such as contaminations as well as grain boundaries due to deficient domain and molecular orientation that impede the charge carrier transport. It is easier to eliminate trap states with DLCs because there are many methods for the macroscopic alignment of the liquid crystalline material. One of those methods is dynamic self-orientation on different surfaces such as using just glass or polymer (PTFE) coated substrates/rods to promote preferential nucleation and epitaxial growth on top.¹⁵⁸ Other methods to generate macroscopic aligned films include mechanical shearing, use of external magnetic field or special surface deposition process such as zone-casting.^{159,160} Any possible structural defects generated with these techniques can be eliminated partially in liquid crystalline materials by thermal annealing due to self-healing ability.

Among different macroscopic alignment methods of LCs, use of external magnetic field is particularly an attractive method because of its potential to translate to organic semiconductor device fabrication. The application of magnetic field to align LCs is a common method for a long time. Although LCs are usually diamagnetic, they may have multiple molecular groups that are polar and non-polar. The polar groups can possess a permanent dipole moment that is resulted from charge separation in the molecule. LCs usually align parallel to the magnetic field to decrease the distortion of the magnetic flux. There are so many ways of using this potential in LCs. One of the promising fields is mixing LC small molecules with polymers to influence polymer orientation in the film. In the work of Kornfield and coworkers, the fluid nature of LC in a single phase is retained both by creating a gel and using a block copolymer self-assembly.¹⁶¹ They synthesized polymers having very long LC midblocks flanked with LC-phobic endblocks that enabled them to produce more dilute gels than previously obtained. The polymer could be dissolved as low as only 3wt% to form gel while retain-

ing the fast dynamics of LC. This is important because this is a method to eliminate crosslinking LCs and having a thermoreversible and uniform system. These gels were aligned by cooling from isotropic to the nematic phase in approximately 1 hour (cooling approximately $0.1^{\circ}\text{C min}^{-1}$) under a field of 8.8 T. Similar templating approach with LCs was also used to align and make 1 cm long peptide amphiphiles (PAs) in water.¹⁶² One of the problems with soft materials in aqueous solutions is that such materials often display a low susceptibility and incompatibility to strong electric fields. However, it was shown that PAs can be aligned and patterned by use of lyotropic LC template in a relatively lower magnetic field (2T). Post processing such as photopolymerization enables to retain the long range order in the PAs and make it easy to wash away LC template. This particular approach can be applied to macroscopically align a wide range of soft matter, since alignment procedure only relies on orientational shear and elastic forces and lacks the requirement for delicate molecular interactions.

Another method to keep the macroscopic alignment in the materials is applying the magnetic field while drying the solvent. It was shown that it is possible to produce highly oriented films of substituted hexabenzocoronene (HBC) by utilizing a magnetic field.¹⁶³ The alignment of the HBC film was achieved by casting a HBC solution with xylene onto a field effective transistor (FET) test wafers positioned horizontal 20 T Bitter magnets at a room temperature. During evaporation of the solvent HBC undergoes a phase transition from the isotropic to a lyotropic LC phase. The actual alignment takes place when the columnar stacks are sufficiently large and mobile to be aligned. Optical microscopy revealed large area HBC monodomains that covered the entire film and WAXS showed that HBC molecules are aligned parallel to the applied field with the π - π stacking axis is parallel to the FET substrate. Producing these semiconductor materials on FET substrate allowed studying the effect of molecular alignment on mobility. With this method, the mobility of the molecules were increased by 25-75 fold and charge carrier mobilities up to $10^{-3} \text{ cm}^2/\text{V}\cdot\text{s}$ were obtained. For channel lengths larger than $2.5 \mu\text{m}$, the fibrils were smaller than the channel length and adversely affected the device performance. However, for smaller channels, it was shown with AFM that fibril superstruc-

tures are oriented perpendicular to the magnetic field direction. Since magnetic field alignment is a non-invasive and contact free way and can be applied to wide variety of self-assembled systems, this method is a promising tool for optimizing the properties and applications of functional materials.

For OPV applications, one of the main concerns is aligning the selected stacking axis (for example π - π stacking) perpendicular to the substrate. This kind of an alignment was achieved by Osuji and coworkers to make nanostructured, porous polymer membrane where uniform alignment of the pores are parallel to the macroscopic transport direction.¹⁶⁴ Rather than using a traditional block copolymer approach, they designed a wedge shaped amphiphilic monomer as the building block to form thermotropic and lyotropic LC mesophases with densely packed monodisperse cylindrical pores with diameters as small as 1 nm. Strong π - π interactions between LC monomers helped to form a physical continuity and structural locking-in of the LC order during cross-linking is targeted by the use of multiple reactive groups per monomer. An external magnetic field is used to direct the self-assembly of the system, resulting in uniform alignment of nanopores over arbitrary length scales in arbitrary orientations as dictated by the geometry of the field relative to the sample. Finally, the retention of the mesophase was achieved with cross-linking. This study gives guidelines molecule design to form distinct pores and orienting π -planes perpendicular to the substrate and both properties are desired and can be used to self-assemble donors in a desired way and leave some space for acceptors such as PCBM. Direct mixing of PCBM with LCs has also been shown to provide functional devices. The dispersion of functionalized C60, such as pyridyl fullerene (PyC60) and PCBM, in a phthalocyanine-based DLCs does not alter the columnar structure of the parent DLC.¹⁶⁵ These blends have been successfully used to fabricate solar cells that have power conversion efficiencies up to 4.1%.¹⁶⁶

LCs do not need to be employed as the main component in OPVs. There are examples that show use of LCs in OPVs in different ways such as using them as molecular additives. Pai and coworkers used new trihydrazone-functionalized cyanopyridine (CPTH-D16) demonstrating an ambient temperature hexagonal columnar liquid crystalline phase as a processing additive for the well-known

P₃HT:PCBM system to construct efficient solar cell.¹⁶⁷ CPTH-D16 was used to form ternary blend of P₃HT:CPTH-D16:PCBM with the optimized amount of 1:0.5:0.5 w/w. It was shown that ternary film showed excellent interpenetrating network with desired channel thickness, which contributes significantly to an efficient exciton dissociation and migration in the photovoltaic devices. Additionally performed current measurements over the ternary film exhibit a profound increase in the mean current value that is almost twenty times more than the mean current value of binary P₃HT:PCBM film. Moreover, an improved photon absorption in the NIR region (700-900 nm) contribute to the achievement of wide absorption properties in the film.

In a recent study a promising nematic liquid crystalline material was used as an electron donor for high-performance OPVs.¹⁶⁸ The electron donor has benzodithiophene terthiophene rhodamine (BTR) group that exhibits good processability and nematic liquid crystalline behavior. The combination of the planar aromatic group and well-positioned solubilizing groups imparted LC behavior that was not observed in the previous reports of similar molecular donors. When BTR powder is sandwiched in between two glass slides, heated and examined under a polarized optical microscope LC transition can be observed. BTR was highly crystalline below 185°C and it had a liquid crystal nematic texture between 185 and 195°C. The nematic phase suggests that BTR molecules have a rigid rod-like shape, which can maintain a long range directional order with their long axes parallel aligned. The advantage of the long-range liquid crystalline order was being able to make solar cell films as thick as 400 nm. When mixed with PCBM, BTR molecule resulted in solar cells with PCE of 9.3% owing to high FF which is 74.1%. This study is a great example of how linear conjugated donor molecules with LC behavior can be obtained and used to create highly efficiency solar cells. With more optimized molecular designs and new processing techniques (using magnetic or electric field to macroscopically align the phases) it should be possible to achieve PCEs higher than even 10%. The ability to make thick films is new and unique to LC small molecule donor BTR until now (excluding reported polymers), and there is a great potential to utilize such a system to make high-efficiency solar cells in the near future.

2.6 MATERIALS AND METHODS

Synthesis and Purification

DPCC₁₂ and N(PhT₃SnBu₃)₃ were prepared according to published literature procedures.⁴⁴ All solvents and reagents were purchased from commercial suppliers (Aldrich, Matrix Scientific) and used without further purification, with the exceptions of N-Bromosuccinimide (NBS), which was recrystallized from water. All reactions were carried out under an inert atmosphere of N₂. Analytical thin-layer chromatography (TLC) was performed on aluminum sheets, precoated with silica gel 60-F254 (Merck 5554). Flash column chromatography was carried out using silica gel 60 (Silicycle) as the stationary phase.

TDPPC₁₂-Br: Protected from light, NBS (558 mg, 3.14 mmol) in CHCl₃ (50mL) was added to a solution of TDPPC₁₂ (2.5 g, 3.9 mmol) in CHCl₃ (100mL) at 0 °C. The reaction was stirred at ambient temperature overnight and the solvent was removed under reduced pressure using rotary evaporator. The residue was subjected to flash column chromatography on SiO₂ (hexanes – DCM, 2:1) to afford the title compound as a purple solid (625 mg, 22%). ¹H NMR (500 MHz, CDCl₃, 298 K): δ = 8.94 (d, J = 3.9 Hz, 1H), 8.68 (d, J = 4.1 Hz, 1H), 7.66 (d, J = 4.9 Hz, 1H), 7.29 (dd, J = 4.7, 4.2 Hz, 1H), 7.25 (d, J = 4.3 Hz, 2H), 4.07 (t, J = 7.9 Hz, 2H), 4.00 (t, J = 7.6 Hz, 2H), 1.79 – 1.68 (m, 6H), 1.47 – 1.37 (m, 6H), 1.37 – 1.21 (m, 36H), 0.89 (t, J = 6.8 Hz, 3H). ¹³C NMR (125 MHz, CDCl₃, 298K): δ = 161.3, 161.1, 140.5, 138.5, 135.5, 135.1, 131.5, 131.2, 131.0, 129.7, 128.7, 118.8, 107.9, 107.6, 42.3, 42.2, 31.9, 30.0, 30.0, 29.9, 29.6, 29.6, 29.5, 29.5, 29.3, 29.2, 29.2, 26.9, 26.8, 22.7, 14.1. MS (MALDI) m/z, with no matrix calculated for C₃₈H₅₅BrN₂O₂S₂ [M+H]⁺ 716.890, found 716.955. T_{C₁₂}: Dry toluene (10 mL) and dry DMF (5 mL) were added to N(PhT₃SnBu₃)₃ and TDPPC₁₂-Br (175 mg, 0.245 mmol) and degassed with N₂. Pd(PPh₃)₄ (10.0 mg, 8.66 mol) was added and the reaction was heated to 120 °C and stirred for 24 h. The reaction mixture was poured into MeOH (150 mL), and the resulting precipitate was collected by vacuum filtration and chromatography was carried on SiO₂ (PhMe – CHCl₃, gradient from 50:50 to 0:100). The blue solid

was recrystallized by slow vapor diffusion of EtOAc into CHCl_3 to afford the title compound as a shiny, blue solid (83 mg, 14%). ^1H NMR (500 MHz, CDCl_3 , 298 K): δ = 8.96 (d, J = 4.2 Hz, 3H), 8.93 (d, J = 3.9 Hz, 3H), 7.64 (d, J = 5.1 Hz, 3H), 7.56 (d, J = 8.6 Hz, 6H), 7.36 (d, J = 4.1 Hz, 3H), 7.33 (d, J = 3.7 Hz, 3H), 7.29 (dd, J = 4.48 Hz, 4.10 Hz, 3H), 7.25 (d, J = 3.9 Hz, 3H), 7.20 (d, J = 9.1 Hz, 6H), 4.10 (t, J = 7.5 Hz, 12H), 1.84 – 1.73 (m, 12H), 1.5 – 1.2, (m, 108H), 0.87 (t, J = 6.8 Hz, 9H), 0.85 (t, J = 6.8 Hz, 9H). ^{13}C NMR (125 MHz, CDCl_3 , 298 K): δ = 161.4, 161.2, 146.8, 143.1, 139.6, 139.4, 136.7, 135.1, 134.7, 130.6, 129.8, 128.7, 128.6, 127.8, 126.7, 126.3, 124.7, 124.5, 123.6, 116.4, 107.9, 107.9, 42.3, 42.2, 31.9, 29.9, 29.6, 29.6, 29.6, 29.5, 29.5, 29.3, 29.2, 29.2, 26.8, 22.7, 14.1. MS (MALDI) m/z , with Dithranol matrix calculated for $\text{C}_{144}\text{H}_{183}\text{N}_7\text{O}_6\text{S}_9\text{H}$ $[\text{M}+\text{H}]^+$ 2397.658, found 2397.636

Experimental Details

NMR spectra were recorded on a Bruker Avance III 500 spectrometer with working frequencies of 500 MHz for ^1H and 125 MHz for ^{13}C . Chemical shifts are reported in ppm and referenced to the residual non-deuterated solvent frequencies (CDCl_3 ; δ 7.27 ppm for ^1H , δ 77.0 ppm for ^{13}C). Mass spectra were obtained on a Bruker Autoflex III MALDI mass spectrometer. Ultraviolet–visible (UV-vis) spectra were recorded on a Perkin Elmer LAMBDA 1050 spectrophotometer. Photovoltaic measurements were recorded while the devices were illuminated by an Oriel Xe solar simulator equipped with and Oriel 130 monochromator and a Keithley 2400 source meter. Filters were used to cut off grating overtones. The solar spectrum was simulated using an AM 1.5 filter with 100 $\text{mW}\cdot\text{cm}^{-2}$ power density. A calibrated silicon reference solar cell with a KG5 filter certified by the National Renewable Energy Laboratory was used to confirm the measurement conditions. AFM characterization was performed using a Bruker Dimension ICON atomic force microscope (Bruker Co.) at ambient conditions. Tapping mode was utilized with single-beam silicon cantilevers with a nominal oscillation frequency of 300 kHz. GIXD measurements were performed at Beamline 8ID-E of the Advanced Photon Source at Argonne National Laboratory. An X-ray wavelength of λ =

1.6868 Å was used and data were collected using a 1-2 s exposure at a sample-detector distance of 204 mm with a Pilatus photodiode array. Impedance spectroscopy measurements were carried out on an AUTOLAB [PGSTAT128N with the FRA32 module for EIS] electrochemical system.

Device Fabrication

Experimental conditions for active layer deposition such as solvent, concentration and solvent composition were optimized. Pre-patterned indium-doped tin oxide (ITO) on glass was used as the transparent bottom electrode. The ITO was scrubbed with soapy water and cleaned by ultrasonically sequentially in hexanes, soapy water, water, and a 1:1:1 solution of acetone/methanol/2-propanol. The electrode was then blown dry in a N₂ stream and transferred into a N₂ glovebox (O₂ and H₂O < 0.1 ppm). Before active layer coating, MoOx (10 nm) was thermally evaporated on ITO surface as the interfacial layer. Bulk heterojunction photovoltaic devices were fabricated from blends of donor small molecule and acceptor phenyl-C₇₁-butyric acid methyl ester (PC₇₁BM). In the optimized conditions, donor/acceptor ratio is fixed at 1:2 for the T_{C₁₂} molecules and 1:3 for T_{EH}, with a total solution concentration of 13.5 mg/ml for T_{C₁₂} and 16 mg/ml for T_{EH} in chloroform. Films were cast by spin-coating at 1500 rpm for T_{C₁₂} and 4000 rpm for T_{EH} in the glovebox for 60 s with no thermal annealing for T_{C₁₂} and 5 minutes of annealing on a hot plate at 100 °C for T_{EH}. Total organic layer thickness ranged from 90-100 nm as determined by AFM. Devices were completed by thermally evaporating 1 nm of LiF then 100 nm of Al through a shadow mask at 1×10^{-6} mbar to yield devices of 4 mm² in area and sealed with a UV-curable epoxy if needed. The devices for space-charge-limited-current (SCLC) measurements were fabricated with a similar procedure. The top electrode was replaced with Au (50 nm) rather than LiF/Al in order to suppress electron injection.

Ultraviolet Photoelectron Spectroscopy

UPS measurements were conducted with a bias of -5 V applied to sample to remove spectrometer effects from secondary electron cut-off. HOMO level of molecules was determined by the following formula, $E_{\text{HOMO}} = h\nu - |E_{\text{SC}} - E_{\text{O}}|$, where $h\nu$ is the photon energy of HeI source (21.2 eV), E_{SC} is secondary electron cutoff and E_{O} is HOMO onset.

Impedance Spectroscopy

Devices were tested over a frequency range of 100 Hz to 1 MHz. The recombination lifetime is calculated from the model fit according to the equation: $\tau_{\text{rec}} = R_{\text{rec}} Q_n$.

Molecular Dynamics Simulation

The force fields, or the interaction potential for both tripod molecules are derived from standard OPLS-AA force field.^{169,170} The SPC/E model is used for water representation and the OPLS-AA based force field developed by Frenkel and Hong is used for chloroform.^{171,172} Four systems are simulated, with the following combination of tripod molecules and solution: $T_{\text{C}_{12}}$ in water, $T_{\text{C}_{12}}$ in chloroform, T_{EH} in water, and T_{EH} in chloroform. In each system, twenty tripod molecules are co-facially stacked in the z -dimension to form a periodic sequence as the initial structure, with a stacking separation of 0.5 nm. The separation is set larger than the normally observed π - π stacking distance (0.37 nm), to allow dynamic optimization. The stacked sequence is then solvated in water and chloroform, with experimental density and placed in a simulation box of $5 \times 5 \times 10$ nm³ and $5.5 \times 5.5 \times 10$ nm³, respectively.¹⁷³ After energy minimization, the solution molecules are further relaxed with 20 ps and 105 ps NVT (constant volume, constant temperature) simulation, for water and chloroform respectively. The triphenylamine core (TPA) of each tripod molecule is position restrained during simulation, with a force constant of 1000 kJ/nm². Potential vs. time and pressure vs. time calculation supports that the respective relaxation time is adequate for each solution.

Subsequent to solution relaxation, the π - π stacking separation is optimized before the production run. The stacking separation is optimized by changing the z-dimension of the simulation box through NPT simulation (constant pressure, constant temperature) where all dimensions of the system are coupled with a constant pressure, since the periodicity of initial structure gives stacking separation proportional to the z-dimension. For water systems, 6 ns of NPT simulation is performed with the same position restraint of solution relaxation. Potential vs. time and z-dimension vs. time are calculated to confirm the stability of the optimization. For chloroform systems, a two-step optimization is carried out, due to the over-estimated density in the initial structures. The first 3 ns NPT simulation is the optimization of chloroform density, which reaches experimental value by expanding the simulation box only in xy dimension. The success of this optimization is confirmed by the stabilization of xy dimension vs. time and potential vs. time calculation. The second 15 ns NPT simulation is the optimization of z-dimension, where all three dimensions are coupled with pressure. This optimization is validated by potential vs. time and z dimension vs. time calculation.

Following the stacking separation optimization, a 3 ns NPT simulation is performed for each system as the production run. The temperature is scaled with Nose-Hoover thermostat, with a characteristic time 0.5 ps; the pressure is scaled with Berendsen barostat, with a characteristic time 1 ps, reference pressure 1 bar, and compressibility $4.5 \times 10^{-5} \text{ bar}^{-1}$ at semi-isotropic coupling. The neighbor searching for nonbonding interactions is calculated up to 1.2 nm and updated every 10 time steps. The long range interaction is handled through the Particle Mesh Ewald (PME) method with a space cutoff of 1.2 nm and Fourier grid spacing of 0.12 nm. There is no position restraint in the production run. The stability of production simulation is verified by potential vs. time calculation and pressure/temperature vs. time calculation. An additional 50 ns simulation for the $T_{C_{12}}$ in water system is performed after the production run, as a reaffirmation for system stability, as no future structural evolution is observed.

3 STEPWISE SELF-ASSEMBLY TO IMPROVE SOLAR CELL MORPHOLOGY

3.1 OBJECTIVES AND SIGNIFICANCE

Organic photovoltaic device efficiencies can be greatly improved by controlling the morphology of donor and acceptor domains in the active layer. Connectivity within donor and acceptor domains is of key importance in order to direct charge carriers efficiently to the electrodes. We report here on self-assembly pathways leading towards optimal morphology of solar cell active layers, using as the donor a hairpin-shaped molecule containing a trans-1,2-diamidocyclohexane core and two arms of diketopyrrolopyrrole conjugated segments, and a C₇₁ fullerene derivative as the electron acceptor. Self-assembly of the donor molecule is driven by the synergistic action of hydrogen bonds and $\pi - \pi$ stacking, and under proper conditions this results in the formation of long supramolecular nanowires that enhance charge transport and device efficiencies. We found that a stepwise cooling process with minimal stirring of solutions is necessary to create by self-assembly robust wires that are not disrupted when acceptor molecules are added. The efficiencies of devices created by this process can be 400-fold greater than those of devices formed by simple mixing of donor and acceptor molecules. The synergistic action of hydrogen bonds and π stacking in donor molecules that create long nanowires by self-assembly results in devices that are 54% more efficient than those built with analogous donor molecules containing only the conjugated structure.

3.2 BACKGROUND

Bulk heterojunction (BHJ) organic photovoltaic (OPV) devices^{174,175} are mostly based on p conjugated polymeric^{23,39,176-178} or small molecule^{42,43,113,134,179,180} donors, intimately mixed with acceptor molecules (most commonly fullerene derivatives) that have appropriately tuned energy levels for separating photo-generated excitons into free charge carriers at their interface. Although organic synthesis is a reliable tool for tuning the optoelectronic properties of these molecules, the

supramolecular aspects necessary to optimize OPV device performance remain a great challenge. The morphology of donor and acceptor domains in the active layer is crucial to device performance because transport of the photo-generated charge carriers occurs through these domains to the electrodes.³⁶ For instance, the size of the donor and acceptor domains should match the exciton diffusion length, which ranges from 5 to 20 nm approximately, to allow exciton splitting and charge carrier transport without recombination.¹⁸¹ Self-assembly is a promising strategy to control the hierarchical organization of organic solar cell components over multiple length scales with high order parameters and reproducibility, and thus offers the opportunity to dramatically boost device efficiencies.^{129,182,183}

BHJ solar cells that use small molecule^{42,43,113,134,179,180} donors (instead of polymers) are gaining attention due to their ease in preparation, the good solubility and precise molar mass of their components. This makes them more scalable, recyclable, and reproducible in terms of properties. Furthermore, recent research has shown that small molecule BHJs can reach power conversion efficiencies (up to 6.7 – 7%)^{43,184} that compete with the most efficient polymer BHJs.³⁹ Molecular design for self-assembly is a great tool to address the issue since a diverse array of motifs can be incorporated into small molecules to instruct precise control over the active layer morphology. Examples of self-assembling small molecule donors in BHJ OPVs are still rare.^{129,135,185}

We reported that the introduction of a hairpin shaped molecule based on trans-diamido cyclohexane (DACH) as a self-assembly motif through hydrogen bonds and sexithiophene as a donor moiety resulted in a 23% increase in device efficiency compared to the sexithiophene alone. The concept explored in this previous work was to test the ability of non-linearly shaped nanowires of donor molecules with cavities as a strategy to create better interfaces between donors and acceptors in OPV devices. We proposed that the grooved architecture of the nanowires would facilitate receptor-ligand type cofacial interactions between the donor assemblies and the spherical fullerene acceptor molecules.¹²⁹

In this work we report the use of a different hairpin-shaped molecule based on thiophene capped DPP units and the self-assembly motif DACH. We selected thiophene capped diketopyrrolopyrrole as the light harvesting motif because this chromophore possesses a high extinction coefficient, absorption in a broad region of the solar spectrum, and high hole mobility according to previously reported diketopyrrolopyrrole-containing derivatives,¹⁸⁶⁻¹⁹⁰ rendering it a more powerful chromophore than sexithiophene. We describe here the optoelectronic and self-assembly properties of this novel molecule and the influence of its self-assembly properties on the performance of BHJ solar cells with the fullerene derivative phenyl-C₇₁-butyric acid methyl ester (PC₇₁BM).

3.3 RESULTS AND DISCUSSION

3.3.1 *Synthesis of hairpin-shaped diketopyrrolopyrrole molecule*

Fig. 3.1b shows the synthetic route to DPPHP. First 5-bromo-2-thiophenecarboxaldehyde **1** was reduced to the corresponding alcohol **2** in the presence of lithium aluminum hydride. Compound **2** was stannylated by reaction with n-butyllithium followed by addition of tributyltin chloride to afford stannane derivative **3**. Compound **4**, which has been previously reported,¹⁹¹ was attached to alcohol **3** via ester formation to yield the double stannane **5**. Finally, a Stille coupling between **5** and monobrominated diketopyrrolopyrrole **6** reported previously by our laboratory, led to the final product DPPHP in 25% yield.

3.3.2 *DPPHP performance in organic photovoltaics. Influence of self-assembly on device efficiency*

DPPHP possesses the required optoelectronic properties for its use in device fabrication. It has broad absorption with $\lambda_{\text{max}}=573$ nm (Fig. 3.2), good coverage of the solar spectrum, and a high extinction coefficient (6.21×10^4). The energy band gap calculated from the absorption onset is 1.91 eV, and the HOMO and LUMO levels at -5.53 eV and -3.62 eV (determined with CV), respectively are well positioned relative to PC₇₁BM which has its HOMO at -4.2 eV and LUMO at -6.1 eV

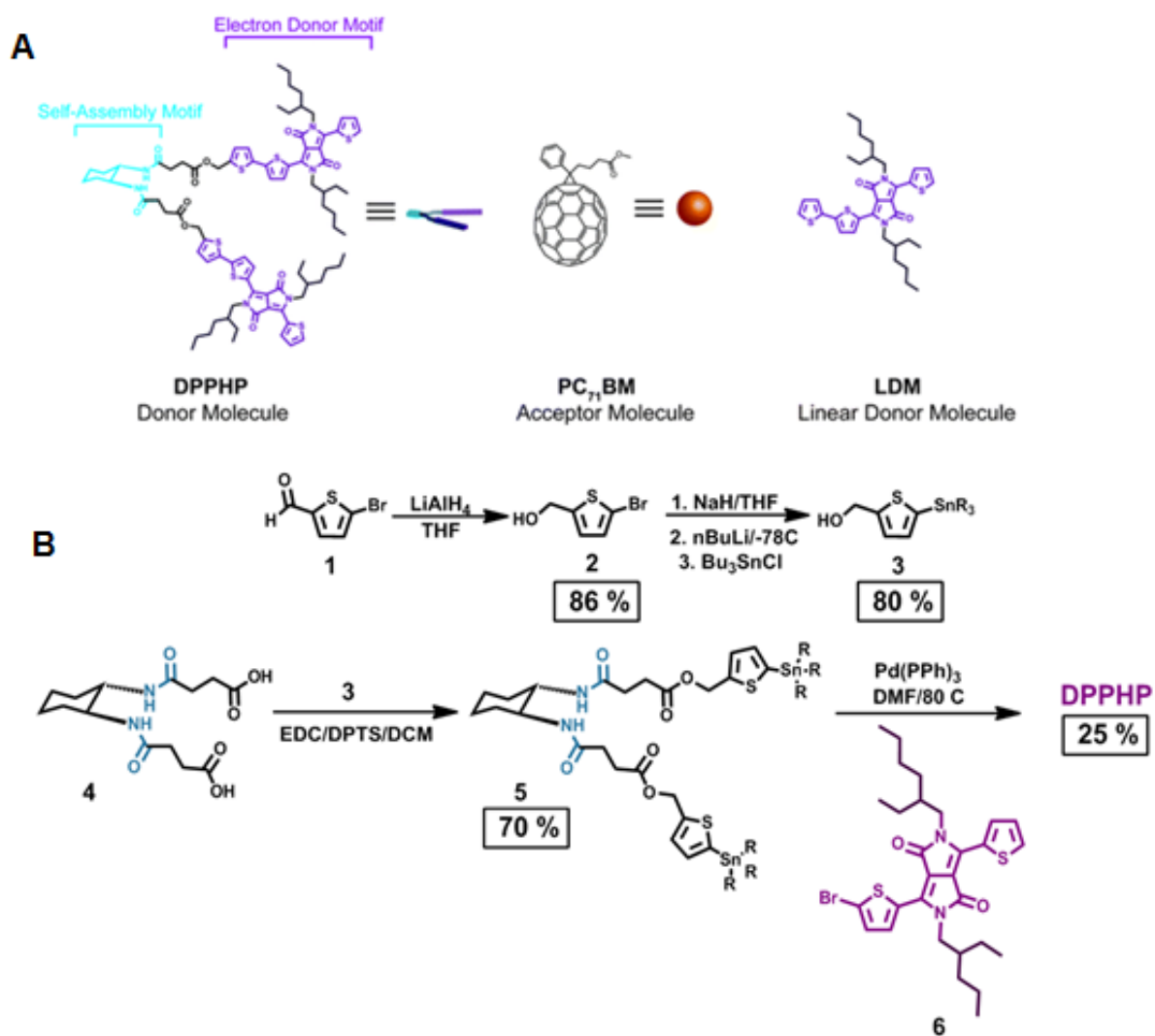


Figure 3.1: Chemical structure of DPPHP, PC₇₁BM and LDM (a), DPPHP synthetic route (b).

(Fig. 3.3b). All of these values are in agreement with previously reported DPP derivatives containing the sequence thiophene – thiophene – DPP – thiophene.^{192,193}

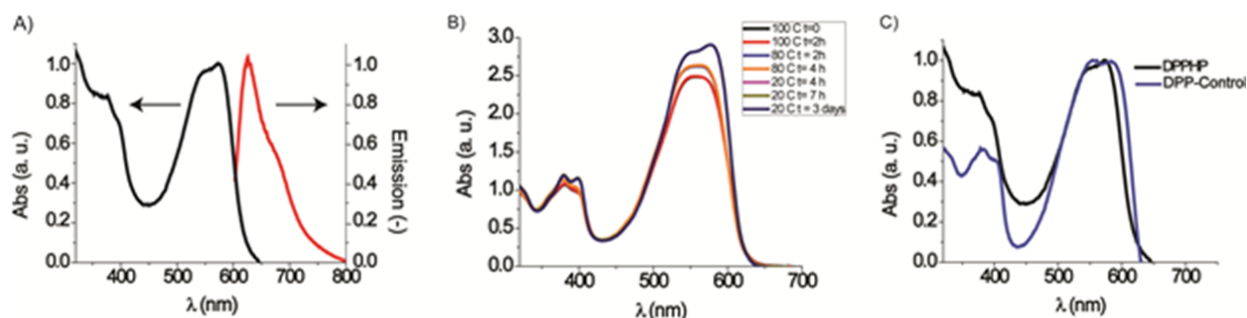


Figure 3.2: Normalized absorption and emission spectra ($\lambda_{\text{exc}} = 573 \text{ nm}$) of DPPHP in chlorobenzene. $[\text{DPPHP}] = 4.5 \times 10^{-3} \text{ M}$. $[\text{DPPHP}] = 0.27 \times 10^{-3} \text{ M}$ for emission measurements (a). Absorption spectra of DPPHP in toluene at different temperatures. $[\text{DPPHP}] = 4.5 \times 10^{-3} \text{ M}$ (b). Normalized absorption spectra of DPPHP and LDM in toluene. $[\text{DPPHP}] = 4.5 \times 10^{-3} \text{ M}$, $[\text{LDM}] = 1.2 \times 10^{-3} \text{ M}$ (c).

The first set of experiments for BHJ solar cell fabrication was based on the assembly of DPPHP and PC_{71}BM in a single step. Solutions of DPPHP (7 mg ml^{-1}) in self-assembly promoting solvents (toluene and chlorobenzene) were prepared and stirred at high temperature for 24 hours before being mixed with a PC_{71}BM (27 mg ml^{-1}) solution in chlorobenzene. The blend was stirred at $80 \text{ }^\circ\text{C}$ for 12 hours to avoid possible clustering of DPPHP and allow mixing of both components. BHJ OPVs fabricated from these solutions (see Fig. 3.3a) resulted in very poor working devices with efficiencies smaller than 0.0014%. In the best device, the short circuit current (J_{SC}) was 0.020 mA cm^{-2} , the fill factor (FF) was 19% and the open circuit voltage (V_{OC}) was 0.35 V. Similar results were found when powders of donor and acceptor components were mixed in the neat state and dissolved together in toluene or chlorobenzene. Different spin-coating rates, annealing temperatures, annealing times, and donor – acceptor ratios were also tested, but failed to show any improvement. Atomic force microscopy (AFM) verified that the films had very smooth surfaces and homogeneous morphologies while obvious aggregates, nanostructures, and fibrous regions were absent (Fig. 3.4).

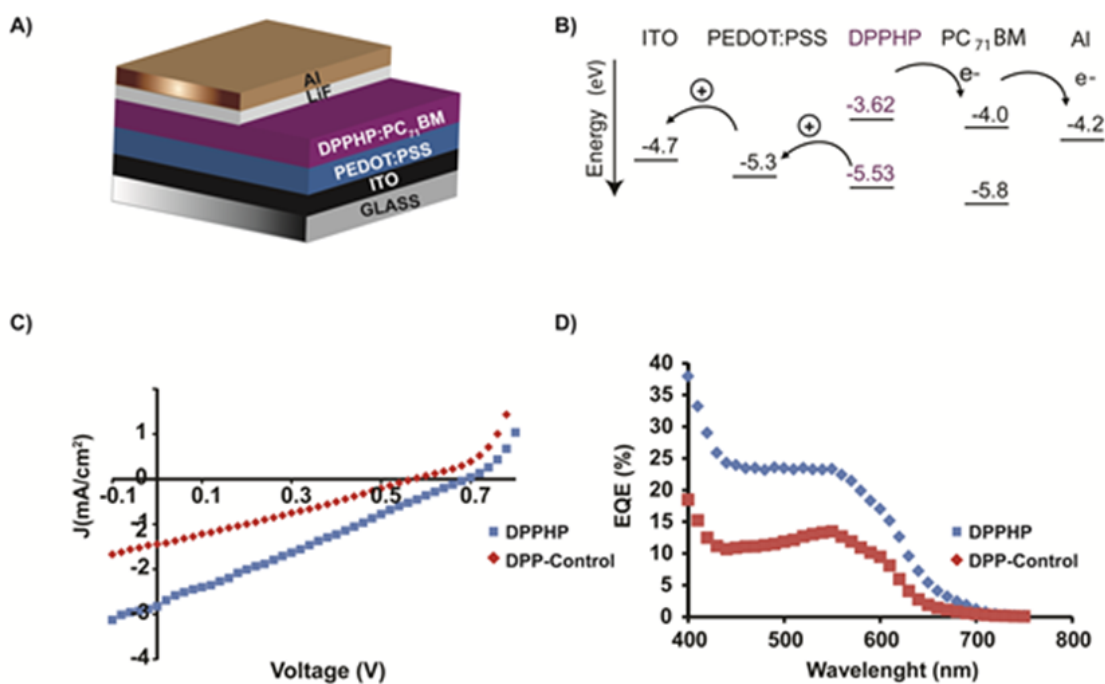


Figure 3.3: Schematic representation of the configuration of the solar cells fabricated (a). Energy diagram of all the components used in the devices described (b). Illuminated J - V curves of DPPHP and LDM (c). External quantum efficiency (EQE) spectra of DPPHP and LDM (d).

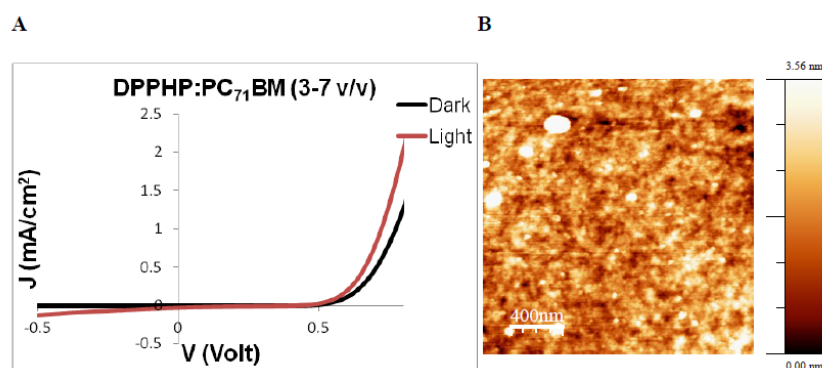


Figure 3.4: JV curve of devices fabricated by in situ self-assembly (a). Morphology of the active layer of devices fabricated by in single step self-assembly (b).

Taken together, the absence of distinct assemblies and low J_{SC} values suggest that the domains required for efficient charge transport were not forming properly. We concluded that the fullerene acceptors interfere with DPPHP self-assembly when the two components are thoroughly mixed (Fig. 3.5, Pathway 1), which in turn inhibits high photocurrents and results in non-functional devices.

In order to promote DPPHP self-assembly, a stepwise strategy was used to create the active layer of the solar cell. The self-assembly process was designed starting from conditions where DPPHP molecules were unassembled and could be gradually incorporated into nanostructures. First, DPPHP (7 mg ml^{-1}) was dissolved in self-assembly promoting solvents and stirred at temperatures close to the boiling point of the solvents for 3 hours. The solutions were gradually cooled down to $80 \text{ }^\circ\text{C}$ (at an approximate rate of $2 \text{ }^\circ\text{C min}^{-1}$) to avoid clustering observed by fast cooling and then cooled down to room temperature without stirring (same cooling rate) (Steps 1, 2 and 3 Fig. 3.5, Pathway 2). Films were prepared immediately after cooling by spin-casting these solutions and AFM (Fig. 3.6a – d) revealed that this approach clearly led to strong nanowire formation. Nanowires from 100 to 400 nm in length and 2.5 nm in height were found in chlorobenzene while toluene promoted assembly of longer nanowires from 100 to 700 nm in length with a height of 8.5 nm. Single nanowires of around 2.5 nm in height are in close agreement with the length of DPPHP molecules modeled in its extended conformation.

The solution that was used for spin-coating the active layer was also studied by cryogenic transmission electron microscopy (cryoTEM) (see Fig. 3.7) indicating that nanowires are already formed in solution. DPPHP bundles appear dark compared to the solvent, as observed in previously reported cryo-TEM studies of block copolymers using toluene as the solvent,¹⁹⁴ where the aggregates formed by these molecules appeared dark compared to the solvent due to the higher density of the aggregates formed relative to toluene. This result was also confirmed by the UV-Vis data (see Fig. 3.2b); the main band observed at $100 \text{ }^\circ\text{C}$ and $80 \text{ }^\circ\text{C}$ has $\lambda_{max} = 560 \text{ nm}$, while a shoulder near 498 nm indicates the formation of H-aggregates induced by face-to-face interactions of the

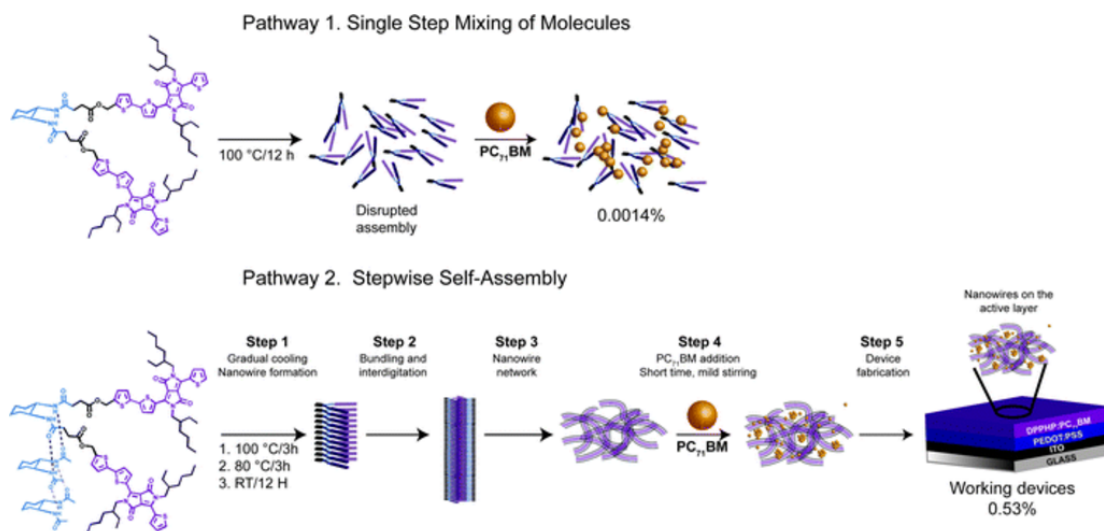


Figure 3.5: Schematic representation of the different preparation pathways used for device fabrication. Pathway 1 (top) shows the single step self-assembly of DPPPHP and PC₇₁BM. Route 2 (bottom) shows the stepwise self-assembly of DPPPHP prior to the addition of PC₇₁BM.

π -conjugated arms of the DPPHP hairpin. After cooling down to room temperature, however, different spectral features were observed; the H-aggregate shoulder remained at the same position, but a red-shifted J-aggregate band at 578 nm appeared as a sign of interdigitation between hairpin stacks. This same observation was also found in the optical properties of the previously reported hairpin-shaped molecule containing sexithiophene electroactive branches.¹⁹¹ The UV-Vis spectra did not change after aging for several days. The absorption spectra of the neat films exhibited a major band from 470 nm to 560 nm and an additional red-shifted J-aggregate peak at 595 nm and a blue-shifted H-aggregate peak at 448 nm (Fig. 3.8). These solutions containing DPPHP nanowire bundles were mixed with a PC₇₁BM solution (27 mg ml⁻¹) for brief periods of time (30 seconds) with mild stirring to allow interaction of DPPHP with acceptor molecules without disrupting the DPPHP assemblies (Step 4, Fig. 3.5, Pathway 2). CryoTEM showed that a combination of DPPHP nanowires and PC₇₁BM aggregates were present in solution (see Fig. 3.7b) and that upon addition of PC₇₁BM the nanostructures formed by DPPHP were still present but their length decreased. BHJ

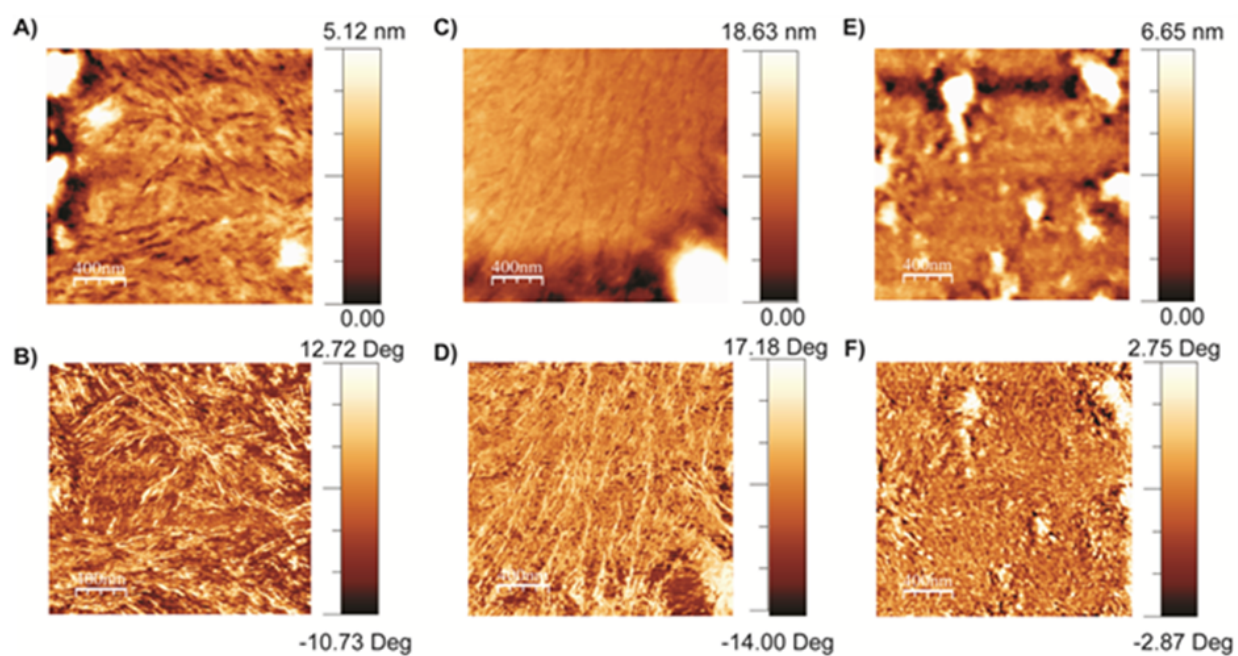


Figure 3.6: AFM height (top row) and phase images (bottom row) of thin films made by spin casting a solution of [DPPHP] = 4.5×10^{-3} M on mica. The scale bar is of 400 nm in all the images. Solution prepared by gradual cooling in chlorobenzene (a and b). Solution prepared by gradual cooling in toluene (c and d). Solution prepared by fast cooling in toluene (e and f).

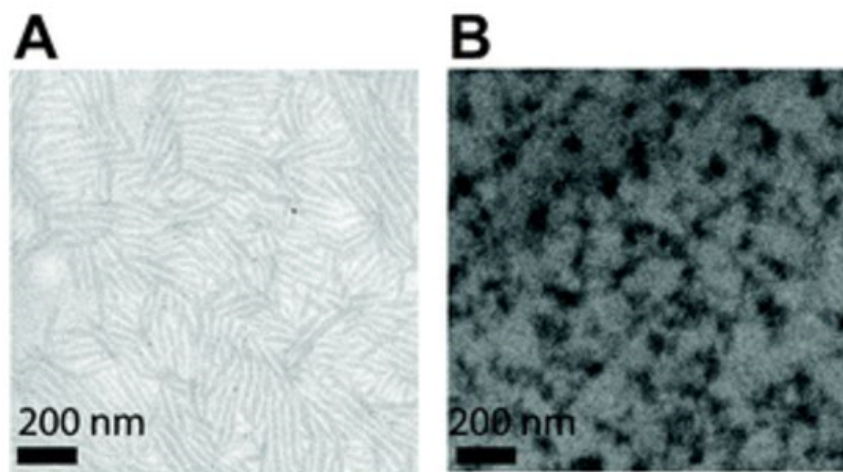


Figure 3.7: Cryo-TEM image of a DPPHP solution in toluene prepared following the stepwise self-assembly pathway. $[\text{DPPHP}] = 7 \text{ mg ml}^{-1}$ (a). Cryo-TEM image of a DPPHP:PC₇₁BM blend in a 1:1 ratio mixed for 30 seconds. $[\text{DPPHP}] = 7 \text{ mg ml}^{-1}$ and $[\text{PC}_{71}\text{BM}] = 27 \text{ mg ml}^{-1}$ (b).

solar cells were fabricated with these solutions and working devices were obtained in all cases (Step 5, Fig. 3.5, Pathway 2). The presence of nanostructures in the active layers was confirmed by AFM (Fig. 3.9 and Fig. 3.10). These results reveal that it is crucial to promote self-assembly of DPPHP in solution prior to the addition of PC₇₁BM in order to have nanowires of the donor molecules in the active layer and obtain functional devices. When DPPHP and PC₇₁BM were dissolved together in chlorobenzene or toluene prior to the slow cooling process, non-functional devices were also obtained. This observation suggests again that the addition of PC₇₁BM at an early stage in the preparation protocol disrupts the formation of DPPHP nanowires.

Table 3.1 shows the photovoltaic characteristics of the DPPHP:PC₇₁BM BHJ solar cells optimized at a spin rate of 1500 rpm, resulting in active layers with 70 nm thickness. A donor – acceptor ratio of 4:1 resulted in 0.21% efficient devices in chlorobenzene and 0.27% in toluene. Systematically increasing the acceptor volume resulted in more efficient devices. Raising the DPPHP:PC₇₁BM ratio from 4:1 to 1:1, the J_{SC} values increased to 2.67 mA cm^{-2} in toluene and to 2.98 mA cm^{-2} in chlorobenzene, but a larger increase in acceptor content led to less efficient devices with lower

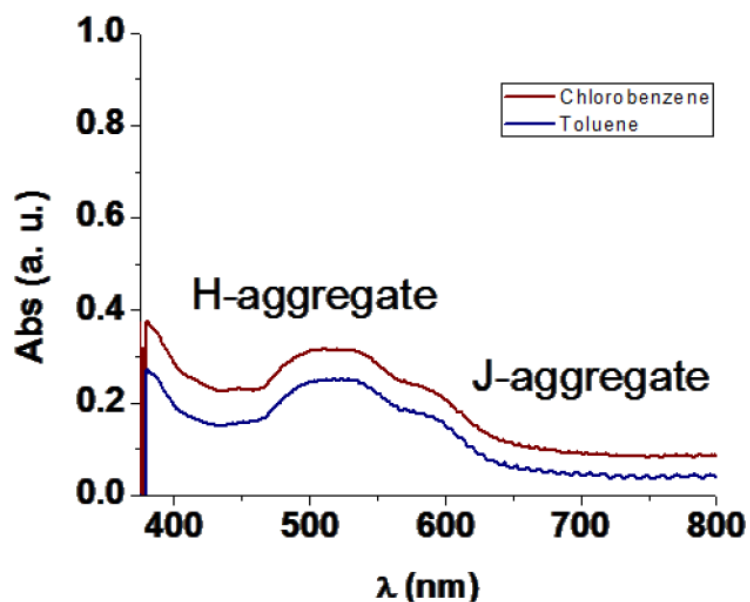


Figure 3.8: Absorption spectra of DPPHP thin films spin cast on mica at 1500 rpm in toluene and chlorobenzene. $[DPPHP] = 4.5 \times 10^{-3} \text{ M}$

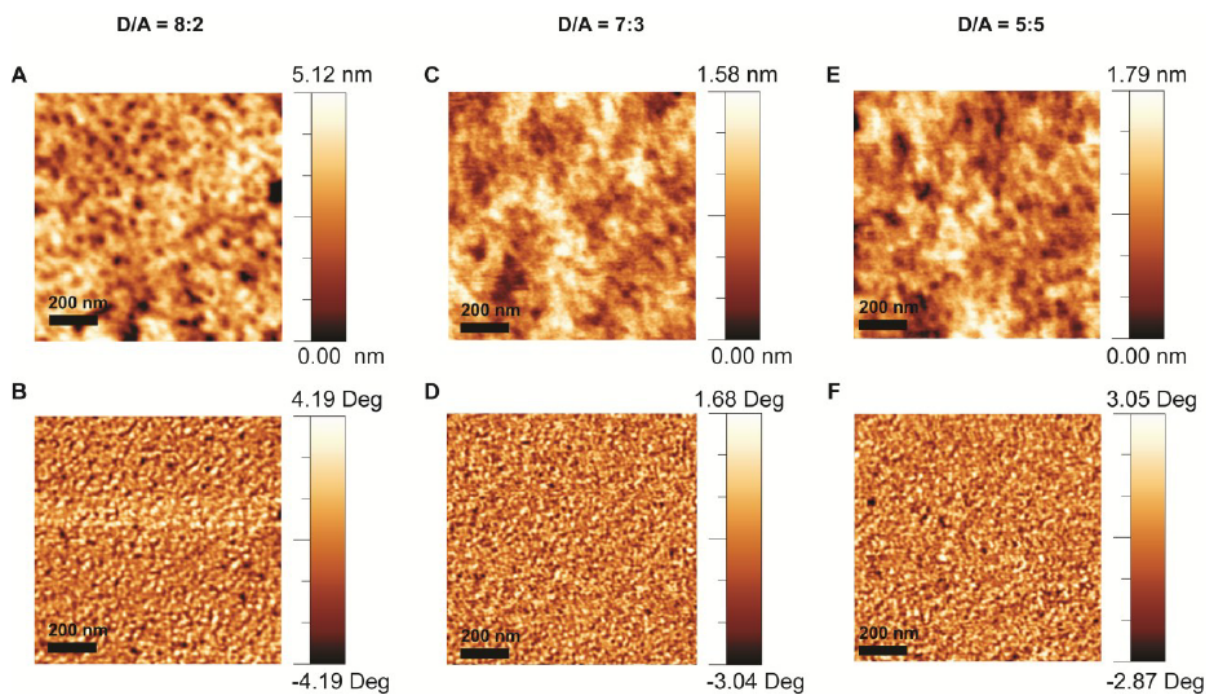


Figure 3.9: AFM of the active layers of DPPHP devices processed from chlorobenzene solutions at different donor/acceptor ratios (Height images in the top row, phase images in the bottom row).

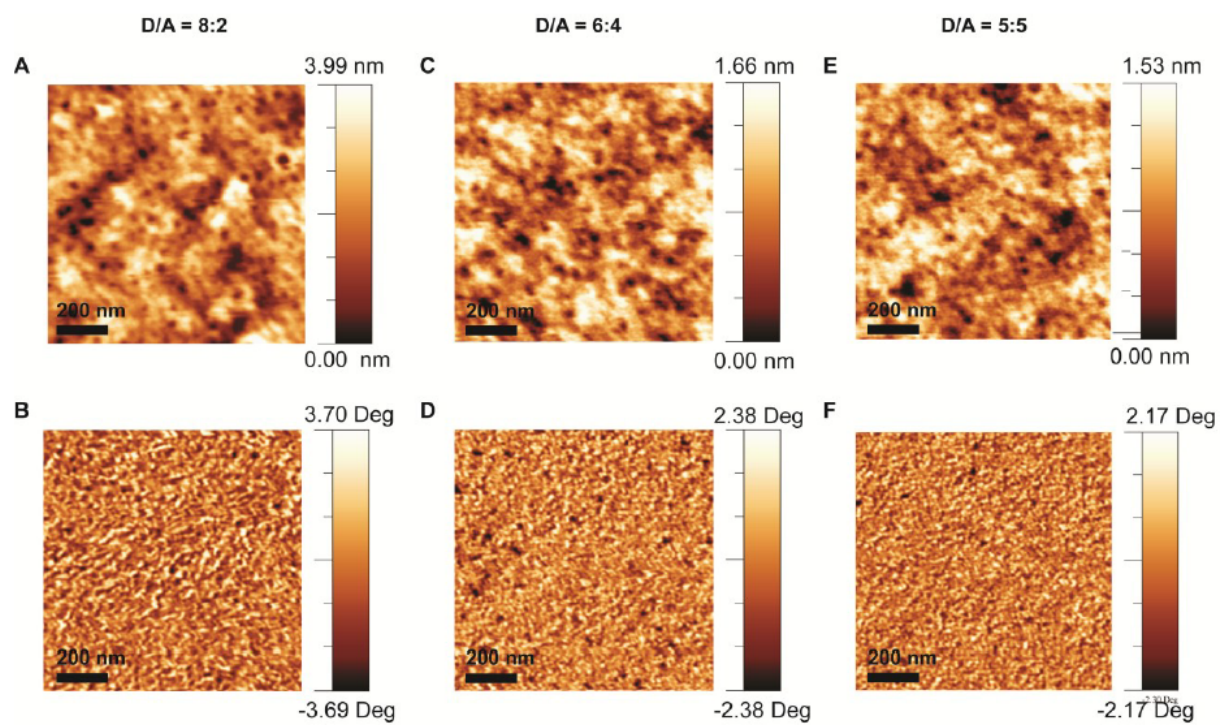


Figure 3.10: AFM of the active layers of DPPHP devices processed from toluene solutions at different donor/acceptor ratios (Height images in the top row, phase images in the bottom row).

J_{SC} and V_{OC} values. Optimized efficiencies of 0.53% in chlorobenzene and 0.43% in toluene were obtained, revealing a 400-fold improvement in efficiency compared to the devices fabricated with non-assembled solutions of DPPHP. These are the highest device efficiencies reported so far to the best of our knowledge, based on systems that utilize hydrogen bonding among donor or acceptor components.^{195–201}

In blends with a large excess of DPPHP, devices cast from toluene are more efficient (Table 3.1, entries 2 and 4) than those cast from chlorobenzene (Table 3.1, entries 1 and 3) due to the presence of larger bundles that are more stable to disruption by PC₇₁BM. As the PC₇₁BM content increases, however, the chlorobenzene devices become more efficient, which is likely due to the better solubility of PC₇₁BM in chlorobenzene than in toluene,²⁰² which helps avoid large, undesired aggregates of PC₇₁BM.

Entry	D : A v/v	Solvent ^a	J_{sc} (mA cm ⁻²)	V_{oc} (V)	FF (%)	PCE (%)
1	4 : 1	Chlorobenzene	1.1	0.74	0.26	0.21
2	4 : 1	Toluene	1.4	0.73	0.27	0.27
3	7 : 3	Chlorobenzene	1.89	0.67	0.28	0.36
4	7 : 3	Toluene	2.17	0.69	0.26	0.39
5	3 : 2	Chlorobenzene	2.51	0.66	0.28	0.47
6	3 : 2	Toluene	2.63	0.66	0.27	0.38
7	1 : 1	Chlorobenzene	2.98	0.66	0.27	0.53
8	1 : 1	Toluene	2.67	0.63	0.26	0.43
9	2 : 3	Chlorobenzene	1.66	0.59	0.25	0.24
10	3 : 7	Chlorobenzene	1.26	0.57	0.25	0.18

Table 3.1: Photovoltaic characteristics of DPPHP:PC₇₁BM blends at 1500 rpm

The nature of self-assembled structures obtained by fast cooling of DPPHP solutions was investigated by AFM. The solutions were directly cooled down to room temperature after stirring them at the boiling point of toluene and chlorobenzene for 3 hours (Fig. 3.7e and f) instead of using the stepwise cooling method (Steps 1, 2 and 3), which led to the optimized devices. In this case, DPPHP was found to form nanowires that are much shorter and less bundled, while large clusters of

aggregated DPPHP could also be found, meaning that a large portion of DPPHP did not assemble into defined nanowires. The devices fabricated using these solutions showed an efficiency of 0.34% after optimization, representing a 36% decrease in power conversion efficiency. These results demonstrate the importance of precisely controlling the self-assembly process to obtain the most appropriate morphology for device optimization.

Even though the efficiency drastically increased using the stepwise self-assembly preparation method due to a great increase in J_{SC} , some parameters such as fill factor might be improved. The shape of the J – V curves clearly indicates a high degree of charge recombination, which translates into low FF values.²⁰³ A common method to address this problem is the fabrication of thinner films. Table 3.2 shows the photovoltaic characteristics of devices fabricated with blends using the optimized 1:1 donor – acceptor ratio at faster spin rates that produce thinner films. In the chlorobenzene blends (Table 3.2, entries 1 and 2), increasing the spin rates to 2000 and 2500 rpm reduced the corresponding device efficiencies from 0.43 to 0.38%, probably due to a decrease in light absorption. However, thinner films cast from toluene yielded devices (Table 3.2, entries 3 and 4) with improved efficiencies of 0.52 and 0.44% at 2000 and 2500 rpm, respectively. Both the FF and the J_{SC} were improved by spin-casting thinner films at 2000 rpm in this case. This result can be rationalized because the nanowires formed in toluene are longer and less disrupted by PC₇₁BM than the nanowires formed in chlorobenzene. Thus, the nanowires are better preserved in thinner layers cast from toluene, resulting in less recombination, whereas the shorter nanowires in chlorobenzene require thicker layers to absorb more light.

Different results were obtained when comparing devices prepared with chlorobenzene or toluene solutions. DPPHP nanowires formed in toluene were larger than those assembled in chlorobenzene at the same concentration. Thus, devices with higher content of DPPHP showed less tendency toward disruption of nanowires by addition of PC₇₁BM in toluene than in chlorobenzene, yielding more highly efficient devices. This can be correlated with the appearance of nanowires on the solar cell active layer. While in toluene nanowires can still be identified, in chlorobenzene they are much

Entry	Solvent	Spin rate (rpm)	J_{sc} (mA cm ⁻²)	V_{oc} (V)	FF (%)	PCE (%)
1	Chlorobenzene	2000	2.29	0.64	0.29	0.43
2		2500	2.05	0.6	0.31	0.38
3	Toluene	2000	2.76	0.69	0.27	0.52
4		2500	2.36	0.65	0.28	0.44

Table 3.2: Photovoltaic characteristics of DPPHP:PC₇₁BM blends at different spin rates

smaller and sometimes not observed in the devices. However, when the amount of PC₇₁BM increases, solubility also plays an important role due to better solubility of PC₇₁BM in chlorobenzene relative to toluene. In this sense, devices made from chlorobenzene solutions performed better as a consequence of better integration of PC₇₁BM in the DPPHP nanowire network, resulting in an improved overall morphology of the active layer.

Different control experiments were performed to demonstrate the importance of a controlled assembly process in which donor molecules are interconnected. A blend of assembled DPPHP and PC₇₁BM was stirred overnight to mechanically disrupt the assemblies and devices were fabricated under the same conditions. The efficiency obtained after optimization dropped to 0.36%, representing a 34% decrease in efficiency. A solution of assembled DPPHP was stirred likewise for 24 hours to mechanically disrupt the nanowires and a reduced amount of fibrous material was found in films spin cast on mica (Fig. 3.11). The efficiency of devices prepared from this solution mixed with PC₇₁BM dropped to 0.34%. In other words, mechanical disruption of DPPHP assemblies leads to decreased device performance.

Additional control experiments were also performed to verify the importance of the DACH self-assembly motif directing the π stacking of aromatic donor segments. In these experiments we used a linear molecule that contains the electronically active arm of the hairpin molecule (see Fig. 3.1a, LDM). Solutions were prepared following the same stepwise procedure as for DPPHP, and devices were fabricated under the same conditions. The most efficient device showed an efficiency of 0.24%

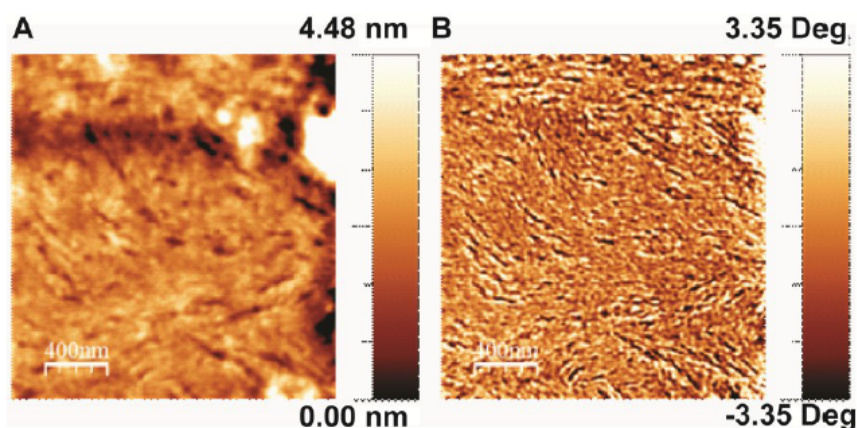


Figure 3.11: AFM height (a) and phase (b) images of a thin film spin cast from an assembled solution of DPPHP which was stirred for 12 hours. The fibers are shorter and less bundled. The scale bar is of 400 nm in both images.

(Fig. 3.3c), with $J_{SC} = 1.43 \text{ mA cm}^{-2}$, $V_{OC} = 0.57$ and $FF = 29\%$. These devices were 54% less efficient than those prepared using the self-assembling hairpin molecule DPPHP (Fig. 3.3c). Moreover, the concentration of electronically active component (thiophene – thiophene – diketopyrrolopyrrole – thiophene) present in the 7 mg ml^{-1} of DPPHP used for device fabrication is 25% smaller than in the same amount of LDM. These results provide clear evidence that self-assembly of the donor molecules plays a crucial role in device performance, since the electronic properties of DPPHP and LDM should be essentially the same (see Fig. 3.2c) and there is a lower concentration of donor segments in DPPHP relative to the control system. Furthermore, the EQE spectra of DPPHP and LDM (Fig. 3.3d) for the optimized devices have a peak of 39% and 19% respectively, which corresponds to the absorption of $PC_{71}BM$, due to the excess of fullerene in the blend. The spectra also show a broad peak between 430 and 650 nm with local maxima of 15% and 25% at around 550 nm, which is consistent with the absorption profiles of DPPHP and LDM.

LDM thin films were studied by AFM (Fig. 3.12) and crystalline domains were observed when the solutions were prepared by the stepwise self-assembly pathway. However, no nanowire formation or bundles were found by AFM or by UV-Vis after aging (Fig. 3.13). The domains of LDM are

disrupted upon acceptor addition, breaking the connections among donor molecules and resulting in inefficient charge transport (Fig. 3.14).

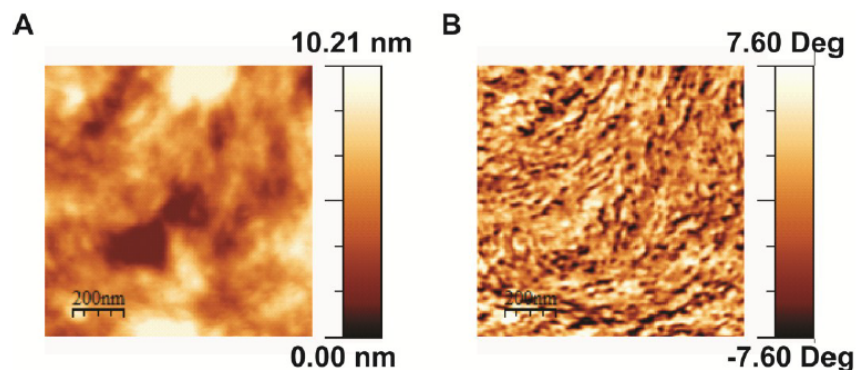


Figure 3.12: AFM height (a) and phase (b) images of a thin film spin cast from LDM in toluene. The solution was prepared by the gradual cooling method. The scale bar is 200 nm in both images.

Space-charge-limited current (SCLC) measurements⁶⁹ were performed to determine the role of self-assembly in the hole transporting properties of DPPHP and LDM. Experimental dark curves of the films can be seen in Fig. 3.15). The mobility values obtained for DPPHP and LDM were 5.5×10^{-5} and $2.5 \times 10^{-5} \text{ cm}^2 \text{ V}^{-1} \text{ s}^{-1}$, respectively, indicating a 45% increase in hole mobility when the self-assembly motifs are present in the molecular structure. This difference in mobility can be attributed to the better interconnection among donor molecules as a result of the self-assembly motif DACH in DPPHP, resulting in a more efficient charge transport and higher efficiency. Future improvements in efficiency are expected by replacing the insulating self-assembly motif with other hairpin structures that are fully conjugated.

3.4 CONCLUSION

We have shown that a self-assembly strategy based on hydrogen bonding and $\pi - \pi$ stacking to create photovoltaic solar cells using small molecules leads to long supramolecular electron donor nanowires that enhance charge transport and device efficiencies. The strategy requires using step-

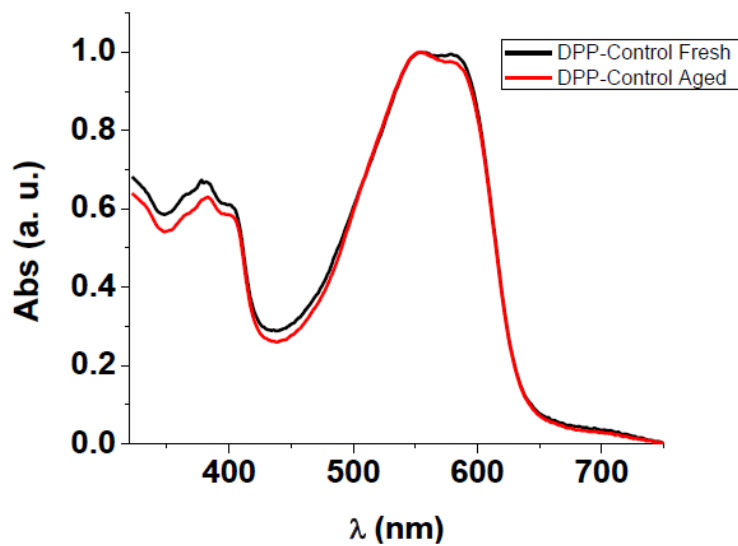


Figure 3.13: UV-vis spectra of fresh and aged LDM solutions in toluene. There are no signs of aggregation after aging.

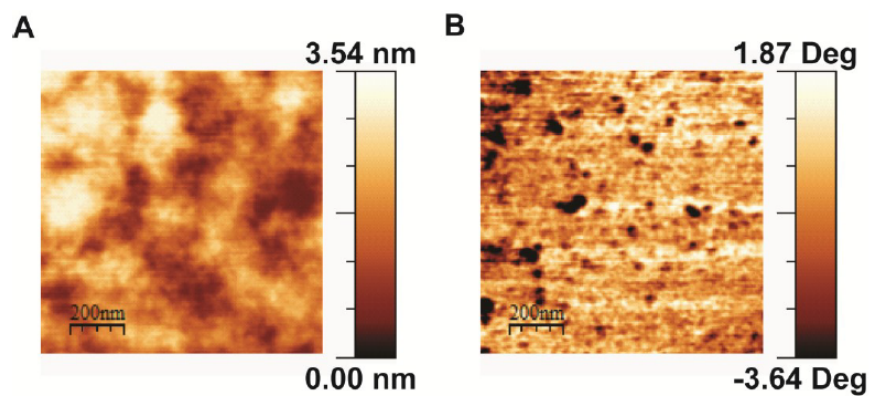


Figure 3.14: AFM height (a) and phase (b) images of the active layer of a LDM device. The LDM solution was prepared in toluene by the gradual cooling method and mildly mixed with PC₇₁BM. The scale bar is 200 nm in both images.

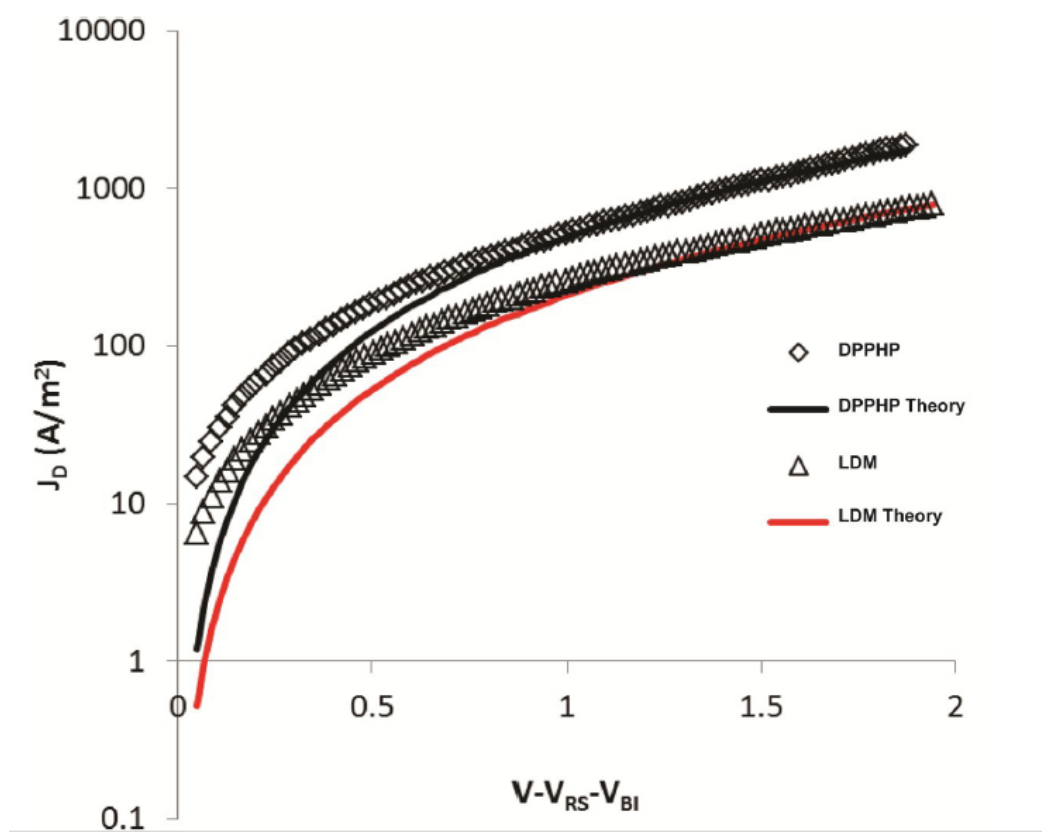


Figure 3.15: Experimental dark-current densities (J_D) for DPPHP:PC₇₁BM and LDM:PC₇₁BM film blend devices at room temperature superimposed with curves calculated by the Child's law.

wise cooling and minimal stirring of solutions to promote self-assembly of robust wires that are not disrupted when acceptor molecules are added. The efficiencies of devices created by this process can be 400-fold greater than those of devices formed by simple mixing of donor and acceptor molecules. We also found that the synergistic action of hydrogen bonds and π stacking in donor molecules that create long nanowires by self-assembly results in devices that are 54% more efficient than those built with analogous donor molecules containing only the conjugated structure.

3.5 MATERIALS AND METHODS

Materials

All chemicals were purchased from commercial sources (Sigma Aldrich, Acros and TCI) and used as received. Anhydrous solvents for synthesis are distilled from a VAC solvent purifier from Vacuum Atmospheres Company. Chlorobenzene and toluene for device fabrication are purchased from Sigma Aldrich and stored in a N₂ glovebox. Deuterated solvents were purchased from Cambridge Isotope Laboratories, Inc. All NMR spectra were taken with compound concentrations of 1-5 mM in CDCl₃. ¹H-NMR and ¹³C-NMR were recorded on a Varian 500 MHz or Bruker 500 MHz NMR spectrometer at 295 K. The molecular weight was analyzed by using a PE Voyager DE-Pro MALDI-TOF-MS instrument.

Synthesis

Synthesis of (5-bromo-thiophene-2-yl)-methanol (2): 5-bromo-2-thiophencarboxaldehyde 1 (6.5 g, 34 mmol) was dissolved in anhydrous THF (40 ml) in an oven-dried two-necked round-bottom flask with a stir bar. The solution was cooled down to 0 °C and a 1M in THF solution of lithium aluminum hydride (8.5 ml, 8.5 mmol) was added dropwise for 10 minutes. After 12 hours the reaction was quenched with 2 ml of NaOH 2M(aq) and extracted with between dichloromethane and water. The organic layer was collected and dried over MgSO₄. The solvent was evaporated under

vacuum and the crude was passed through a silica column to eliminate rests of starting material using dichloromethane as the eluent. Compound 2 was obtained as a yellow oil in 86% yield (5.7 g, 0.0295 mmol). $^1\text{H-NMR}$ (500 MHz, CDCl_3): δ 6.89 (d, 1H), 6.69 (d, 1H), 4.64 (d, 2H), 3.30 (sbroad, OH).

Synthesis of (5-tributylstannyl-thiophene-2-yl)-methanol (3): Compound 2 (5 g, 26 mmol) was dissolved in anhydrous THF (40 ml) in an oven-dried two-necked round-bottom flask with a stir bar and rigorously degassed with nitrogen flow during 10 minutes. The solution was cooled down to 0 °C and NaH in mineral oil (60%) (1.14 g, 28 mmol) was added. The reaction was allowed to run for one hour. After this time the reaction was cooled down in an acetone/dry ice bath to -78 °C under nitrogen. n-Butyllithium (2.5 M in hexanes, 12 ml, 31 mmol) was introduced dropwise by a syringe in a period of 10 minutes into the flask. The reaction was stirred for 3 more hours at -78 °C. Tributylstannyl chloride (17 ml, 65 mmol) was added with a syringe to the flask and the acetone/dry ice bath was removed to allow the reaction to reach room temperature. After 12 hours, the reaction mixture was transferred to a round-bottom flask and the solvent was evaporated under vacuum. The crude was dissolved in hexanes and passed through a short silica gel column. The filtrate was placed under reduce pressure to eliminate the solvent. Compound 3 was obtained as a dark yellow oil in 80% yield (8.04 g, 20 mmol). $^1\text{H-NMR}$ (500 MHz, CDCl_3): δ 6.90 (d, 2H), 6.73 (d, 2H), 4.69 (d, 4H), 1.63 (m, 6H), 1.36-1.32 (m, 12H), 0.93 (q, 9H). $^{13}\text{C-NMR}$ (125 MHz, CDCl_3): δ 144.02, 126.89, 125.65, 125.50, 60.06, 27.83, 27.16, 13.70.

Synthesis of 5: Compounds 41 (11 mg, 0.034 mmol) and 3 (30 mg, 0.075 mmol) are placed in a round-bottom flask with a stir bar and dissolved in anhydrous dichloromethane (5 ml). N-ethyl-N'-(dimethylaminopropyl)carbodiimide (EDC, 43 mg, 0.22 mmol) and 4-(dimethylamino)pyridinium-4-toluenesulfonate (DPTS, 67 mg, 0.22 mmol) were subsequently added to the reaction mixture. The reaction was stirred for 48 hours and after completion the reaction crude was extracted between dichloromethane and $\text{NaHCO}_3(\text{aq})$ (50 ml x 1), water (50 ml x 2) and brine (50 ml x 1). The organic phase was dried over MgSO_4 . Compound 5 was obtained after silica gel column chromatog-

raphy (dichloromethane, dichloromethane/methanol 10:1) as a colorless oil in 54% yield (20 mg, 0.018 mmol). $^1\text{H-NMR}$ (500 MHz, CDCl_3): δ 6.90 (d, 2H), 6.73 (d, 2H), 5.35-5.28 (dd, 4H), 3.65 (sbroad, 2H), 2.09-.94 (m, 2H), 2.72-2.71 (m, 4H), 2.48-2.42 (m, 4H), 1.80-1.74 (m, 4H), 1.28-1.19 (s, 2H), 1.67-1.50 (m, 12H), 1.38-1.29 (m, 12H), 1.13-1.08 (t, 12H), 1.01-0.83 (q, 18H). $^{13}\text{C-NMR}$ (125 MHz, CDCl_3): 172.25, 172.12, 143.08, 135.25, 129.45, 128.15, 126.86, 60.67, 53.69, 32.26, 30.78, 29.59, 28.77, 27.94, 27.34, 26.99, 24.86, 13.73, 10.89. δ ESI (m/z): $(\text{M} + \text{Na})^+$ Calculated for $\text{C}_{48}\text{H}_{82}\text{N}_2\text{O}_6\text{S}_2\text{Sn}_2$: 1086.3658; found: 1110.872.

Synthesis of LDM: Compound 62 (37 mg, 0.06 mmol) and 2-tributylstannyl-thiophene (25 mg, 0.06 mmol) are placed in an oven-dried two-neck round-bottom flask with a stir bar and dissolved in anhydrous DMF (2 ml). The reaction is rigorously degassed under nitrogen flow for 10 minutes and heated to 80 °C. $\text{Pd}(\text{PPh}_3)_4$ (70.0061 mg, mmol) is added. After 12 hours the reaction is cooled down and passed through a short column of celite to remove $\text{Pd}(0)$. The column was washed with dichloromethane several times. The solvent was evaporated under reduced pressure and the product was purified by silica gel column chromatography (hexanes/dichloromethane 8:2). DPP-Control was obtained as a purple solid in 55% yield (20 mg, 0.033 mmol). $^1\text{H-NMR}$ (500 MHz, CDCl_3): δ 8.92 (d, 1H), 8.87 (d, 1H), 7.62 (d, 1H), 7.33-7.31 (m, 3H), 7.27 (d, 1H), 7.08 (t, 1H), 4.05-4.01 (m, 4H), 1.98-1.82 (m, 2H), 1.39-1.25 (m, 16 H), 0.92-0.84 (m, 12H). $^{13}\text{C-NMR}$ (125 MHz, CDCl_3): δ 161.81, 161.65, 142.85, 140.07, 139.94, 136.19, 135.22, 130.48, 129.90, 128.46, 128.31, 128.0, 126.33, 125.21, 124.81, 108.12, 108.09, 45.91, 39.24, 39.08, 30.32, 30.19, 28.35, 23.64, 23.52, 23.13, 14.12, 10.57. ESI (m/z): $(\text{M} + \text{H})^+$ Calculated for $\text{C}_{34}\text{H}_{42}\text{N}_2\text{O}_2\text{S}_3$: 606.9045; found: 608.103.

Synthesis of DPPHP: Compounds 5 (52 mg, 0.047mmol) and 62 (72mg, 0.12 mmol) are placed in an oven-dried two-neck round-bottom flask with a stir bar and dissolved in anhydrous DMF (ml). The reaction mixture is rigorously degassed under nitrogen flow for 10 minutes and heated to 80 °C. $\text{Pd}(\text{PPh}_3)_4$ (11 mg, 20%) is added. After 12 hours the reaction is cooled down and passed through a short column of celite to remove $\text{Pd}(0)$. The column was washed with dichloromethane several times. The solvent was evaporated under reduced pressure and the product was purified

by silica gel column chromatography (hexanes/dichloromethane 8:2). DPPHP was obtained as a purple solid in 25% yield (17 mg, 0.011 mmol). ^1H -RMN (CDCl_3): δ 8.92 (d, 2H), 8.86 (d, 2H), 7.64 (d, 2H), 7.24 (d, 2H), 7.00-7.02 (m, 4H), 6.96 (t, 2H), 6.20 (1H, NH), 6.07 (1H, NH), 5.30 (d, 2H), 5.23 (d, 2H), 4.08 (m, 8H), 2.73-2.62 (m, 4H), 2.49-2.42 (m, 4H), 2.03 (m, 4H), 1.73 (s, 4H), 1.35-1.31 (m, 32 H), 0.93-0.85 (m, 24H). ^{13}C -RMN (125 MHz, CDCl_3): δ 164.29, 161.11, 140.25, 138.43, 135.12, 131.43, 130.88, 129.40, 128.48, 118.89, 107.83, 107.4, 53.64, 42.21, 32.40, 31.95, 26.70, 22.40, 14.10, 10.57. ESI (m/z): (M + H)⁺ Calculated for $\text{C}_{84}\text{H}_{106}\text{N}_6\text{O}_{10}\text{S}_6$: 1552.16; found: 1553.399

UV-Visible Spectroscopy (UV-Vis)

UV-Vis spectra in solution were collected on a PerkinElmer Lambda 1050 spectrophotometer using a quartz cell of 0.1 cm path length. Transmission spectroscopy was collected in the same instrument using a mica slide as a background.

Fluorescence Spectroscopy

Fluorescence spectra were performed on an ISS PC photon counting fluorometre using a quartz cell of 1 cm path length, in which all emission spectra were collected at a 90° angle at room temperature.

Atomic Force Microscopy

AFM characterization was performed using a Bruker Dimension ICON atomic force microscope (Bruker Co.) at ambient conditions. Tapping mode was utilized with single-beam silicon cantilevers with a nominal oscillation frequency of 300 kHz.

Cryo Transmission Electron Microscopy

CryoTEM was performed using a JEOL 1230 transmission electron microscope operating at 100kV fitted with a LaB6 filament. A 5 μL drop of the sample in toluene was deposited on a 300 mesh

copper grid with a lacey carbon support (Electron Microscopy Sciences), blotted with filter paper, and plunge frozen using liquid nitrogen as a cryogen with a Vitrobot Mark IV (FEI) vitrification robot at ambient temperature and humidity. The samples were placed into a Gatan 626 cryo-holder using a cryo-transfer stage and imaged using a Gatan 831 CCD camera.

Cryo Transmission Electron Microscopy

Electrochemical measurements were done by cyclic voltammetry on a three electrode setup (EGG Princeton Applied Research potentiostat model 263A). DPPHP was drop cast from chlorobenzene solution (3.2×10^{-3} M) onto the working electrode. The film was immersed into anhydrous chlorobenzene after degassing the solvent and scanned at 100 mV/s using tetrabutylammonium hexafluorophosphate (NBu_4PF_6) as the electrolyte. A gold working electrode, a silver pseudoreference electrode and a platinum counterelectrode were used. Ferrocene/ferrocenium (Fc/Fc⁺) redox couple was used as the internal standard and an absolute energy level of -4.8 vs vacuum was assigned. Electrochemical potential is reported vs SCE, which has an energy of -4.44 eV vs vacuum. The HOMO level of DPPHP was determined by equation 1. The LUMO level was calculated by equation 2.

$$E_{\text{HOMO}} = - (E_{\text{ox onset}} + 4.80) \text{ (eV)} \text{ (eq 1)} \quad E_{\text{LUMO}} = E_{\text{gopt}} + E_{\text{HOMO}} \text{ (eV)} \text{ (eq 2)}$$

Device Fabrication

Experimental conditions such as film thickness, DPPHP and DPP-Control concentration and solvent composition were optimized. Prepatterned indium-doped tin oxide (ITO) on glass was used as the transparent bottom electrode. The ITO was scrubbed with soap water and cleaned by ultrasonically in hexanes, soapy water, water, and a 1:1:1 solution of acetone/methanol/2-propanol. The electrode was then blown dry in a N_2 stream. The ITO surface was cleaned by UV-ozone treatment, and thin film of PEDOT:PSS (Clevios P VP Al 4083) was immediately spin-cast on top. The PEDOT:PSS film was dried at 120 °C for 20 minutes and transferred into a N_2 glovebox (O_2

and $\text{H}_2\text{O} < 0.1$ ppm). Bulk heterojunction photovoltaic devices were fabricated from blends of DPPHP or DPP-Control and phenyl-C₇₁-butyric acid methyl ester (PC₇₁BM). Solutions of 7 mg/mL of DPPHP or DPP-Control were prepared according to the stepwise self-assembly protocol in either chlorobenzene or toluene and solutions of 27 mg/mL PC₇₁BM (filtered through 0.22 nm porous polytetrafluoroethylene filters) were prepared in chlorobenzene. The blends were prepared adding the PC₇₁BM solution to a previously assembled solution of DPPHP or LDM and mixing for periods of time between 0.5 to 5 minutes. Films were cast by spin-coating at various speeds in the glove-box for 60 s. Total organic layer thickness ranged from 70-80 nm as determined by profilometry. Devices were completed by thermally evaporating 6 Å of LiF then 100 nm of Al through a shadow mask at 1×10^{-6} mbar to yield devices of 4 mm² in area and sealed with a UV-curable epoxy.

Device Measurement

Two-terminal measurements were performed using a Keithley 2400 source meter. Photovoltaic measurements were done while the devices were illuminated by an Oriel Xe solar simulator equipped with an Oriel 130 monochromator. Filters were used to cut off grating overtones. The solar spectrum was simulated using an AM 1.5 filter with 100 mW/cm² power density. A calibrated silicon reference solar cell with a KG5 filter certified by the National Renewable Energy Laboratory was used to confirm the measurement conditions.

Device Measurement

SCLS experiments were used to measure the hole mobility of 40:60 blends of DPPHP/PC₇₁BM and LDM/PC₇₁BM in a solar cell configuration. These devices were fabricated under identical conditions to the reported solar cells except that the LiF/Al was replaced with Au in order to suppress electron injection. Hole mobility were estimated using the experimental data and theory reported by V. D. Mihailetschi et al.⁶⁹ V_{RS} = Voltage Drop across the ITO series resistance and V_{BI} = Built-in voltage.

4 IMPROVING SOLAR CELL EFFICIENCY THROUGH COMPETITIVE HYDROGEN BONDING: A METHOD FOR TUNING ACTIVE LAYER MORPHOLOGY

4.1 OBJECTIVES AND SIGNIFICANCE

The morphology of the active layer in organic photovoltaics is critical in the optimization of device efficiencies. Most strategies aimed at improving morphology are focused mainly on annealing methods or the use of solvent additives. By using diketopyrrolopyrrole derivatives as donors and [6,6]-phenyl-C₇₁-butyric acid methyl ester as electron acceptors, we report here on the effect of hydrogen bonding on active layer morphology and solar cell efficiency. We specifically compared two asymmetric derivatives, one containing an amide bond capable of forming hydrogen bonds with one containing an ester bond in the same position. Although both molecules have very similar optoelectronic properties, films of the ester revealed greater crystallinity and $\pi - \pi$ stacking as characterized by grazing incidence X-ray diffraction. In great contrast, active layers formed with the amide derivative formed short fiber-like supramolecular aggregates with much smaller domain sizes and less order as characterized by atomic force microscopy and X-ray diffraction. Interestingly, devices fabricated with the amide – fullerene combination have a greater short circuit current (J_{SC}) leading to a 50% increase in power conversion efficiency compared to devices formed with the ester derivative. We conclude that the effective competition of hydrogen bonding over extensive $\pi - \pi$ stacking results in morphologies that lead to higher photovoltaic efficiencies.

4.2 BACKGROUND

Organic photovoltaics (OPVs) have attracted great attention due to their low-cost processing,²⁰⁴ ease of synthesis, and molecular design versatility.^{93,112,181,205} Recently, single-cell device power conversion efficiencies (PCE) for bulk heterojunction polymer systems over 7%^{67,206–209} and small

molecule systems with PCE over 6 – 8%^{43,132,180} have been reported. Systems with covalent polymers as electron donors remain the best performing materials, but their inherent polydispersity generates batch-to-batch variability,¹¹³ and it has been found that PCE is dependent on molecular weight, which may not always be easy to reproduce.¹⁰⁸ On the other hand, small molecules offer the advantage of a precise molecular weight and high purity without batch-to-batch variation, and possibly enhanced local crystallinity, which translates into higher mobilities.²¹⁰ However, the high degree of crystallinity can limit the solubility necessary for solution processing and create nonuniform morphologies in the active layer.⁹¹ High PCE small molecule designs currently focus on optimizing electronic properties, using the so-called push – pull principle,²¹¹ but improving the morphology of the active layer is a much less explored topic, even though it is a crucial parameter to obtain high performing devices.^{103,119}

Supramolecular chemistry is emerging as a strategy to use noncovalent interactions between monomers to generate ordered structures²¹² for a broad spectrum of applications that range from energy to medicine.²¹³ To date, there are only a few reports on how performance in OPVs is affected by noncovalent interactions, such as π – π stacking^{135,214} or hydrogen bonding, either with symmetric^{215–218} or asymmetric designs.^{219,220} There is precedence for using self-assembly to direct the arrangement of electronically active molecules on films.^{121,191,221–225} Our first attempts at assembling molecules for OPVs involved conjugation of a 1,2-cyclohexyldiamide hydrogen-bonding group to a sexithiophene to form a hairpin-shaped organogelator.¹²⁹ The design was later modified with a diketopyrrolopyrrole dye to improve the electronic properties.¹³⁰ Both hairpin designs formed long fibers on thin films, which were the result of initial H-aggregates that in turn bundled via J-aggregation to form large assemblies. In both cases, we found that functional devices were obtained only under conditions that promoted self-assembly, but it was difficult to control the degree of aggregation.

We report here on two electron donor molecules with or without the ability to form hydrogen bonds. These molecules were designed to be symmetric (S-Amide and S-Ester) or asymmetric

(A-Amide and A-Ester). Both designs have a diketopyrrolopyrrole (DPP) core, which is a well-known low band gap dye used in polymer and small molecule OPV devices.^{42,179,226–228} Additional thiophene groups separate the core from the cyanovinyl amide or ester groups at the ends of the molecules, which are electron-withdrawing and serve to lower the band gap of the material²²⁹ The amide groups provide hydrogen-bonding ability and offer a second driving force for self-assembly beyond $\pi - \pi$ stacking. Our hypothesis was that self-assembly promoted by hydrogen bonding among the donors should lead to films with better connectivity, higher hole mobility, and ultimately better OPV performance. The control molecules without ability to form hydrogen bonds contained an ester moiety in the same position as the amide.

4.3 RESULTS AND DISCUSSION

Fig. 4.1 shows the synthetic pathway of the different symmetric (S-Amide, S-Ester) and asymmetric (A-Amide and A-Ester) donor molecules. The synthesis of dibromo-DPP **1** has been reported elsewhere.¹³⁵ The alkyl tails used in all molecules are to the best of our knowledge a racemic mixture of butyl – octyl stereoisomers. Stille coupling of **1** and **2** afforded dialdehyde **3**, to which branched alkyl-cyanovinyl moieties **4** or **5** were coupled via Knoevenagel condensation. Initial atomic force microscopy (AFM) analysis of films of the symmetric donors suggested strong aggregation that decreased solubility; for that reason, we synthesized asymmetric derivatives, with only one benzyl cyanovinyl electron-withdrawing group at one terminus of the molecule and a phenyl-capped thiophene on the other. Preparation of the asymmetric derivatives utilized initially a similar pathway to that used with S-Amide and S-Ester. For this purpose, **1** was coupled to one equivalent of **2** to afford **6**, and precursor **7** was coupled to **6** via Stille coupling to afford **8**. Lastly, O-benzylcyanoacetate or N-benzyl-2-cyanoacetamide groups were coupled using a Knoevenagel condensation to afford A-Ester and A-Amide, respectively.

The optical properties of the compounds synthesized were characterized using UV – vis spectroscopy. Fig. 4.2 shows normalized spectra in solution and on thin films for all four molecules. The

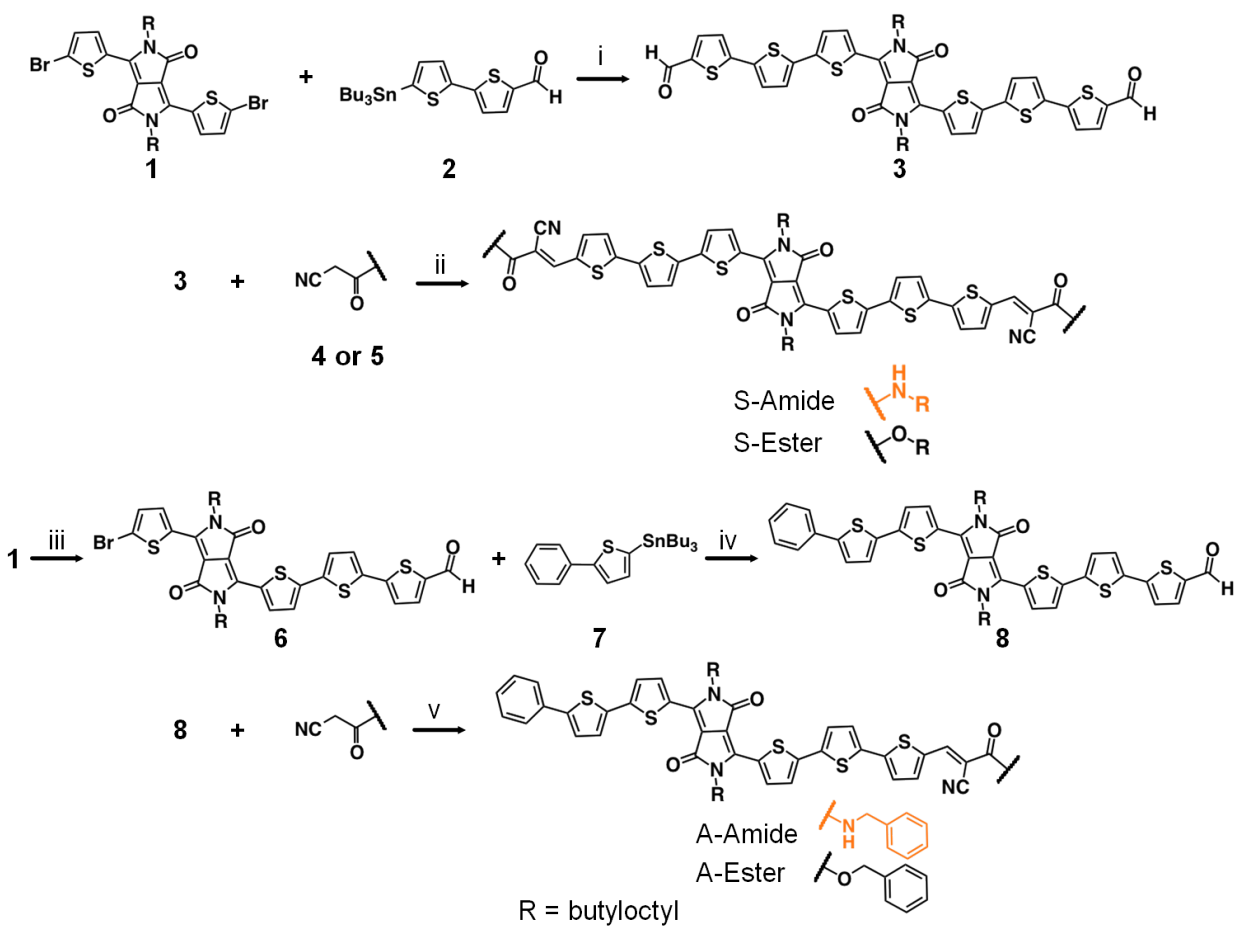


Figure 4.1: Synthesis of Symmetric and Asymmetric Donors. a(i) $\text{Pd}(\text{PPh}_3)_4$, DMF, 100 °C, 74%. (ii) Piperidine, CHCl_3 , 70 °C, 46% (S-Amide), 74% (S-Ester). (iii) 2, $\text{Pd}(\text{PPh}_3)_4$, DMF, 100 °C, 39%. (iv) $\text{Pd}(\text{PPh}_3)_4$, DMF, 100 °C, 81%. (v) Piperidine, CHCl_3 , 70 °C, 33% (A-Amide), 21% (A-Ester).

S-Amide and S-Ester compounds exhibit very similar absorption spectra in solution (CHCl_3). Both spectra show two absorption bands, one with maximum absorption wavelength (λ_{max}) at about 630 nm, and a band with lower absorption intensity in the UV region near 450 nm. When these solutions are cast onto glass substrates, the dried films for both compounds exhibit vibronic broadening at 630 nm and a red shift at λ_{max} , with the S-Ester having a more pronounced shift than the S-Amide in the 450 nm region. Appearance of fine vibronic bands is associated with interchain $\pi - \pi$ stacking and increased conjugation,²³⁰ which in turn indicates molecular aggregation. The absorption band at 450 nm also increases in intensity in both cases. S-Amide does show much improved light absorbing ability, given that its maximum extinction coefficient is nearly 60% higher than that of S-Ester (Fig. 4.3). Overall, the absorption spectra reveal that S-Ester has a greater tendency to aggregate on films.

The solution spectra of A-Amide and A-Ester differ from the symmetric versions. Because of the asymmetric design, there is less conjugation than in S-Amide and S-Ester, which causes the absorbance to blue shift slightly. Both molecules have a λ_{max} at 630 nm, but the main difference is the smaller absorption intensity of the band at 450 nm. The spectra of films are also markedly different in the asymmetric molecules. Although the S-Amide and the S-Ester both showed somewhat similar aggregation tendencies, the A-Amide shows only a slight vibronic shift of λ_{max} , but the A-Ester shows an enhanced bathochromic shift of λ_{max} and a more pronounced increase in absorption at 400 nm, which suggests that A-Ester has stronger interactions in the solid phase that leads to more efficient excitonic coupling, hence reduced energy gap. Unlike S-Amide and S-Ester, the extinction coefficients of A-Amide and A-Ester differ by roughly 15%, with A-Amide having greater light absorbing capability (Fig. 4.3).

The energy of the frontier molecular orbitals was calculated by performing cyclic voltammetry (CV) on thin films of the four molecules. The HOMO and LUMO levels were calculated from the onset of the first oxidation and reduction potentials, respectively. The HOMO – LUMO gap (E_g) was determined from the orbital energy difference. Fig. 4.4 shows the CV trace for films of the four

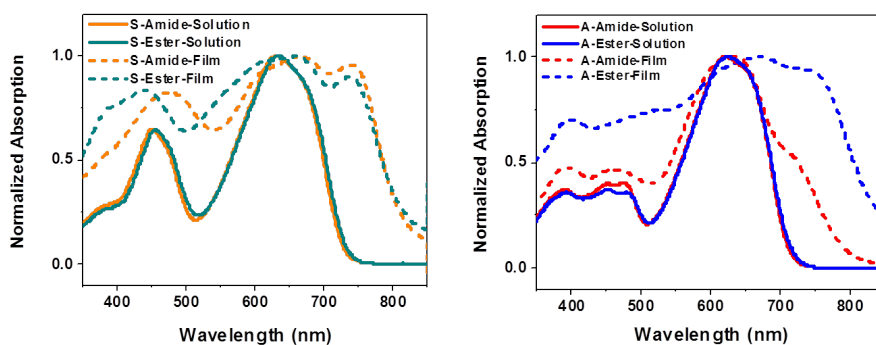


Figure 4.2: Absorption spectra of symmetric and asymmetric donors in CHCl_3 and on film.

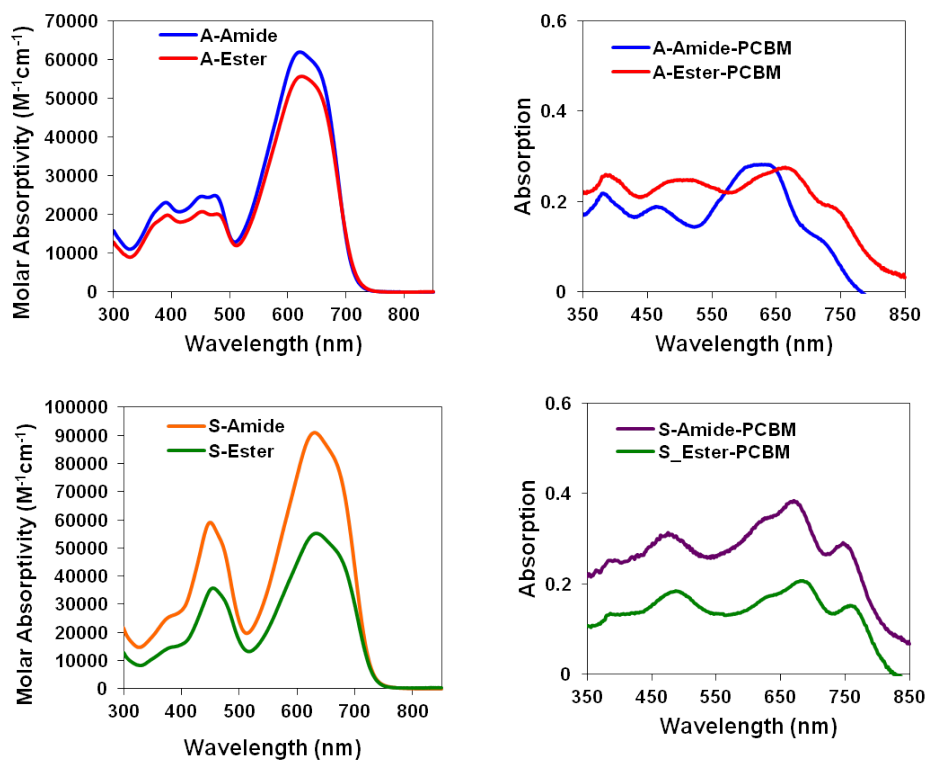


Figure 4.3: Absolute absorption of the four molecules in CHCl_3 (left) and unnormalized film absorption with PCBM under maximum PCE conditions (right).

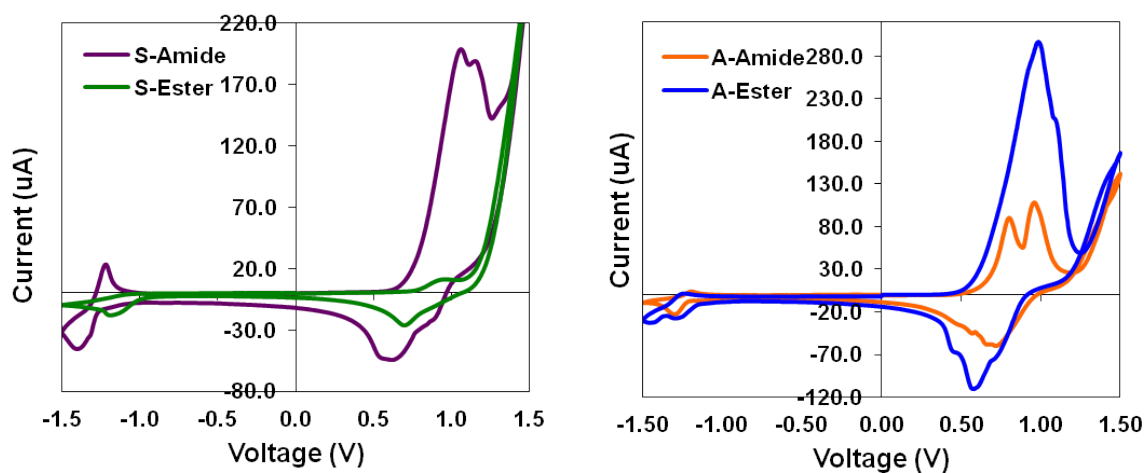


Figure 4.4: Cyclic voltammograms of S-Amide, S-Ester, A-Amide and A-Ester.

	solution λ_{\max} (nm)	film λ_{\max} (nm)	ϵ at $\lambda_{\max} \times 10^4$ ($M^{-1}cm^{-1}$)	E_g (eV) ^a	HOMO (eV) ^b	LUMO (eV) ^b
S-Amide	630	664	9.10	2.04	-5.44	-3.40*
S-Ester	633	656	5.53	1.68	-5.39	-3.71
A-Amide	621	633	6.20	1.86	-5.33	-3.47
A-Ester	624	666	5.58	1.71	-5.28	-3.57

^aMeasured from $E_g = \text{LUMO} - \text{HOMO}$. ^bMeasured from redox potentials $E_{\text{ox}}/E_{\text{red}}$ from CV vs Ag/AgNO₃. * indicates that appearance of prereluction waves complicated the assignment of the LUMO level, which may explain the difference in E_g between S-Amide and S-Ester despite their similar absorption onsets.

Table 4.1: Electronic Properties of Donors.

molecules, obtained using a three-electrode system. Films were deposited on the working electrode from 10 mM CHCl₃ solutions of the four molecules. Oxidation potentials are reported versus the nonaqueous reference electrode Ag/AgNO₃ and calibrated against the ferrocene/ferrocenium redox couple. Table 4.1 shows the calculated electronic properties of the four molecules.

The presence of hydrogen bonding was established using FTIR spectra of films cast from 10 mM CHCl₃ solutions on an ATR Ge crystal (Fig. 4.5, Fig. 4.6). In these films cast from CHCl₃, the C=O peak is difficult to characterize because of overlapping absorption bands. However, on the basis of the presence of the free NH stretching band at 3440 cm⁻¹ for the S-amide, we conclude that assemblies of this compound in the films do not exhibit significant levels of hydrogen bonding.²³¹ On the other hand, the NH stretching frequency of 3360 cm⁻¹ in the A-Amide indicates

the presence of significant hydrogen bonding in these films.²²³ Measurements on blends of PC₇₁BM and the four molecules were also performed, which showed the N – H stretch unchanged. Although these measurements could only be performed on drop-cast films, we assume a similar behavior to hold true in the spin-coated films, namely the ability to hydrogen bond in the case of A-Amide and not S-Amide. Both ester versions, not surprisingly, show no ability to hydrogen bond. Since thiophenes are electron-donating groups, we expected that conjugation between the chromophore and the hydrogen-bonding groups would have an effect on the amide's capacity for hydrogen bonding. For this reason, FTIR was performed on films of precursors 4 and N-benzyl-2-cyanoacetate (needed for S-Amide and A-Amide, respectively). The N – H stretching of both S-Amide and A-Amide remains at higher wavenumbers than in their respective precursors, which suggests that conjugation to chromophores lowers their ability to engage in hydrogen bonding.

4.3.1 Photovoltaic Properties and Morphology of Symmetric Donors

Photovoltaic devices of S-Amide and S-Ester were fabricated by using donor/PC₇₁BM blends at a 1:1 weight ratio. A schematic of device architecture is shown in Fig. 4.7. For both blends, chlorobenzene (CB) was used as the solvent. As shown in Table 4.2, the PCE of the S-Amide solar cell is higher than that of the S-Ester compound by a factor of two. Also, both symmetric donor molecules show reasonable open circuit voltage (V_{OC}) and fill factor (FF) for a small molecule organic photovoltaic. However, the low short circuit currents (J_{SC}) of the devices limit their performance with PCE values lower than 1%.

device	V_{OC} (V)	J_{SC} (mA/cm ²)	FF (%)	PCE (%)
S-Amide	0.86 ± 0.01	1.1 ± 0.1	40 ± 3	0.37 ± 0.05
S-Ester	0.63 ± 0.03	0.7 ± 0.1	32 ± 1	0.15 ± 0.03

^aAverage performance of four devices.

Table 4.2: Photovoltaic Device Performance of Symmetric Donor Molecules with PC₇₁BM_a

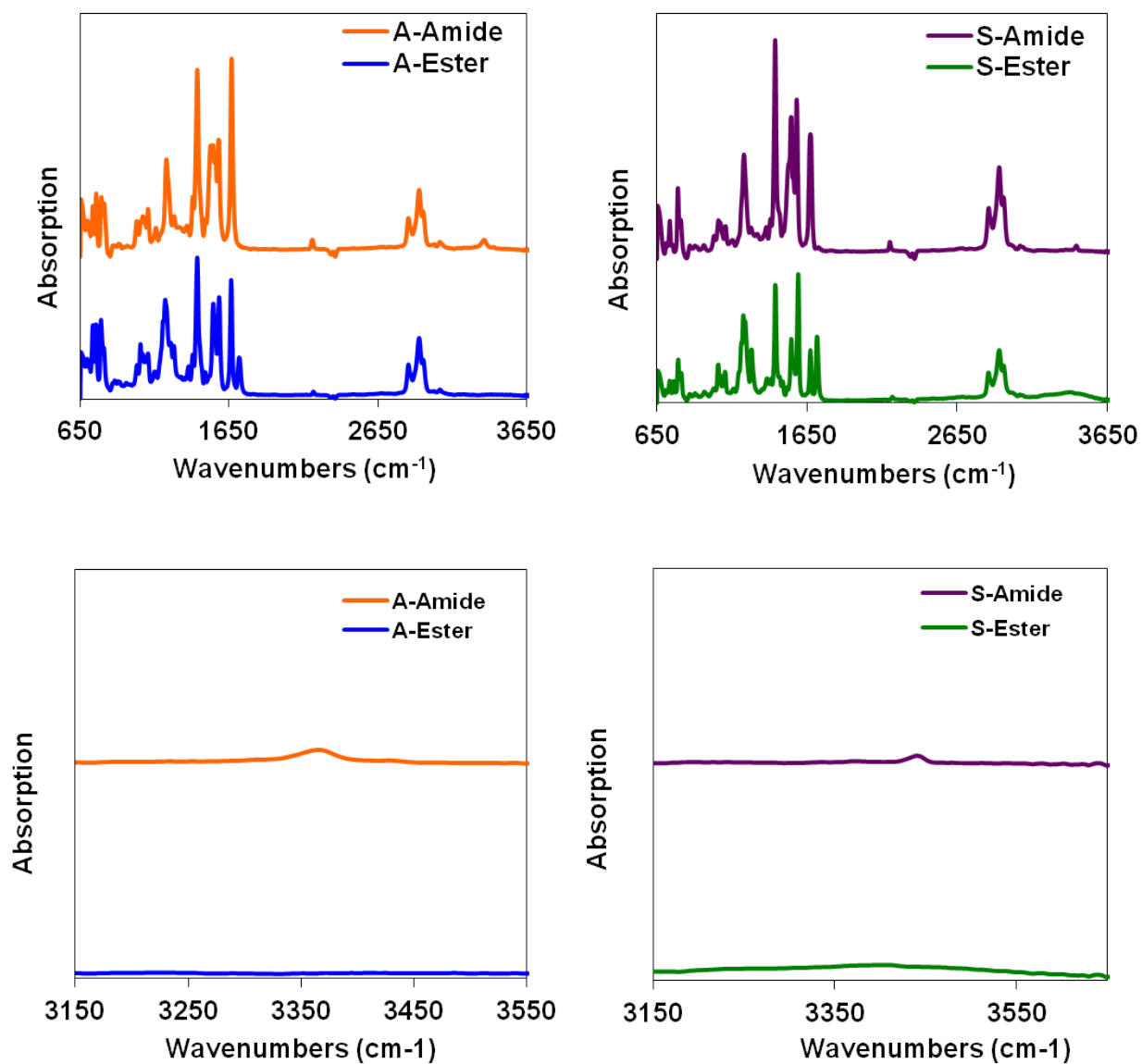


Figure 4.5: Infrared spectra of S-Amide and S-Ester (left) and A-Amide and A-Ester (right) with a close-up view of amide region (bottom).

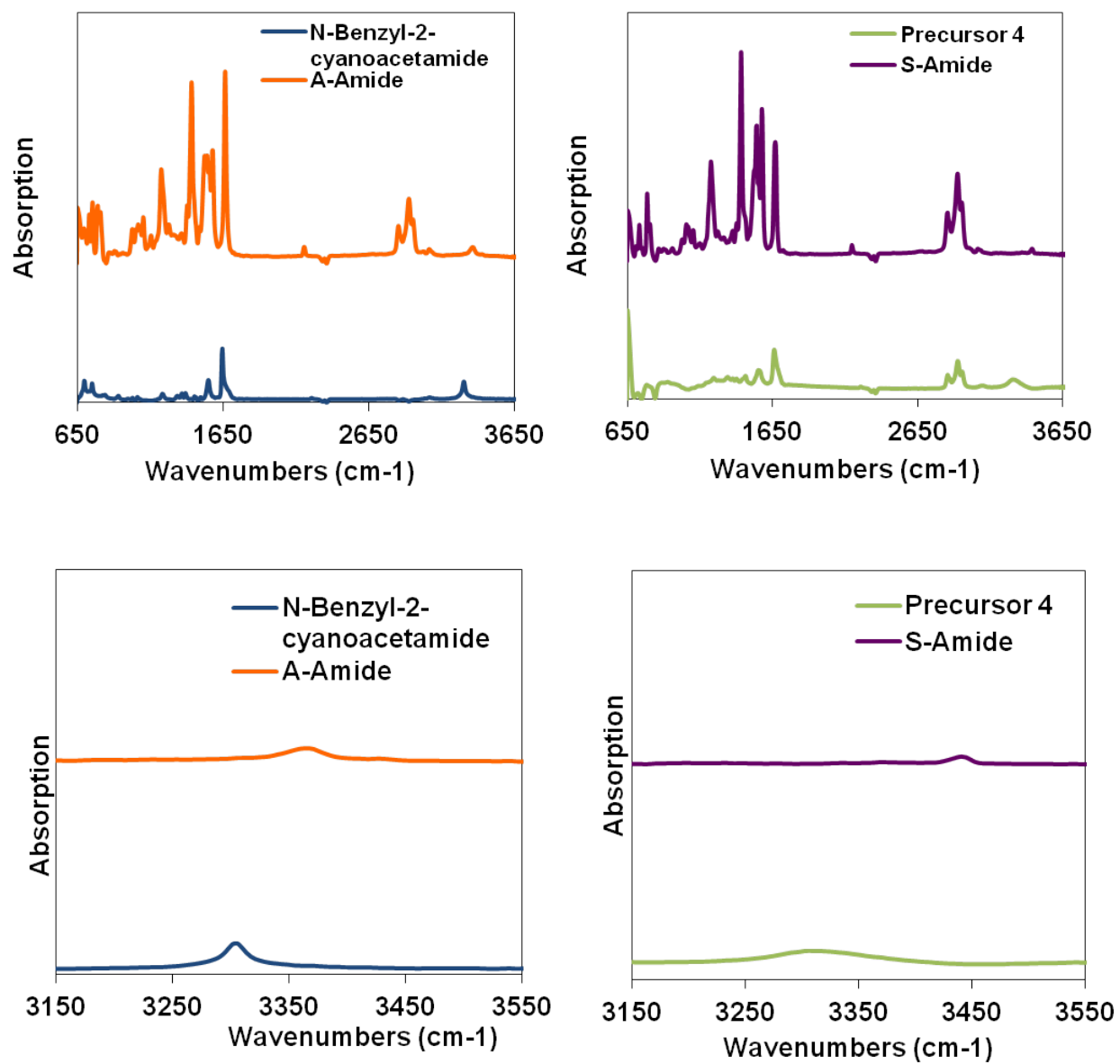


Figure 4.6: Infrared spectra of A-Amide with N-benzyl-2-cyanoacetate (left) and S-Amide with precursor 4 (right) with a close-up view of amide region (bottom).

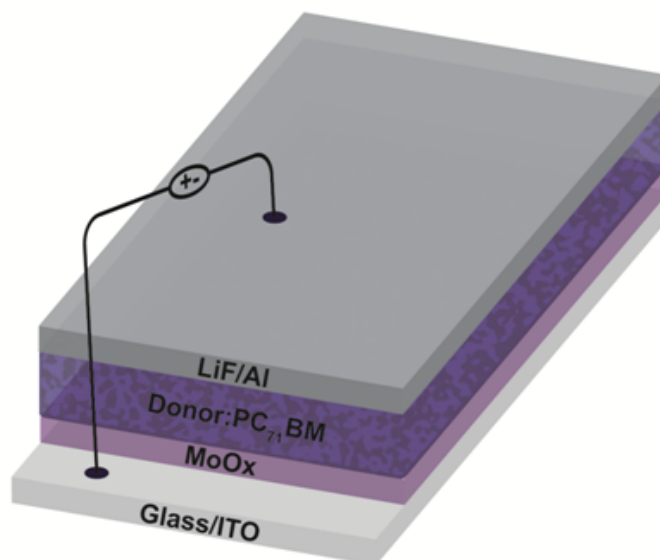


Figure 4.7: Schematic illustration of solar cell architecture used in this study

To understand the cause of the low performance, active layer morphologies of S-Amide and S-Ester devices were characterized with AFM (Fig. 4.8). A rough surface with large spherical features is observed in the topography images of both donor/PC₇₁BM blends. The aggregate size is smaller for S-Amide film compared to S-Ester, which correlates with the higher efficiency and higher V_{OC} observed for solar cell. The large aggregates formed (around 500 nm) were an indication of strong phase separation between the donor molecules and PC₇₁BM. This also limits exciton formation at the donor – acceptor interface and explains the low J_{SC} observed in devices. Although solvent additives were used to improve the device performance (Fig. 4.9, Table 4.3), much higher efficiency could not be achieved for symmetric donor molecules. We then studied the asymmetric derivatives, which were found to be more soluble.

Device	$V_{OC}(V)$	$J_{SC}(mA/cm^2)$	FF (%)	PCE (%)
S-Amide+NB	0.87 ± 0.03	1.9 ± 0.1	38 ± 1	0.61 ± 0.05
S-Ester+DIO	0.50 ± 0.03	0.9 ± 0.4	18 ± 5	0.09 ± 0.06

Table 4.3: Optimized solar cell results of symmetric molecules with solvent additives.

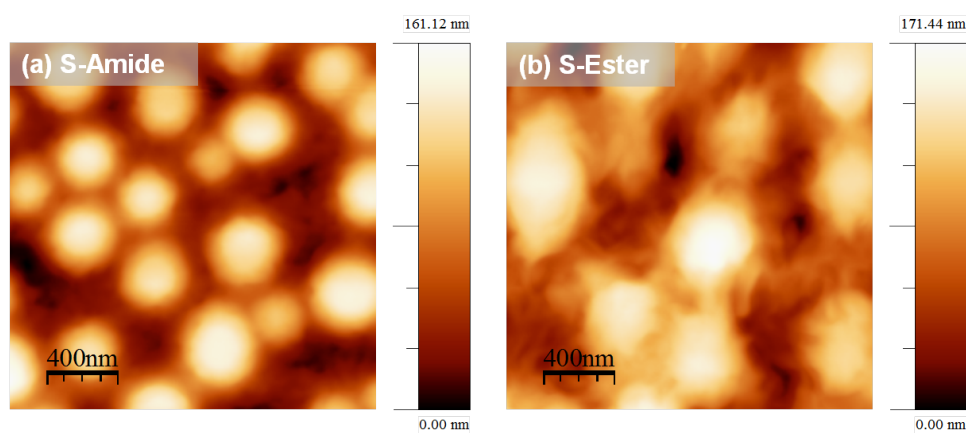


Figure 4.8: AFM topography images of solar cell morphology of (a) S-Amide/PC₇₁BM and (b) S-Ester/PC₇₁BM.

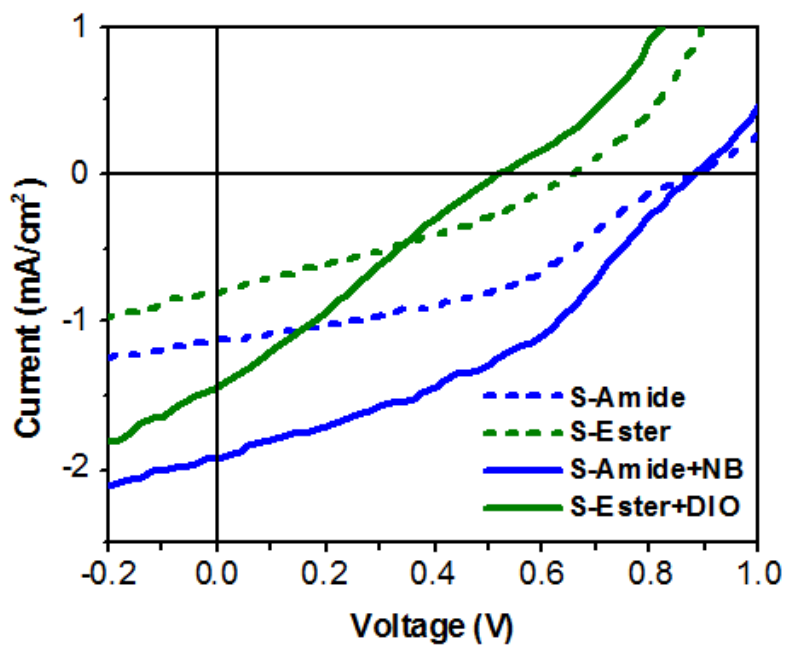


Figure 4.9: J-V characteristic of optimized solar cells of symmetric molecules with PC₇₁BM under illumination

4.3.2 Photovoltaic Properties of Asymmetric Donor Molecules

Photovoltaic devices containing A-Amide and A-Ester molecules were fabricated using donor / PC₇₁BM blends at 1:1 weight ratio. For both blends, CB was used as the primary solvent. As shown in Fig. 4.10 and Table 4.4, devices from asymmetric molecules show superior performance compared to symmetric molecules. PCE of A-Amide molecule reached $3.65 \pm 0.04\%$, which is more than two-fold higher performance relative to A-Ester cells ($1.45 \pm 0.10\%$). When the two devices are compared, they have the same V_{OC} value due to similar frontier orbitals. The A-Ester device has slightly higher FF, but it has much lower J_{SC} compared to that of the A-Amide, which lowers PCE. The difference in J_{SC} can be directly observed in an external quantum efficiency (EQE) plot in Fig. 4.10. The A-Ester device has lower EQE values almost at every wavelength compared to those of A-Amide. At the donor absorption maximum around 630 nm, the EQE value is only 20% for A-Ester, while it is 60% for A-Amide. In addition, the effect of solvent additives on device performance was studied. DIO was chosen because of its ability to dissolve PC₇₁BM selectively, while nitrobenzene (NB) was chosen because it is a nonsolvent for both phases and improves the crystallinity.^{97,232} For A-Amide, NB (0.2 v%) resulted in higher performing devices, while for the A-Ester, 1,8-diiodooctane (DIO, 0.2 v%) worked best. Addition of a higher amount of solvent additives was observed to decrease the device performance. Interestingly, PCE did not significantly improve when DIO was used for A-Amide and NB for A-Ester (Fig. 4.11, Table 4.5). NB addition to the A-Amide device improved both FF and J_{SC} values, which resulted in PCE values of $4.57 \pm 0.13\%$. DIO addition to A-Ester significantly improved J_{SC} and FF values of the device and enabled reaching PCEs of $2.83 \pm 0.20\%$. Under the best performing conditions, the A-Amide shows 50% improvement in PCE compared to the A-Ester, which mainly stems from higher J_{SC} and superior photon to electron conversion over the visible range. On the other hand, the A-Ester+DIO device has a higher FF value due to a larger shunt resistance (R_{SH}) compared to the A-Amide+NB device. A higher R_{SH} for A-Ester+DIO indicates less charge recombination and fewer defects in the active layer.²³³ Better stacking of A-Ester molecules in film as revealed with bathochromic shift in UV –

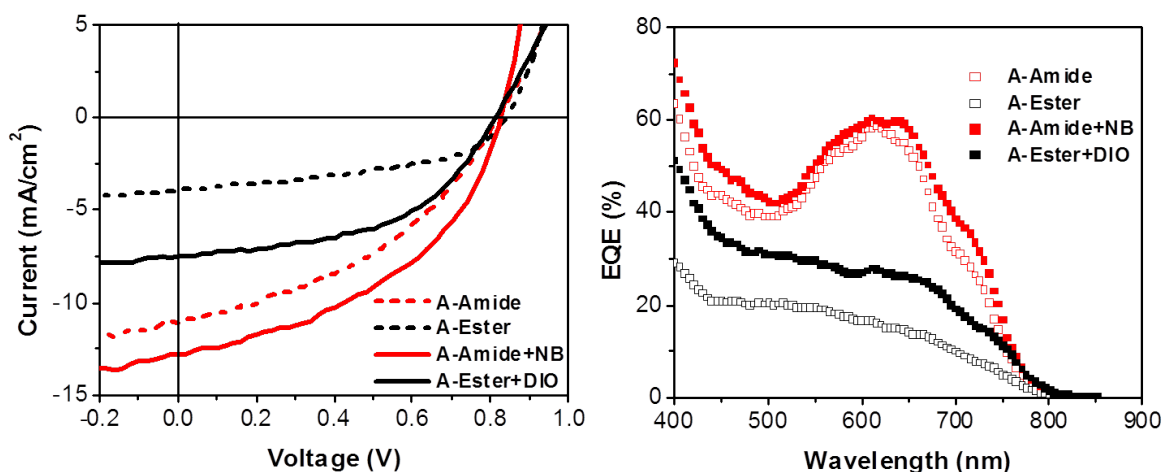


Figure 4.10: (a) $J - V$ characteristics of optimized photovoltaic devices of asymmetric molecules with $PC_{71}BM$ under illumination (AM 1.5). (b) EQE of the same devices.

device	V_{OC} (V)	J_{SC} (mA/cm ²)	FF (%)	PCE (%)	R_{SH} (Ωcm^2) ^c	R_S (Ωcm^2) ^d	μ_h (cm ² /V s ⁻¹)
A-Amide	0.82 ± 0.01	11.0 ± 0.3	41 ± 1	3.65 ± 0.04 (3.69) ^b	217 ± 13	23.3 ± 2.9	$1.3 \pm 0.5 \times 10^{-5}$
A-Ester	0.84 ± 0.01	3.9 ± 0.2	44 ± 1	1.45 ± 0.10 (1.55)	524 ± 10	39.7 ± 3.7	$6.4 \pm 0.8 \times 10^{-6}$
A-Amide+NB	0.83 ± 0	12.6 ± 0.2	44 ± 1	4.57 ± 0.13 (4.74)	215 ± 27	14.1 ± 2.2	$3.2 \pm 0.6 \times 10^{-5}$
A-Ester+DIO	0.81 ± 0	7.0 ± 0.4	50 ± 1	2.83 ± 0.20 (3.11)	570 ± 66	34.9 ± 5.6	$1.1 \pm 0.3 \times 10^{-5}$

^aAverage performance of four devices. ^bBest PCE of four devices. ^cMeasured from the slope of illuminated curves around J_{SC} . ^dMeasured from the slope of illuminated curves around V_{OC} .

Table 4.4: Optimized photovoltaic device results of asymmetric molecules with $PC_{71}BM$.^a

vis spectra seems to reduce the structural defects and increase R_{SH} of the solar cell. However, lower R_S for A-Amide+NB device is an indication of having lower intrinsic resistance in the active layer and a better morphology assuming similar contact resistance for both A-Ester and A-Amide due to similar energy levels.²³⁴

Improvement in the A-Amide device morphology upon addition of NB should increase hole mobility, which would explain the decrease in R_S . In addition, an increase in the hole mobility of the A-Amide device can explain the higher device efficiency compared to the A-Ester device. The hole mobilities of active layers were measured using the space charge limited current (SCLC) method, and the results indeed correlate with photovoltaic device results (Fig. 4.12, Table 4.4); the

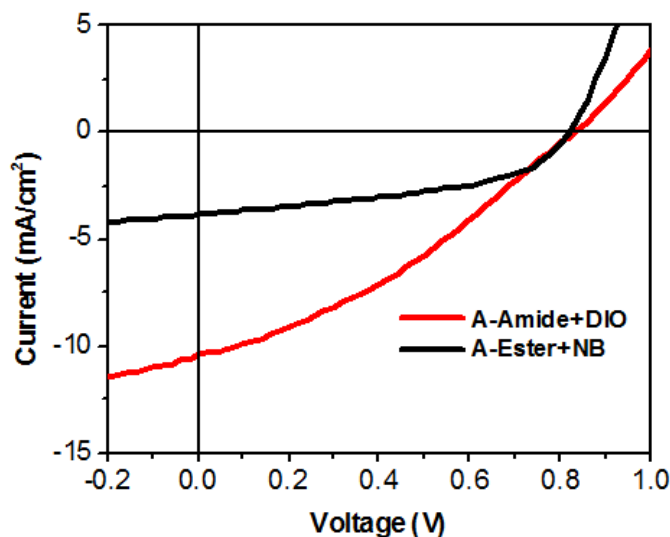


Figure 4.11: J-V characteristic of optimized solar cells of asymmetric molecules with different solvent additives under illumination.

Device	$V_{oc}(V)$	$J_{sc}(mA/cm^2)$	FF (%)	PCE (%)
A-Amide+DIO	0.83 ± 0.01	9.7 ± 0.1	37 ± 2	2.95 ± 0.14
A-Ester+NB	0.81 ± 0	3.6 ± 0.2	47 ± 1	1.37 ± 0.08

Table 4.5: Optimized photovoltaic device results of asymmetric molecules with PC₇₁BM.^a

A-Amide film has a higher hole mobility ($1.3 \pm 0.5 \times 10^{-5} \text{ cm}^2 \text{ V}^{-1} \text{ s}^{-1}$) compared to the A-Ester film ($6.4 \pm 0.8 \times 10^{-6} \text{ cm}^2 \text{ V}^{-1} \text{ s}^{-1}$). These mobility values are comparable to other DPP-based small molecules when measured with same method.²³⁵ A higher hole mobility can result in larger J_{sc} and FF values. The improvement in J_{sc} is due to increased generation of free charge carriers, while the higher FF is due to better conduction of charge carriers. Higher hole mobility in the A-Amide device produces more free charge carriers that in turn increase the J_{sc} of the device. The addition of NB increases the hole mobility of the A-Amide film and increases J_{sc} . The addition of DIO increases the hole mobility of the A-Ester and similarly improves both J_{sc} and FF. Overall, we did not observe a direct correlation between hole mobility and FF between different molecules, but there is a slight improvement in FF for the same devices upon addition of solvent additive as there is an improvement in the hole mobility. On this basis, we hypothesize that the A-Amide film

with hydrogen bonding capability improves the photovoltaic device performance with a lower R_s and a higher hole mobility compared to the A-Ester film. For that reason, the improvement in PCE of A-Amide compared to A-Ester is mainly due to superior electrical properties rather than absorption. Moreover, solvent additives improve the hole mobilities further, and to understand this phenomenon, we must analyze the morphology and structural order in the active layers.

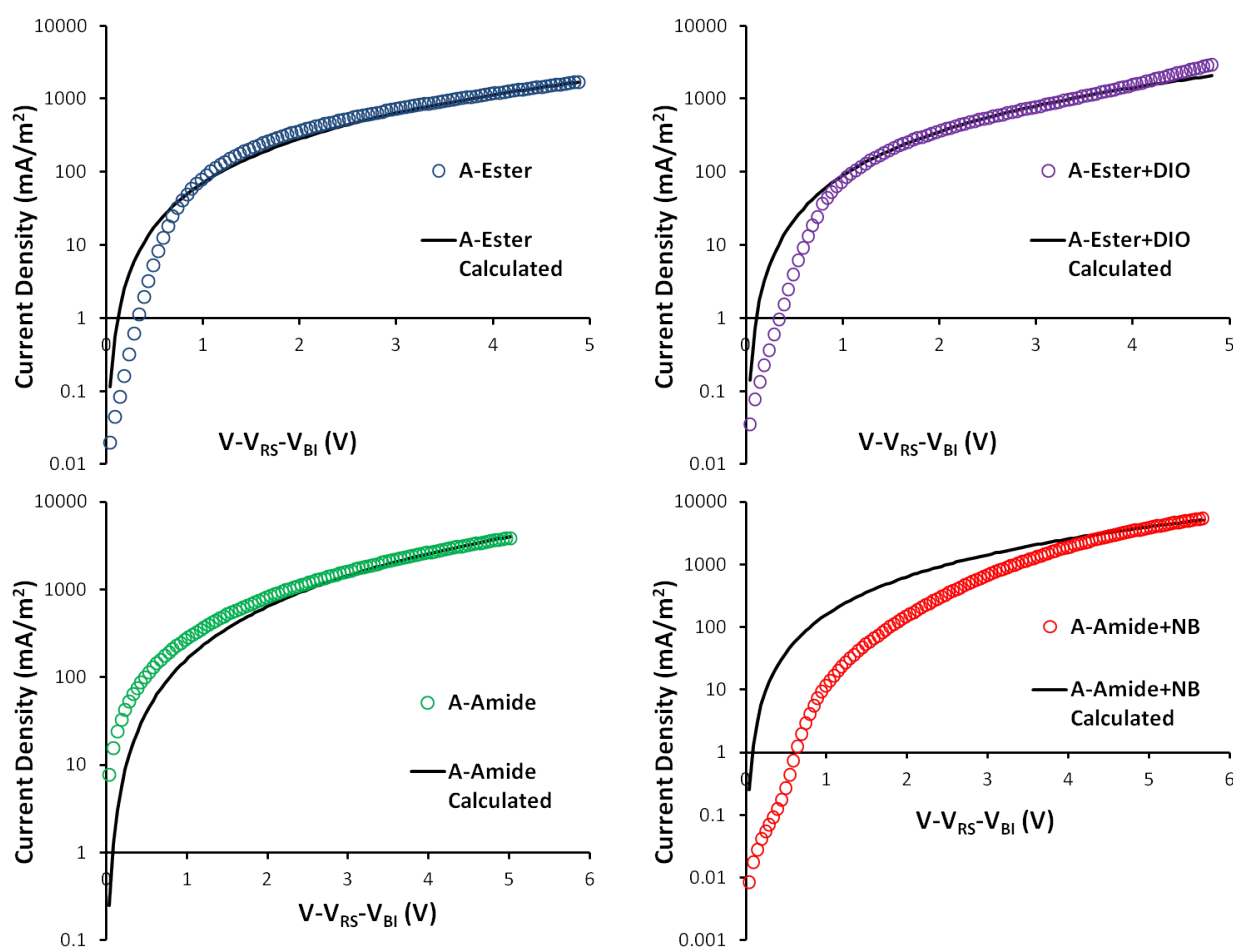


Figure 4.12: Experimental dark-current densities of A-Ester and A-Amide blends measured at room temperature in a hole only device configuration (empty marker). Experimental dark-current densities superimposed with curves calculated with SCLC theory (solid line)

4.3.3 Active Layer Morphology

As pointed out earlier, optimized active layer morphology with a small domain size (below 100 nm) is extremely important for organic photovoltaic efficiency. Segregation of active layer components at the nanoscale is required to achieve high performance due to the limited exciton diffusion length in organic materials.²⁶ Thus, to evaluate the nanoscale morphology of the photovoltaic devices investigated here, both AFM and transmission electron microscopy (TEM) were used for characterization of films. AFM topography images of the active layer of A-Amide and A-Ester blends cast from CB show a major difference in domain size (Fig. 4.13a,d). The A-Amide blend has a smoother surface with smaller features compared to the A-Ester, which shows large (around 200 nm) spherical aggregates. These large aggregates are responsible for the low J_{SC} and PCE of the A-Ester device since this morphology reduces the interfacial area between donor and acceptor domains. Given that the absorption of the two molecules is similar, the variation in charge generation is mostly due to the difference in interfacial area between the donor and acceptor. The smaller domains in the A-Amide blend help generate more free charges and give rise to a higher J_{SC} and EQE at all wavelengths. The use of NB as a solvent additive results in an interpenetrated morphology in the A-Amide blend with reduced domain size, but the opposite happens when DIO is used (Fig. 4.13b,c). The higher and lower PCEs of A-Amide when using NB and DIO, respectively, can thus be attributed to domain size because larger domain size reduces the J_{SC} of the solar cell. The opposite is true for A-Ester films in which NB does not improve morphology or device performance, while DIO improves both greatly (Fig. 4.13e,f). Addition of DIO in this case significantly reduces the size of the large aggregates yielding a more interpenetrated morphology. For that reason, the A-Ester+DIO device exhibits much higher J_{SC} and PCE values. BHJ thin films were also characterized with TEM, and as expected the A-Amide film cast from CB shows small scale features (see Fig. 4.14). For the A-Ester film, spherical aggregates observed in AFM appear as dark spots in TEM, which indicate aggregated PC₇₁BM domains.^{81,236} At the same time, the A-Amide film shows more connected domains with

addition of NB and much larger domains with DIO. As observed by AFM with the A-Ester, NB increases aggregate size (200 – 300 nm), while DIO decreases it.

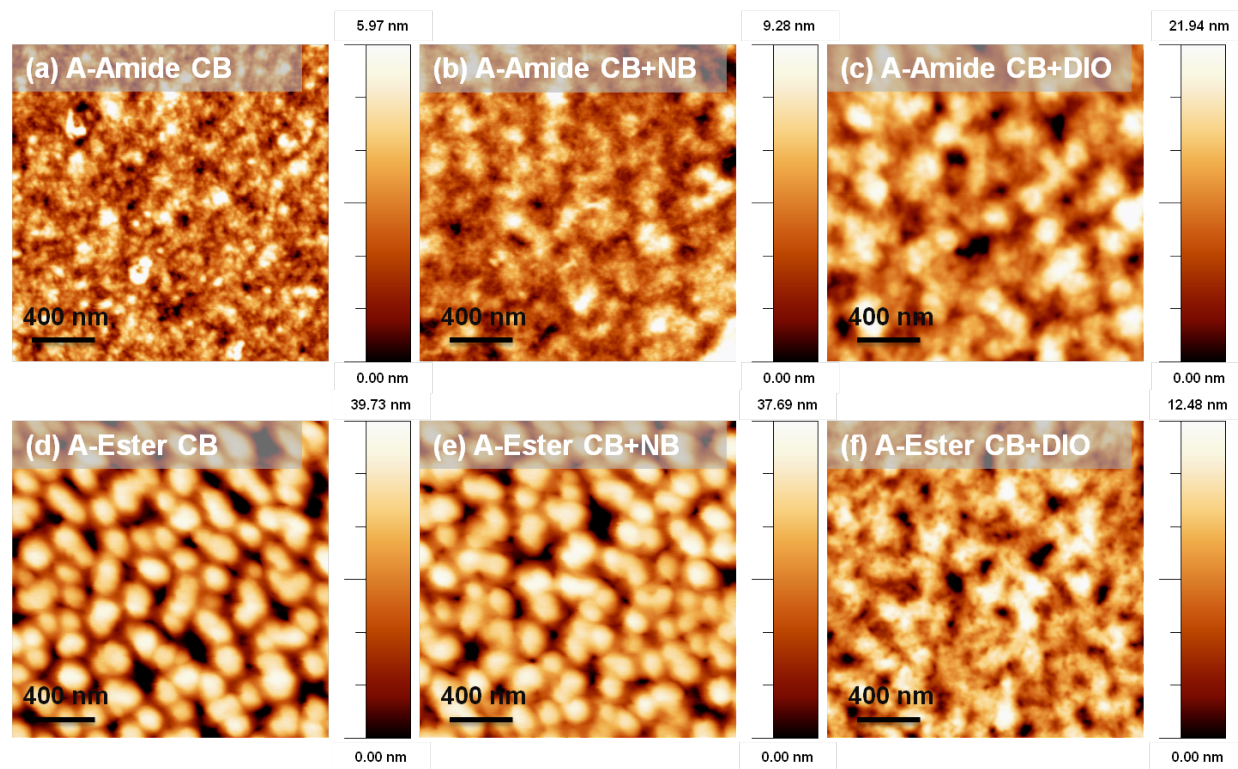


Figure 4.13: AFM images of donor/ $PC_{71}BM$ blends cast either from single solvent (a,d) or from solvent mixtures (b,c,e,f).

4.3.4 Structural Order in the Active Layer

Grazing incidence X-ray diffraction (GIXD) was used to determine the packing and orientation of molecules within the active layer. Fig. 4.15 shows the 2D GIXD images of asymmetric molecules and $PC_{71}BM$ blends. The ring around 1.35 \AA^{-1} (0.47 nm) in all images corresponds to the molecular dimensions of $PC_{71}BM$.¹⁰⁰ When cast from only CB, A-Amide and A-Ester show a significant difference in diffraction rings. In the A-Amide only, the (100) ring can be observed around 0.45 \AA^{-1} (1.4 nm), which is the distance expected for alkyl groups on adjacent stacked molecules. The use of solvent additives decreases slightly the alkyl – alkyl distance in the A-Amide without any

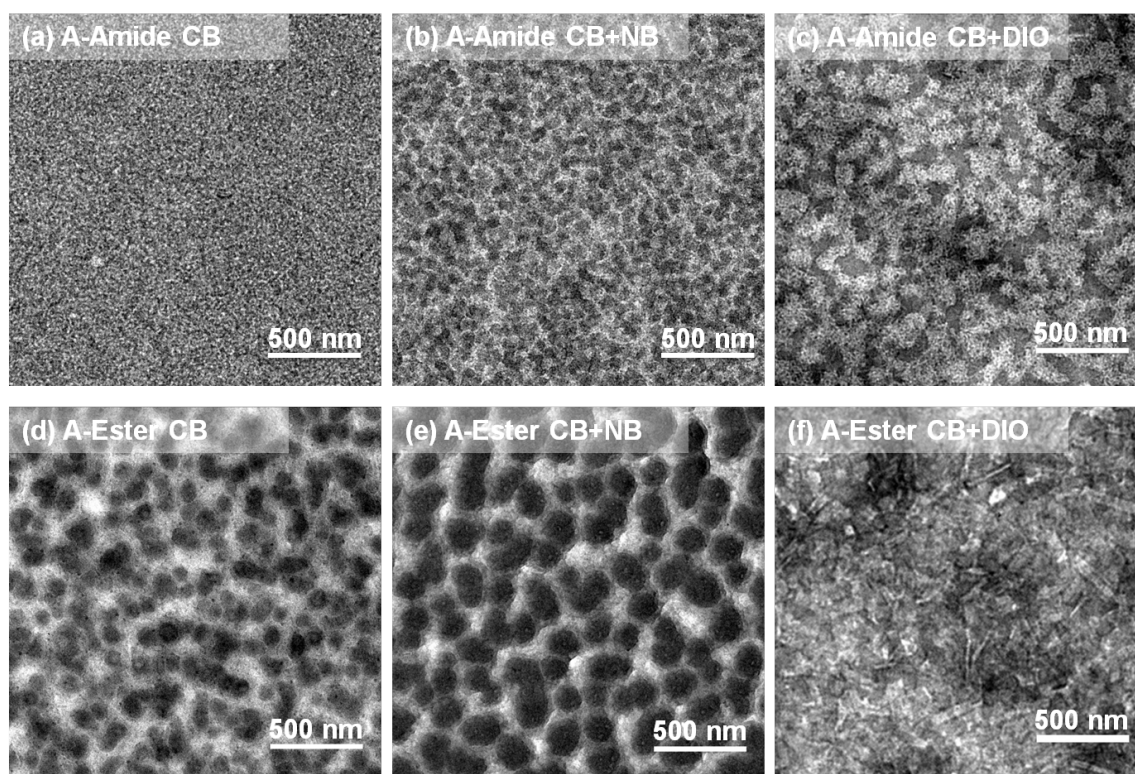


Figure 4.14: TEM images of donor/ $PC_{71}BM$ blends cast either from single solvent (a,d) or from solvent mixtures (b,c,e,f.)

other changes detected by GIXD. Compared to the A-Amide, the A-Ester film reveals higher crystallinity with the presence of additional features. Higher-order peaks can be seen for the (100) ring, which indicate a higher degree of stacking. The spacing corresponding to the (100) ring is very similar to that in the A-Amide around 1.4 nm. This is expected since the molecules have only minor structural differences. In the A-Ester film, the (010) peak observed around 1.73 \AA^{-1} (0.37 nm) is the characteristic spacing for $\pi - \pi$ stacking. Addition of NB does not change the shape or position of the GIXD rings of the A-Ester blend, but DIO appears to induce diffraction at certain angles and loss of circular shape of the rings. This phenomenon is also observed for the neat films (Fig. 4.16). We interpret these results as an indication that hydrogen bonding in the A-Amide films interrupts the crystallization behavior observed in the A-Ester films. This edge-on crystalline order is characteristic of most organic semiconductors including polythiophene.²³⁷

GIXD results were analyzed in order to quantitatively compare the differences between the active layers. The quantitative data for paracrystallinity (g), crystal size (La), and Herman's orientation parameter (S) are shown in Table 4.6. Values for g and La were calculated using three rings when available, and otherwise they were calculated using only one ring as described by MacDonald et al.²³⁸ In the g scale, 0% corresponds to a perfect crystal, 10% to a paracrystal, and 100% corresponds to a gaseous state with maximum disorder.^{239,240} For $g_{(100)}$, the A-Amide film is more amorphous (crystal size of 7 – 8 nm) than the A-Ester one (crystal size up to 18 nm). The use of solvent additives affects crystallinity in the alkyl stacking direction; NB improves the crystallinity of the A-Amide slightly, while DIO maximizes crystallinity of the A-Ester. DIO also enhances the $\pi - \pi$ stacking of the A-Ester and results in a smaller $g_{(010)}$ value and higher $La_{(010)}$ value. Similarly, DIO has previously been shown to increase crystallinity by improving $\pi - \pi$ stacking during the solution to film transition process for DPP-based polymers.²⁴¹ To the contrary, DIO does not increase crystallization for the A-Amide film because aggregation is dominated by hydrogen bonding for the A-Amide molecule. The greater crystallinity of the A-Ester with the addition of DIO is likely the reason for the higher FF and J_{SC} values in devices of the blend. The orientation of (100) rings is also assessed with the S

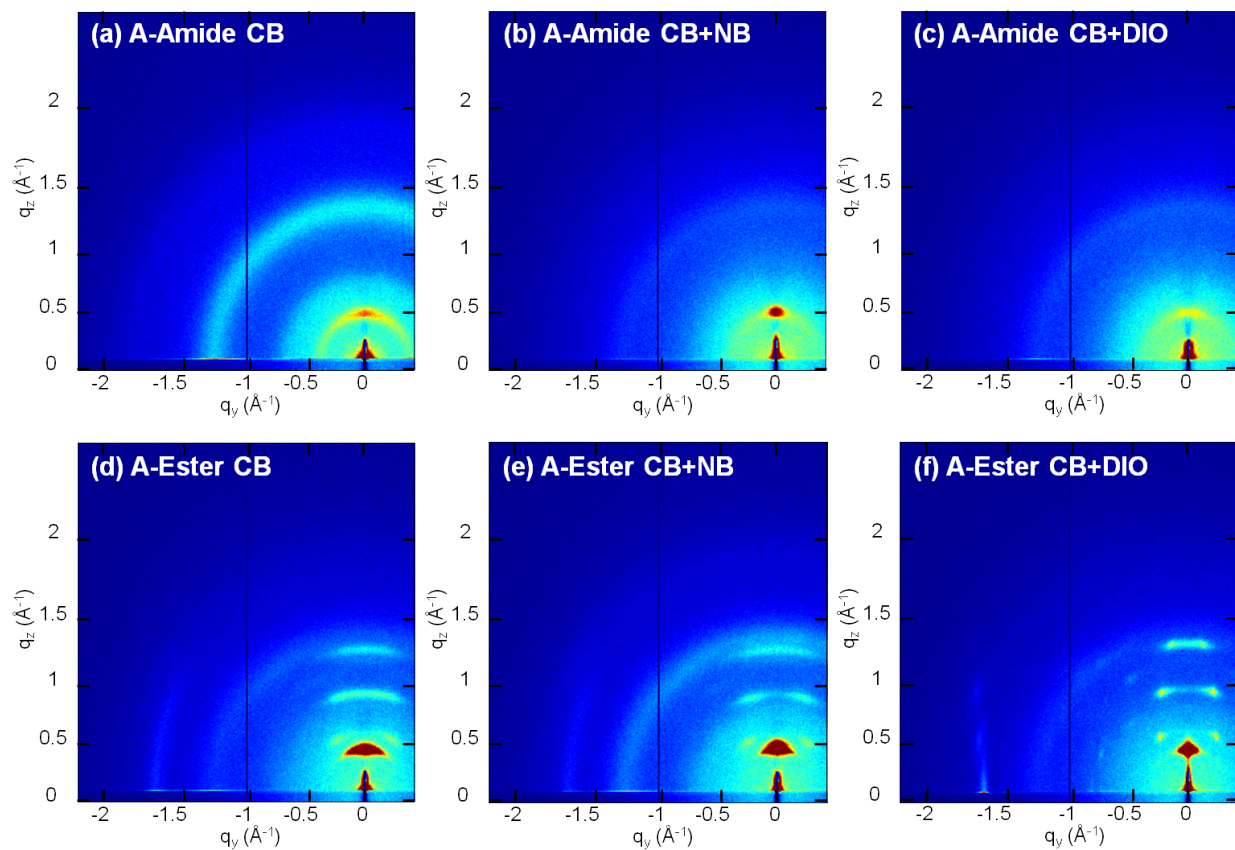


Figure 4.15: GIXD of donor/PC₇₁BM blends cast from single solvent (a,d) or from solvent mixtures (b,c,e,f).

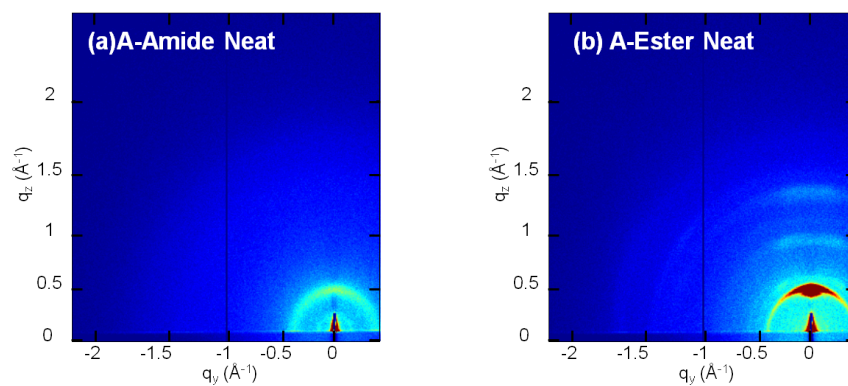


Figure 4.16: GIXD of asymmetric molecules for neat films (a, b).

film	$g_{(100)}$ (%)	$La_{(100)}$ (nm)	$g_{(010)}$ (%)	$La_{(010)}$ (nm)	$S_{(100)}$ (orientation)
A-Amide CB	15.9	7.1	N.A.	N.A.	0.36
A-Amide CB+NB	14.3	8.6	N.A.	N.A.	0.52
A-Amide CB+DIO	15.9	7.0	N.A.	N.A.	0.48
A-Ester CB	8.7	15.2	8.9	6.4	0.83
A-Ester CB+NB	8.5	18.3	8.8	6.6	0.81
A-Ester CB+DIO	7.6	16.3	6.5	12.2	0.79

^aN.A., not available.

Table 4.6: Calculated GIXD Parameters for Donor/PC₇₁BM Blends.^a

parameter. S scales lie in the range of 1 to -0.5 , 1 being completely in-plane, 0 being isotropic, and -0.5 being out-of-plane.²⁴² A-Amide films have S values of 0.4 – 0.5, which indicate an alkyl – alkyl stacking orientation between isotropic and in-plane. The A-Ester films, on the other hand, have S values of 0.8 and higher, which indicate that A-Ester molecules stack more in the in-plane direction.

It is surprising that the more amorphous A-Amide blends without $\pi - \pi$ stacking result in better performing devices. Although we always intended to use hydrogen bonding to improve photovoltaic device efficiency, our results contradict recent studies using similar end groups, where the performance is lowered due to a molecule's ability to hydrogen bond.^{215,216} The performance of the A-Amide donor could be understood in the context of a recent report by Salleo et al.²⁴³ In their studies with polymers, they concluded that the most important feature for device performance is the presence of interconnected aggregates, even if they are small and disordered. In our system, the A-Amide molecules can assemble into short fiber-like structures (especially after NB addition as can be seen in the AFM and TEM images, also shown in Fig. 4.17) interconnected with each other over longer distances, which can help with charge transport across the film. Another recent study has shown that amorphous donor domains can form better (more diffuse) interfaces with amorphous PCBM domains and enhance the charge separation.²⁴⁴ For that reason, use of molecules that are weakly crystalline yet possess some aggregation tendency (in this case through hydrogen bonding) can be favorable for solar cell active layers. The idealized microstructure of the A-Amide and A-Ester active layer is shown in Fig. 4.18.

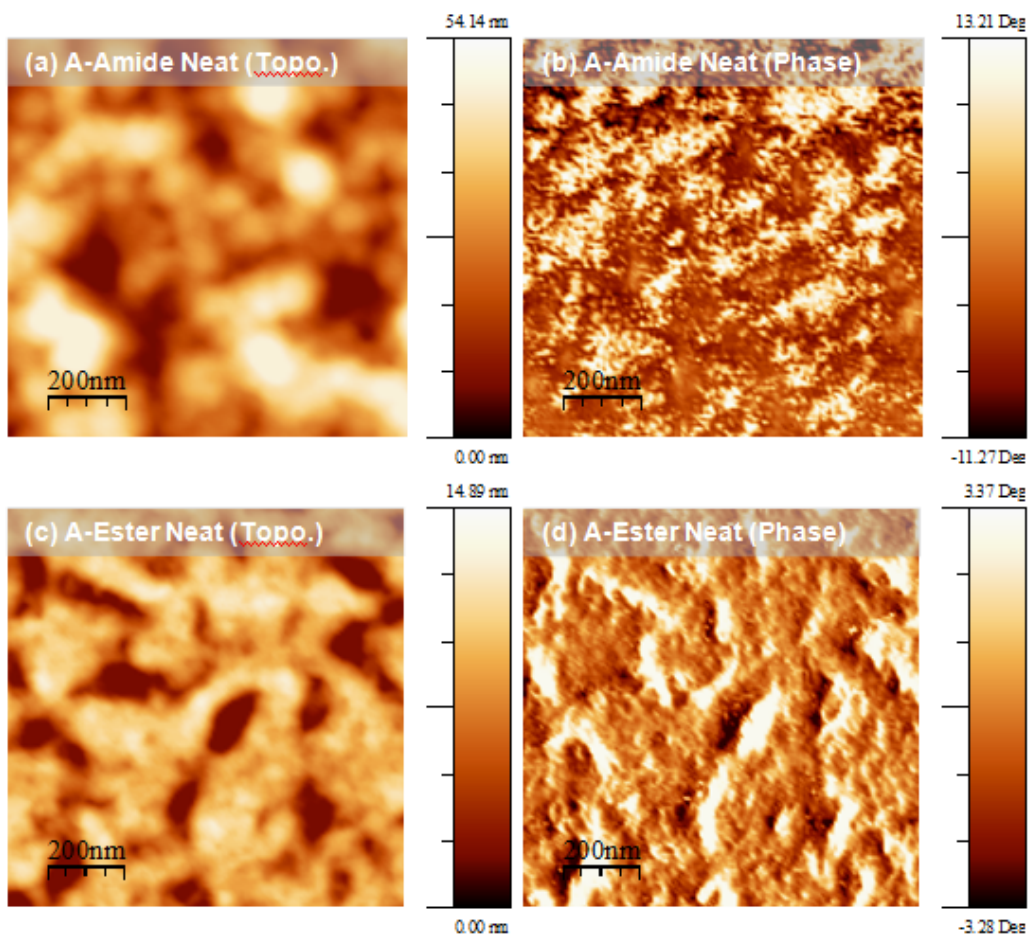


Figure 4.17: AFM topography (a,c) and phase (b,d) images of A-Amide and A-Ester neat films respectively, casted on mica from chlorobenzene and annealed at 100°C for 5 minutes.

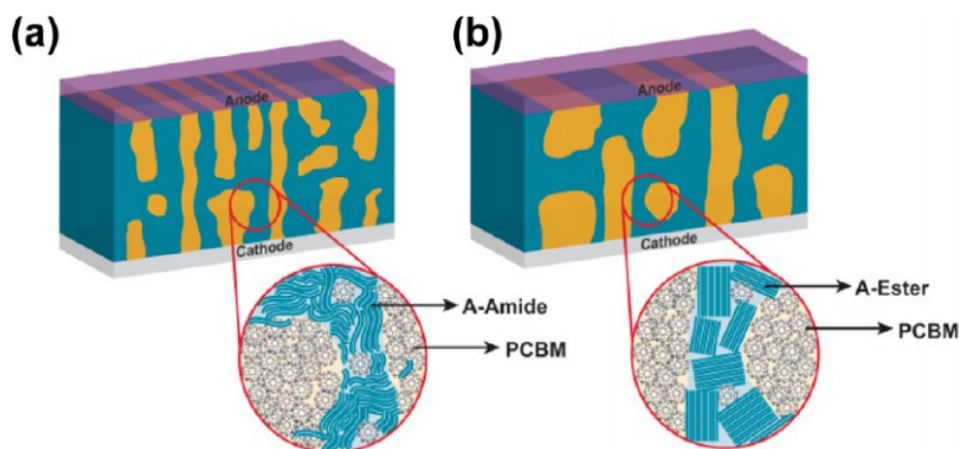


Figure 4.18: Schematic illustration of active layer morphology for A-Amide (a) and A-Ester devices (b).

4.4 CONCLUSION

By using asymmetric electron donor small molecules based on diketopyrrolopyrrole, we have investigated here the effect of hydrogen bonding on solar cell active layer morphologies and device performance. The strategy used involved the replacement of an ester for an amide bond in otherwise identical molecules. While the optoelectronic properties of amide and ester derivatives were found to be similar in solution, we found large morphological differences between them in solar cell active layers, which we attribute to hydrogen-bonding interactions. We hypothesize that hydrogen-bonding interactions compete effectively with long-range $\pi - \pi$ stacking of the conjugated molecules, which results in interconnected and smaller nanoscale donor domains relative to the ester derivative. This effect nearly doubles the efficiency of solar cells containing amide as opposed to ester active layers. Given that $\pi - \pi$ stacking is a ubiquitous interaction in organic photovoltaics that can generate long-range crystallinity, the general strategy of a competing intermolecular interaction is a valuable strategy to optimize function.

4.5 OUTLOOK

The fact that the anisotropic charge carrier mobility directly affecting the device performance for organic materials poses both advantages and challenges to applications. The ability of the preferential stacking and strong assembly of organic materials can result in high carrier mobilities in the desired direction for organic transistors applications for example. The same ability can be very problematic when it comes to organic photovoltaic applications due to the necessity of using a second material and the complexities it brings. For that reason, it is important to be able to utilize different supramolecular approaches for organic materials and their applications.

Assembly of soft material and forming frameworks has been studied extensively. One of the attractive areas is forming polymeric frameworks in 3D to create light weight and porous materials for different applications such as sensing and gas storage or even catalysis.²⁴⁵ One of the challenges in this field is that many organic materials have higher flexibility and rotational freedom especially with increasing length and such an amorphous network usually tries to avoid formation of pores. If the pore size is comparable to the size of the monomers, even intercalation and filling of the pores with the linkers can occur. This can limit the formation of larger pores which can be more desirable for certain applications such as OPVs in which it is desirable to fill in that pores with the molecular acceptor that is usually a modified fullerene. A better pore size control can be achieved by covalently organic frameworks (COF). COFs combine the low-weight and high versatility in molecular design with precise engineering of building blocks to form porous structures. The pore geometry can be tetragonal or hexagonal and it can be in the micro or meso range.²⁴⁶ Besides the size of the pores, it is equally important to engineer the pore walls and surface to make an interface that is compatible with the specific application requirements. Jiang and coworkers synthesized and used azide-appended phenylene block to construct COFs with azide-integrated walls and tuned its density by use of a third component that is naked phenylene blocks.²⁴⁷ The purpose of using azide units is to make an easy click reaction with alkynes to form triazole-linked groups on the COF wall surfaces. This kind

of an approach can be useful for specific purposes and applications such as functionalizing the COF walls with “fullerene friendly” units to attract them to form p/n junctions at the interface.

The chemistry becomes a little complicated sometimes when semiconducting units are considered for COFs. For that reason, more preferred way of controlling the pore size is using templating strategies. Banerjee and coworkers used ZnO nanorods as templates to make hollow COF tubes.²⁴⁸ Here, ZnO nanorod was synthesized separately and later placed in the monomer solution to grow COF around them. With a dilute acid treatment, ZnO nanorods were selectively removed to get the hollow (60-100 nm diameter) and microporous COF. Unfortunately, this type of an approach is not easily translatable to OPV research. For the construction of organic bulk heterojunction solar cells, this could be of major importance, as the size of the electron and hole-conducting phase should be in the range of ~ 10 nm to ensure efficient exciton separation. Another aspect to think is being able to use such system to conjugated materials, or at least being able to delocalize the π electrons for longer ranges. In most cases with conjugated molecule based COFs, those molecules are chemically unstable and lack intrasheet π -conjugation, thereby significantly limiting their application. In one of the recent studies, it was reported that chemically stable, electronically conjugated organic framework with open nanochannels, in which the π -conjugation-spans two dimensional sheets.¹²⁵ Triphenylene hexamine and butylpyrene tetraone based COF has really important physical characteristics such as extended π -delocalization, ability to host guest molecules and hole mobility. Such a system can be useful to build high-performance-conjugated molecules with high surface area for different applications such as organic electronics and energy storage. However, the shortcomings of COF systems for translatable organic electronic research is the difficult processing of such systems. In most of the cases, covalently bonded and cross-linked conjugated polymer networks always yield powders. It is difficult to melt or dissolve such powders and thus cannot be manufactured into thin films.

On the other hand, recently developed organic frameworks based on supramolecular approaches offers a solution for the processability problem. Li and coworkers demonstrated that a single-layer

2D supramolecular organic framework can be generated in solution using a robust self-assembling strategy in water.²⁴⁹ This was achieved with stacking forbidden triphenylbenzene based molecule with three hydrophilic carbamoyl groups introduced to central benzene ring to suppress 1D stacking of the triangular preorganized molecule. The controlled 2D framework formation is achieved with mixing the parent molecule with cucurbit[8]uril in a 2:3 molar ratio. Strong complexation of the two molecule stabilizes the structure and give periodic honeycomb 2D framework that is called a supramolecular organic framework (SOF) that is solution processable. This is a great alternative to covalent 2D polymers that usually requires ultrahigh vacuum and high temperature processing. Multi-component self-assembly and complexation can be directed with different forces, and one of the promising and more directing interaction is hydrogen bonding. As discussed in this and previous chapter, hydrogen bonding was used in supramolecular research extensively and it is getting more attention recently in the organic electronics field.

Intermolecular hydrogen bond between N-H and C=O plays an important role in gelation with organogelators based on urea or aminoacids. Amino acid based organogelators are important for bio-applications because they are biocompatible and easy to functionalize. On the other hand, urea can help forming gels through directional hydrogen bonds and provide a more stable gel especially when combined with π - π stacking of the aromatic rings. There have been several studies including our, that showed how hydrogen bonding can improve the device performance in organic semiconductors. In one example, organogels based on thienylvinylene anthracene have been reported for the fabrication of single-nanofiber OFETs.²⁵⁰ The supramolecular organization in fibers rely on both hydrogen bonding and π - π stacking and lead to higher performance compared to film-casting versions, with a field effect mobility of $0.48 \text{ cm}^2 \text{ V}^{-1} \text{ s}^{-1}$. However, it is important to mention that this kind of a strong interaction is not actually desired in active layers of organic photovoltaics. For example, an electron-rich tetra- or hexathiophene was co-self-assembled with an electron-poor perylene bisimide to obtain p/n heterojunction nodes and although a fibrillar nanomorphology was obtained in the film no performance regarding the devices was reported.²⁵¹ The reason for that is because the

better the self-assembly of the molecule, the lower its mixing with the other component and that limits the p/n junction interfacial area, as well the charge collection in the electrodes in photovoltaic system.

For the given reasons, utilizing self-assembly in OPVs is quite challenging but it can be achieved with balancing forces and more control over assembly. In that respect, multicomponent assembly strategies can be useful in those systems. The ideal situation would be using multicomponent assembly to give order to electron donor to form the skeleton of the active layer first and then incorporating the acceptor layer and diffusing it in the possible voids or less rigid areas of the film in a way to make 20-50 nm scale domains. Incorporating the acceptor such as PCBM can be the trivial part of this work in the beginning because it is always possible to place it on top and diffuse it in, and few studies showed in the past that it is possible to attain similar device performance with this strategy when compared to initial mixing and spin coating together on the film approach. For that reason, the main emphasis should be on the donor molecule design and utilization of the multicomponent self-assembly. The use of multiple different molecules facilitates the molecular design aiming for a directed growth of tailored supramolecular structures. The known preference for linear alignment of the H-bonds, in combination with complementary located proton donors and proton acceptors on different molecular species, allows intuitive predictions of the supramolecular arrangements. One of the important advantage of these systems is also improved solubility. Strong self-assembly components such as hydrogen bonding groups usually decreases the solubility of the molecules especially when more conjugated groups are in the consideration to integrate with the main molecule. One of the interesting examples of this was achieved with co-deposition of melamine and PTCDI on Ag/Si(111) surface to synthesize a porous honeycomb network.²⁵² In the same study, it was also shown that the pores in the network can be used for the co-location of several other molecules including C₆₀. For OPV application, this approach needs to be taken to a certain thickness level rather than a single layer. Combining multicomponent hydrogen bonding strategy with supramolecular liquid crystals may help achieving the thickness required for a typical

OPV (100-200 nm) and a macroscopic level order at the same time. This approach can benefit from the liquid crystals literature which has many examples for multi-component small molecules with complementary hydrogen bonding that was used to achieve LC behavior.²⁵³

4.6 MATERIALS AND METHODS

Materials

Unless otherwise specified, all reagents were used without further purification. 2-phenylthiophene, butyllithium, tributyltin chloride, 2-butyl-1-octanol, p-toluenesulfonyl chloride, benzyl cyanoacetate, cyanoacetic acid, N-methylpiperazine, tetrakis(triphenylphosphine) palladium [Pd(PPh₃)₄], triphenylphosphine, anhydrous acetonitrile, anhydrous dimethylsulfoxide (DMSO), sodium azide, triethylamine (NEt₃) and piperidine (vacuum distilled over NaOH pellets and stored under nitrogen) were obtained from Sigma-Aldrich; 2,2-bithiophene carboxaldehyde was obtained from TLC America; N-benzyl-2-cyanoacetate was obtained from Santa Cruz Biotechnology; dimethylformamide (DMF), dichloromethane (DCM), hexanes, ethyl acetate (EtOAc) and hydrochloric acid (HCl) were obtained from Avantor Performance Materials; pyridine was obtained from Alfa Aesar; chloroform (CHCl₃), tetrahydrofuran (THF) and methanol (MeOH) were obtained from BDH; 1-Ethyl-3-(3-dimethylaminopropyl)carbodiimide (EDC) and hydroxybenzotriazole hydrate (HOBT) were obtained from Advanced Chemtech. 4-(Dimethylamino)pyridinium-4-toluenesulfonate was prepared according to previously published procedure. Anhydrous solvents were degassed on a Vacuum Atmospheres 103991 system. Proton NMR spectra were performed on a Varian Inova 500 or Agilent DD MR-400 with working frequencies of 500 and 400 Mhz, respectively. Carbon NMR spectra were obtained using a Bruker Avance III 500 spectrometer, with working frequency of 125.6 MHz for ¹³C nuclei. Chemical shifts are reported in parts per million (ppm) and referenced to the residual nondeuterated solvent frequencies (CDCl₃: δ 7.26 ppm for ¹H, δ 77.36 ppm for ¹³C). High-resolution mass spectra were recorded on an Agilent Model 6210 LC-TOF multimode ionization

(MMI) or a Bruker Autoflex III MALDI mass spectrometers. Ultraviolet–visible (UV-vis) spectra were recorded on a Perkin Elmer LAMBDA 1050 spectrophotometer. Cyclic voltammetry was performed using an EG&G Princeton Applied Research Potentiostat (Model 263A), using a three-electrode system, with a Au disk working electrode, Pt wire counter electrode, a Ag/AgNO₃ non-aqueous reference electrode (Bioanalytical Systems, Inc., models MF-2014, mF-2062 and MW-1032, respectively). Working electrodes were polished with a suspension of aluminum particles and on a nylon pad (Bioanalytical Systems, Inc. model MF-2060). Infrared spectra were obtained using a Thermo Nicolet, Nexus 870 spectrometer. Photovoltaic measurements were done while the devices were illuminated by an Oriel Xe solar simulator equipped with and Oriel 130 monochromator and a Keithley 2400 source meter. Filters were used to cut off grating overtones. The solar spectrum was simulated using an AM 1.5 filter with 100 mW/cm² power density. A calibrated silicon reference solar cell with a KG5 filter certified by the National Renewable Energy Laboratory was used to confirm the measurement conditions. AFM characterization was performed using a Bruker Dimension ICON atomic force microscope (Bruker Co.) at ambient conditions. Tapping mode was utilized with single-beam silicon cantilevers with a nominal oscillation frequency of 300 kHz. Conventional TEM of the samples were imaged using Hitachi HT-7700 TEM at 80-100 kV. 2D-GIXD measurements were performed at Beamline 8ID of the Advanced Photon Source at Argonne National Laboratory. An x-ray wavelength of $\lambda = 1.6868 \text{ \AA}$ was used and data were collected using a 1-2 s exposure at a sample-detector distance of 204 mm with a Pilatus photodiode array.

Synthesis

5'-(tributylstannyl)-2,2'-bithiophene-5-carbaldehyde (2) was synthesized using a modified procedure from the literature. 2,2-Bithiophene-5-carboxaldehyde (0.5 g, 2.57 mmol) was placed in an oven-dried 250 mL Schlenk flask. The flask was degassed by three vacuum/nitrogen cycles. Anhydrous THF (30 mL) was injected and the solution was cooled to -78°C. N-methylpiperazine (0.313 mL, 2.83 mmol) was then injected, followed by n-butyllithium (1.13 mL, 2.5M in hexane, 2.83

mmol), after which the reaction was stirred for 20 min. The reaction was then warmed to -20°C , followed by a second addition of *n*-butyllithium (1.13 mL, 2.5 M in hexane, 2.83 mmol) and left stirring for another 30 min. Tributyltin chloride was then added (0.831 mL, 3.08 mmol) and the cooling bath was removed. After warming to room temperature, the reaction was quenched with 1 M HCl (20 mL). The crude was concentrated under vacuum, diluted in water (200 mL) and extracted with hexanes. The organic phase was separated and dried over magnesium sulfate (MgSO_4), followed by solvent removal under vacuum. Column chromatography in 1:1 DCM/hexanes afforded **5** as a yellow liquid (1.05 g, 85%). $^1\text{H-NMR}$ (500 MHz; CDCl_3): δ 9.85 (s, 1H), 7.66 (d, $J = 4.0$ Hz, 1H), 7.47 (d, $J = 3.4$ Hz, 1H), 7.25 (d, $J = 4.0$ Hz, 1H), 7.11 (d, $J = 3.4$ Hz, 1H), 1.61-1.54 (m, 6H), 1.35 (m, 6H), 1.15-1.12 (m, 6H), 0.91 (t, $J = 7.3$ Hz, 9H). $^{13}\text{C-NMR}$ (126 MHz; CDCl_3): δ 183.0, 147.9, 141.61, 141.53, 141.3, 137.9, 136.9, 127.6, 124.3, 29.3, 27.6, 14.0, 11.3 HRMS calc m/z for $\text{C}_{21}\text{H}_{32}\text{OS}_2\text{Sn}$: $[\text{M}+\text{H}]^+$ 485.0997, found 485.0993.

Compound 3. In a 250 mL oven-dried Schlenk flask, **1** (0.240 g, 0.302 mmol), **2** (0.321 g, 0.664 mmol) and tetrakis(triphenylphosphine) palladium(0) (0.068 g, 0.0601 mmol) were placed. The flask was then degassed by three vacuum/nitrogen cycles. Degassed DMF, 40 mL was then injected into the flask and the solution mixture was stirred for 12 h at 120°C under nitrogen. After cooling to room temperature, the reaction mixture was poured into water (300 mL) with brine (30 mL). The precipitate was filtered over Celite, washed with additional water (100 mL) and the Celite was then washed with DCM until the washings were faint blue color. Residual water was removed in a separatory funnel. DCM was removed under vacuum and the product was purified by column chromatography (100% DCM) to afford **2** as a dark green solid (0.229 g, 74%). $^1\text{H-NMR}$ (500 MHz; CDCl_3): δ 9.78 (s, 2H), 8.84 (d, $J = 4.1$ Hz, 2H), 7.59 (d, $J = 3.9$ Hz, 2H), 7.22 (d, $J = 3.9$ Hz, 4H), 7.17 (t, $J = 4.5$ Hz, 4H), 3.95 (d, $J = 7.6$ Hz, 4H), 1.87 (m, 2H), 1.27-1.17 (m, 36H), 0.82-0.77 (m, 12H). $^{13}\text{C-NMR}$ (126 MHz; CDCl_3): δ 182.7, 161.7, 146.4, 142.4, 141.8, 139.5, 137.9, 137.7, 137.1, 136.6, 129.2, 127.4, 126.3, 125.6, 124.8, 109.0, 46.6, 38.3, 32.2, 31.7, 31.4, 30.1, 28.9, 26.7, 23.5, 23.0, 14.5 HRMS calc m/z for $\text{C}_{56}\text{H}_{64}\text{N}_2\text{O}_4\text{S}_6$: 1020.319, found 1020.317.

S-Amide. 3 (0.120 g, 0.117 mmol) was placed in a 100 mL flask and dissolved in CHCl_3 (20 mL). 4 (0.074 g, 0.293 mmol) and piperidine (0.116 mL, 1.17 mmol) were then added and the solution was stirred at 70 °C for 12 h. After cooling to room temperature, the solution was diluted with DCM (100 mL) and washed with 1 M HCl (30 mL). The organic phase was collected and the solvent removed under vacuum. The product was purified by column chromatography (1%MeOH/ 1%Et₃N/ DCM) to afford S-Amide as a dark green solid (0.080 g, 46%). ¹H-NMR (500 MHz; CDCl_3): δ 8.93 (d, J = 4.2 Hz, 2H), 8.34 (s, 2H), 7.61 (d, J = 4.2 Hz, 2H), 7.34 (t, J = 3.9 Hz, 4H), 7.27 (d, J = 3.9 Hz, 2H), 7.25 (d, J = 4.0 Hz, 2H), 6.23 (t, J = 5.8 Hz, 2H), 4.04 (d, J = 7.6 Hz, 4H), 3.35 (t, J = 6.0 Hz, 4H), 1.96 (m, 2H), 1.62-1.58 (m, 2H), 1.24 (m, 64H), 0.91 (m, 24H). ¹³C-NMR (126 MHz; CDCl_3): δ 161.9, 160.8, 145.2, 144.3, 141.9, 139.6, 138.6, 137.9, 137.1, 136.6, 135.6, 129.3, 127.5, 126.5, 125.8, 125.0, 117.7, 109.1, 100.0, 46.7, 44.3, 38.3, 32.19, 32.17, 31.82, 31.65, 31.4, 30.08, 29.97, 29.2, 29.0, 27.0, 26.7, 23.47, 23.34, 23.02, 23.00, 14.48, 14.44 HRMS calc m/z for C₈₆H₁₁₆N₆O₄S₆ 1488.738, found 1490.736.

S-Ester. 3 (0.110 g, 0.108 mmol) was placed in a 100 mL flask and dissolved in CHCl_3 (20 mL). 5 (0.068 mL, 0.268 mmol) and piperidine (0.106 mL, 1.08 mmol) were then added and the solution was stirred at 70 °C for 12 h. After cooling to room temperature, the solution was diluted with DCM (100 mL) and washed with 1 M HCl (30 mL). The organic phase was collected and the solvent removed under vacuum. The product was purified by column chromatography (DCM) to afford S-Ester as a dark green solid (0.120 g, 74%). ¹H-NMR (500 MHz; CDCl_3): δ 8.92 (d, J = 4.2 Hz, 2H), 8.21 (s, 2H), 7.64 (d, J = 4.1 Hz, 2H), 7.31 (d, J = 4.0 Hz, 2H), 7.28 (d, J = 4.1 Hz, 2H), 7.23 (d, J = 3.9 Hz, 4H), 4.19 (d, J = 5.8 Hz, 4H), 4.02 (d, J = 7.6 Hz, 4H), 1.95 (m, 2H), 1.76 (m, 2H), 1.34-1.24 (m, 64H), 0.88 (m, 24H). ¹³C-NMR (126 MHz; CDCl_3): δ 163.4, 161.9, 146.6, 146.2, 141.8, 139.7, 139.3, 138.2, 137.1, 136.3, 135.2, 129.4, 127.8, 126.5, 125.7, 125.0, 116.1, 109.1, 98.5, 46.7, 38.3, 37.6, 32.2, 31.64, 31.51, 31.36, 31.18, 30.08, 29.95, 29.2, 28.9, 27.0, 26.7, 23.46, 23.31, 23.02, 23.00, 14.5 HRMS calc m/z for C₈₆H₁₁₄N₄O₆S₆ 1490.706, found 1490.707.

2-Butyloctyl 4-methylbenzenesulfonate (9). In a 250 mL flask, 2-butyl-1-octanol (20 g, 107 mmol) was dissolved in 40 mL of pyridine and cooled to 0 °C. p-Toluenesulfonyl chloride (19.4 g, 102 mmol) was then added and the solution was left stirring for 12 h. The crude was poured onto 150 mL of 4 M HCl and extracted with hexane. The organic phase was dried over MgSO₄, and the solvent was removed under vacuum to afford 7 as a colorless liquid (34.88g, 96%). ¹H-NMR (500 MHz; CDCl₃): δ 7.79 (d, J = 8.3 Hz, 2H), 7.34 (d, J = 8.0 Hz, 2H), 3.91 (d, J = 5.3 Hz, 2H), 2.45 (s, 3H), 1.58 (m, 1H), 1.25-1.11 (m, 16H), 0.85 (m, 6H). ¹³C-NMR (126 MHz; CDCl₃): δ 144.9, 133.4, 130.1, 128.3, 73.2, 37.9, 32.1, 30.9, 30.6, 29.8, 29.0, 26.8, 23.2, 23.0, 22.0, 14.45, 14.34 HRMS calc m/z for C₁₉H₃₂O₃S: [M+Na]⁺ 363.1964, found 363.1964.

5-(azidomethyl)undecane (10). In a 100 mL flask, 9 (5 g, 14.68 mmol) was dissolved in DMSO (20 mL); sodium azide was then added (1.91 g, 29.4 mmol) and the solution was heated to 70 °C for 12 h. After cooling to room temperature, the crude was diluted with water (200 mL) and extracted with ethyl acetate. The organic phase was collected, dried over MgSO₄, and the solvent was removed under vacuum to afford 8 as a colorless liquid (3.10 g, 99%). ¹H-NMR (500 MHz; CDCl₃): δ 3.23 (d, J = 5.9 Hz, 2H), 1.55 (m, 1H), 1.28 (m, 16H), 0.91-0.88 (m, 6H). ¹³C-NMR (126 MHz; CDCl₃): δ 55.3, 38.2, 31.85, 31.79, 31.5, 29.6, 28.9, 26.6, 23.0, 22.7, 14.15, 14.11 HRMS not possible due to sample fragmentation under several conditions. Elemental analysis: C: calc 68.20%, found 67.85±1.5%; N: calc 19.88%, found 19.79±1.3%.

2-butyloctan-1-amine (11). In a 100 mL flask, 10 (3.10 g, 14.68 mmol) and triphenylphosphine (4.62 g, 17.6 mmol) were dissolved in THF (20 mL). The solution was heated at 70 °C for 12 h, then 5 mL of water were added and the solution was left stirring for another hour. After cooling to room temperature, the crude was concentrated under vacuum, diluted with water and extracted with DCM. The product was purified by column chromatography (5% MeOH/DCM, then 5% MeOH/5% NEt₃/ DCM) to afford 9 as a colorless liquid (2.44 g, 90%). ¹H-NMR (500 MHz; CDCl₃): δ 2.60 (d, J = 5.2 Hz, 2H), 1.45 (m, 2H), 1.26 (m, 16H), 0.91 (m, 6H). ¹³C-NMR (126 MHz; CDCl₃):

δ 45.5, 41.1, 32.3, 31.9, 31.6, 31.3, 30.1, 29.3, 27.1, 23.5, 23.0, 14.5 HRMS calc m/z for $C_{12}H_{27}N$: $[M+H]^+$ 186.2223, found 186.2216.

N-(2-butyloctyl)-2-cyanoacetamide (4). In a 250 mL flask, cyanoacetic acid (1.38 g, 16.1 mmol) was suspended in DCM (10 mL), then Et_3N (2.25 mL, 16.2 mmol) was added. Once all acid was dissolved, EDC (3.1 g, 16.2 mmol) and HOBT (1.65 g, 16.2 mmol) were added in succession. After approximately one minute, a solution of 10 (2 g, 10.78 mmol) in DCM (5 mL) was added in one portion, after which the reaction was left stirring for 12 h. The crude was diluted with DCM, and extracted with water. After collecting the organic phase, the solvent was removed under vacuum and the product was purified by column chromatography (1% MeOH/DCM) to give 10 as a clear yellow liquid (2.55 g, 94%). 1H -NMR (500 MHz; $CDCl_3$): δ 6.04 (s, 1H), 3.38 (s, 2H), 3.24 (t, $J = 6.0$ Hz, 2H), 1.53 (m, 1H), 1.27 (m, 16H), 0.89 (m, 6H). ^{13}C -NMR (126 MHz; $CDCl_3$): δ 161.0, 115.2, 77.4, 44.0, 38.1, 32.13, 32.04, 31.7, 29.9, 29.1, 26.9, 26.2, 23.3, 23.0, 14.45, 14.40 HRMS calc m/z for $C_{15}H_{28}N_2O$: 252.2202, found 252.2199.

2-Butyloctyl 2-cyanoacetate (5). In a 250 mL flask, cyanoacetic acid (1.37 g, 16.1 mmol) was suspended in DCM (10 mL), then 4-(dimethylamino)pyridinium-4-toluenesulfonate (DPTS, 4.83 g, 16.1 mmol) was added. Once all acid was dissolved, EDC (3.09 g, 16.1 mmol) was added. After approximately one minute, a solution of 2-butyl-1-octanol (2 g, 10.73 mmol) in DCM (5 mL) was added in one portion, after which the reaction was left stirring for 12 h. The crude was diluted with DCM, and extracted with water. After collecting the organic phase, the solvent was removed under vacuum and the product was purified by column chromatography (20% EtOAc/hexane) to give 11 as a colorless liquid (2.60 g, 96%). 1H -NMR (500 MHz; $CDCl_3$): δ 4.12 (d, $J = 5.8$ Hz, 2H), 3.46 (s, 2H), 1.67 (m, 1H), 1.34-1.27 (m, 16H), 0.89 (q, $J = 7.0$ Hz, 6H). ^{13}C -NMR (126 MHz; $CDCl_3$): δ 163.4, 113.3, 77.4, 70.1, 37.5, 32.1, 31.3, 31.0, 29.9, 29.2, 26.9, 25.1, 23.3, 23.0, 14.45, 14.39 HRMS calc m/z for $C_{15}H_{27}NO_2$: $[M+Na]^+$ 276.1934, found 276.1931.

Compound 6. In a 250 mL oven-dried Schlenk flask, 1 (0.510 g, 0.642 mmol), 2 (0.310 g, 0.578 mmol) and tetrakis(triphenylphosphine) palladium(0) (0.073 g, 0.065 mmol) were placed. The flask

was then degassed by three vacuum/nitrogen cycles. Degassed DMF (60 mL) was then injected into the flask and the solution mixture was stirred for 12h at 100 °C under nitrogen. After cooling to room temperature, the reaction mixture was poured into water (300 mL) with brine (30 mL). The precipitate was filtered over Celite, washed with additional water (100 mL) and the Celite was then washed with DCM until the washings were faint blue color. Residual water was removed in a separatory funnel. DCM was removed under vacuum and the product was purified by column chromatography (30%hexane/DCM) to afford 3 as a dark blue solid (0.230 g, 39%). ¹H-NMR (400 MHz; CDCl₃): δ 9.87 (s, 1H), 8.89 (d, J = 4.2 Hz, 1H), 8.61 (d, J = 4.2 Hz, 1H), 7.68 (d, J = 4.0 Hz, 1H), 7.32 (m, J = 11.7 Hz, 2H), 7.27 (d, J = 3.5 Hz, 1H), 7.25 (d, J = 4.2 Hz, 1H), 7.21 (d, J = 4.2 Hz, 1H), 4.01 (d, J = 7.7 Hz, 2H), 3.94 (d, J = 7.8 Hz, 2H), 1.90 (m, 2H), 1.26 (m, 32H), 0.85 (m, 12H). ¹³C-NMR (126 MHz; CDCl₃): δ 182.8, 161.87, 161.68, 146.4, 142.4, 142.0, 140.2, 139.2, 137.84, 137.66, 137.1, 136.7, 135.5, 131.7, 131.5, 129.1, 127.5, 126.4, 125.7, 124.9, 119.2, 108.70, 108.62, 46.64, 46.60, 38.3, 38.1, 32.17, 32.11, 31.62, 31.45, 31.33, 31.17, 30.07, 30.01, 28.90, 28.71, 26.66, 26.47, 23.44, 23.39, 23.0, 14.46, 14.39. HRMS calc m/z for C₄₇H₅₉BrN₂O₃S₄: 906.2592, found 906.2586.

Tributyl(5-phenylthiophen-2-yl)stannane (7). 2-Phenylthiophene (0.5 g, 3.12 mmol) was placed in an oven-dried 100 mL Schlenk flask and degassed by three vacuum/nitrogen cycles. Anhydrous THF (30 mL) was injected and the solution was cooled to -78 °C. N-butyllithium (1.25 mL, 2.5M in hexanes, 3.12 mmol) was then injected, and the reaction was left stirring for 30 min. Tributyltin chloride (0.841 mL, 3.12 mmol) was then injected and the cooling bath was removed. After warming to room temperature, the reaction was quenched by adding water (5 mL). The crude was then concentrated under vacuum, diluted with water (200 mL), 1 M NaOH (50 mL) and extracted with hexanes. The organic phase was collected, dried under MgSO₄, followed by solvent removal under vacuum to afford 6 as a colorless liquid (1.35 g, 96%). This compound was found to be unstable to column chromatography; if isolated, this product should be used in subsequent steps without further purification. ¹H-NMR (500 MHz; CDCl₃): δ 7.63 (d, J = 7.2 Hz, 2H), 7.43 (d, J = 3.3 Hz,

1H), 7.36 (t, J = 7.8 Hz, 3H), 7.14 (d, J = 3.3 Hz, 1H), 1.59 (m, 6H), 1.36 (m, 6H), 1.14-1.11 (m, 6H), 0.89 (m, 9H). ¹³C-NMR (126 MHz; CDCl₃): δ 150.3, 137.2, 136.8, 134.9, 129.22, 129.12, 127.4, 126.28, 126.25, 124.6, 77.4, 29.3, 27.6, 14.0, 11.2 HRMS calc m/z for C₂₂H₃₄SSn: 450.1403, found 450.1410.

Compound 8. 6 (0.230 g, 0.242 mmol), 7 (0.130 g, 0.290 mmol) and tetrakis(triphenylphosphine) palladium(0) (0.027 g, 0.024 mmol) were placed in an oven-dried 250 mL Schlenk flask. The flask was degassed by three vacuum/nitrogen cycles. Degassed DMF (40 mL) was then injected into the flask and the solution mixture was stirred for 12h at 100 °C under inert atmosphere. After cooling to room temperature, the reaction mixture was poured into water (300 mL) with brine (30 mL). The precipitate was filtered over Celite, washed with additional water (100 mL) and the Celite was then washed with DCM until the washings were faint blue color. Residual water was removed in a separatory funnel. DCM was removed under vacuum and the product was purified by column chromatography (30%hexane/DCM) to afford 4 as a dark blue solid (0.194 g, 81%). ¹H-NMR (500 MHz; CDCl₃): δ 9.86 (s, 1H), 8.96 (d, J = 4.1 Hz, 1H), 8.88 (d, J = 4.1 Hz, 1H), 7.67 (d, J = 3.8 Hz, 1H), 7.61 (d, J = 7.8 Hz, 2H), 7.40 (t, J = 7.6 Hz, 2H), 7.32-7.28 (m, 7H), 7.25 (d, J = 3.6 Hz, 1H), 4.04 (d, J = 5.9 Hz, 4H), 1.97 (m, 2H), 1.35-1.24 (m, 36H), 0.89-0.84 (m, 12H). ¹³C-NMR (126 MHz; CDCl₃): δ 182.8, 161.97, 161.81, 146.5, 145.6, 143.3, 142.4, 141.4, 140.2, 139.0, 138.0, 137.7, 137.4, 136.70, 136.51, 135.6, 133.9, 129.4, 128.4, 128.2, 127.5, 126.5, 126.2, 126.0, 125.7, 124.92, 124.83, 124.5, 109.1, 108.65, 108.62, 46.6, 38.3, 32.2, 31.7, 31.4, 30.1, 28.9, 26.7, 23.5, 23.0, 14.5 HRMS calc m/z for C₅₇H₆₆N₂O₃S₅: 986.368, found 986.371.

A-Amide. 8 (0.100 g, 0.101 mmol) was placed in a 100 mL flask and dissolved in CHCl₃ (20 mL). N-benzylcyanoacetate (0.088 g, 0.505 mmol) was added, followed by piperidine (0.200 mL, 2.00 mmol). The solution was stirred at 70 °C for 4 h. After cooling to room temperature, the solution was diluted with DCM (100 mL) and washed with 1 M HCl (30 mL). The organic phase was collected and the solvent removed under vacuum. The crude was suspended in acetonitrile and filtered, to remove excess starting material. The product was purified by column chromatography

(DCM, then 1%MeOH/DCM) to afford A-Amide as a dark blue solid (0.0383 g, 33%). $^1\text{H-NMR}$ (400 MHz; CDCl_3): δ 8.96 (d, $J = 4.2$ Hz, 1H), 8.89 (d, $J = 4.2$ Hz, 1H), 8.37 (s, 1H), 7.62-7.61 (m, 3H), 7.42-7.27 (m, 13H), 7.24 (t, $J = 2.9$ Hz, 2H), 6.54 (t, $J = 5.8$ Hz, 1H), 4.60 (d, $J = 5.7$ Hz, 2H), 4.04 (d, $J = 7.1$ Hz, 4H), 1.97 (m, 2H), 1.35-1.24 (m, 36H), 0.85 (m, 12H). $^{13}\text{C-NMR}$ (126 MHz; CDCl_3): δ 161.90, 161.76, 160.8, 145.65, 145.55, 144.7, 143.3, 141.4, 140.1, 138.95, 138.87, 138.1, 137.51, 137.47, 136.8, 136.3, 135.6, 135.4, 133.9, 129.39, 129.24, 128.43, 128.28, 127.5, 126.44, 126.29, 126.0, 125.7, 124.92, 124.89, 124.5, 117.5, 109.1, 108.6, 99.4, 46.6, 44.9, 38.34, 38.31, 32.21, 32.19, 31.7, 31.4, 30.12, 30.09, 30.06, 28.97, 28.95, 26.7, 23.5, 23.0, 14.5 HRMS calc m/z for $\text{C}_67\text{H}_{74}\text{N}_4\text{O}_3\text{S}_5$: 1142.436, found 1142.435.

A-Ester. 8 (0.0940 g, 0.0952 mmol) was placed in a 100 mL flask and dissolved in CHCl_3 (20 mL). Benzyl-cyanoacetate (0.077mL, 0.500 mmol) was added, followed by piperidine (0.200 mL, 2.00 mmol). The solution was stirred at 70 °C for 12 h. After cooling to room temperature, the solution was diluted with DCM (100 mL) and washed with 1 M HCl (30 mL). The organic phase was collected and the solvent removed under vacuum. The crude was suspended in acetonitrile and filtered, to remove excess starting material. The product was purified by column chromatography (5%hexane/DCM, then DCM) to afford A-Ester as a dark blue solid (0.0423g, 21%). $^1\text{H-NMR}$ (500 MHz; CDCl_3): δ 8.96 (d, $J = 4.2$ Hz, 1H), 8.89 (d, $J = 4.1$ Hz, 1H), 8.26 (s, 1H), 7.67 (d, $J = 3.9$ Hz, 1H), 7.62 (d, $J = 7.2$ Hz, 2H), 7.45-7.27 (m, 16H), 5.34 (s, 2H), 4.05 (d, $J = 7.0$ Hz, 4H), 1.98 (m, 2H), 1.34-1.24 (m, 36H), 0.87-0.84 (m, 12H). $^{13}\text{C-NMR}$ (126 MHz; CDCl_3): δ 162.7, 161.54, 161.40, 146.7, 146.2, 145.2, 143.0, 141.0, 139.74, 139.71, 139.4, 138.55, 138.53, 138.1, 137.2, 136.5, 135.8, 135.3, 135.1, 134.6, 133.5, 129.17, 129.08, 128.71, 128.57, 128.26, 128.11, 127.92, 127.5, 126.13, 125.99, 125.7, 125.4, 124.64, 124.56, 124.2, 115.9, 108.8, 108.3, 97.59, 97.56, 67.9, 46.3, 38.07, 38.03, 31.9, 31.4, 31.1, 29.82, 29.80, 28.67, 28.64, 26.4, 23.2, 22.7, 14.2 HRMS calc m/z for $\text{C}_67\text{H}_{73}\text{N}_3\text{O}_4\text{S}_5$: 1143.421, found 1143.423.

Cyclic Voltammetry

S-Amide, S-Ester, A-Amide and A-Ester were drop-cast from a 10mM CHCl₃ solution onto the working electrode. The thin film was immersed into anhydrous acetonitrile under Argon and scanned at a rate of 100 mV/s using 100 mM tetrabutylammonium hexafluorophosphate (NBu₄PF₆) in acetonitrile as the supporting electrolyte. The ferrocene/ferrocenium (Fc/Fc⁺) redox couple was used as an external standard and was assigned an absolute energy level of -4.8 eV vs. vacuum. Potential is reported vs. Ag/AgNO₃ (non-aqueous reference electrode). The HOMO levels were determined by the equation $\text{HOMO} = -4.8 + (\text{EoxFc/Fc}^+ - \text{EoxM})$ where EoxFc/Fc⁺ and EoxM are the onset oxidation potentials of ferrocene and M, where M = S-Amide, S-Ester, A-Amide and A-Ester. The LUMO levels were obtained by the equation $\text{LUMO} = -4.8 + (\text{EoxFc/Fc}^+ - \text{EredM})$, where EredM are the onset reduction potentials of M. The CV traces for all four molecules show quasireversible oxidation waves in the region of 0.5-1 V. The reduction potentials occur in the -1 V region and present reversible behavior for all four molecules, but S-Amide presented a pre-reduction wave that made assigning a reduction potential difficult; for this reason, the difference in E_g reported in the manuscript for S-Amide and S-Ester is approximately 0.4 eV, even though their onset absorption would seem to indicate they should have nearly identical values for E_g.

Infrared Spectroscopy

Films of S-Amide, S-Ester, A-Amide, A-Ester, precursor 4 and N-benzyl-2-cyanoacetamide were cast from a 10 mM CHCl₃ solution on a Ge crystal. Films of blends were prepared by drop-casting 10mg/mL chlorobenzene solutions of S-Amide, S-Ester, A-Amide and A-Ester with PCBM in a 1:1 weight ratio onto a Ge crystal. Although drop-casting blends does not reproduce device conditions exactly, we feel the results shown can be extrapolated to spin-coated conditions with sufficient accuracy. Attenuated total reflectance (ATR) spectra were offset for clarity. Hydrogen bonding can be detected by FTIR when the C=O and N-H stretching vibrations shift to lower wavenumbers when hydrogen bonding is present. The C=O stretch could not be unambiguously assigned, as three peaks

of similar intensity appear in the region of 1650 cm^{-1} . The N-H stretching peak is the weak peak at 3440 cm^{-1} for S-Amide and 3360 cm^{-1} for A-Amide. The relatively low signal is mainly due to N-H being a single bond, among the much more abundant C=C and C-H stretching signals (from thiophene and alkyl tails, respectively). S-Ester was a special case in the sense that it presented a broad shoulder in the amide region, which we attribute to abnormal background subtraction caused by the poor film quality when drop-cast from CHCl_3 ; in the later films from chlorobenzene (with PCBM), where the quality of the film was slightly better, the shoulder disappears. As mentioned in the text, to investigate the effect of conjugation on the strength of hydrogen bonding, S-Amide and A-Amide were compared with the precursors **4** and N-benzyl-2-cyanoacetamide, respectively. Precursor **4** shows the N-H stretching as a broad peak at 3300 cm^{-1} and N-benzyl-2-cyanoacetamide at 3310 cm^{-1} . The close up views show the precursors **4** and N-benzyl-2-cyanoacetate having the N-H stretch at lower wavenumbers than S-Amide and A-Amide, respectively, which is a sign that upon conjugation to a chromophore, the strength of the hydrogen bonding ability decreases. Lastly, the blends with PCBM show the N-H signal unchanged upon mixing donor and acceptor, which is a good indication of hydrogen bonding for A-Amide, and as mentioned in the manuscript, no significant hydrogen bonding for S-Amide. Since the blends were drop-cast from chlorobenzene, they had to be air dried, which increased the CO_2 signal, as can be seen in the region of 2360 cm^{-1} in the PCBM blends. Although we expected all amides to be able to hydrogen bond, we believe S-Amide was not able to do so because the π - π stacking dominated the assembly; also, the terminal alkyl tails were branched, and being flexible, could have interfered with the otherwise favorable hydrogen bonding.

UV-Vis Spectroscopy

Extinction coefficient was determined by UV-Vis in standard solutions of the four molecules at 0.1, 0.05, 0.025 and 0.0125 mM in CHCl_3 , and the average of the four spectra was plotted; film studies were done using two conditions, drop-casting from 10mM CHCl_3 solutions, to test the maximum

degree of aggregation, and spin-coating with PCBM under device conditions with the maximum PCE.

Devices

Experimental conditions for active layer deposition such as solvent, concentration and solvent composition were optimized. Pre-patterned indium-doped tin oxide (ITO) on glass was used as the transparent bottom electrode. The ITO was scrubbed with soapy water and cleaned by ultrasonically sequentially in hexanes, soapy water, water, and a 1:1:1 solution of acetone/methanol/2-propanol. The electrode was then blown dry in a N₂ stream and transferred into a N₂ glovebox (O₂ and H₂O < 0.1 ppm). Before active layer coating, MoOx (10 nm) was thermally evaporated on ITO surface as the interfacial layer. Bulk heterojunction photovoltaic devices were fabricated from blends of donor small molecule and acceptor phenyl-C₇₁-butyric acid methyl ester (PC₇₁BM). In the optimized conditions, donor/acceptor ratio is fixed to 1:1, with a total solution concentration of 22 mg/ml in chlorobenzene. Films were cast by spin-coating at 2000 rpm in the glovebox for 60 s and annealed on a hot plate at 100°C for 5 minutes. Total organic layer thickness ranged from 60-70 nm as determined by AFM. Devices were completed by thermally evaporating 1 nm of LiF then 100 nm of Al through a shadow mask at 1 x 10⁻⁶ mbar to yield devices of 4 mm² in area and sealed with a UV-curable epoxy if needed. The devices for space-charge-limited-current (SCLC) measurements were fabricated with a similar procedure. Hole transport layer were replaced with PEDOT:PSS (Clevios P VP Al 4083) and the top electrode is replaced with Au (50 nm) rather than LiF/Al in order to suppress electron injection.

Hole mobility were estimated using the data showed in Fig. 4.12 with the following equation:

$$J = \frac{9}{8} \frac{\epsilon \mu_0}{L^3} V^2 \quad (1)$$

where J is current, ϵ is relative permittivity of the material (assumed as 3 for most organic materials), L is the thickness of the film, V is the applied voltage and μ is the mobility. For the absolute

Sample	Thickness (nm)
A-Amide	70
A-Amide + NitroBenzene	100
A-Ester	75
A-Ester +DIO	90

Table 4.7: Thicknesses of active layer blends measured with AFM

voltage, the voltage drop across the ITO due to series resistance (V_{RS}) and built in voltage (V_{BI}) was subtracted from the applied voltage.⁶⁹ The only remaining unknown L , the thickness of active layer, was measured with AFM (Table 4.7). These results were used to determine the hole mobility of each active layer.

Microscopy

AFM measurements were either performed on the fabricated solar cell device or on a separate sample prepared with the same spin coating parameters used for device on a freshly cleaved mica substrate. AFM images are processed with WSxM software. Samples for conventional transmission electron microscopy (TEM) were prepared by fishing the active layer that floats on water onto a copper TEM grid. To float the active layer in water a sacrificial PEDOT:PSS layer is coated on a glass and active layer is spin coated on PEDOT:PSS layer.

GIXD

GIXD samples were prepared on silicon chips by spin coating donor/acceptor solutions with the same conditions used for devices. All samples were illuminated with X-ray for a short period of time (1-2 s) with an incident angle of 0.2° .

Orientational distribution of the crystallographic features can be quantitatively described in terms of an orientational order parameter S (Herman's orientation parameter). Where separate orientational parameters f_{\perp} and f_{\parallel} used to represent the orientation of polymeric crystallites,

respectively, along the plane of the film surface and along the axis normal to the surface are determined from the geometrically corrected scattered intensity. S can be calculated by knowing f_{\perp} (eq.1) which is calculated with the cosine function (eq. 2) as given below.

$$S = \frac{1}{2}(3f_{\perp} - 1) \quad (2)$$

$$3f_{\perp} = \langle \cos^2 \chi \rangle = \frac{\int_0^{\pi/2} I(\chi)(\cos^2 \chi)(\sin \chi) d\chi}{\int_0^{\pi/2} I(\chi)(\sin \chi) d\chi} \quad (3)$$

From a practical perspective, S is a quantity that varies between -0.5 and 1, where value of 1 (-0.5) indicates parallel (orthogonal) orientation of the normal of a crystallographic plane relative to substrate normal. Conversely, a completely isotropic distribution of the crystallographic planes leads to an S value of 0.

5 SUMMARY AND FUTURE OUTLOOK

The work in this thesis presents a link between molecular design and self-assembly of organic donor dyes and their influences on microstructure and organic solar cell device performance. We showed that the shape of tripodal small molecule with triphenylamine core and diketopyrrolopyrrole chromophores can be used to study the effect of self-assembly on solar cells (Chapter 2). Despite having similar optoelectronic properties, these two homologous dyes gave generated different film morphology and device performance. For the same dye, branched alkyl solubilizing chains inhibit the self-assembly of these tripodal molecules, while linear side chains promote the self-assembly of one-dimensional nanowires. These nanowires increased the solar cell performance 50% compared to non-assembling tripodal molecules owing to a significant gain in fill factor. This improvement was attributed to nanowires reducing trap states in the active layer.

Apart from molecular shape, we showed that hydrogen bonding can be used to direct the assembly of hairpin-shaped donor molecules to form one-dimensional nanowires (Chapter 3). Self-assembly of the nanowires were result of a synergistic action of hydrogen bonds and $\pi - \pi$ stacking. The assembly found to be dependent on the processing conditions which is using stepwise cooling and minimal stirring of solutions to promote self-assembly of robust wires. In the case of continuous stirring without the controlled heat treatment the device efficiency was 400-fold less compared to nanowire case. In addition, the devices from the long nanowires were 54% more efficient than those built with analogous donor molecules containing on the the conjugated structure.

Synergistic action of hydrogen bonding with $\pi - \pi$ stacking was useful however, the overall device efficiency in such systems remained low due to large domain size. The true potential of hydrogen bonding was discovered when used in a competing fashion with $\pi - \pi$ stacking (Chapter 4). Competing hydrogen bonding is achieved in a linear and asymmetric electron donor small molecules with amide groups. Replacement of amide to an ester in the same molecule allowed studying the effect of hydrogen bonding exclusively. While the optoelectronic properties of amide

and ester derivatives were found to be similar in solution, large morphological differences between them in solar cell active layers was found. In the amide version, hydrogen bonding interactions compete effectively with long range $\pi - \pi$ stacking of the conjugated molecules and resulting in inter-connected and smaller nanoscale donor domains relative to ester derivative. This difference in morphology of amide derivative yielded in greater short circuit current and 50% improvement in solar cell efficiency compared to devices formed with the ester derivative.

Based on the results presented in Chapter 2, it was shown that non-planar conjugated parts have potential to sterically hinder and prevent $\pi - \pi$ stacking. This approach can be useful in designing new acceptor molecules for OPVs. The common acceptor molecule that is used is PCBM that has an ability to intercalate between crystalline donor domains due to its amorphous nature. This is important for high efficient OPV systems because the donor domains in their active layer are usually more ordered and crystalline. Such donor domains need to be filled and surrounded with more amorphous and easily mixing acceptor domains. For that reason, one of the most important features of a newly designed acceptor molecule is its ability to not to assemble strongly. In addition, high cost of PCBM is not desirable to achieve the goal of more affordable OPVs and hence the new acceptor molecules should be much cheaper. We believe both of this problems can be addressed by perylene monoimides: they are small and cheap conjugated molecules with decent absorption and more importantly they can be easily functionalized with non-planar groups to prevent stacking.²⁵⁴ If our current efforts have a promising outcome, this can be a translatable to next generation OPV devices.

Based on the results presented in Chapter 4, we found out that it is very crucial to shrink the domain size in the active layer for DPP based molecules to obtain high efficiency. Although the approach shown here focuses on donor-donor molecule interactions, we assumed that we can benefit from favorable donor-acceptor interactions to achieve smaller domain size for DPP systems. Favorable donor-acceptor interactions can be achieved with functional groups on an additional donor molecules that can act similar to organic solvents such as chlorobenzene.²⁵⁵ Our initial efforts in

utilizing a third component with chlorobenzene functional groups gave promising results with an enhanced OPV performance. We believe this strategy can provide instructive guidelines for further development in the field of ternary blend OPVs.

REFERENCES

1. Edenhofer, O. *et al.* *Renewable Energy Sources and Climate Change Mitigation: Special Report of the Intergovernmental Panel on Climate Change* en (Cambridge University Press, Nov. 2011).
2. *International Energy Outlook 2013* 2013.
3. *International Energy Outlook 2011*
4. *Hidden Costs of Energy: Unpriced Consequences of Energy Production and Use* (National Academies Press, Washington, D.C., May 2010).
5. Darling, S. B. & You, F. The case for organic photovoltaics. en. *RSC Advances* **3**, 17633–17648 (2013).
6. Gil, A. *et al.* State of the art on high temperature thermal energy storage for power generation. Part 1 — Concepts, materials and modellization. *Renewable and Sustainable Energy Reviews* **14**, 31–55 (2010).
7. Thirugnanasambandam, M., Iniyan, S. & Goic, R. A review of solar thermal technologies. *Renewable and Sustainable Energy Reviews* **14**, 312–322 (2010).
8. Gust, D., Moore, T. A. & Moore, A. L. Solar Fuels via Artificial Photosynthesis. *Accounts of Chemical Research* **42**, 1890–1898 (2009).
9. NREL: National Center for Photovoltaics Home Page
10. NREL: Photovoltaics Research - Silicon Materials and Devices R&D
11. Darling, S. B., You, F., Veselka, T. & Velosa, A. Assumptions and the levelized cost of energy for photovoltaics. en. *Energy & Environmental Science* **4**, 3133–3139 (2011).
12. Powell, D. M. *et al.* Crystalline silicon photovoltaics: a cost analysis framework for determining technology pathways to reach baseload electricity costs. en. *Energy & Environmental Science* **5**, 5874–5883 (2012).
13. Kalowekamo, J. & Baker, E. Estimating the manufacturing cost of purely organic solar cells. *Solar Energy* **83**, 1224–1231 (2009).
14. Espinosa, N., Hösel, M., Angmo, D. & Krebs, F. C. Solar cells with one-day energy payback for the factories of the future. en. *Energy Environ. Sci.* **5**, 5117–5132 (2012).
15. Fthenakis, V. M. & Kim, H. C. Photovoltaics: Life-cycle analyses. *Solar Energy. Progress in Solar Energy* **1** **85**, 1609–1628 (2011).
16. Raugei, M., Bargigli, S. & Ulgiati, S. Life cycle assessment and energy pay-back time of advanced photovoltaic modules: CdTe and CIS compared to poly-Si. *Energy* **32**, 1310–1318 (2007).
17. Liang, Y. *et al.* For the Bright Future — Bulk Heterojunction Polymer Solar Cells with Power Conversion Efficiency of 7.4%. en. *Advanced Materials* **22**, E135–E138 (2010).

18. Yue, D., Khatav, P., You, F. & Darling, S. B. Deciphering the uncertainties in life cycle energy and environmental analysis of organic photovoltaics. en. *Energy & Environmental Science* **5**, 9163–9172 (2012).
19. Zhang, S., Ye, L. & Hou, J. Breaking the 10% Efficiency Barrier in Organic Photovoltaics: Morphology and Device Optimization of Well-Known PBDTTT Polymers. en. *Advanced Energy Materials*, NA–NA (2016).
20. Scharber, M. C. & Sariciftci, N. S. Efficiency of bulk-heterojunction organic solar cells. *Progress in Polymer Science. Topical issue on Conductive Polymers* **38**, 1929–1940 (2013).
21. Nicholson, P. G. & Castro, F. A. Organic photovoltaics: principles and techniques for nanometre scale characterization. en. *Nanotechnology* **21**, 492001 (2010).
22. Su, Y.-W., Lan, S.-C. & Wei, K.-H. Organic photovoltaics. en. *Materials Today* **15**, 554–562 (2012).
23. Li, G., Zhu, R. & Yang, Y. Polymer solar cells. en. *Nature Photonics* **6**, 153–161 (2012).
24. Peumans, P., Yakimov, A. & Forrest, S. R. Small molecular weight organic thin-film photodetectors and solar cells. *Journal of Applied Physics* **93**, 3693–3723 (2003).
25. Scully, S. R. & McGehee, M. D. Effects of optical interference and energy transfer on exciton diffusion length measurements in organic semiconductors. *Journal of Applied Physics* **100**, 034907 (2006).
26. Shaw, P. E., Ruseckas, A. & Samuel, I. D. W. Exciton Diffusion Measurements in Poly(3-hexylthiophene). en. *Advanced Materials* **20**, 3516–3520 (2008).
27. Hoppe, H. & Sariciftci, N. S. Organic solar cells: An overview. *Journal of Materials Research* **19**, 1924–1945 (2004).
28. Jao, M.-H., Liao, H.-C. & Su, W.-F. Achieving a high fill factor for organic solar cells. en. *Journal of Materials Chemistry A* **4**, 5784–5801 (2016).
29. Hu, L. *et al.* Highly efficient alternating photocurrent from interactive organic – radical dimers: A novel light-harvesting mechanism for optoelectronic conversion. *Chemical Physics Letters* **484**, 177–180 (2010).
30. *Solar Spectral Irradiance: Air Mass 1.5*
31. Beliatis, M. J. *et al.* Organic solar cells with plasmonic layers formed by laser nanofabrication. en. *Physical Chemistry Chemical Physics* **15**, 8237–8244 (2013).
32. Gruber, M. *et al.* Thermodynamic Efficiency Limit of Molecular Donor-Acceptor Solar Cells and its Application to Diindenoperylene/C60-Based Planar Heterojunction Devices. en. *Advanced Energy Materials* **2**, 1100–1108 (2012).
33. Scharber, M. C. *et al.* Design Rules for Donors in Bulk-Heterojunction Solar Cells — Towards 10% Energy-Conversion Efficiency. en. *Advanced Materials* **18**, 789–794 (2006).
34. Cheng, Y.-J., Yang, S.-H. & Hsu, C.-S. Synthesis of Conjugated Polymers for Organic Solar Cell Applications. *Chemical Reviews* **109**, 5868–5923 (2009).

35. Van Mullekom, H. A. M., Vekemans, J. A. J. M., Havinga, E. E. & Meijer, E. W. Developments in the chemistry and band gap engineering of donor – acceptor substituted conjugated polymers. *Materials Science and Engineering: R: Reports* **32**, 1–40 (2001).
36. Bakulin, A. A. *et al.* The Role of Driving Energy and Delocalized States for Charge Separation in Organic Semiconductors. en. *Science* **335**, 1340–1344 (2012).
37. Peet, J. *et al.* Efficiency enhancement in low-bandgap polymer solar cells by processing with alkane dithiols. en. *Nature Materials* **6**, 497–500 (2007).
38. Hou, J., Chen, H.-Y., Zhang, S., Li, G. & Yang, Y. Synthesis, Characterization, and Photovoltaic Properties of a Low Band Gap Polymer Based on Silole-Containing Polythiophenes and 2,1,3-Benzothiadiazole. *Journal of the American Chemical Society* **130**, 16144–16145 (2008).
39. Small, C. E. *et al.* High-efficiency inverted dithienogermole-thienopyrrolodione-based polymer solar cells. en. *Nature Photonics* **6**, 115–120 (2012).
40. Zhou, H. *et al.* Development of Fluorinated Benzothiadiazole as a Structural Unit for a Polymer Solar Cell of 7.8% Efficiency. en. *Angewandte Chemie International Edition* **50**, 2995–2998 (2011).
41. He, Z. *et al.* Single-junction polymer solar cells with high efficiency and photovoltage. en. *Nature Photonics* **9**, 174–179 (2015).
42. Loser, S. *et al.* A Naphthodithiophene-Diketopyrrolopyrrole Donor Molecule for Efficient Solution-Processed Solar Cells. *Journal of the American Chemical Society* **133**, 8142–8145 (2011).
43. Sun, Y. *et al.* Solution-processed small-molecule solar cells with 6.7% efficiency. en. *Nature Materials* **11**, 44–48 (2012).
44. Cui, C. *et al.* High-Performance Organic Solar Cells Based on a Small Molecule with Alkylthio-Thienyl-Conjugated Side Chains without Extra Treatments. en. *Advanced Materials* **27**, 7469–7475 (2015).
45. Zhang, Q. *et al.* Small-molecule solar cells with efficiency over 9%. en. *Nature Photonics* **9**, 35–41 (2015).
46. Wienk, M. M. *et al.* Efficient Methano[70]fullerene/MDMO-PPV Bulk Heterojunction Photovoltaic Cells. en. *Angewandte Chemie International Edition* **42**, 3371–3375 (2003).
47. Guo, X. *et al.* High efficiency polymer solar cells based on poly(3-hexylthiophene)/indene-C70 bisadduct with solvent additive. en. *Energy & Environmental Science* **5**, 7943–7949 (2012).
48. Liao, S.-H., Li, Y.-L., Jen, T.-H., Cheng, Y.-S. & Chen, S.-A. Multiple Functionalities of Polyfluorene Grafted with Metal Ion-Intercalated Crown Ether as an Electron Transport Layer for Bulk-Heterojunction Polymer Solar Cells: Optical Interference, Hole Blocking, Interfacial Dipole, and Electron Conduction. *Journal of the American Chemical Society* **134**, 14271–14274 (2012).
49. Shoaee, S. *et al.* Charge Photogeneration for a Series of Thiazolo-Thiazole Donor Polymers Blended with the Fullerene Electron Acceptors PCBM and ICBA. en. *Advanced Functional Materials* **23**, 3286–3298 (2013).

50. Kang, T. E. *et al.* Photoinduced Charge Transfer in Donor – Acceptor (DA) Copolymer: Fullerene Bis-adduct Polymer Solar Cells. *ACS Applied Materials & Interfaces* **5**, 861–868 (2013).
51. Gomez, E. D. & Loo, Y.-L. Engineering the organic semiconductor-electrode interface in polymer solar cells. en. *Journal of Materials Chemistry* **20**, 6604–6611 (2010).
52. Hains, A. W., Liu, J., Martinson, A. B. F., Irwin, M. D. & Marks, T. J. Anode Interfacial Tuning via Electron-Blocking/Hole-Transport Layers and Indium Tin Oxide Surface Treatment in Bulk-Heterojunction Organic Photovoltaic Cells. en. *Advanced Functional Materials* **20**, 595–606 (2010).
53. Irwin, M. D. *et al.* Consequences of Anode Interfacial Layer Deletion. HCl-Treated ITO in P₃HT:PCBM-Based Bulk-Heterojunction Organic Photovoltaic Devices. *Langmuir* **26**, 2584–2591 (2010).
54. Rockett, A. *The Materials Science of Semiconductors* en (Springer Science & Business Media, Nov. 2007).
55. Yip, H.-L. & Jen, A. K.-Y. Recent advances in solution-processed interfacial materials for efficient and stable polymer solar cells. en. *Energy & Environmental Science* **5**, 5994–6011 (2012).
56. He, Y., Zhang, J., Hou, S., Wang, Y. & Yu, Z. Schottky barrier formation at metal electrodes and semiconducting carbon nanotubes. *Applied Physics Letters* **94**, 093107 (2009).
57. Liu, Z., Kobayashi, M., Paul, B. C., Bao, Z. & Nishi, Y. Contact engineering for organic semiconductor devices via Fermi level depinning at the metal-organic interface. *Physical Review B* **82**, 035311 (2010).
58. Ishii, H., Sugiyama, K., Ito, E. & Seki, K. Energy Level Alignment and Interfacial Electronic Structures at Organic/Metal and Organic/Organic Interfaces. en. *Advanced Materials* **11**, 605–625 (1999).
59. Braun, S., Salaneck, W. R. & Fahlman, M. Energy-Level Alignment at Organic/Metal and Organic/Organic Interfaces. en. *Advanced Materials* **21**, 1450–1472 (2009).
60. Jin, S.-H. *et al.* Optimization of process parameters for high-efficiency polymer photovoltaic devices based on P₃HT PCBM system. *Solar Energy Materials and Solar Cells* **91**, 1187–1193 (2007).
61. Kim, Y. *et al.* Organic Photovoltaic Devices Based on Blends of Regioregular Poly(3-hexylthiophene) and Poly(9,9-dioctylfluorene-co-benzothiadiazole). *Chemistry of Materials* **16**, 4812–4818 (2004).
62. Huang, C. J., Grozea, D., Turak, A. & Lu, Z. H. Passivation effect of Al-LiF electrode on C₆₀ diodes. *Applied Physics Letters* **86**, 033107 (2005).
63. Lee, C. H., Yu, G., Moses, D., Heeger, A. J. & Srdanov, V. I. Nonlinear transient photovoltaic response in Al C₆₀ Au devices: Control of polarity with optical bias. *Applied Physics Letters* **65**, 664–666 (1994).

64. Hamed, A., Sun, Y. Y., Tao, Y. K., Meng, R. L. & Hor, P. H. Effects of oxygen and illumination on the in situ conductivity of C₆₀ thin films. *Physical Review B* **47**, 10873–10880 (1993).
65. Brabec, C. J., Shaheen, S. E., Winder, C., Sariciftci, N. S. & Denk, P. Effect of LiF/metal electrodes on the performance of plastic solar cells. *Applied Physics Letters* **80**, 1288–1290 (2002).
66. Tseng, W.-H. *et al.* Investigations of efficiency improvements in poly(3-hexylthiophene) based organic solar cells using calcium cathodes. *Solar Energy Materials and Solar Cells* **95**, 3424–3427 (2011).
67. He, Z. *et al.* Simultaneous Enhancement of Open-Circuit Voltage, Short-Circuit Current Density, and Fill Factor in Polymer Solar Cells. *en. Advanced Materials* **23**, 4636–4643 (2011).
68. He, Z. *et al.* Enhanced power-conversion efficiency in polymer solar cells using an inverted device structure. *en. Nature Photonics* **6**, 591–595 (2012).
69. Mihailetschi, V. D., Xie, H. X., de Boer, B., Koster, L. J. A. & Blom, P. W. M. Charge Transport and Photocurrent Generation in Poly(3-hexylthiophene): Methanofullerene Bulk- Heterojunction Solar Cells. *en. Advanced Functional Materials* **16**, 699–708 (2006).
70. Friedel, B. *et al.* Effects of Layer Thickness and Annealing of PEDOT:PSS Layers in Organic Photodetectors. *Macromolecules* **42**, 6741–6747 (2009).
71. Tong, S. W. *et al.* Improvement in the hole collection of polymer solar cells by utilizing gold nanoparticle buffer layer. *Chemical Physics Letters* **453**, 73–76 (2008).
72. Lindquist, N. C., Luhan, W. A., Oh, S.-H. & Holmes, R. J. Plasmonic nanocavity arrays for enhanced efficiency in organic photovoltaic cells. *Applied Physics Letters* **93**, 123308 (2008).
73. Meyer, J., Khalandovsky, R., Görrn, P. & Kahn, A. MoO₃ Films Spin-Coated from a Nanoparticle Suspension for Efficient Hole-Injection in Organic Electronics. *en. Advanced Materials* **23**, 70–73 (2011).
74. Krebs, F. C. Air stable polymer photovoltaics based on a process free from vacuum steps and fullerenes. *Solar Energy Materials and Solar Cells. Degradation and Stability of Polymer and Organic Solar Cells* **92**, 715–726 (2008).
75. Lobez, J. M., Andrew, T. L., Bulović, V. & Swager, T. M. Improving the Performance of P₃HT – Fullerene Solar Cells with Side-Chain-Functionalized Poly(thiophene) Additives: A New Paradigm for Polymer Design. *ACS Nano* **6**, 3044–3056 (2012).
76. Kodali, H. K. & Ganapathysubramanian, B. Computer simulation of heterogeneous polymer photovoltaic devices. *Modelling and Simulation in Materials Science and Engineering* **20**, 35015–35033 (2012).
77. Chen, W., Nikiforov, M. P. & Darling, S. B. Morphology characterization in organic and hybrid solar cells. *en. Energy & Environmental Science* **5**, 8045–8074 (2012).
78. Moon, J. S., Lee, J. K., Cho, S., Byun, J. & Heeger, A. J. “Columnlike” Structure of the Cross-Sectional Morphology of Bulk Heterojunction Materials. *Nano Letters* **9**, 230–234 (2009).
79. Herzing, A. A., Richter, L. J. & Anderson, I. M. 3D Nanoscale Characterization of Thin-Film Organic Photovoltaic Device Structures via Spectroscopic Contrast in the TEM 1. *The Journal of Physical Chemistry C* **114**, 17501–17508 (2010).

80. Kozub, D. R. *et al.* Polymer Crystallization of Partially Miscible Polythiophene/Fullerene Mixtures Controls Morphology. *Macromolecules* **44**, 5722–5726 (2011).
81. Bavel, S. v., Sourty, E., With, G. d., Veenstra, S. & Loos, J. Three-dimensional nanoscale organization of polymer solar cells. en. *Journal of Materials Chemistry* **19**, 5388–5393 (2009).
82. Garcia, R. & Pérez, R. Dynamic atomic force microscopy methods. *Surface Science Reports* **47**, 197–301 (2002).
83. Dante, M., Peet, J. & Nguyen, T.-Q. Nanoscale Charge Transport and Internal Structure of Bulk Heterojunction Conjugated Polymer / Fullerene Solar Cells by Scanning Probe Microscopy. *The Journal of Physical Chemistry C* **112**, 7241–7249 (2008).
84. Groves, C., Reid, O. G. & Ginger, D. S. Heterogeneity in Polymer Solar Cells: Local Morphology and Performance in Organic Photovoltaics Studied with Scanning Probe Microscopy. *Accounts of Chemical Research* **43**, 612–620 (2010).
85. Sirringhaus, H. *et al.* Two-dimensional charge transport in self-organized, high-mobility conjugated polymers. en. *Nature* **401**, 685–688 (1999).
86. Herman, D. J., Goldberger, J. E., Chao, S., Martin, D. T. & Stupp, S. I. Orienting Periodic Organic–Inorganic Nanoscale Domains Through One-Step Electrodeposition. *ACS Nano* **5**, 565–573 (2011).
87. Wu, W.-R. *et al.* Competition between Fullerene Aggregation and Poly(3-hexylthiophene) Crystallization upon Annealing of Bulk Heterojunction Solar Cells. *ACS Nano* **5**, 6233–6243 (2011).
88. Kiel, J. W., Eberle, A. P. R. & Mackay, M. E. Nanoparticle Agglomeration in Polymer-Based Solar Cells. *Physical Review Letters* **105**, 168701 (2010).
89. Padinger, F., Rittberger, R. & Sariciftci, N. Effects of Postproduction Treatment on Plastic Solar Cells. en. *Advanced Functional Materials* **13**, 85–88 (2003).
90. Ng, A. *et al.* Annealing of P₃HT:PCBM Blend Film — The Effect on Its Optical Properties. *ACS Applied Materials & Interfaces* **5**, 4247–4259 (2013).
91. Lloyd, M. T., Anthony, J. E. & Malliaras, G. G. Photovoltaics from soluble small molecules. *Materials Today* **10**, 34–41 (2007).
92. Wang, X. *et al.* High-Resolution Spectroscopic Mapping of the Chemical Contrast from Nanometer Domains in P₃HT:PCBM Organic Blend Films for Solar-Cell Applications. en. *Advanced Functional Materials* **20**, 492–499 (2010).
93. Li, G. *et al.* High-efficiency solution processable polymer photovoltaic cells by self organization of polymer blends. en. *Nature Materials* **4**, 864–868 (2005).
94. Zhao, Y., Xie, Z., Qu, Y., Geng, Y. & Wang, L. Solvent-vapor treatment induced performance enhancement of poly(3-hexylthiophene):methanofullerene bulk-heterojunction photovoltaic cells. *Applied Physics Letters* **90**, 043504 (2007).
95. Zhou, H. *et al.* High-Efficiency Polymer Solar Cells Enhanced by Solvent Treatment. en. *Advanced Materials* **25**, 1646–1652 (2013).

96. Lee, J. K. *et al.* Processing Additives for Improved Efficiency from Bulk Heterojunction Solar Cells. *Journal of the American Chemical Society* **130**, 3619–3623 (2008).
97. Lou, S. J. *et al.* Effects of Additives on the Morphology of Solution Phase Aggregates Formed by Active Layer Components of High-Efficiency Organic Solar Cells. *Journal of the American Chemical Society* **133**, 20661–20663 (2011).
98. Kim, Y., Yeom, H. R., Kim, J. Y. & Yang, C. High-efficiency polymer solar cells with a cost-effective quinoxaline polymer through nanoscale morphology control induced by practical processing additives. en. *Energy & Environmental Science* **6**, 1909–1916 (2013).
99. Chen, H.-Y. *et al.* Fast-Grown Interpenetrating Network in Poly(3-hexylthiophene): Methanofullerenes Solar Cells Processed with Additive. *The Journal of Physical Chemistry C* **113**, 7946–7953 (2009).
100. Szarko, J. M. *et al.* When Function Follows Form: Effects of Donor Copolymer Side Chains on Film Morphology and BHJ Solar Cell Performance. en. *Advanced Materials* **22**, 5468–5472 (2010).
101. Osaka, I., Saito, M., Koganezawa, T. & Takimiya, K. Thiophene – Thiazolothiazole Copolymers: Significant Impact of Side Chain Composition on Backbone Orientation and Solar Cell Performances. en. *Advanced Materials* **26**, 331–338 (2014).
102. Liang, Y. *et al.* Conjugated block copolymers and co-oligomers: from supramolecular assembly to molecular electronics. en. *Journal of Materials Chemistry* **17**, 2183–2194 (2007).
103. Babu, S. S., Möhwald, H. & Nakanishi, T. Recent progress in morphology control of supramolecular fullerene assemblies and its applications. en. *Chemical Society Reviews* **39**, 4021–4035 (2010).
104. Mativetsky, J. M., Wang, H., Lee, S. S., Whittaker-Brooks, L. & Loo, Y.-L. Face-on stacking and enhanced out-of-plane hole mobility in graphene-templated copper phthalocyanine. en. *Chemical Communications* **50**, 5319–5321 (2014).
105. Geng, Y. *et al.* A theoretical discussion on the relationships among molecular packings, intermolecular interactions, and electron transport properties for naphthalene tetracarboxylic diimide derivatives. en. *Journal of Materials Chemistry* **21**, 15558–15566 (2011).
106. Jo, S. B., Lee, W. H., Qiu, L. & Cho, K. Polymer blends with semiconducting nanowires for organic electronics. en. *Journal of Materials Chemistry* **22**, 4244–4260 (2012).
107. Kim, J.-H. *et al.* Organic Solar Cells Based on Three-Dimensionally Percolated Polythiophene Nanowires with Enhanced Charge Transport. *ACS Applied Materials & Interfaces* **6**, 5640–5650 (2014).
108. Dou, L. *et al.* 25th Anniversary Article: A Decade of Organic/Polymeric Photovoltaic Research. en. *Advanced Materials* **25**, 6642–6671 (2013).
109. Gunes, S., Neugebauer, H. & Sariciftci, N. S. Conjugated Polymer-Based Organic Solar Cells. *Chemical Reviews* **107**, 1324–1338 (2007).

110. Li, W., Furlan, A., Hendriks, K. H., Wienk, M. M. & Janssen, R. A. J. Efficient Tandem and Triple-Junction Polymer Solar Cells. *Journal of the American Chemical Society* **135**, 5529–5532 (2013).
111. Liu, Y. *et al.* Aggregation and morphology control enables multiple cases of high-efficiency polymer solar cells. en. *Nature Communications* **5**, 5293 (2014).
112. Brabec, C. J. *et al.* Polymer – Fullerene Bulk-Heterojunction Solar Cells. en. *Advanced Materials* **22**, 3839–3856 (2010).
113. Mishra, A. & Bäuerle, P. Small Molecule Organic Semiconductors on the Move: Promises for Future Solar Energy Technology. en. *Angewandte Chemie International Edition* **51**, 2020–2067 (2012).
114. Hoppe, H. & Sariciftci, N. S. Morphology of polymer/fullerene bulk heterojunction solar cells. en. *Journal of Materials Chemistry* **16**, 45–61 (2006).
115. Nguyen, L. H. *et al.* Effects of Annealing on the Nanomorphology and Performance of Poly (alkylthiophene) : Fullerene Bulk-Heterojunction Solar Cells. en. *Advanced Functional Materials* **17**, 1071–1078 (2007).
116. Peet, J., Senatore, M. L., Heeger, A. J. & Bazan, G. C. Bulk Heterojunction Solar Cells: The Role of Processing in the Fabrication and Optimization of Plastic Solar Cells (Adv. Mater. 14 – 15/2009). en. *Advanced Materials* **21**, 1521–1527 (2009).
117. Wei, G., Wang, S., Sun, K., Thompson, M. E. & Forrest, S. R. Solvent-Annealed Crystalline Squaraine: PC70BM (1:6) Solar Cells. en. *Advanced Energy Materials* **1**, 184–187 (2011).
118. Hoven, C. *et al.* Improved Performance of Polymer Bulk Heterojunction Solar Cells Through the Reduction of Phase Separation via Solvent Additives. *Advanced Materials* **22**, E63–E66 (2010).
119. Beaujuge, P. M. & Fréchet, J. M. J. Molecular Design and Ordering Effects in π -Functional Materials for Transistor and Solar Cell Applications. *Journal of the American Chemical Society* **133**, 20009–20029 (2011).
120. Wang, M. & Wudl, F. Top-down meets bottom-up: organized donor – acceptor heterojunctions for organic solar cells. en. *Journal of Materials Chemistry* **22**, 24297–24314 (2012).
121. Schmidt-Mende, L. *et al.* Self-Organized Discotic Liquid Crystals for High-Efficiency Organic Photovoltaics. en. *Science* **293**, 1119–1122 (2001).
122. Feng, X. *et al.* Supramolecular Organization and Photovoltaics of Triangle-shaped Discotic Graphenes with Swallow-tailed Alkyl Substituents. *Advanced Materials* **20**, 2684–2689 (2008).
123. Carrasco-Orozco, M. *et al.* New Photovoltaic Concept: Liquid-Crystal Solar Cells Using a Nematic Gel Template. *Advanced Materials* **18**, 1754–1758 (2006).
124. Sun, Q., Park, K. & Dai, L. Liquid Crystalline Polymers for Efficient Bilayer- Bulk- Heterojunction Solar Cells. *The Journal of Physical Chemistry C* **113**, 7892–7897 (2009).
125. Guo, C. *et al.* Conjugated Block Copolymer Photovoltaics with near 3% Efficiency through Microphase Separation. *Nano Letters* **13**, 2957–2963 (2013).

126. Kang, S. J. *et al.* A Supramolecular Complex in Small-Molecule Solar Cells based on Contorted Aromatic Molecules. en. *Angewandte Chemie International Edition* **51**, 8594–8597 (2012).
127. Lin, Y. *et al.* Cooperative Assembly of Hydrogen-Bonded Diblock Copolythiophene/Fullerene Blends for Photovoltaic Devices with Well-Defined Morphologies and Enhanced Stability. *Chemistry of Materials* **24**, 622–632 (2012).
128. Xin, H., Kim, F. S. & Jenekhe, S. A. Highly Efficient Solar Cells Based on Poly(3-butylthiophene) Nanowires. *Journal of the American Chemical Society* **130**, 5424–5425 (2008).
129. Tevis, I. D., Tsai, W.-W., Palmer, L. C., Aytun, T. & Stupp, S. I. Grooved Nanowires from Self-Assembling Hairpin Molecules for Solar Cells. *ACS Nano* **6**, 2032–2040 (2012).
130. Ruiz-Carretero, A. *et al.* Stepwise self-assembly to improve solar cell morphology. en. *Journal of Materials Chemistry A* **1**, 11674–11681 (2013).
131. Aytun, T., Barreda, L., Ruiz-Carretero, A., Lehrman, J. A. & Stupp, S. I. Improving Solar Cell Efficiency through Hydrogen Bonding: A Method for Tuning Active Layer Morphology. *Chemistry of Materials* **27**, 1201–1209 (2015).
132. Zhou, J. *et al.* Solution-Processed and High-Performance Organic Solar Cells Using Small Molecules with a Benzodithiophene Unit. *Journal of the American Chemical Society* **135**, 8484–8487 (2013).
133. Kyaw, A. K. K. *et al.* Improved Light Harvesting and Improved Efficiency by Insertion of an Optical Spacer (ZnO) in Solution-Processed Small-Molecule Solar Cells. *Nano Letters* **13**, 3796–3801 (2013).
134. Walker, B. *et al.* Nanoscale Phase Separation and High Photovoltaic Efficiency in Solution-Processed, Small-Molecule Bulk Heterojunction Solar Cells. en. *Advanced Functional Materials* **19**, 3063–3069 (2009).
135. Lee, O. P. *et al.* Efficient Small Molecule Bulk Heterojunction Solar Cells with High Fill Factors via Pyrene-Directed Molecular Self-Assembly. en. *Advanced Materials* **23**, 5359–5363 (2011).
136. De Bettignies, R. *et al.* Planarized Star-Shaped Oligothiophenes as a New Class of Organic Semiconductors for Heterojunction Solar Cells. en. *Advanced Materials* **15**, 1939–1943 (2003).
137. Ripaud, E., Rousseau, T., Leriche, P. & Roncali, J. Unsymmetrical Triphenylamine-Oligothiophene Hybrid Conjugated Systems as Donor Materials for High-Voltage Solution-Processed Organic Solar Cells. en. *Advanced Energy Materials* **1**, 540–545 (2011).
138. Hu, Z. *et al.* Synthesis and photovoltaic properties of solution-processable star-shaped small molecules with triphenylamine as the core and alkyl cyanoacetate or 3-ethylrhodanine as the end-group. en. *RSC Advances* **4**, 5591–5597 (2014).
139. Lin, Y., Zhang, Z.-G., Bai, H., Li, Y. & Zhan, X. A star-shaped oligothiophene end-capped with alkyl cyanoacetate groups for solution-processed organic solar cells. en. *Chemical Communications* **48**, 9655–9657 (2012).
140. Min, J. *et al.* Alkyl Chain Engineering of Solution-Processable Star-Shaped Molecules for High-Performance Organic Solar Cells. *Advanced Energy Materials* **4**, 1301234 (2014).

141. Chandran, D. & Lee, K.-S. Diketopyrrolopyrrole: A versatile building block for organic photovoltaic materials. *Macromolecular Research* **21**, 272–283 (2013).
142. Thelakkat, M. Star-Shaped, Dendrimeric and Polymeric Triarylaminines as Photoconductors and Hole Transport Materials for Electro-Optical Applications. en. *Macromolecular Materials and Engineering* **287**, 442–461 (2002).
143. Faramarzi, V. *et al.* Light-triggered self-construction of supramolecular organic nanowires as metallic interconnects. en. *Nature Chemistry* **4**, 485–490 (2012).
144. Lin, Y., Cheng, P., Li, Y. & Zhan, X. A 3D star-shaped non-fullerene acceptor for solution-processed organic solar cells with a high open-circuit voltage of 1.18 V. en. *Chemical Communications* **48**, 4773–4775 (2012).
145. Pan, J.-Y. *et al.* Star-Shaped D – A Small Molecules Based on Diketopyrrolopyrrole and Triphenylamine for Efficient Solution-Processed Organic Solar Cells. *ACS Applied Materials & Interfaces* **5**, 972–980 (2013).
146. Tang, A. *et al.* Significant improvement of photovoltaic performance by embedding thiophene in solution-processed star-shaped TPA-DPP backbone. en. *Journal of Materials Chemistry A* **1**, 5747–5757 (2013).
147. Hess, B., Kutzner, C., van der Spoel, D. & Lindahl, E. GROMACS 4: Algorithms for Highly Efficient, Load-Balanced, and Scalable Molecular Simulation. *Journal of Chemical Theory and Computation* **4**, 435–447 (2008).
148. Autiero, I., Saviano, M. & Langella, E. Molecular dynamics simulations of PNA – PNA and PNA – DNA duplexes by the use of new parameters implemented in the GROMACS package: a conformational and dynamics study. en. *Physical Chemistry Chemical Physics* **16**, 1868–1874 (2014).
149. Keasar, C. & Rosenfeld, R. Empirical modifications to the Amber/OPLS potential for predicting the solution conformations of cyclic peptides by vacuum calculations. English. *Folding and Design* **3**, 379–388 (1998).
150. Norin, M., Haeffner, F., Hult, K. & Edholm, O. Molecular dynamics simulations of an enzyme surrounded by vacuum, water, or a hydrophobic solvent. *Biophysical Journal* **67**, 548–559 (1994).
151. Su, M.-S. *et al.* Improving Device Efficiency of Polymer/Fullerene Bulk Heterojunction Solar Cells Through Enhanced Crystallinity and Reduced Grain Boundaries Induced by Solvent Additives. en. *Advanced Materials* **23**, 3315–3319 (2011).
152. Proctor, C. M., Love, J. A. & Nguyen, T.-Q. Mobility Guidelines for High Fill Factor Solution-Processed Small Molecule Solar Cells. en. *Advanced Materials* **26**, 5957–5961 (2014).
153. Mihailitchi, V. *et al.* Electron Transport in a Methanofullerene. en. *Advanced Functional Materials* **13**, 43–46 (2003).
154. Bisquert, J. & Mora-Seró, I. Simulation of Steady-State Characteristics of Dye-Sensitized Solar Cells and the Interpretation of the Diffusion Length. *The Journal of Physical Chemistry Letters* **1**, 450–456 (2010).

155. Guerrero, A., Ripolles-Sanchis, T., Boix, P. P. & Garcia-Belmonte, G. Series resistance in organic bulk-heterojunction solar devices: Modulating carrier transport with fullerene electron traps. *Organic Electronics* **13**, 2326–2332 (2012).
156. Pisula, W., Feng, X. & Müllen, K. Tuning the Columnar Organization of Discotic Polycyclic Aromatic Hydrocarbons. en. *Advanced Materials* **22**, 3634–3649 (2010).
157. Arikainen, E. O. *et al.* Effects of side-chain length on the charge transport properties of discotic liquid crystals and their implications for the transport mechanism. en. **5**, 2161–2165 (1995).
158. Bunk, O., Nielsen, M. M., Sølling, T. I., van de Craats, A. M. & Stutzmann, N. Induced Alignment of a Solution-Cast Discotic Hexabenzocoronene Derivative for Electronic Devices Investigated by Surface X-ray Diffraction. *Journal of the American Chemical Society* **125**, 2252–2258 (2003).
159. Lee, J.-H., Choi, S.-M., Pate, B. D., Chisholm, M. H. & Han, Y.-S. Magnetic uniaxial alignment of the columnar superstructure of discotic metallomesogens over the centimetre length scale. **16**, 2785–2791 (2006).
160. Tracz, A. *et al.* Uniaxial Alignment of the Columnar Super-Structure of a Hexa (Alkyl) Hexaperi-hexabenzocoronene on Untreated Glass by Simple Solution Processing. *Journal of the American Chemical Society* **125**, 1682–1683 (2003).
161. Kempe, M. D., Scruggs, N. R., Verduzco, R., Lal, J. & Kornfield, J. A. Self-assembled liquid-crystalline gels designed from the bottom up. *Nature Materials* **3**, 177–182 (2004).
162. Asdonk, P. v. d., Keshavarz, M., M. Christianen, P. C. & J. Kouwer, P. H. Directed peptide amphiphile assembly using aqueous liquid crystal templates in magnetic fields. *Soft Matter* **12**, 6518–6525 (2016).
163. Shklyarevskiy, I. O. *et al.* High Anisotropy of the Field-Effect Transistor Mobility in Magnetically Aligned Discotic Liquid-Crystalline Semiconductors. *Journal of the American Chemical Society* **127**, 16233–16237 (2005).
164. Feng, X. *et al.* Scalable Fabrication of Polymer Membranes with Vertically Aligned 1 nm Pores by Magnetic Field Directed Self-Assembly. *ACS Nano* **8**, 11977–11986 (2014).
165. J. Jurow, M. *et al.* Controlling morphology and molecular packing of alkane substituted phthalocyanine blend bulk heterojunction solar cells. *Journal of Materials Chemistry A* **1**, 1557–1565 (2013).
166. Dao, Q. D. *et al.* Efficiency enhancement in mesogenic-phthalocyanine-based solar cells with processing additives. *Applied Physics Letters* **101**, 263301 (2012).
167. N, A. T., M, A. K. & Pai, R. K. Hexagonal columnar liquid crystals as a processing additive to a P3HT:PCBM photoactive layer. *New Journal of Chemistry* **39**, 8439–8445 (2015).
168. Sun, K. *et al.* A molecular nematic liquid crystalline material for high-performance organic photovoltaics. *Nature Communications* **6**, 6013 (2015).

169. Jorgensen, W. L., Maxwell, D. S. & Tirado-Rives, J. Development and Testing of the OPLS All-Atom Force Field on Conformational Energetics and Properties of Organic Liquids. *Journal of the American Chemical Society* **118**, 11225–11236 (1996).
170. *Contributors* (ed Yaws, C. L.) viii (William Andrew Publishing, Norwich, NY, 2009).
171. Caleman, C. *et al.* Force Field Benchmark of Organic Liquids: Density, Enthalpy of Vaporization, Heat Capacities, Surface Tension, Isothermal Compressibility, Volumetric Expansion Coefficient, and Dielectric Constant. *Journal of Chemical Theory and Computation* **8**, 61–74 (2012).
172. Chatterjee, S., Debenedetti, P. G., Stillinger, F. H. & Lynden-Bell, R. M. A computational investigation of thermodynamics, structure, dynamics and solvation behavior in modified water models. *The Journal of Chemical Physics* **128**, 124511 (2008).
173. *Densities of Halohydrocarbons* en (eds Frenkel, M. & Marsh, K. N.) (Springer-Verlag, Berlin/Heidelberg, 2003).
174. Blom, P. W. M., Mihailetschi, V. D., Koster, L. J. A. & Markov, D. E. Device Physics of Polymer:Fullerene Bulk Heterojunction Solar Cells. en. *Advanced Materials* **19**, 1551–1566 (2007).
175. Yang, F., Shtein, M. & Forrest, S. R. Controlled growth of a molecular bulk heterojunction photovoltaic cell. en. *Nature Materials* **4**, 37–41 (2004).
176. Bijleveld, J. C., Verstrijden, R. A. M., Wienk, M. M. & Janssen, R. A. J. Copolymers of diketopyrrolopyrrole and thienothiophene for photovoltaic cells. en. *Journal of Materials Chemistry* **21**, 9224–9231 (2011).
177. Wienk, M. M., Turbiez, M., Gilot, J. & Janssen, R. A. J. Narrow-Bandgap Diketo-Pyrrolo-Pyrrole Polymer Solar Cells: The Effect of Processing on the Performance. en. *Advanced Materials* **20**, 2556–2560 (2008).
178. Wienk, M. M., Struijk, M. P. & Janssen, R. A. J. Low band gap polymer bulk heterojunction solar cells. *Chemical Physics Letters* **422**, 488–491 (2006).
179. Tamayo, A. B., Walker, B. & Nguyen*, T.-Q. A Low Band Gap, Solution Processable Oligothiophene with a Diketopyrrolopyrrole Core for Use in Organic Solar Cells. *The Journal of Physical Chemistry C* **112**, 11545–11551 (2008).
180. Zhou, J. *et al.* Small Molecules Based on Benzo[1,2-b:4,5-b']dithiophene Unit for High-Performance Solution-Processed Organic Solar Cells. *Journal of the American Chemical Society* **134**, 16345–16351 (2012).
181. Thompson, B. C. & Fréchet, J. M. J. Polymer – Fullerene Composite Solar Cells. en. *Angewandte Chemie International Edition* **47**, 58–77 (2008).
182. Sofos, M. *et al.* A synergistic assembly of nanoscale lamellar photoconductor hybrids. en. *Nature Materials* **8**, 68–75 (2008).
183. Palmer, L. C. & Stupp, S. I. Molecular Self-Assembly into One-Dimensional Nanostructures. *Accounts of Chemical Research* **41**, 1674–1684 (2008).

184. Van der Poll, T. S., Love, J. A., Nguyen, T.-Q. & Bazan, G. C. Non-Basic High-Performance Molecules for Solution-Processed Organic Solar Cells. en. *Advanced Materials* **24**, 3646–3649 (2012).
185. Wicklein, A., Ghosh, S., Sommer, M., Würthner, F. & Thelakkat, M. Self-Assembly of Semiconductor Organogelator Nanowires for Photoinduced Charge Separation. *ACS Nano* **3**, 1107–1114 (2009).
186. Bürckstümmer, H., Weissenstein, A., Bialas, D. & Würthner, F. Synthesis and Characterization of Optical and Redox Properties of Bithiophene-Functionalized Diketopyrrolopyrrole Chromophores. *The Journal of Organic Chemistry* **76**, 2426–2432 (2011).
187. Kimura, M. *et al.* Photochemical Behavior of Zinc(II) Tetraphenylporphyrin in Nanoscale-fibers Made of *trans*-1,2-Bis(alkylamide)cyclohexane Derivatives. *Chemistry Letters* **29**, 1088–1089 (2000).
188. Kobayashi, S. *et al.* Preparation of Helical Transition-Metal Oxide Tubes Using Organogelators as Structure-Directing Agents. *Journal of the American Chemical Society* **124**, 6550–6551 (2002).
189. Hanabusa, K., Yamada, M., Kimura, M. & Shirai, H. Prominent Gelation and Chiral Aggregation of Alkylamides Derived from *trans*-1,2-Diaminocyclohexane. en. *Angewandte Chemie International Edition in English* **35**, 1949–1951 (1996).
190. Pal, A., Besenius, P. & Sijbesma, R. P. Self-Sorting in Rodlike Micelles of Chiral Bisurea Bolaamphiphiles. *Journal of the American Chemical Society* **133**, 12987–12989 (2011).
191. Tsai, W.-W., Tevis, I. D., Tayi, A. S., Cui, H. & Stupp, S. I. Semiconducting Nanowires from Hairpin-Shaped Self-Assembling Sexithiophenes. *The Journal of Physical Chemistry B* **114**, 14778–14786 (2010).
192. Tamayo, A. B., Tantiwiwat, M., Walker, B. & Nguyen, T.-Q. Design, Synthesis, and Self-assembly of Oligothiophene Derivatives with a Diketopyrrolopyrrole Core. *The Journal of Physical Chemistry C* **112**, 15543–15552 (2008).
193. Karsten, B. P. & Janssen, R. A. J. Chain Length Dependence in Diketopyrrolopyrrole/Thiophene Oligomers. en. *Macromolecular Chemistry and Physics* **212**, 515–520 (2011).
194. Oostergetel, G. T., Esselink, F. J. & Hadziioannou, G. Cryo-Electron Microscopy of Block Copolymers in an Organic Solvent. *Langmuir* **11**, 3721–3724 (1995).
195. Imahori, H. *et al.* Hydrogen Bonding Effects on the Surface Structure and Photoelectrochemical Properties of Nanostructured SnO₂ Electrodes Modified with Porphyrin and Fullerene Composites. *The Journal of Physical Chemistry B* **109**, 18465–18474 (2005).
196. Sagawa, T., Yoshikawa, S. & Imahori, H. One-Dimensional Nanostructured Semiconducting Materials for Organic Photovoltaics. *The Journal of Physical Chemistry Letters* **1**, 1020–1025 (Apr. 2010).
197. Huang, C.-H., McClenaghan, N. D., Kuhn, A., Hofstraat, J. W. & Bassani, D. M. Enhanced Photovoltaic Response in Hydrogen-Bonded All-Organic Devices. *Organic Letters* **7**, 3409–3412 (2005).

198. Huang, C.-H., McClenaghan, N. D., Kuhn, A., Bravic, G. & Bassani, D. M. Hierarchical self-assembly of all-organic photovoltaic devices. *Tetrahedron. Supramolecular Chemistry of Fullerenes* **62**, 2050–2059 (2006).
199. Hasobe, T. *et al.* Organic solar cells. Supramolecular composites of porphyrins and fullerenes organized by polypeptide structures as light harvesters. en. *Journal of Materials Chemistry* **17**, 4160–4170 (2007).
200. Jørgensen, M., Norrman, K. & Krebs, F. C. Stability/degradation of polymer solar cells. *Solar Energy Materials and Solar Cells. Degradation and Stability of Polymer and Organic Solar Cells* **92**, 686–714 (2008).
201. Sánchez, L., Martín, N. & Guldi, D. M. Hydrogen-Bonding Motifs in Fullerene Chemistry. en. *Angewandte Chemie International Edition* **44**, 5374–5382 (2005).
202. Walker, B. *et al.* A Systematic Approach to Solvent Selection Based on Cohesive Energy Densities in a Molecular Bulk Heterojunction System. en. *Advanced Energy Materials* **1**, 221–229 (2011).
203. Vandewal, K., Tvingstedt, K., Gadisa, A., Inganäs, O. & Manca, J. V. On the origin of the open-circuit voltage of polymer – fullerene solar cells. en. *Nature Materials* **8**, 904–909 (2009).
204. Lin, Y., Li, Y. & Zhan, X. Small molecule semiconductors for high-efficiency organic photovoltaics. en. *Chemical Society Reviews* **41**, 4245–4272 (2012).
205. You, J. *et al.* A polymer tandem solar cell with 10.6% power conversion efficiency. en. *Nature Communications* **4**, 1446 (2013).
206. Jo, J. *et al.* Enhanced Efficiency of Single and Tandem Organic Solar Cells Incorporating a Diketopyrrolopyrrole-Based Low-Bandgap Polymer by Utilizing Combined ZnO/Polyelectrolyte Electron-Transport Layers. en. *Advanced Materials* **25**, 4783–4788 (Sept. 2013).
207. Li, K. *et al.* Development of Large Band-Gap Conjugated Copolymers for Efficient Regular Single and Tandem Organic Solar Cells. *Journal of the American Chemical Society* **135**, 13549–13557 (2013).
208. Hendriks, K. H., Heintges, G. H. L., Gevaerts, V. S., Wienk, M. M. & Janssen, R. A. J. High-Molecular-Weight Regular Alternating Diketopyrrolopyrrole-based Terpolymers for Efficient Organic Solar Cells. en. *Angewandte Chemie International Edition* **52**, 8341–8344 (2013).
209. Zhang, M. *et al.* Efficient Polymer Solar Cells Based on Benzothiadiazole and Alkylphenyl Substituted Benzodithiophene with a Power Conversion Efficiency over 8%. en. *Advanced Materials* **25**, 4944–4949 (2013).
210. Roncali, J. Molecular Bulk Heterojunctions: An Emerging Approach to Organic Solar Cells. *Accounts of Chemical Research* **42**, 1719–1730 (2009).
211. Walker, B., Kim, C. & Nguyen, T.-Q. Small Molecule Solution-Processed Bulk Heterojunction Solar Cells. *Chemistry of Materials* **23**, 470–482 (2011).
212. Stupp, S. I. & Palmer, L. C. Supramolecular Chemistry and Self-Assembly in Organic Materials Design. *Chemistry of Materials* **26**, 507–518 (2014).

213. Aida, T., Meijer, E. W. & Stupp, S. I. Functional Supramolecular Polymers. en. *Science* **335**, 813–817 (2012).
214. He, G. *et al.* Efficient small molecule bulk heterojunction solar cells with high fill factors via introduction of π -stacking moieties as end group. en. *Journal of Materials Chemistry A* **1**, 1801–1809 (2013).
215. Kim, K.-H. *et al.* Influence of intermolecular interactions of electron donating small molecules on their molecular packing and performance in organic electronic devices. en. *Journal of Materials Chemistry A* **1**, 14538–14547 (2013).
216. Xiao, Z. *et al.* Hydrogen bonding in bulk heterojunction solar cells: A case study. *Scientific Reports* **4** (2014).
217. Yassin, A., Leriche, P., Allain, M. & Roncali, J. Donor – acceptor – donor (D – A – D) molecules based on isoindigo as active material for organic solar cells. en. *New Journal of Chemistry* **37**, 502–507 (2013).
218. Siram, R. B. K., Stephen, M., Ali, F. & Patil, S. Investigation of Phase Separation in Bulk Heterojunction Solar Cells via Supramolecular Chemistry. *The Journal of Physical Chemistry C* **117**, 9129–9136 (2013).
219. Schulze, B. M. *et al.* Consequences of hydrogen bonding on molecular organization and charge transport in molecular organic photovoltaic materials. en. *Journal of Materials Chemistry A* **2**, 1541–1549 (2013).
220. Kumar, R. J., Subbiah, J. & Holmes, A. B. Enhancement of efficiency in organic photovoltaic devices containing self-complementary hydrogen-bonding domains. en. *Beilstein Journal of Organic Chemistry* **9**, 1102–1110 (2013).
221. Tevis, I. D. *et al.* Self-Assembly and Orientation of Hydrogen-Bonded Oligothiophene Polymorphs at Liquid – Membrane – Liquid Interfaces. *Journal of the American Chemical Society* **133**, 16486–16494 (2011).
222. Stone, D. A., Tayi, A. S., Goldberger, J. E., Palmer, L. C. & Stupp, S. I. Self-assembly and conductivity of hydrogen-bonded oligothiophene nanofiber networks. en. *Chemical Communications* **47**, 5702–5704 (2011).
223. Hill, J. P. *et al.* Self-Assembled Hexa-peri-hexabenzocoronene Graphitic Nanotube. en. *Science* **304**, 1481–1483 (2004).
224. Jonkheijm, P. *et al.* Transfer of π -Conjugated Columnar Stacks from Solution to Surfaces. *Journal of the American Chemical Society* **125**, 15941–15949 (2003).
225. Matmour, R. *et al.* Oligo(p-phenylenevinylene)–Peptide Conjugates: Synthesis and Self-Assembly in Solution and at the Solid–Liquid Interface. *Journal of the American Chemical Society* **130**, 14576–14583 (2008).
226. Li, W., Roelofs, W. S. C., Wienk, M. M. & Janssen, R. A. J. Enhancing the Photocurrent in Diketopyrrolopyrrole-Based Polymer Solar Cells via Energy Level Control. *Journal of the American Chemical Society* **134**, 13787–13795 (2012).

227. Qu, S. & Tian, H. Diketopyrrolopyrrole (DPP)-based materials for organic photovoltaics. en. *Chemical Communications* **48**, 3039–3051 (2012).
228. Peng, Q. *et al.* Enhanced solar cell performance by replacing benzodithiophene with naphthodithiophene in diketopyrrolopyrrole-based copolymers. en. *Chemical Communications* **48**, 11452–11454 (2012).
229. Chen, Y., Wan, X. & Long, G. High Performance Photovoltaic Applications Using Solution-Processed Small Molecules. *Accounts of Chemical Research* **46**, 2645–2655 (2013).
230. Hoeben, F. J. M., Jonkheijm, P., Meijer, E. W. & Schenning, A. P. H. J. About Supramolecular Assemblies of π -Conjugated Systems. *Chemical Reviews* **105**, 1491–1546 (2005).
231. Skrovanek, D. J., Howe, S. E., Painter, P. C. & Coleman, M. M. Hydrogen bonding in polymers: infrared temperature studies of an amorphous polyamide. *Macromolecules* **18**, 1676–1683 (1985).
232. Chang, L., Lademann, H. W. A., Bonekamp, J.-B., Meerholz, K. & Moulé, A. J. Effect of Trace Solvent on the Morphology of P₃HT:PCBM Bulk Heterojunction Solar Cells. en. *Advanced Functional Materials* **21**, 1779–1787 (2011).
233. Nikiforov, M. P. *et al.* Detection and role of trace impurities in high-performance organic solar cells. en. *Energy & Environmental Science* **6**, 1513–1520 (2013).
234. Qi, B. & Wang, J. Fill factor in organic solar cells. en. *Physical Chemistry Chemical Physics* **15**, 8972–8982 (2013).
235. Lee, J. W., Choi, Y. S. & Jo, W. H. Diketopyrrolopyrrole-based small molecules with simple structure for high VOC organic photovoltaics. *Organic Electronics* **13**, 3060–3066 (2012).
236. Liu, F. *et al.* Relating Chemical Structure to Device Performance via Morphology Control in Diketopyrrolopyrrole-Based Low Band Gap Polymers. *Journal of the American Chemical Society* **135**, 19248–19259 (2013).
237. Müller-Buschbaum, P. The Active Layer Morphology of Organic Solar Cells Probed with Grazing Incidence Scattering Techniques. en. *Advanced Materials* **26**, 7692–7709 (2014).
238. Lilliu, S. *et al.* Dynamics of Crystallization and Disorder during Annealing of P₃HT/PCBM Bulk Heterojunctions. *Macromolecules* **44**, 2725–2734 (2011).
239. Rivnay, J. *et al.* Structural origin of gap states in semicrystalline polymers and the implications for charge transport. *Physical Review B* **83**, 121306 (2011).
240. Hindeleh, A. M. & Hosemann, R. Paracrystals representing the physical state of matter. en. *Journal of Physics C: Solid State Physics* **21**, 4155 (1988).
241. Gao, J. *et al.* Elucidating Double Aggregation Mechanisms in the Morphology Optimization of Diketopyrrolopyrrole-Based Narrow Bandgap Polymer Solar Cells. en. *Advanced Materials* **26**, 3142–3147 (2014).
242. Rogers, J. T., Schmidt, K., Toney, M. F., Bazan, G. C. & Kramer, E. J. Time-Resolved Structural Evolution of Additive-Processed Bulk Heterojunction Solar Cells. *Journal of the American Chemical Society* **134**, 2884–2887 (2012).

243. Noriega, R. *et al.* A general relationship between disorder, aggregation and charge transport in conjugated polymers. en. *Nature Materials* **12**, 1038–1044 (2013).
244. Collins, B. A. *et al.* Absolute Measurement of Domain Composition and Nanoscale Size Distribution Explains Performance in PTB7:PC71BM Solar Cells. en. *Advanced Energy Materials* **3**, 65–74 (2013).
245. Trewin, A. & Cooper, A. I. Porous Organic Polymers: Distinction from Disorder? en. *Angewandte Chemie International Edition* **49**, 1533–1535 (Feb. 2010).
246. Côté, A. P., El-Kaderi, H. M., Furukawa, H., Hunt, J. R. & Yaghi, O. M. Reticular Synthesis of Microporous and Mesoporous 2D Covalent Organic Frameworks. *Journal of the American Chemical Society* **129**, 12914–12915 (Oct. 2007).
247. Nagai, A. *et al.* Pore surface engineering in covalent organic frameworks. en. *Nature Communications* **2**, 536 (2011).
248. Pachfule, P., Kandmabeth, S., Mallick, A. & Banerjee, R. Hollow tubular porous covalent organic framework (COF) nanostructures. en. *Chemical Communications* **51**, 11717–11720 (2015).
249. Zhang, K.-D. *et al.* Toward a Single-Layer Two-Dimensional Honeycomb Supramolecular Organic Framework in Water. *Journal of the American Chemical Society* **135**, 17913–17918 (2013).
250. Hong, J.-P., Um, M.-C., Nam, S.-R., Hong, J.-I. & Lee, S. Organic single-nanofiber transistors from organogels. *Chemical Communications*, 310–312 (2009).
251. Sugiyasu, K., Kawano, S.-i., Fujita, N. & Shinkai, S. Self-Sorting Organogels with p–n Heterojunction Points. *Chemistry of Materials* **20**, 2863–2865 (2008).
252. Theobald, J. A., Oxtoby, N. S., Phillips, M. A., Champness, N. R. & Beton, P. H. Controlling molecular deposition and layer structure with supramolecular surface assemblies. en. *Nature* **424**, 1029–1031 (2003).
253. Xu, J., He, C., Toh, K. C. & Lu, X. Intermolecular Interaction in Multicomponent Supramolecular Complexes through Hydrogen-Bonding Association. *Macromolecules* **35**, 8846–8851 (2002).
254. Li, C. *et al.* Rainbow Perylene Monoimides: Easy Control of Optical Properties. en. *Chemistry – A European Journal* **15**, 878–884 (2009).
255. Park, S. *et al.* Enhancement of Organic Photovoltaic Efficiency via Nanomorphology Control using Conjugated Polymers Incorporating Fullerene Compatible Side-Chains. *Macromolecules* **48**, 337–345 (2015).

VITA

TANER AYTUN

2220 Campus Drive, Evanston, IL 60208 • 773-677-5970 • taner@u.northwestern.edu

EDUCATION

-
- Northwestern University, McCormick School of Engineering, Evanston, IL** December 2016
 Ph. D. candidate in Materials Science and Engineering, GPA: 3.71
 Dissertation: Self-assembly of Small Molecule Donors for Organic Photovoltaic Applications
 Advisor: Samuel Isaac Stupp, Ph.D.
- Northwestern University, Kellogg School of Management, Evanston, IL** Summer 2014
 Completed a highly selective summer program in Management for Scientists and Engineers
 Topics included: Strategy, Finance, Risk and Uncertainty, Intellectual Property, Marketing, Accounting, and Leadership
- Sabanci University, Istanbul, Turkey** June 2010
 M. S. in Materials Science and Engineering, GPA: 3.72
 Thesis: Building Lithium Fluoride Nanoparticle Films for Organic Photovoltaics
 Advisor: Cleva Ow-Yang, Ph.D.
- Sabanci University, Istanbul, Turkey** June 2008
 B. S. in Materials Science and Engineering, Cumulative GPA: 3.65; Minor: Chemistry, GPA: 3.94

RESEARCH and WORK EXPERIENCE

-
- Research Assistant**, Northwestern University, Evanston, IL Nov. 2010-Nov. 2016
 The Stupp Laboratory, PI: Samuel. I. Stupp, Ph.D.
- Develop new materials and self-assembly strategies for 20-50% more efficient and organic solar cells
 - Study self-assembly, microstructure and optoelectronic properties of new donor molecules and the effects on solar performance
 - Write solar energy-related sections for U.S. Department of Energy research grant
 - Write proposals for X-ray experiments at Advance Photon Source of Argonne National Lab
 - Published 6 peer-reviewed articles in high impact journals, submitted 3 manuscripts
- Research Assistant**, Sabanci University, Istanbul, TURKEY Sep. 2008-June 2010
 Ow-Yang Laboratory, PI: Cleva Ow-Yang, Ph.D.
- Utilized diblock copolymer micelles to synthesize lithium fluoride nanoparticles for the first time in literature
 - Studied assembly of particles in 2D arrays on various substrates and transfer printing arrays of sub-10 nanometer nanoparticles
 - Co-authored and wrote reports for \$70,000 research grant and authored the proposal for \$13,500 research grant
 - Published 5 peer-reviewed articles in high impact journals
- Visiting Scientist**, Max Planck Institute for Metals Research, GERMANY Summer 2009 & Feb. 2010
 Low Dimensional Metastable Materials Department, Supervisor: Ayse Turak, Ph.D.
- Explored electronic properties of lithium fluoride nanoparticle film, and used it to improve organic solar cell efficiency
 - Received stipend support \$4000 from the Institute and published 3 articles in collaboration with Ow-Yang
- Undergraduate Research Assistant**, Sabanci University, Istanbul, TURKEY
 March 2006 – June 2008
- Utilized diblock copolymer micelles to synthesize inorganic nanoparticles, studied coating, size and optical properties
 - Performed atomic force microscope to evaluate size and map mechanical properties
 - Presented the work in national and international conferences and published 2 peer-reviewed articles
- Student Intern**, NV Bekaert SA, Zvevegem, BELGIUM Summer 2007
 Bekaert Technology Center, Materials Science Department, PI: Guy Anne, Ph.D.
- Designed and conducted experiments to quantify phase transformation in pearlitic steels with surface characterization techniques (Auger photoelectron spectroscopy and X-ray photoelectron spectroscopy)
 - Analyzed the data and revised the characterization strategy, delivered presentations and reports to company executive

TEACHING EXPERIENCE

Teaching Assistant, Northwestern University Dept. of Materials Science and Engineering, Evanston, IL
Fall 2013& 2014

Course Name: *Microstructural Dynamics*

- Held weekly office hours to guide junior level students, graded homework and gave feedback, taught special topic lecture
- Organized the lab materials and provided technical support, coordinated students

Teaching Assistant, Sabanci University Dept. of Materials Science and Engineering, Istanbul, TURKEY
Spring 2009& 2010

Course Name: *Electrical, Optical and Magnetic Properties of Materials*

- Held weekly recitation sessions and office hours to discuss class material and to guide problem solving
- Graded homework, monitored individual student progress to motivate and to improve learning, gave feedbacks to professor

Teaching Assistant, Sabanci University Dept. of Materials Science and Engineering, Istanbul, TURKEY
Fall 2009

Course Name: *Materials Characterization*

- Held part of the labs, gave assignments and graded reports. Managed other teaching assistants and their labs
- Coordinated 5 professors and scheduled lecture times, prepared and graded exams

Teaching Assistant, Sabanci University Dept. of Materials Science and Engineering, Istanbul, TURKEY
Fall 2008

Course Name: *Thermodynamics of Materials*

- Held weekly recitation sessions and office hours to discuss class material and to guide problem solving
- Coordinated minilab sessions, graded homework and exams

Teaching Assistant, Sabanci University Dept. of Materials Science and Engineering, Istanbul, TURKEY
Fall 2007

Course Name: *Introduction to Materials Science and Engineering*

- Designed and implemented new laboratory experiments for 150 students taking the class, collected and graded reports
- Attended the recitation session of missing teaching assistants, manage discussion and solved the problems

Peer Assistant, Sabanci University Academic Support Program, Istanbul, TURKEY Fall 2004

Course Name: *Science of Nature*

- Led 20 freshmen students per classes twice weekly in discussion, lecture, and problem solving as well as holding office hours once a week for 2 years

Volunteer, Sabanci University Civic Involvement Project, Istanbul, TURKEY 2003-2004

- Taught alternative subjects with enjoyable tasks to 20 students in an underprivileged elementary school

LEADERSHIP EXPERIENCE

President, The Turkish Intercultural Club, Northwestern University May. 2013 – Oct.2014

- Revived a dormant club, increased number of members from 0 to 10, through organizing activities and advertising
- Received funding to hold Turkish water marbling art workshops and classes with full attendance, promoted cultural interaction

Undergraduate Research Mentor, Northwestern University Feb. 2013 – Spring 2015

- Wrote proposals, mentored, trained, and directly supervised 2 undergraduate students for conducting research
- Supervised proposal writing and wrote letters of recommendation for summer internships and over \$12,000 in grants

Undergraduate Research Mentor, Sabanci University 2008 – 2009

- Supervised a senior student for his graduation project and guided him to present the work at an international conference and to write a peer-reviewed article that was published in a respected journal.

FELLOWSHIPS, AWARDS, & HONORS

- Fulbright Opportunity Grant Recipient (Reimbursement up to \$2260 for travel and visa costs) Aug. 2010
- Dr. Gursel Sonmez Research Award (Sabanci University) for being 1 of 4 top graduate student of year - \$800 June 2010
- Institute for Complex Adaptive Matter Junior Travel Grant, received 3 times
 - For performing experiments in the group of Prof. Francesco Stellacci at MIT, Boston - \$3,000 Dec. 2009-Jan. 2010
 - For presenting work at the 2008 Materials Research Society Meeting in Boston) - \$2,000 Dec. 2008
 - For presenting work at the 2007 Materials Research Society Meeting in Boston) - \$2,000 Dec. 2007
- Full fellowship (includes dorm and tuition) for M.S. study awarded by Sabanci University – \$39,000 Sep. 2008 – June 2010
- Graduate Student Fellow, for M.S. study awarded by the Turkish National Science Foundation - \$20,000 Oct. 2008-Aug. 2010
 - Given to only 100-150 applicants throughout the nation each year.
- Sabanci University, Faculty of Engineering and Natural Science, High Honor Certificate for 4 semesters
- Sabanci University High Honor Scholarship (tuition exemption and stipend) throughout undergraduate education for ranking 28th among 1.5 million applicants nation-wide university entrance exam - \$94,000 2003-2008

SKILLS AND INTERESTS

- **Languages:** *English:* fluent; *Turkish:* native fluency
- **Laboratory Skills:** Atomic force microscopy, scanning electron microscopy, transmission electron microscopy, grazing incidence X-ray diffraction, photoelectron spectroscopy, UV-Vis spectroscopy, optical microscopy, Fourier transform infrared spectroscopy, nanoindentation, dynamic light scattering, electrical characterization/probe station, solar cell fabrication, organic dye formulation, nanoparticle synthesis, polymer science, polymers, thin films, organic solar cells, nanocomposites, soft materials, self-assembly.
- **Computer Skills:** Microsoft Office, Origin, Adobe Illustrator, Adobe Photoshop, Macromedia Dreamweaver, C++
- **Other Interests:** Skiing, flamenco dancing, running, travelling, water marbling (ebru), cooking

PUBLICATIONS

1. A. Dannenhoffer, R. Kazantsev, A. Weingarten, J. Beokhoven, T. **Aytun**, L. Palmer, S. Stupp "Nucleation and Growth of Solution Dispersible Light-Absorbing Crystals via Molecular Self-Assembly" *in preparation*.
2. C. M. Rubert-Pérez, Z. Álvarez-Pinto, F. Chen, T. **Aytun**, S. I. Stupp "Mimicking the Bioactivity of FGF-2 Using Supramolecular Nanoribbons" *in preparation*.
3. A. Dannenhoffer, D. Fairfield, D. Huang, T. **Aytun**, H. Sai, L. Palmer, S. Stupp "Switching from Proton to CO₂ Reduction using pH Responsive Perylene Monoimide Assemblies" *in preparation*.
4. B. Harutyunyan, A. Dannenhoffer, S. Kewalramani, T. **Aytun**, D. Fairfield, S. Stupp, M. Bedzyk "X-ray Scattering Studies of 2D Nanosheets: Self-Assembled Photocatalytic Perylene Monoimide Amphiphiles" *submitted*.
5. R. Kazantsev, A. Dannenhoffer, A. Weingarten, B. Phelan, B. Harutyunyan, T. **Aytun**, D. Fairfield, A. Narayanan, J. Beokhoven, H. Sai, A. Senesi, P. O'Dogherty, L. Palmer, M. Bedzyk, M. Wasielewski, S. Stupp "Quantum Phase Transitions in Photocatalytic Supramolecular Scaffolds" *submitted*.
6. T. **Aytun**, P. J. Santos, C. J. Bruns, D. Huang, A. R. Koltanow, M. Olvera, S. I. Stupp "Self-Assembling Tripodal Small-Molecule Donors for Bulk Heterojunction Solar Cells" *J. of Phys. Chem. C* **120(7)**, 3602-3611 (2016).
7. T. **Aytun**^{*}, L. Barreda^{*}, A. Ruiz-Carratero, J. A. Lehrman, S. I. Stupp "Improving Solar Cell Efficiency through Hydrogen Bonding: Effects on Active Layer Morphology and Structure" *Chem. Mater.* **27(4)**, 1201-1209 (2015).
8. M. D. Yilmaz, T. **Aytun**, M. Frasconi, S. T. Schneebeli, S. I. Stupp, J. F. Stoddart, "Photocurrent generation from a low band gap and green BODIPY-based electrochromic polymer" *Synth. Met.* **197**, 52-57 (2014).

9. C. W. Ow-Yang, J. Jia, **T. Aytun**, M. Zamboni, A. Turak, K. Saritas, Y. Shigesato "Work function tuning of tin-doped indium oxide electrodes with solution-processed lithium fluoride" **Thin Solid Films** **559**, 58-63 (2014).
10. A. Ruiz-Carratero*, **T. Aytun***, C. Bruns, C. J. Newcomb, W.-W. Tsai, S. I. Stupp, "Stepwise Self-Assembly to Improve Solar Cell Morphology" **Journal of Materials Chemistry A** **1**, 11674-11681 (2013).
11. S. Sampath, A. N. Basuray, K. J. Hartlieb, **T. Aytun**, S. I. Stupp, J. F. Stoddart, "Direct Exfoliation of Graphite to Graphene in Aqueous Media with Diazaperopyrenium Dications" **Adv. Mater.** **25**, 2740-2745 (2013).
12. S. Inceoglu, **T. Aytun**, Y. Z. Menciloglu, I. Ozen, A. J. Avestro, M. H. Acar, "Morphological Similarity of a tri-block copolymer processed at ambient and elevated temperatures" **Korea-Australia Rheology J.** **24** (4), 313-321 (2012).
13. A. Turak, **T. Aytun**, Clewa Ow-Yang, "Solution Processed LiF Anode Modification for P3HT:PCBM Solar Cells" **Appl. Phys. Lett.** **100**, 253303 (2012).
14. A. Solmaz, **T. Aytun**, J. Deuschle, C.W. Ow-Yang, "Nanoscale Elastic Modulus Variation in Loaded Polymeric Micelle Reactors" **Langmuir** **28** (28), 10592-10596 (2012).
15. I.D. Tevis, W.-W. Tsai, L.C. Palmer, **T. Aytun**, S.I. Stupp, "Grooved Nanowires from Self-Assembling Hairpin Molecules for Solar Cells" **ACS Nano** **6** (3), 2032-2040 (2012).
16. **T. Aytun**, A. Turak, G. Halek, I. Baikie, F. Maye, C. Ow-Yang, "Solution-Processed LiF for Work Function Tuning in Electrode Bilayers" **Nano Lett.** **12** (1), 39-44 (2012).
17. O. el-Atwani, **T. Aytun**, O. F. Mutaf, V. Srot, P. A. van Aken, and C. W. Ow-Yang, "Determining the Architecture of ZnO Polystyrene-block-Poly(2-vinylpyridine) Micellar Reactors for ZnO Nanoparticle Synthesis", **Langmuir** **26** (10), 7431-7436 (2010).
18. **T. Aytun**, O.F. Mutaf, O.J. el-Atwani, C.W. Ow-Yang, "Nanoscale Composition Mapping of Segregation in Micelles with Tapping Mode AFM" **Langmuir** **24** (24), 14183-14187 (2008).

* equal contribution

SELECTED CONFERENCE PRESENTATIONS

1. **T. Aytun**, "Improving Solar Cell Efficiency Through Hydrogen Bonding: Effects on Active Layer Morphology", Nanotechnology for Development of Advanced Solar and Energy Devices; Ankara, TURKEY; Sep.22nd-24th 2014, *invited*.
2. **T. Aytun**, A. Turak, G. Halek, I. Baikie, C. Ow-Yang, "A Solution-Processed Alternative for Electrode Bilayers", Materials Research Society 2010 Fall Meeting; Boston, Massachusetts, USA; 29th Nov.-3rd Dec. 2010.
3. A. Solmaz, **T. Aytun**, J. Deuschle, C. Ow-Yang, "Chemomechanical Mapping of Metal Loaded Diblock Copolymer Micelles via Tapping Mode Atomic Force Microscope", Materials Research Society 2010 Fall Meeting; Boston, Massachusetts, USA; 29th Nov.-3rd Dec. 2010.
4. A. Solmaz, **T. Aytun**, O. F. Mutaf, C. W. Ow-Yang, "Relating the Nanoscale Compositional and Mechanical Property Variation in Micelle Reactors by TM-AFM", XI International Scanning Probe Microscopy Conference; Madrid; Spain; 17th-19th June 2009.
5. **T. Aytun**, O. F. Mutaf, O. el-Atwani, V. Srot, P. A. van Aken, C. W. Ow-Yang, "Reverse Diblock Copolymer Micelles used for the Synthesis of Inorganic Nanoparticles: Monitoring the Reaction Progress via Electron Microscopy and AFM", Materials Research Society 2008 Fall Meeting; Boston, Massachusetts, USA; 1st-5th December 2008.